Towards an Efficient Spin-Photon Interface Based on Cavity-Coupled NV Centres in Diamond Membranes



Laiyi Weng

Mansfield College

University of Oxford

A thesis submitted for the degree of

Doctor of Philosophy

Hilary 2020

Declaration of Authorship

I, Laiyi Weng, declare that this thesis titled, "Towards an Efficient Spin-Photon Interface Based on Cavity-Coupled NV Centres in Diamond Membranes" and the work presented in it are my own. I confirm that:

- This work was done wholly or mainly while in candidature for a research degree at this University.
- Where any part of this thesis has previously been submitted for a degree or any other qualification at this University or any other institution, this has been clearly stated.
- Where I have consulted the published work of others, this is always clearly attributed.
- Where I have quoted from the work of others, the source is always given. With the exception of such quotations, this thesis is entirely my own work.
- I have acknowledged all main sources of help.
- Where the thesis is based on work done by myself jointly with others, I have made clear exactly what was done by others and what I have contributed myself.

"*Keep it simple, keep it honest, keep it real. "*

Abstract

Quantum computation and information processing is an exciting multi-disciplinary field, whose objective is to harness the power of superposition and entanglement of quantum states to establish a new regime of computation for Mankind. This work demonstrates our efforts, in both materials and device engineering, towards building an efficient spin-photon interface for a promising solid-state spin qubit, namely the nitrogen-vacancy (NV) centre in diamond. Improvement in optical coherence of NV centre is realised via the novel laser-writing fabrication technique and quantified using high-resolution spectroscopy. A new metric concerning the charge-state stability of the NV centre is introduced to better translate the measured NV quality to entanglement generation efficiency. To address the low branching ratio of NV emission into the zero-phonon line (ZPL) transition, a hybrid open-cavity device incorporating low-dimensional micro-structured NV-containing diamond membrane is fabricated and characterised. In addition to the more commonly quoted emission enhancement factor, the collection efficiency of the cavity device is also quantified via numerical simulations. Combining all observed improvements in key metrics under the framework of double-heralding entanglement schemes, a two order of magnitude increase in entanglement generate rate can be expected. The established simulation methodology is widely applicable in the design and analysis of similar devices with an emitter-in-cavity setup.

Acknowledgements

It felt unreal when I first realised that I had spent almost a decade living in Oxford. Transitioning from an undergraduate to a research student was both challenging and exciting. Fortunately, the following years of my PhD were made so enjoyable thanks to all the past and present members of the Photonic Nanomaterials Group.

Firstly, I would like to express my gratitude towards the amazing post-docs in the group, Phil, Aurelien, Sam, Will, Shannon and Amit, for your training, advice and insightful discussions. Particular thanks go to Sam for your unconditional support, especially during my downtimes; you are an excellent role model both in and out of the lab. Shazeaa deserves a special thanks for bringing the group together and spoiling us with a constant supply of bakery. Thanks also go to Larry and Lucas for having spent many hours with me in the dark for the joint works. Further thanks must go to Ben, Andrew and Patrick for the collaboration on laser-writing projects.

I am also truly thankful to Hangyu Liu, Yunzhou Chen, Paul Hill, Ross Leyman and Prof. Erdan Gu at the University of Strathclyde for their enormous effort in developing the membrane fabrication techniques. Ben Green, Colin Stephen and Yashna Lekhai of the University of Warwick are gratefully acknowledged for the help with sample preparation. Phil, Aurelien and Lucas are acknowledged for cavity fabrication.

Of course, the greatest thanks have to go to my supervisor Prof.Jason Smith for his brilliant guidance and patient mentoring. It has always been enjoyable to discuss new ideas with you and learn from your analytical mindset. This project could not be completed without your support through some of the more difficult times.

Finally, I would like to thank my parents for your endless love and unconditional support. I have been living away from home since a young teenager, but you always have my back when things do not go as planned. I cannot be here without them.

Contents

Declaration of Authorship i

Abstract iii

Acknowledgements iv

Contents v

List of Figures xi

List of Tables xxiii

List of Abbreviations xxvi

Physical Constants xxvii

List of Symbols xxviii

1 Introduction and Literature Review 1

1.1 Measurement-Based Entanglement . . . 2

1.1.1 Entanglement Fidelity and Node Requirements . . . 5

1.1.2 Optical Coherence and Spectral Lineshapes . . . 8

1.1.3 Spectral Diffusion of Optical Transitions . . . 10

1.1.4 Frequency-Mismatched Photons . . . 12

1.1.5 Entanglement Success Probability . . . 14

1.2 NV Centres in Diamond . . . 15

1.2.1 Entanglement Generation with NVs . . . 18

1.2.2 Optical Coherence of NV ZPL Transitions . . . 20

1.2.3 Charge-State Stability Under Resonant Excitation . . . 21

1.3 NV Centres in Optical Resonators . . . 23

1.4 Project Goals and Thesis Outline . . . 27

2 Theoretical Background **31**

2.1 Nitrogen-Vacancy Centre in Diamond . . . 31

2.1.1 Electronic Structure of Negatively-Charged NV . . . 32

2.1.2 Excited-State Fine Structure at Low-Temperature . . . 33

2.1.3 Line-Broadening Effects of NV ZPL Transitions . . . 35

2.1.3.1 Temperature Broadening . . . 35

2.1.3.2 Spectral Diffusion . . . 36

2.1.4 Photo-Induced Charge-State Switching . . . 37

2.2 Cavity Quantum Electrodynamics . . . 39

2.2.1 Free-Space Spontaneous Emission . . . 40

2.2.2 In-Cavity Spontaneous Emission . . . 41

2.2.3 The Purcell Factor . . . 42

2.2.4 Emission Enhancement of Cavity-Coupled NVs . . . 43

2.3 Single-Medium Fabry-Perot Cavity . . . 45

2.3.1 Resonance Condition . . . 45

2.3.2 Finesse and Quality Factor . . . 46

2.3.3 The Transfer Matrix Model . . . 48

2.3.3.1 Field Propagation and the Propagation Matrix . . . 49

2.3.3.2 Interface Scattering and the Matching Matrix . . . 51

2.3.4 Distributed Bragg Reflector . . . 52

2.3.5 Solving for Single-Medium DBR Cavity . . . 54

2.3.6 Gaussian and Hermite-Gaussian Modes . . . 55

2.3.7 Transverse-Mode Coupling . . . 57

2.4 Hybrid-Medium Fabry-Perot Cavity . . . 59

2.4.1 Analytical Description . . . 59

2.4.2 Air-Like and Diamond-Like Modes . . . 61

2.4.3 Expected Finesse and Cavity Enhancement . . . 63

2.4.4 Scattering Loss at Diamond Membrane Surfaces . . . 65

3 Experimental Methods **68**

3.1 NV Generation and Membrane Fabrication . . . 68

3.1.1 Membrane Fabrication . . . 71

3.2 Dry Etching protocols . . . 72

3.3 X-Ray Photoelectron Spectroscopy . . . 73
3.4 Scanning Confocal Microscopy . . . 75
3.4.1 Cavity-Coupling Assembly . . . 76
3.5 Optical Characterizations . . . 78
3.5.1 Lineshape Fitting . . . 78
3.5.2 Excited-State Lifetime . . . 79
3.5.3 Power Saturation Measurement . . . 81
3.5.3.1 Dealing with Spatially Modulated Background . . . 82
3.5.4 Hanbury Brown-Twiss Measurement . . . 83
3.5.4.1 Dealing with Fluctuating Signal . . . 85
3.5.5 Dipole Orientation Determination . . . 86
3.6 Photoluminescence Excitation Measurement . . . 88
3.6.1 Post-Analysis Protocol and PLE Validation Rate . . . 90
3.6.2 Determination of ZPL Linewidths . . . 91
3.6.3 Charge-State Conversion Probabilities . . . 93
3.6.4 'Forced' and 'Conditioned' Repump Modes . . . 94

4 Finite-Difference Time-domain Simulation 95
4.1 Theoretical Background . . . 96
4.2 Simulation Setup . . . 99
4.2.1 Simulation Objects and Cavity Mirrors . . . 100
4.2.2 Monitor Placement . . . 101
4.2.3 Yee Cell Meshing Accuracy . . . 102
4.3 Analysis Methodology . . . 103
4.3.1 Time-Dependent Emission Analysis . . . 104
4.3.2 Spatially-Resolved Collection Analysis . . . 106
4.3.3 Predicting Observable Enhancement of Photon Output . . . 107
4.4 Simulation Figure of Merits . . . 109
4.4.1 Emission Enhancement Factor . . . 109
4.4.2 Cavity Quality Factor . . . 110
4.4.3 Cavity Finesse and Round-Trip Loss . . . 112
4.4.4 Calculating Mode Volume . . . 112
4.5 Single-Medium Air Cavity . . . 114

4.5.1 Depth of Cavity Feature: 0D-2D Interaction . . . 114
4.5.1.1 Modulation of 2D Guided Modes . . . 116
4.5.2 Cavity Length Tuning: Short- v.s. Long-Cavity Limit . . . 117
4.5.3 Radius of Curvature: Beam Penetration and Coating Materials . . . 119
4.5.3.1 Beam Focusing Effect in Short-Cavity Limit . . . 119
4.5.3.2 Trends in Long-Cavity Limit . . . 122
4.5.4 Mirror Reflectivity: Optimising Device Photon Output . . . 123
4.6 Hybrid-Medium Air-Diamond Cavity . . . 126
4.6.1 Dipole Emission in Free-Standing Membrane . . . 126
4.6.2 Photon Output of Air-Like and Diamond-Like Modes . . . 128
4.6.3 Other Cavity Figure of Merits . . . 130
4.6.4 Fitting Simulated Cavity Mode Map with Analytical Model . . . 131
4.7 Conclusions . . . 133

5 NV Centre in Diamond Membranes 135

5.1 Membranes with Ion-Implanted NVs . . . 135
5.1.1 Ion-implanted NVs in Bulk Samples . . . 135
5.1.1.1 Implantation Parameters . . . 136
5.1.1.2 Defect Density and Implantation Yield . . . 137
5.1.1.3 ZPL Distribution of Implanted NVs . . . 139
5.1.2 NV Quenching in First Generation Membranes . . . 140
5.1.2.1 XPS Investigation and Fabrication Optimization . . . 141
5.1.3 NVs in Second Generation Membranes . . . 143
5.1.3.1 Surface Morphology of Second Generation Membranes . . . 144
5.2 Membranes with Laser-written NVs . . . 146
5.3 Optical Coherence of NV ZPL Transitions . . . 149
5.3.1 Sample Catalogue . . . 149
5.3.2 637nm Excitation Power Optimization . . . 150
5.3.3 575nm Repump and Long-Lived Dark State . . . 152
5.3.4 Transition Linewidths Comparison . . . 155
5.3.5 Switching Probabilities and Long-Lived Bright States . . . 157
5.4 Conclusions . . . 159

6 Low-Temperature Cavity-Coupling of NV ZPL **162**

6.1 On-Mirror Characterization . . . 163

6.1.1 Spectrum Analysis and ZPL Branching Ratio . . . 164

6.1.2 Power Saturation and ZPL Branching Ratio . . . 166

6.1.3 Excited-State Lifetime and HBT . . . 168

6.1.4 Polarization and Dipole Orientation . . . 169

6.1.5 Summary of On-Mirror Characterization . . . 171

6.2 Benchmark Cavity Characterizations . . . 171

6.2.1 Finesse of Single-Medium Cavity . . . 172

6.2.2 Low-Temperature System Linewidth Stability . . . 174

6.3 Cavity-Coupling of A4-NV4 . . . 176

6.3.1 Excited-State Lifetime . . . 177

6.3.2 Power Saturation of Cavity-Couple ZPL . . . 179

6.3.3 HBT Measurement . . . 180

6.3.4 Membrane Thickness at Location of A4-NV4 . . . 182

6.3.5 Finesse of Hybrid-Medium Cavity . . . 183

6.3.6 Cavity D5 - Only ZPL Power Saturation . . . 185

6.3.7 Summary of In-Cavity Characterization . . . 186

6.4 Preliminary Emission Rate Analysis . . . 186

6.5 Conclusions . . . 188

7 FDTD Analysis of Cavity-Coupling Results **190**

7.1 Analysis Methodology Adaptation . . . 190

7.1.1 Modifications to Emission Analysis . . . 191

7.1.2 Constructing Free-Space NV Spectrum . . . 193

7.1.3 Calibrating Analytical ZPL Branching Ratio . . . 194

7.1.4 Emission and Collection Analysis - Membrane-On-Mirror . . . 196

7.1.5 Validating Analytical ZPL Linewidth with Convergence Test . . . 197

7.1.6 Lateral Photon Channeling in Membrane . . . 198

7.2 Ideal High-Q Cavity Simulation . . . 200

7.2.1 Simulation Setup and Cavity Mode Structure . . . 201

7.2.2 Emission Analysis . . . 205

7.2.3 Validating Analytical ZPL Linewidth . . . 206

7.2.4 Collection and ZPL Output Analysis . . . 207
7.2.5 High-Q Simulation vs Experimental Data . . . 209
7.3 Realistic Low-Q Cavity Simulations . . . 209
7.3.1 Shallow Low-Q Cavity . . . 210
7.3.2 Deep Low-Q Cavity . . . 212
7.3.3 Low-Q vs Experimental Data . . . 214
7.4 Completing the Emission Rate Analysis Table . . . 215
7.4.1 Emission Analysis with an Alternative Approach . . . 216
7.5 Conclusions . . . 217

8 Conclusions and Outlook **219**
8.1 Conclusions . . . 219
8.2 Future Prospects . . . 222

Bibliography **225**

List of Figures

1.1 Illustration of a measurement-based entanglement setup with two qubits, a 50/50 beam-splitter and two detectors. Both qubits have an identical L-shaped level structure where $|0\rangle$ and $|1\rangle$ are long-lived states and $|1\rangle$ is connected to $|e\rangle$ by resonant excitation. The transition between $|0\rangle$ and $|e\rangle$ is prohibited by certain selection rules. Reprinted with permission from [11]. 3

1.2 The coherent optical control of ZPL transitions with a post-selection scheme. Reprinted with permission from [20]. 12

1.3 Entanglement fidelity **(a)** in the bad detector regime and **(b)** in the intermediate detector regime. Δ_{em} is the frequency-detuning between incident photons, κ_{eff} is the cavity-coupled emission rate of the qubits and γ_{dt} (γ_{r} in plot) is the detector response rate where the detector timing resolution is $t_{\text{dt}}=1/\gamma_{\text{dt}}$. Reprinted with permission from [26]. 14

1.4 **(a)** An illustration of NV's optical transitions between its $^3A_2$ ground-state and the ^3E excited-state. Red lines mark the radiative transitions, and blue lines mark the strong (solid) and weak (dashed) non-radiative transitions. Adapted from [30]. **(b)** A typical NV PL spectrum at 4K where only ≈4% of the photon is branched into the ZPL transition. . . . 16

1.5 An illustration of entanglement generation under the Barrett & Kok scheme using NV centres in diamond. The two spin-dependent ZPL transitions used in the procedure are the non-cyclic A_1 transition for spin-polarisation, and the cyclic E_{y} transition for optical readout (more details about NV electronic structure in section (2.1)). Reprinted with permission from [22]. 18

1.6 **(a)** The transition frequency tuning of the ZPL transitions between two NV centres. The depicted A_1 and E_{y} transitions (more details in section (2.1)) are selected for entanglement generation as illustrated in fig. (1.5). **(b)** Demonstration of indistinguishable photon generation. Reprinted with permission from [22]. 19

1.7 The charge-state and post-selection procedures before attempting for entanglement generation operations. Reprinted with permission from [22]. . 22

1.8 **(a)** A microring resonator, reprinted with permission from [49]. **(b)** The 1D and 2D photonic crystal cavitiesm, reprinted with permission from [45, 51].**(c)** The Fabry-Perot microcavities. 25

1.9 Illustration of project goals including **(a)** the realisation of membrane-in-cavity setup and **(b)** the usage of laser-writing technique for coherent NV generation in diamond membranes. 27

2.1 **(a)** The nitrogen-vacancy centre in diamond. Reprinted with permission from [30]; **(b)** A typical NV spectrum containing both NV^0 and NV^-. Reprinted with permission from [58]. 32

2.2 **(a)** The energy level structure of NV^- charge-state where the green box shows the states of interest. Adapted from [59]; **(b)** The spin-polarization process between the NV ground- and excited-states at room temperature. The red lines mark the radiative transitions and solid (dashed) blues lines represent strong (weak) non-radiative transitions. Adapted from [30]. . . 33

2.3 **(a)** The evolution of excited-state sub-levels under the influences of spin-orbit, spin-spin and transverse strain Adapted from [61]; **(b)** Excited-states fine structure plotted as a function of transverse strain δ_x. In addition to the parameters shown in **(a)**, a spin mixing term Δ'' is also included in the spin-Hamiltonian. Calculation based on the model established by [60]. . . 34

2.4 The temperature dependence of ZPL linewidth. Reprinted with permission from [37]. 36

2.5 A PLE dataset taken from a laser-written NV centre to demonstrate the effect of spectral diffusion. 37

2.6 Wavelength dependent conversion cycle between NV^0 and NV^-. Reprinted with permission from [65]. 38

2.7 Illustration of the bi-directional charge-state conversion processes of NV centres: **(a)** NV^- is converted to NV^0 by absorbing two photons in succession which is followed by an Auger process to leave a free-moving electron in the conduction band; **(b)** NV^0 is converted to NV^- by absorbing two photons in succession which leaves a free-moving hole in the conduction band. Reprinted with permission from [41]. 38

2.8 Illustration of a two-level atom in an optical resonator. Adapted from [13]. 39

2.9 An illustration of a planar-planar Febry-Perot cavity with supported resonant modes with a mode index of q=1, 2, 10. 45

2.10 Cavity transmission spectrum: **(a)** in frequency units; **(b)** in phase units with varying coefficient of finesse F_c showing cavity linewidth variation. . 46

2.11 **(a)** Calculated $\mathcal{F}$ using eqs. (2.36), (2.38) and (2.39). **(b)** The percentage difference between $\mathcal{F}_{exa}$ (eq. (2.36)) and $\mathcal{F}_{loss}$ (eq. (2.39)). At R= 0.95 the error is 2.5%. 47

2.12 Illustration of field propagation through a lossless homogeneous medium. 49

2.13 Illustration of field scattering at the interface between two different dielectric media. 51

2.14 Illustration of a DBR stack with a normal incident plane wave propagating from left to right. All layer thicknesses are $\frac{1}{4}\lambda$. 52

2.15 **(a)** Field propagation profile through a N=5 DBR stack; **(b)** The mirror transmission spectrum with increasing N. 53

2.16 The electric field profile along z-axis calculated using the transfer matrix model. 54

2.17 Calculated **(a)** cavity transmission spectrum and **(b)** cavity finesse $\mathcal{F}$ as a function of DBR pair number N. The transfer matrix results $\mathcal{F}_{\text{tmm}}$ are compared to $\mathcal{F}_{\text{ana}}$ from eq. (2.38) and $\mathcal{F}_{\text{loss}}$ from eq. (2.39). 54

2.18 Calculated **(a)** cavity transmission spectrum and **(b)** cavity finesse $\mathcal{F}$ as a function of cavity mode index q. The transfer matrix results $\mathcal{F}_{\text{tmm}}$ are compared to $\mathcal{F}_{\text{ana}}$ and $\mathcal{F}_{\text{loss}}$ from section (2.3.2). 55

2.19 The schematic drawing of the Gaussian beam expression. 55

2.20 A fundamental Gaussian mode supported by a planar-concave cavity. Additional phase shift of $\pi/2$ is applied to create a node at the surface of the planar mirror. $\mathcal{R}$ is the mirror radius of curvature. 57

2.21 Mode profile of **(a)** the $\text{TEM}_{5,0,0}$ and **(b)** the $\text{TEM}_{4,2,4}$ modes. These two modes are both supported by a cavity length of $L_q \approx L_{q-1}$, suggesting coupling interaction between the two is likely. 58

2.22 An illustration of a planar-planar Fabry-Perot with two different media. . 59

2.23 Cavity mode structure of a hybrid-medium cavity visualized as **(a)** a deviation from a single-medium cavity or **(b)** the hybridization of the diamond-like and air-like modes in each sub-cavity medium. Diamond membrane thickness t_{d} is set to 1500nm. 61

2.24 The field intensity profiles of **(a)** an air-like mode cavity and **(b)** an diamond-like mode cavity. Both graphs are calculated using 1D TMM. 62

2.25 The energy density profiles of **(a)** an air-like mode cavity and **(b)** an diamond-like mode cavity. Compared to fig. (2.24), the energy density profile gives a better visualization of the spatial extend of the cavity mode. 62

2.26 **(a)** A comparison between expected cavity finesse calculated using analytical and numerical TMM descriptions. **(b)** The numerical 'modal length' L_{mod} calculated using TMM treatment. 64

2.27 Calculated expected cavity enhancement F which is proportional to $q\mathcal{F}_{\text{tmm}}/L_{\text{mod}}$. 65

2.28 Calculated $\mathcal{F}_{\text{ana,scat}}$ and $\mathcal{F}_{\text{loss,scat}}$ for **(a)** a low-R and **(b)** a high-R cavity as a function of RMS surface roughness σ, both in log-log scales. The R= 0.998/0.99999 mirror pair is also the specification used in our experimental setup. 66

3.1 A flow chart of sample preparation and NV fabrication steps in bulk diamond plates. 69

3.2 Illustration of different vacancy creation methods: **(a)** conventional ion-implantation followed by annealing; **(b)** single-pulse laser-writing technique followed by annealing. 70

3.3 Experimental apparatus designed for acid boiling treatment. The diamond sample is placed in the glass thimble, which has a porous filtering base, and nitrate salt is added into the thimble. The thimble is then placed in a standard beaker where the acid is added to immerse the sample and nitrate salt. 71

3.4 The diamond membrane fabrication workflow, starting the bulk sample contains a layer of fabricated NVs near surface. Detailed description in text. 72

3.5 The ICP/RIE dry etching equipment. Photon and illustration in courtesy of Hangyu Liu. 73

3.6 An example of XPS spectrum obtained from the as-received CVD diamond sample. 74

3.7 A schematic drawing of the beam scanning confocal microscope used in this work. 75

3.8 **(a)** The experimental apparatus for low-temperature experiments. **(b)** An photo of the confocal microscope on top of the bath cryostat in the enclosure box. 76

3.9 **(a)** An illustration of the cavity assembly used in this work where all the piezo positioners are from Attocube. The top five mini-piezos are ANGt50, ANGp50, ANPx51 (x2) and ANPz51. The bottom long-range piezos are ANPx100 (x2) and ANPz100. The low-temperature objective lens is LT-ASWDO/0.82. **(b)** An image of a 4x4mm diamond membrane on the planar mirror. **(c)** An image of a 300x300μm featured mirror. 77

3.10 **Left:** Calculated Voigt linewidth w_{V} given a fixed Lorentzian linewidth w_{L} and a varying Gaussian linewidth w_{G}. **Right:** Plots of a pure Lorentzian profile, a pure Gaussian profile and a Voigt profile obtained by convoluting the former two functions. The broadening effect due to the Gaussian contribution is better visualized as the difference between the Voigt profile and the Lorentzian profile $w_{\mathrm{V}}-w_{\mathrm{L}}$ instead of w_{G}. 78

3.11 A schematic drawing of excited-lifetime measurement setup. The dashed orange line represents the fibre connections. 79

3.12 An example of lifetime data which is fitted with a tri-exponential decay function. The fitted lifetimes in the are t_{def}= 13.92ns, t_{bg}= 0.96ns and t_0= 0.07ns. 80

3.13 A P_{sat} measurement with spatially uniform background fitted with a simple saturation function. 81

3.14 **(a)** The linear I_{bg} fitting scheme. In the bottom panel A_{lin} is left as a free parameter. **(b)** The polynomial I_{bg} fitting scheme. The fit in bottom panel utilized the analytically extracted H_{bg} in the top panel and the scaling factor A_{pol} is left as a free parameter. 82

3.15 A schematic drawing of the experimental setup of HBT measurement. The dashed line represents fibre connections. 83

3.16 Illustration of dipole **(a)** rotation and **(b)** projection on to the x-y plane. 86

3.17 Workflow diagram of PLE measurement. Most of the device control units and data acquisition sequences are synchronized against a trigger pulse from the 637nm laser control unit. 89

3.18 An illustration of PLE measurement sequence in the 'force repump' mode. 89

3.19 Examples of PLE scans of NV ZPL transitions **(a)** when no photo-ionization took place, and **(b)** where a half-peak signal was recorded due to mid-scan photo-ionization. 90

3.20 PLE data post-analysis algorithm for obtaining reliable measurement of homogeneous linewidth of NV ZPL transition. 91

3.21 The overall ZPL linewidth is obtained by fitting the summation of all scan1 data and the homogeneous ZPL linewidth is obtained by fitting a Lorentzian function to the summation of all validated scan1 data. 92

3.22 Histograms and geometric distributions fits to obtain **(a)** the recharge probability p_{rec}=0.71 and **(b)** the ionization probability p_{ion}=0.06. Given that p_{val}=0.93 which is larger than p_{rec} and p_{ion} is very small, this laser-written NV is very favourable for entanglement generation. 93

3.23 Measurement sequence with 'conditioned repump'. 94

4.1 An illustration of the Yee cell: the electric field components are calculated along the edges and the magnetic field components are calculated perpendicular to the faces. 97

4.2 **(a)** An illustration of simulated cavity structure including both the planar and the featured mirrors. The blue arrow represents the electric dipole source. **(b)** An schematic drawing showing the main geometric variables: cavity length L, depth of cavity feature L_{depth}, cavity radius of curvature $\mathcal{R}$ and mirror separation L_{2D}. 100

4.3 Illustration of simulation monitor setup: **(a)** the f-domain edge monitors; **(b)** the f-domain cross-section monitors; **(c)** the index monitor, f-domain beam profile monitor and t-domain field decay monitors. The f-domain monitors are marked in orange, the t-domain monitors are marked as red cross, the index monitor is in blue and dipole source is marked as the blue arrow. 101

4.4 **(a)** The rendered 'step' geometry of the cavity feature at accuracy setting 3. **(b)** Various mesh accuracy settings and the corresponding average cell sizes and simulated mode positions. 103

4.5 Mesh cell size convergence test. 103

4.6 Illustration of the dividing line between the 'cavity photon' and the non-cavity photon' temporal groups: **(a)** the time signal of the initial dipole pulse; the corresponding t-domain data from **(b)** a q=16 long cavity and **(c)** a q=2 short cavity. The actual field decay time is much longer than the plotted time axes. 104

4.7 The simulation timeline comparison between the cavity and non-cavity sub-simulations. 105

4.8 Field profile of the simulation region for **(a)** the cavity photon group from the main simulation and **(b)** the non-cavity photon group from the secondary simulation. 105

4.9 Monitors associated with each spatial loss channels. 106

4.10 Experimental configurations corresponding to different dielectric environment: (a) the free-space bulk configuration; (b) the membrane-on-mirror configuration; (c) the membrane-in-cavity configuration (including the on and off-resonance scenarios). 108

4.11 An example of a stable Q convergence test on the t-domain data range. . 111

4.12 Illustration of cylindrical symmetry used for mode volume approximation. 113

4.13 A comparison between mode volume by integration V_{int}, mode volume by enhancement V_{eff} and mode volume by Gaussian mode analysis V_{ana} for a $\mathcal{R}$=3μm cavity. 114

4.14 **(a)** A schematic illustration of L_{depth} dependence investigation. **(b)** Summary of data obtained from a radius of curvature $\mathcal{R}$=2μm cavity at cavity length of q=1 to 4 while varying L_{depth}. Plot is in log scale for better visualization. 115

4.15 The cavity mode cross-section profile for the $\mathcal{R}$=2μm q=4 cavity at **(a)** the short-cavity and **(b)** the long-cavity limit. 115

4.16 Illustration of the supported guided modes in a multi-layer structure for $L_{2\text{D}}$= $\lambda/2$, $\lambda/4$ and $\lambda/8$. The $\lambda/2$ intra-cavity layer supports the most guided modes whereas in the $\lambda/8$ case half of the guided modes are not supported. The $\lambda/4$ layer combines with DBR layers to support guided modes. 116

4.17 Plots showing the effect of mirror separation modulation extends to **(a)** cavity confinement capabilities and **(b)** photon collection distributions. . 117

4.18 **(a)** A schematic of cavity length q tuning and **(b)** the obtained $P_{\text{out}}^{\text{dev}}$ results. 118

4.19 The distinction between short- and long- cavity limit visualized in **(a)** cavity quality factor Q plot and **(b)** cavity finesse $\mathcal{F}$ plot. The TMM Q does converge towards the analytical Q in large q limit. 118

4.20 **(a)** Collection and **(b)** emission analysis of the $\mathcal{R}$=4μm cavity, as a function of mode index q. 119

4.21 **(a)** A schematic drawing of $\mathcal{R}$ and **(b)** the obtained $P_{\text{out}}^{\text{dev}}$ graph. 119

4.22 **(a)** The collection analysis in absolute photon collection P_{ch} and **(b)** the emission analysis F, both as a function of $\mathcal{R}$ for q=1 cavities. 120

4.23 The mode profiles of **(a)** the $\mathcal{R}$=2μm and **(b)** the 12μm cavities. 120

4.24 Comparison of the energy density product distribution for **(a)** $\mathcal{R}$=2μm and **(b)** 12μm. Note that the energy density maxima in the $\mathcal{R}$=2μm cavity is located within the DBR coating layers (red arrow). 121

4.25 Cavity simulation results of Ta-Si versus Ti-Si coating systems: **(a)** overall photon output $P_{\text{out}}^{\text{dev}}$, **(b)** quality factor Q and **(c)** mode volume V_{eff} in comparison with analytical model. 122

4.26 **(a)** The ZPL photon output $P_{\text{out}}^{\text{dev}}$ and **(b)** the collection analysis P_{ch} for a medium/long cavity at q=5, as a function of $\mathcal{R}$. 123

4.27 **(a)** The cavity Q and V_{eff} and **(b)** the resulting emission enhancement F for a medium/long cavity at q=5, as a function of $\mathcal{R}$. 123

4.28 **(a)** Device ZPL photon output $P_{\text{out}}^{\text{dev}}$ and **(b)** emission enhancement F analysis for a medium-sized (q=4 given q_{max}=9) $\mathcal{R}$=3µm cavity as a function of increasing DBR pairs N_{plan}-N_{feat}. 124

4.29 The channel-dependent cavity loss distribution in terms of absolute photon output P^{ch} for a medium-sized (q=4 given q_{max}=9) $\mathcal{R}$=3µm cavity as a function of increasing DBR pairs N_{plan}-N_{feat}. 124

4.30 Simulated **(a)** ZPL photon output $P_{\text{out}}^{\text{dev}}$ and **(b)** emission enhancement F from both the short- and long-cavity simulations as a function of N_{plan}. . 125

4.31 Collection analysis in the **(a)** short-cavity and **(b)** long-cavity limit (q=4) while varying N_{plan}. 125

4.32 Free-standing membrane simulations with membrane thickness at q_{d}=1 and q_{d}=1.5. The total photon output P_{out} is calculated for both top and bottom collection. 127

4.33 **(a)-(b)** The dipole emission profile of the q_{d}=1 and q_{d}=1.5 diamond membrane on a DBR mirror. 127

4.34 Simulated energy density profiles $n^2|\mathcal{E}|^2$ for **(a)** the air-like mode and **(b)** the diamond-like mode. 128

4.35 Simulated **(a)** photon output P_{out} and emission enhancement F for both types of modes. 129

4.36 Simulated collection analysis: **(a)** the air-like hybrid-medium cavity; **(b)** the diamond-like hybrid-medium cavity; **(c)** the single-medium cavity. . . 129

4.37 Comparison of **(a)** cavity quality factor Q and **(b)** mode volume V_{int} between the hybrid-medium and the single medium cavity. 130

4.38 Simulated cavity mode map for **(a)** the air-like mode and **(b)** the diamond-like mode. The x-axis is in frame-number instead of cavity length because a length re-scaling is required to adapt the numerical simulation to 1D analyitcal model. 131

4.39 Fitting the cavity mode map of th air-like mode at q_{d}=2. Fitting is done separately for each mode family. 132

4.40 Fitting the cavity mode map of the diamond-like mode at q_{d}=2.5. Fitting is done separately for each mode family. 132

5.1 Cross-polar images revealing strain distribution in **(a)** a CVD and **(b)** a HPHT bulk sample; **(c)** A DiamondView image showing growth sector boundaries in the HPHT sample. 136

5.2 SRIM simulation results showing the average ion stopping range for the ion energies at **(a)** 75KeV and **(b)** 52KeV. 137

5.3 Preliminary room-temperature characterizations to confirm the creation of NV centres after ion-implantation and annealing. 137

5.4 Low temperature confocal scans from all four samples: NVs with a single ZPL are circled in white; NVs with ≥2 ZPL are circled in red; non-NV defects or unstable NVs are marked with black crosses. 138

5.5 The summations of all NV spectrum (>100 on average) measured in each ion-implanted sample. The overall ZPL distribution of sample A, B and D are fitted with a Gaussian FWHM of 0.086nm, 0.064nm and 0.045nm respectively. 140

5.6 An example of observed defect quenching under laser exposure in the first generation samples. 141

5.7 The chlorine-related XPS trace at around 200eV binding energy measured from **(a)** Gen1-m1 and **(b)** Gen1-m2 membranes. 142

5.8 **(a)** A typical confocal scan image of a 25x25μm area showing reduced NV density in membrane Gen2-m2; **(b)** PL emission spectrum of NV5 in the area. The background baseline in HBT data gives an estimate of the minimal $g^{(2)}(0)$ achievable given the background count rate at the NV location. 144

5.9 **(a)** The excited-state lifetime and **(b)** HBT results of NV5 in the area. The background baseline in HBT data gives an estimate of the minimal $g^{(2)}(0)$ achievable given the background count rate at the NV location. . . 144

5.10 Optical microscope images of sample Gen2-m3: **(a)** stock plate as received from laser-slicing at 30μm thickness; **(b)** sample at 5μm transferred to the DBR mirror after bulk-thinning on a silicon wafer; **(c)** finished membrane after final pure O_2 etch on the DBR mirror. 145

5.11 AFM scans of **(a)** Gen2-m2 and **(b)** Gen2-m3 after the O_2 etching recipe adjustment where improvement in surface quality has been shown on both samples. Sparse etching pits as appeared in **(a)** remains a problem even with the improved O_2 etch recipe. 146

5.12 **(a)** The laser-writing fabrication plan. The writing is carried out at five depths indicated by different colours. **(b)** Because the writing is not carried out at near-surface locations, the 30μ post-slice sample has to be etched from both sides. 147

5.13 Confocal scanning images **(a)** before annealing and **(b)** after annealing. The zoomed-in image in **(a)** shows the GR1 visibility threshold at row11. After annealing, the NVs formed beyond this row are expected to have the least lattice damage. 148

5.14 The PL spectrum at laser-written sites: **(a)** clear GR1 feature at 740nm is observed before annealing; **(b)** NV ZPL is observed at 637nm after annealing. 148

5.15 Example of ZPL linewidth extracted from PLE data of ion-implanted NV66 in sample B: **(left)** the raw scan1 dataset; **(right)** validated and aligned scan1 sequences. 150

5.16 A dataset of raw PLE measurement validate rate p_{val} versus 637nm excitation power taken from NV66 in sample B. The power settings are coarsely divided into two groups. 151

5.17 **(a)** The averaged PLE signal intensity above background (≈140cts/s) and **(b)** the homogeneous linewidth $\delta\nu_{\text{hom}}$ as a function of 637nm excitation power. Some power broadening is observable, but there is not enough data point to get a good fit. 151

5.18 The emission spectrum of the supercontinuum laser when set to 575nm emission wavelength. 152

5.19 500 measurement sequences using **(a)** 575nm and **(b)** 532nm repump lasers. Both scan1 and scan2 data are shown before validation process. . . 153

5.20 Number of using **(a)** 575nm and **(b)** 532nm repump lasers. 153

5.21 Linewidth measurement using both 575nm and 532nm repump lasers. The homogeneous linewidths are fitted to be $\delta\nu_{\text{hom}}$=260/400MHz and the total linewidths are $\delta\nu_{\text{tot}}$=11.2/4.2GHz (575nm/532nm). 154

5.22 A scatter plot of total and homogeneous linewidth from all samples listed in table (5.6). Sample B/C are grouped together as 'ion-implanted CVD, bulk' and sample G/H are grouped together as 'laser-writing CVD, shallow'. 155

5.23 A PLE dataset from NV3 in sample F: **(a)** summary of 1000 raw scans and **(b)** a scatter plot of single-scan linewidth versus relative resonance position. The data points that are closer to the blue dotted line suffers less from the spectral diffusion. 156

5.24 A comparison of PLE validation rate p_{val} for the ion-implanted and laser-written NVs. 157

5.25 A scatter plot of the recharge probability p_{rec} against the validation rate p_{val}. Data from all NVs from all samples listed in table (5.6) are included. 158

5.26 The recharge probability p_{rec} plotted against the ionization probability p_{ion}. Data of p_{ion} is only available from laser-written NVs under 'conditioned' repump mode. The blue dashed line is a visual guidance of $p_{\text{rec}}+p_{\text{ion}}=1$. 159

5.27 Histograms of recharge/ionization probability calculation from a laser-written NV8 in sample F. 159

6.1 Experimental configurations corresponding to different dielectric environment: **(a)** the free-space bulk configuration; **(b)** the membrane-on-mirror configuration; **(c)** the membrane-in-cavity configuration (including the on and off-resonance scenarios). The NV location is marked with red dotted circles. 162

6.2 An optical microscope image of the Gen2-m3 membrane: **(left)** showing the whole membrane sample; **(right)** a zoomed-in image of the area of interest. The mirrored 't3' mark is a graphitic orientation marker engraved by laser-writing and the faint rectangular grids (150μm across) are the FIB-milled registration marks for defect relocation. 163

6.3 On-mirror PL images of Gen2-M3 sample in area **(a)** A1 and **(b)** A4. All the spectrum-confirmed active NVs in the areas are marked with red circles. Excitation power of 532nm laser is around 1.5mW. 164

6.4 Zoomed-in PL images of A4-NV4 **(a)** without any collection filter and **(b)** with a narrow-band 638/3nm band-pass filter. 164

6.5 The low-temperature NV spectrum **(a)** over the entire NV emission range and **(b)** around both the NV^0 and NV^- ZPL regions. Both the spectrum are in low-resolution setting of the spectrometer with a resolution of 0.13nm. 165

6.6 An example showing false background subtraction due to fluorescence modulation resulting in a negative area under the curve. Data were taken from A4-NV13 from the same area. 166

6.7 Power saturation measurement of A4-NV4: **(a)(c)** from the full spectral range; **(b)(d)** in the ZPL region only. Both background components in the 'total signal' dataset are calibrated with a polynomial fit H_{bg} of the 'spatial background' dataset with a scaling factor A_{pol}. 167

6.8 **(a)** The excited-state lifetime of A4-NV4 taken at room-temperature and **(b)** the fitting parameters used. 168

6.9 **(a)** Room-temperature HBT measurement of A4-NV4 and **(b)** the corresponding fitting parameters used. 169

6.10 Dipole orientation measurement of the strain-splitted ZPL transitions. . . 170

6.11 A map of cavity features on the high reflectivity cavity mirror that is used in this chapter. 172

6.12 A typical cavity mode spectrum taken at integration time of 0.05sec using the supercontinuum laser excitation in transmission setup. 173

6.13 Fitted cavity linewidth versus spectrometer integration time in bath cryostat on the isolation enclosure platform. 174

6.14 A comparison of cavity mode shape between **(a)** a low-temperature spectrum integrated for 60sec and **(b)** a room-temperature spectrum integrated for 20secs. 175

6.15 **(a)** 60 frames of cavity-coupled NV ZPL spectrum over a span of 1hr. Each frame has an integration time of 60sec. **(b)** Integrated the photon count rate from each spectrum frame in **(a)**. 175

6.16 Confocal scanning image of a cavity formed at the location of A4-NV4 with the B5 cavity feature. 176

6.17 Scanning confocal PL images at the A4-NV4 location **(a)** without and **(b)** with a 638/3nm narrow band-pass filter. 177

6.18 High resolution cavity spectrum map showing the fundamental mode of the q=16 mode family sweeping through the ZPL of A4-NV4 **(a)** in tuning voltage scale and **(b)** with voltage scale calibrated to optical length scale. Using eq. (2.68), a fit to the mode tuning is drawn as a red line in **(b)**. The color scale of is adjusted to better show the sweeping direction. . . . 177

6.19 The **(a)** excited lifetime and **(b)** spectrum data taken at four different cavity mode positions. The lifetime data at position 4 is taken with a different bin width and fitted with a single exponential decay to accommodate the low count rate at that mode position. . . . 178

6.20 Cavity-coupled ZPL power saturation data: **(a)** calibration of H_{bg} with the off-defect 'spatial background' dataset; **(b)** 'total signal' fitted with eq. (3.10) given H_{bg} and a free-fitting scaling factor A_{pol}. . . . 180

6.21 HBT of the cavity-coupled ZPL emission from A4-NV4. The ZPL emission is spectrally filtered with a 638/3nm narrow band-pass filter. The lower-bound and upper-bound background baselines are obtained from on-resonance and off-resonance signal-to-noise ratios, respectively. They indicate the expected range of $g^{(2)}(0)$ value if no background emission is present. . . . 181

6.22 A single cavity mode spectrum of a hybrid-medium cavity showing the variation of longitudinal mode spacing which makes the identification of cavity mode index less trivial. . . . 182

6.23 Cavity mode maps from a $\mathcal{R}$=25μm cavity in **(a)** original piezo tuning voltage axis and **(b)** fitted and re-scaled optical cavity length axis. The calculated mode positions of all five longitudinal modes are plotted in **(b)** as red solid lines using the fitting parameters obtained from eq. (2.68). . . . 183

6.24 The cavity mode spectrum of the fundamental modes from the q=16-18 mode families in the hybrid-medium air-diamond cavity. . . . 184

6.25 Mode structure of cavity D5 at q=11. . . . 185

6.26 Cavity-coupled ZPL power saturation data from cavity D5: **(a)** H_{bg} with off-defect 'spatial background' data; **(b)** 'total signal' fitted with eq. (3.10) given the calibrated H_{bg} from **(a)**. . . . 185

7.1 Extracting parameters for the PSB profile S^0_{psb} from a reference PL spectrum from a reference NV in a bulk lattice. . . . 193

7.2 **(a)** Index profile in x-z cross-section to show the simulation structure. **(b)** The dipole emission profile in x-z cross-section. The dipole is placed 66nm away from the DBR-diamond interface. . . . 195

7.3 Plots of **(a)** he simulated device enhancement spectrum $F^{\text{mir}}(\lambda)$ and the calculated emitter spectrum $S^0(\lambda)$ using w_{zpl}=2GHz and ζ^*=5.9%; **(b)** the combined emitter-cavity enhancement spectrum $F^{\text{mir}}(\lambda)S^0(\lambda)$. . . . 195

7.4 Convergence test of the ZPL linewidth w_{zpl} term in $S^0(\lambda)$ and its influence on key variable including the emission enhancement factors and ZPL branching ratio. . . . 198

7.5 **(a)** Index profile in x-z cross-section to show the simulation structure. **(b)** The dipole emission profile in x-z cross-section. The dipole is placed 66nm away from the top surface. 199

7.6 The simulated emission spectrum $F^{\text{mem}}(\lambda)$ of the membrane-only simulation. 199

7.7 2D cross-section plots of refractive index to show the cavity simulation structure. 201

7.8 A comparison cavity mode spectrum: **(a)** the measured spectrum from chapter (6); **(b)** the simulated collection spectrum through the planar mirror; **(c)** the simulated emission enhancement spectrum from the Purcell monitors. 202

7.9 Mode profile of the fundamental modes from the q=15-17 mode families. Note for the q=15 and 17 modes the field intensity is relatively even across the air-diamond interface but for q=16 mode the field intensity is much stronger in the air portion of the cavity. 203

7.10 The axial distribution profiles of the q= 16 mode: **(a)** mode field intensity $|\mathcal{E}|^2$ and **(b)** cavity mode energy density product $n^2|\mathcal{E}|^2$. 204

7.11 Mode profiles of the higher order TEM modes in the q=16 mode family. . 204

7.12 High-Q cavity plots of **(a)** the simulated device enhancement spectrum $F^{\text{on}}(\lambda)$ and the calculated emitter spectrum $S^0(\lambda)$ using w_{zpl}=2GHz and ζ^*=5.9%; **(b)** the combined emitter-cavity enhancement spectrum $F^{\text{on}}(\lambda)S^0(\lambda)$. 205

7.13 Convergence test of the ZPL linewidth w_{zpl} term in $S^0(\lambda)$ and its influence on key variable including the emission enhancement factors and ZPL branching ratio. 207

7.14 **(a)** The t-domain field decay data over all wavelength. **(b)-(c)** The 2D cross-sectional field profile of the non-cavity and cavity photons respectively. 208

7.15 Low-Q cavity plots of **(a)** the simulated device enhancement spectrum $F^{\text{on}}(\lambda)$ and the calculated emitter spectrum $S^0(\lambda)$ using w_{zpl}=2GHz and ζ^*=5.9%; **(b)** the combined emitter-cavity enhancement spectrum $F^{\text{on}}(\lambda)S^0(\lambda)$. 211

7.16 The cavity mode structure and the q=16 fundamental mode profile of **(a)(c)** the shallow and **(b)(d)** the deep cavity simulation. 212

7.17 A comparison of collection distribution between shallow high-Q, shallow low-Q and deep low-Q simulations: **(a)** the collection efficiency distribution η_{ch} and **(b)** the absolute power distribution P_{ch}. 214

List of Tables

1.1 Summary of PLE results from previous literature works. Most linewidth estimates are taken from the best presented figures in each work. Micro-structured diamond samples are listed next to each other and the their thicknesses are given as t in the notes column. 20

1.2 A summary of cavity metrics from note-able literature demonstrations of cavity-coupled NV experiments. 24

2.1 The planar mirror reflectivity R_{plan} modification for different diamond membrane thickness. The coating pairs is set to 6 for demonstration and m is a positive integer. 63

2.2 The detailed cavity parameters for a number of key q_{d} values. 65

3.1 Typical etching parameters of the Ar/Cl_2 and O_2 etching recipes used in this work. 73

4.1 Conversion table from cavity mode index q to optical cavity length L for a single-medium air cavity constructed for NV ZPL wavelength at 637nm. The conversion to the corresponding physical cavity length for a single-medium diamond cavity is also given. 100

4.2 DBR coating parameters: number of coating pairs N, substrate thickness t, mirror transmission T and expected finesse $\mathcal{F}_{\text{tmm}}$. The value of $\mathcal{F}_{\text{tmm}}$ is calculated using TMM for a q= 1 cavity. The value of T is also calculated using TMM and fine-tuned with substrate thickness t_{sub}. 101

4.3 A template of collection analysis and emission analysis for a given simulation structure. The contributions from both cavity photon and non-cavity photon are considered. The emission enhancement F and ZPL photon output P are also included. 107

4.4 A description of cavity performance modulation in terms of 2D planar separation L_{2D} and 2D mode index q_{2D}. Both m and n are positive integers. 116

4.5 Membrane-on-mirror simulation results with membrane thickness at q_{d}=1 and q_{d}=1.5. The photon collection takes placed at the bottom of the simulation region. 128

4.6 Simulation variable used to generate the cavity mode maps. 131

4.7 The fitting results for each mode family in the air-like and diamond-like simulations. The simulated membrane thickness is t_d=264nm for the air-like cavity and t_d=330nm for the diamond-like mode. All the cavity lengths are in optical cavity length. 133

5.1 Sample identities and implantation parameters. 136

5.2 Number of NV centres per 10x10µm scan area. The nitrogen conversion rate is calculated by counting NVs with a single ZPL as a single defect and averaging all the other NVs with multiple ZPLs as a double defect site. . . 138

5.3 Summary of % element fraction on the surfaces of first generation membranes. 142

5.4 Membrane morphologies at different stages of fabrication process. 143

5.5 Membrane surface roughness evolution at different fabrication stages. . . . 145

5.6 A summary of samples information from which PLE data is gathered. A sample is considered a 'membrane" if its thickness is below 10µm. Above this thickness, the optical properties of NV centres are largely unaffected by the far-side surface [28]. 149

6.1 A summary of key data measured in the on-mirror configuration. 171

6.2 The geometric parameters of fabricated cavity features: $\mathcal{R}$ is the radius of curvature of the concave cavity feature and q is the cavity mode index. . 172

6.3 The cavity figure of merits measured in a transmission setup at room-temperature. The measured cavity finesse is compared to the expected values calculated using analytical expression $\mathcal{F}_{\text{ana}}$, TMM treatment $\mathcal{F}_{\text{tmm}}$ and FDTD simulation $\mathcal{F}_{\text{fdtd}}$. 173

6.4 Lifetime fitting parameters. 178

6.5 The hybrid-medium cavity figure of merits of fundamental modes from q=16-18 mode families measured around 640nm. Data is averaged from 5 repeated readings. 184

6.6 An analysis template of NV emission rates γ and ZPL branching ratio ζ in all experimental configurations. The quantities in bold font are available from either experimental measurements or FDTD simulations. The emission enhancement of ZPL photon $F_{\text{zpl}}^{\text{on/mir}}$ needs to be derived from FDTD simulation. 187

6.7 The emission rate analysis for A4-NV4 when its ZPL is coupled to the q=16 fundamental mode of cavity B5. The table is filled with all the available information from previous in-cavity measurements. 187

6.8 Summary of the measured variables up till now and the remaining variables to be determined from FDTD simulations. 188

6.9 A summary of key measured quantities from this chapter. 188

7.1 Realistic parameters used in the on-mirror simulation to find the analytical ZPL branching ratio ζ^*. 194

7.2 Collection and ZPL output analysis of the on-mirror simulation. The overall photon output $P_{\text{out}}^{\text{mir}/0}$ in the on-mirror configuration at the ZPL frequency is calculated using eq. (4.9b). 196

7.3 A summary of the simulation data obtained from on-mirror simulation. . 197

7.4 Collection and ZPL output analysis of the membrane-only simulation. The overall ZPL photon output P towards the top and bottom of the simulation region are both listed. 200

7.5 Cavity figure of merits of the q=16 mode. The expected finesse $\mathcal{F}_{\text{ana}}$ and $\mathcal{F}_{\text{tmm}}$ are also included. Note that these are single frequency readings. The multi-frequency integration results are presented in later sections. 203

7.6 Collection and ZPL output analysis of the high-Q cavity simulation where P^{on} is the dipolepower in simulated structure and P^0 is the sourcepower in a homogeneous medium. 208

7.7 Collection and ZPL output analysis of the shallow low-Q cavity simulation where P^{on} is the dipolepower in simulated structure and P^0 is the sourcepower in a homogeneous medium. 212

7.8 Collection and ZPL output analysis of the deep low-Q cavity simulation where P^{on} is the dipolepower in simulated structure and P^0 is the sourcepower in a homogeneous medium. 213

7.9 A failed attempt to complete emission rate analysis for A4-NV4 in cavity B5 with the help of FDTD simulations. The numbers with a '*' sign are calculated using low-Q simulation results which are mostly lower-bound estimations. 216

7.10 An alternative approach to complete the emission analysis based on the fact that F_{psb} is almost constant in all three conditions. 216

7.11 A comparison of cavity metrics between the high-Q, the low-Q and the experimental results. The low-Q data are averaged between the shallow and deep cavity simulations. The cavity metrics are full-spectrum emission enhancement $F_{\text{full}}^{\text{on}/\text{mir}}$, ZPL photon output $P_{\text{zpl}}^{\text{on}/\text{mir}}$, ZPL emission enhancement $F_{\text{zpl}}^{\text{on}/\text{mir}}$, ZPL branching ratio ζ and device photon collection efficiency η. 217

List of Abbreviations

AFM	**A**tomic **F**orce **M**icroscopy
CQED	**C**avity **Q**uantum **E**lectro**d**ynamics
CVD	**C**hemical **V**apour **D**eposition
CW	**C**ontinuous **W**ave
DBR	**D**istributed **B**ragg **R**eflector
FDTD	**F**inite-**d**ifference **T**ime-**d**omain
FIB	**F**ocused **I**on **B**eam
FP	**F**abry-**P**erot
FWHM	**F**ull **W**idth **H**alf **M**aximum
HBT	**H**anbury-**B**rown-**T**wiss
HPHT	**H**igh-**p**ressure **H**igh-**t**emperature
LDoS	**L**ocal **D**ensity **o**f **S**tates
NA	**N**umerical **A**perture
PID	**P**roportional **I**ntegral **D**erivative
PL	**P**hoto**l**uminescence
PLE	**P**hoto**l**uminescence **E**xcitation
PSB	**P**honon **S**ideband
PCC	**P**hotonic **C**rystal **C**avity
SPAD	**S**ingle **P**hoton **A**valanche **D**etector
SNR	**S**ignal to **N**oise **R**atio
TEM	**T**ransverse **E**letro**m**agnetic
XPS	**X**-ray **P**hotoelectron **S**pectroscopy
ZPL	**Z**ero-**p**honon **L**ine

Physical Constants

Planck's Constant	$h = 6.626\,07 \times 10^{-34}\,\mathrm{J\,s}$
Reduced Planck's Constant	$\hbar = 1.054\,57 \times 10^{-34}\,\mathrm{J\,s}$
Speed of Light	$c = 2.997\,92 \times 10^{8}\,\mathrm{m\,s^{-1}}$
Vaccuum Permittivity	$\epsilon_0 = 8.854\,18 \times 10^{-12}\,\mathrm{F\,m^{-1}}$

List of Symbols

Q	Quality Factor	-
$\mathcal{F}$	Finesse	-
F	Emission Enhancement (Purcell Factor)	-
V	Mode Volume	μm^3
L	Cavity Length	μm
$\mathcal{R}$	Radius of Curvature	μm
$\mathcal{L}$	Cavity Round-trip Loss	ppm
$q/m/n$	Longitudinal and Transverse Mode Indices	-
n	Refractive Index	-
R	Reflectivity	-
T	Transmission	-
ξ	Dipole Orientation Factor	-
ζ	ZPL Branching Ratio	-
η	Efficiency	-
γ	Decay Rate	Hz
κ	Cavity Decay Rate	Hz
g	Cavity Coupling Parameter	Hz
$\mathcal{E}$	Electric Field	Vm^{-1}
$\mathcal{B}$	Magnetic Field	T
λ	Wavelength	nm
v	Frequency	rad
ω	Angular Frequency	Hz
$\Delta\lambda/\Delta v/\Delta\omega$	Free Spectral Range	nm/Hz/rad
$\delta\lambda/\delta v/\delta\omega$	Spectral Linewidth	nm/Hz/rad

For my beloved parents and my dearest friends...

Chapter 1

Introduction and Literature Review

In the modern age of information technology, the massive outburst of the amount of human-generated data has put an ever-increasing demand on computation power available to us. Since the invention of the classical computer, orders of magnitude of performance boost has been realised via the miniaturisation of processing circuit thanks to the technology advancements in the electronics industry. However, this approach is prone to reach a fundamental limit in the near future, and a break down of Moore's law [1] can be anticipated. Clearly, an alternative direction is desired, and the tide has turned towards applying quantum mechanics to control quantum systems and harness the power of superposition and entanglement to provide unprecedented computational capability.

In the past decades, a collaborative effort of researchers from a wide range of academic background has made some remarkable progress in developing all aspects of quantum computation. A recent quantum computation advancement published by Google [2] has raised the eyebrows of the general public. The demonstrated state-of-art quantum machine solved a specialised computation problem in a 'fast' polynomial time when no classical computer is expected to run the same task faster than a 'slow' exponential time. That is to say, a classical computer has to double its size to keep up with each additional qubit integrated into the quantum computer. Ever since the conceptualisation of quantum computer [3] in 1982, its powerful computational capability in certain types of tasks has been envisaged by many theoretical studies including the first practical example presented [4] in 1994 about the factorisation of large numbers. Now that after two and half decades, the realisation of quantum computer's dominance over the classical computer is undoubtedly a remarkable achievement and an encouraging milestone.

The core hardware in a quantum computer is the quantum bit, or qubit. The basic requirements for a qubit are set out by the DiVincenzo's criteria [5] including scalability, controlled initialisation and manipulation, long coherence time and efficient readout. The machine in [2] is made of superconducting qubits which follow a circuit-based design. Such a design relies on nm-scale qubit spacing to facilitate local entanglement. This poses many challenges, especially in terms of scalability.

Instead of relying on local interactions, measurement-based entanglement schemes are first theorised by [6, 7] and demonstrated by [8, 9] as an alternative approach. By exploiting the act of measurement to 'measure out' the unwanted terms in the product state of two or more qubit systems, entanglement is established in a probabilistic way. This scheme allows remote entanglement between distant qubits or nodes (multiple qubits) such that a large-scale distributed quantum network can be formed.

In the following topical reviews, an introduction to the measurement-based entanglement scheme is firstly presented, followed by a discussion of the associated hardware requirements in the context of the solid-state qubit. Focus is then given to the applicability and current state of diamond nitrogen-vacancy centre (NV) as a spin-based solid-state node in the distributed quantum network.

1.1 Measurement-Based Entanglement

Measurement-based entanglement builds on the idea of 'path erasure' that was proposed by Cabrillo et al. in 1999 [6]. In their paper, a simple two-atom setup with a detector between the atoms is used. The key is that when a photon detection event is recorded, the detector can not distinguish from which atom the photon is originated. Hence, only the collective state of the system is measured, but the state of each node is not known. This way, an entangled state of two atoms can be established.

In the original proposal by Cabrillo et al., direct photon detection is used, and weak excitation limit is assumed such that occasions of simultaneous excitation of both atoms can be neglected. In a later work by Barrett & Kok [10], a more robust entanglement scheme is theorised where two-qubit entanglement state is generated using a 50/50 beam-splitter via

single-photon interference effect. Under this framework, photon loss does not deteriorate the fidelity (more in section (1.1.1)) of the entangled state but only affects entanglement generation rate, rending this method robust against most common experimental errors.

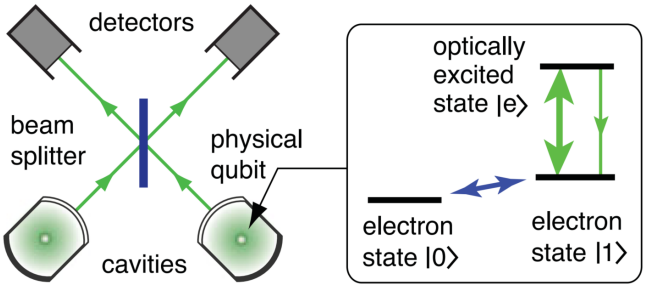

Figure 1.1: Illustration of a measurement-based entanglement setup with two qubits, a 50/50 beam-splitter and two detectors. Both qubits have an identical L-shaped level structure where $|0\rangle$ and $|1\rangle$ are long-lived states and $|1\rangle$ is connected to $|e\rangle$ by resonant excitation. The transition between $|0\rangle$ and $|e\rangle$ is prohibited by certain selection rules. Reprinted with permission from [11].

In this work, we explore the implementation of solid-state qubit systems, such as the nitrogen-vacancy (NV) centre, under the Barrett & Kok entanglement scheme. Hence a description of the corresponding operation procedure is beneficial to first give some context and secondly help derive further experimental metrics.

Considering two qubits with identical L-shaped level structures as illustrated in fig. (1.1), the entanglement generation procedure of the Barrett & Kok scheme is executed as follows:

1. **State initialisation:**

   The state initialisation process is identical for both atom qubits. The population of the atomic system is firstly polarised into one of the ground-states via some other mechanisms, e.g. the spin-polarisation process in NV centre (more in section (1.2)).

   Then, a $\pi/2$ pulse between $|0\rangle$ and $|1\rangle$ is applied to create an equal superposition state $\frac{1}{\sqrt{2}}(|0\rangle+|1\rangle)$ for each qubit. So the product state of the two-qubit system is written as:

   $$\frac{1}{2}(|00\rangle + |01\rangle + |10\rangle + |11\rangle) \tag{1.1}$$

2. **Resonant excitation and system relaxation:**

After initialisation, both qubits are resonantly excited to $\frac{1}{\sqrt{2}}(|0\rangle + |e\rangle)$ by applying a π pulse corresponding to the $|1\rangle \rightarrow |e\rangle$ transition. Now the system state is:

$$\frac{1}{2}(|00\rangle + |0e\rangle + |e0\rangle + |ee\rangle) \tag{1.2}$$

Given sufficient time for excited-state relaxation, the number of photons emitted by the two-qubit system can be 0 ($|00\rangle$), 2 ($|ee\rangle$) or 1 ($|0e\rangle/|e0\rangle$). The posterior state of the system after relaxation is then given by one of the four parities in eq. (1.1).

3. **Transmission and photon detection:**

   Due to the bunching effect at the beam splitter, three possible measurement outcomes can be observed at the detectors: no photon incidence on either detector, a two-photon incidence on one of the detectors, and a one-photon incidence on one of the detectors. The corresponding posterior state are $|00\rangle$, $|11\rangle$, and $|01\rangle/|10\rangle$, respectively.

   In an experimental setting, it is easy to omit the measurement rounds with the $|00\rangle$ parity. If perfect detector that distinguishes one-photon and two-photon incidences are available, or like the work by Cabrillo et al. that operates in the weak excitation limit, we can definitively ignore the measurement rounds with the $|11\rangle$ parity too. The system is then in an entangled state given by:

$$\frac{1}{\sqrt{2}}(|10\rangle \pm e^{i\phi}|01\rangle) \tag{1.3}$$

   where ϕ is the relative phase due to optical path length difference.

4. **Flipping state and repeating step (2)-(3):**

   Unfortunately, omitting the $|11\rangle$ posterior state is not as straightforward in real-world experiments due to imperfect detector, photon loss and experimental noise. In the Barrett & Kok scheme, this issue is dealt with by proceeding to a second round of detection.

   After recording a click on either of the detectors, the posterior system state is in either $|11\rangle$, $|01\rangle$ or $|10\rangle$. A π pulse between $|0\rangle$ and $|1\rangle$ is applied which flips $|0\rangle \rightarrow |1\rangle$ and $|1\rangle \rightarrow |0\rangle$. By repeating the resonant excitation and relaxation process, the $|11\rangle$

from the first round of detection is now in the $|00\rangle$ posterior state which gives no photon incidence in the second round of detection. Both $|01\rangle$ ad $|10\rangle$ parities continues to give one-photon incidence on one detector.

Hence, under the condition that a one-photon detection in two successive rounds of detection, the system is prepared in one of maximally entangled Bell states:

$$\frac{1}{\sqrt{2}}(|10\rangle \pm |01\rangle) \tag{1.4}$$

where the relative phase ϕ in eq. (1.3) is converted to a global phase. The exact resultant Bell state depends on the sequence of detector clicking events between the two measurement rounds. These two states are referred to as the $|\Psi^{\pm}\rangle$ states in the Bell basis.

The Barrett & Kok and similar two-photon detection schemes are also referred to as 'double-heralding' schemes, as the entanglement is prepared in a heralded, probabilistic manner with two rounds of detection. The overall entanglement generation probability is thus:

$$P_{\text{succ}} = \frac{1}{2}\eta^2 \tag{1.5}$$

where η is the overall photon efficiency of the qubit device, which will be broken down in more detail in section (1.1.5) for general qubit systems and in section (1.2.3) in the case of NV centre.

One intrinsic benefit of measurement-based entanglement scheme is scalability. By repeating the same parity projection with additional qubits, multi-qubit entangled states (graph states) can be created and used as a resource for quantum computing. The successful implementation of this scheme between two distant NV centres will be discussed in section (1.2.1).

1.1.1 Entanglement Fidelity and Node Requirements

In theory, the double-heralding entanglement schemes, such as the Barrett & Kok scheme described as above, are capable of generating Bell states with unit fidelity. However, false detection outcomes can still occur due to potential errors in each of the operation steps.

To quantify the quality of the generated entanglement state, a metric called 'state fidelity' of the prepared state with respect to the target Bell states is defined as [6]:

$$\text{Fidelity} = \langle \Psi | \rho | \Psi \rangle \tag{1.6}$$

where ρ is the density matrix of the prepared state. Symbol F is normally used to represent fidelity, but it is not used here to avoid confusion with the Purcell factor F, which is used more frequently in this work. With eq. (1.6), one essentially compares the resemblance between the prepared state ρ and the target Bell state $|\Psi\rangle$. A fidelity of 1 is obtained if they are identical. Any error during preparation, manipulation, evolution or measurement of the system will deteriorate entanglement fidelity.

Perhaps an easier way to visualise the loss of fidelity is to think of it as the 'leakage of quantum information' stored in an ideal entanglement state. As mentioned before, a key requirement of measurement-based entanglement is to 'hide' the origin of the measured photons via path erasure. This places two demands on the qubit systems [12]: firstly, 'no memory' of photon emission should be identifiable at each qubit; secondly, photon emissions from both qubits have to be coherent and formally indistinguishable. Failure to meet either requirement causes a quantum information leakage (decoherence) to the environment. Such decoherence will reveal the 'which path' information of the detected photon, and ultimately deteriorates entanglement fidelity.

Considering a simple two-level system, the coherence time T_2 between the two states is given by [13]:

$$\frac{1}{T_2} = \frac{1}{2T_1} + \frac{1}{T_2^*} \tag{1.7}$$

where T_1 is the population decay constant that accounts for the population relaxation, and T_2^* is the pure dephasing constant that concerns any population-conserving dephasing processes. Any population relaxation process naturally possess a dephasing effect such that it contributes both T_1 and T_2^* components towards the overall T_2 coherence. Most dephasing processes have a short time-scale because no energy change is involved. There also exists slower dephasing processes which is resolvable compared to the T_1 time, e.g. the spectral diffusion process in solid-state qubits, as will be explained in section (1.1.3). In general, the description given by eq. (1.7) applies to both the spin coherence between

spin states and the optical coherence of transitions between two electronic energy levels.

For a solid-state spin qubit, the 'no memory' requirement mainly concerns the spin coherence in the solid-state environment. Sources of decoherence include phonons, electronic spins and nuclear spins. Small electric field fluctuations caused by phonon movement can distort the orbital states of the electronic spin. The interaction strength depends on the electron-phonon coupling between the defect and all possible phonon modes. The energy level structure can be directly modified by lattice deformation and strain. Taking NV centre in diamond as an example, the ground-state spin degree of freedom is dominated by two-photon Raman scattering processes at higher temperatures and Orbach-type processes at lower temperatures [14]. Both of these are T_1 processes, and low-temperature conditions are often required to suppress phonon interactions.

The interaction between the qubit spin and nearby electronic and nuclear spins are mostly T_2^* processes. A qubit electron spin experiences a large nuclear spin bath where each nuclear spin couples to the qubit spin via hyperfine interaction. The effective magnetic field associated with the nuclear spin bath changes its value and direction on an ns-timescale which introduces additional dephasing. Fortunately, this is less of an issue for diamond since the most abundant carbon isotope, ^{12}C, has no nuclear spin. On the other hand, direct dipole-dipole interaction between nearby electronic spin and the qubit spin is more dominant due to large electron dipole moments. Sources of unwanted electronic spins include impurity and charged lattice defects whose presence can be reduced by careful material engineering.

The photon indistinguishability requirement mainly concerns the optical coherence of the electronic transition. The expression of indistinguishability I can be written as [15, 16]:

$$I = \frac{T_2}{2T_1} \tag{1.8}$$

In a solid-state system where the qubit is embedded in a crystal lattice, T_2 decoherence can be caused by a number of mechanisms. Firstly, unlike trapped atoms or ions where T_1 is often equated with the radiative lifetime τ_{rad}, the isolation of qubit in a solid is compromised due to presence of nearby impurities and lattice imperfections. Such defects provide non-radiative decay pathways that contribute to the population relaxation process

hence introducing additional T_1-type decoherence. By including both radiative and non-radiative components, T_1 time of an optical transition in a solid-state system is given as:

$$\frac{1}{T_1} = \frac{1}{\tau_{\text{rad}}} + \frac{1}{\tau_{\text{nrad}}} \tag{1.9}$$

where $\tau_{\text{rad/nrad}}$ are radiative and non-radiative lifetimes.

T_2^*-type dephasing process is also very common in solids due to local perturbations such as lattice strain and local electric field fluctuation. One particular abundant source of dephasing is nearby charged defects. Depending on the time-scale of the charge movement, T_2^*-type dephasing could show up in experimental data in different ways. A more detailed discussion of T_2^*-type dephasing and its relationship to the observable spectral lineshapes are given in the next section.

1.1.2 Optical Coherence and Spectral Lineshapes

The coherence of optical transition is one of the focuses of our work and a basic description of the T_2 coherence time of a two-level system has been given in eq. (1.7). In real-world experiments, optical measurement in the frequency-domain is often used to gain insight into the decoherence processes that are present. In this section, we introduce the concepts of homogeneous and inhomogeneous linewidths that are used throughout this work. These definitions are devised to help with the analysis of experimental data and are not necessarily compatible with more formal definitions from atomic physics.

First of all, we define the homogeneous linewidth, $\delta\upsilon_{\text{hom}}$, as the transition linewidth from single optical transitions. Converting eq. (1.7) we find an expression of $\delta\upsilon_{\text{hom}}$ as:

$$\delta\upsilon_{\text{hom}} = \frac{1}{\pi T_2} = \frac{1}{2\pi T_1} + \frac{1}{\pi T_2^*} = \frac{1}{2\pi}\left(\frac{1}{\tau_{\text{rad}}} + \frac{1}{\tau_{\text{nrad}}}\right) + \frac{1}{\pi T_2^*} \tag{1.10}$$

and in rate terms:

$$\delta\upsilon_{\text{hom}} = \frac{1}{2\pi}(\gamma_{\text{rad}} + \gamma_{\text{nrad}} + \gamma^*) \tag{1.11}$$

where $\gamma_{\text{rad/nrad}}$ are the radiative and non-radiative decay rate and $\gamma^* = 2/T_2^*$ is the pure dephasing rate.

Note that the above expressions only apply when the dephasing mechanism is faster than T_1 such that they are not distinguishable during the same optical cycle. This scenario is analogous to the impact approximation of collision broadening in atomic physics where charge movement is fast compared to T_1. In such cases, both T_1 and T_2^* processes yield Lorentzian lineshapes [17] and hence can be treated together in experimental data.

Next, in order to account for dephasing processes that are much slower than T_1, we define the inhomogeneous linewidth $\delta\nu_{\text{inhom}}$ as:

$$\delta\nu_{\text{inhom}} = \frac{1}{\pi T_2^*} = \frac{1}{2\pi}\gamma^* \tag{1.12}$$

Since these dephasing processes are slow, e.g. the spectral diffusion in solid-state systems, the effect of $\delta\nu_{\text{inhom}}$ is observed as a frequency shift in single-cycle measurements. This scenario is also analogous to the collision broadening but in the limit of quasi-static approximation, i.e. charges are considered static for the duration of T_1 lifetime.

It is only in time-averaged measurement that $\delta\nu_{\text{inhom}}$ convolves with $\delta\nu_{\text{hom}}$ to give a measurable total linewidth $\delta\nu_{\text{tot}}$. The contribution of $\delta\nu_{\text{inhom}}$ towards $\delta\nu_{\text{tot}}$ is characterised by a Gaussian distribution which is difficult to quantify directly. Instead, given that $\delta\nu_{\text{hom}}$ has a measurable Lorentzian shape from single-cycle measurements, the observable lineshape of $\delta\nu_{\text{tot}}$ is often found to be a Voigt function which can be deconvolved to give $\delta\nu_{\text{inhom}}$. More details about lineshape functions are given in section (3.5.1).

The linewidth discussion in this work, such as that in section (5.3), does not usually quote $\delta\nu_{\text{inhom}}$ directly due to its derivative nature and lack of direct visualisation. Instead, we quantify the optical coherence using mainly the measurable homogeneous linewidth $\delta\nu_{\text{hom}}$ and time-averaged total linewidth $\delta\nu_{\text{tot}}$. The line broadening effect caused by slow dephasing processes, such as the spectral diffusion of NV transitions, are visualised as the difference between $\delta\nu_{\text{hom}}$ and $\delta\nu_{\text{tot}}$ instead of $\delta\nu_{\text{inhom}}$.

Now, coming back to eq. (1.8), photon indistinguishability I can also be written using the linewidth/rate expression derived above for single-cycle transitions:

$$I = \frac{T_2}{2T_1} = \frac{\gamma_{\text{rad}} + \gamma_{\text{nrad}}}{\gamma_{\text{rad}} + \gamma_{\text{nrad}} + \gamma^*} \tag{1.13}$$

It is apparent that in order to maximize I, optical transitions needs to coherent, i.e. free of non-radiative decay and fast dephasing processes. Such kind of optical transitions is also referred to as 'lifetime-limited' transition. Taking NV centre as an example, lifetime-limited transition was first observed from naturally occurring NV centre in 2006 [18], but only found in fabricated NVs in 2017 using novel laser-writing technique [19].

Note that the effect of slow dephasing processes is not directly included in eq. (1.13). A more detailed demonstration of the effect of these processes is given in section (1.1.3).

Using eq. (1.13) it is also possible to improved I by enhancing the radiative decay rate γ_{rad} such that $\gamma_{\text{rad}} \gg (\gamma_{\text{nrad}}, \gamma^*)$. This could be made feasible using optical resonator. In this work, due to the generally low coupling strength between NV and our cavity device, such a mechanism is not considered in the analysis.

Frequency-matching is another requirement for photon interference type measurements. In principle, frequency drift is not a decoherence process, and photon indistinguishability should be observable if the frequency-mismatch does not exceed the inverse of detector timing resolution. So given a certain detector resolution, it is desirable to have some frequency tuning capability, e.g. the Stark shift tuning and of NV ZPL transitions [18]. A more detailed discussion about frequency-detuned photons in the context of two-photon interference is presented in section (1.1.4).

1.1.3 Spectral Diffusion of Optical Transitions

A common issue with low-symmetry optical transitions in solid-state systems is the frequency drift due to the fluctuating local electric field caused by random charge movements. This can lead to an intermittent frequency mismatch Δ_{ex} between the optical transition and the resonant excitation laser. This longer time-scale dephasing effect is referred to as 'spectral diffusion'. The major concerns with spectral diffusion are the drop of excitation efficiency η_{ex} and the loss of optical coherence as shown in section (1.1.2).

According to eq. (1.10), the single-cycle transition lineshape is described by a Lorentzian profile with a homogeneous linewidth of $\delta\upsilon_{\text{hom}}$. In a time-average measurement, distribution of frequency drifts due to slow dephasing process is described by a Gaussian profile

whose linewidth is referred to as the inhomogeneous linewidth $\delta\nu_{\text{inhom}}$. As a result, the time-averaged total linewidth $\delta\nu_{\text{tot}}$ is the convolution of $\delta\nu_{\text{hom}}$ and $\delta\nu_{\text{inhom}}$.

Because the transitions in entanglement generation schemes are all driven resonantly, frequency drifts due to slow dephasing processes can cause frequency mismatch between the excitation laser and optical transition, hence are very detrimental. To quantify this, we conveniently define the excitation efficiency η_{ex} using linewidth measurements as:

$$\eta_{\text{ex}} = \frac{\delta\nu_{\text{hom}}}{\delta\nu_{\text{tot}}} \tag{1.14}$$

This efficiency term represents the probability of coincidence between a fixed-frequency excitation laser and a drifting optical transition. We note that the expression for η_{ex} is also equivalent to that of the degree of indistinguishability I in eq. (1.13). Hence by expressing η_{ex} as in eq. (1.14), the optical coherence of the emitted photon is also addressed in the entanglement success rate P_{succ} via η_{ex}.

Another way to quantify the decoherence due to inhomogeneous broadening is to drive the transition and observe the resulting Rabi oscillation. The optically driven Rabi oscillation is associated with a damping constant τ_{damp} [20]:

$$\frac{1}{\tau_{\text{damp}}} = \frac{3}{4T_1} + \frac{1}{2T_2^*} \tag{1.15}$$

from which T_2^* can be determined. The excitation detuning Δ_{ex} increases the optical Rabi frequency according to [21]:

$$\Omega = \sqrt{\Omega_0^2 + \Delta_{\text{ex}}^2} \tag{1.16}$$

where Ω_0 is the on-resonance optical Rabi frequency. In principle, τ_{damp} of each individual oscillation is not affected by Ω. However, photon interference measurements are usually acquired over a large number of optical cycles. The summation of individual oscillations with varied Ω leads to a collapse of overall observed τ_{damp}. Consequently, the observed degree of indistinguishability in photon interference experiments is deteriorated.

An *in situ* post-selection protocol is demonstrated by [20, 22] to mitigate the effect of spectral diffusion of NV ZPL transitions. In this protocol, the two-photon interference

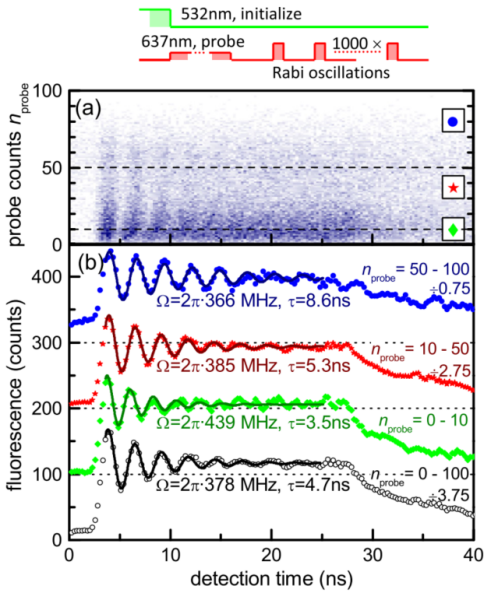

Figure 1.2: The coherent optical control of ZPL transitions with a post-selection scheme. Reprinted with permission from [20].

and entanglement operations only follow if a strong resonant fluorescence is observed after a probe pulse fig. (1.2). The conditioned decision making ensures a good overlap between the optical transition and the excitation laser. Reasonable entanglement fidelity is achievable using this protocol at the cost of reduced attempt rate.

1.1.4 Frequency-Mismatched Photons

Frequency mismatch between incident photons onto the beam-splitter could be due to inherent transition energy difference or intermittent energy level fluctuation (spectral diffusion). Because frequency mismatch is not a decoherence process, quantum interference should be attainable by exploiting the time-energy uncertainty relationship of quantum mechanics. A series of work by [23, 24] revealed that the two-photon Hong-Ou-Mandel interference [25] persists in the form of quantum beats when photon frequencies are mismatched if the analysis is done in a time-resolved way.

A similar treatment of the Barrett-Kok scheme is first theorised by [26] and demonstrated by [27] with ion-traps. Here we define the frequency detuning between two emitted photons as Δ_{em}, the cavity decay rate as κ and the detector response rate as γ_{dt} which corresponds to a timing resolution $t_{\mathrm{dt}} = 1/\gamma_{\mathrm{dt}}$. The effective cavity-coupled emission rate of the qubit is then $\kappa_{\mathrm{eff}} = 2g^2/\kappa$, where g is the cavity coupling parameter.

Following the approach in [26], three scenarios are considered depending on the detector performance:

1) Ideal detector regime: $t_{\mathrm{dt}} \ll 1/\Delta_{\mathrm{em}}$.

In this regime, the detector gives precise photon arrival times t_1 and t_2 from both measurement rounds. Without going through the derivations, the final system state is written as:

$$\frac{1}{\sqrt{2}}(|01\rangle \pm e^{i\Delta_{\mathrm{em}}(t_1-t_2)}|10\rangle) \tag{1.17}$$

which is equivalent to eq. (1.3) except the inclusion of Δ_{em} in the relative phase term. Regardless of arrival times, the final state is always a maximally entangled state.

To understand this, one can consider Δ_{em} as carrying the 'which-path' information, which can reduce the entanglement fidelity. Due to the idealised time-domain resolving power of the detector, the frequency-domain information is blurred out and effectively erased by the detector. As a result, unity fidelity is achieved with an ideal detector.

2) Bad detector regime: $t_{\mathrm{dt}} \gg (1/\Delta_{\mathrm{em}}, \kappa_{\mathrm{eff}})$.

In this regime, the detector can not resolve the arrival time at all but it does indicate whether a click is registered. In this case the entanglement fidelity is given by:

$$\frac{1}{2}\left(1 + \frac{\kappa_{\mathrm{eff}}^2}{\kappa_{\mathrm{eff}}^2 + \Delta_{\mathrm{em}}^2}\right) \tag{1.18}$$

The fidelity increases towards unity for large κ_{eff}, as shown in fig. (1.3)(a). This makes sense because κ_{eff} represents the spectral linewidth of cavity photons. When $\kappa_{\mathrm{eff}} \gg \Delta_{\mathrm{em}}$, the photons becomes indistinguishable spectrally and carries no 'which-path' information.

3) Intermediate detector regime: $t_{\mathrm{dt}} \sim (1/\Delta_{\mathrm{em}}, 1/\kappa_{\mathrm{eff}})$.

In this regime, the relative magnitudes between all three parameters matter and trends from both previous scenarios apply as shown in fig. (1.3)(b). The fidelity increases toward unity for $\Delta_{\mathrm{em}} \ll (\kappa_{\mathrm{eff}}, 1/t_{\mathrm{dt}})$ and it scales approximately quadratically with $\Delta_{\mathrm{em}}/\gamma_{\mathrm{dt}}$. It is estimated that to achieve a fidelity larger than 0.99, the

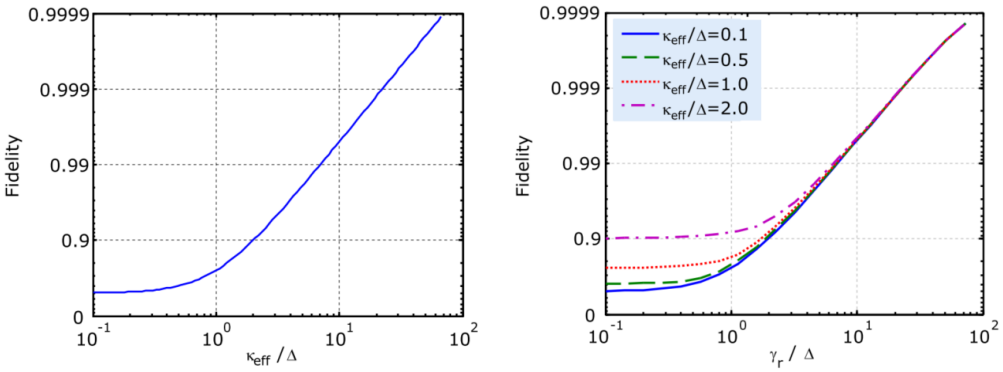

(a) **(b)**

Figure 1.3: Entanglement fidelity **(a)** in the bad detector regime and **(b)** in the intermediate detector regime. Δ_{em} is the frequency-detuning between incident photons, κ_{eff} is the cavity-coupled emission rate of the qubits and γ_{dt} (γ_r in plot) is the detector response rate where the detector timing resolution is t_{dt}=$1/\gamma_{dt}$. Reprinted with permission from [26].

detector performance has to satisfy:

$$\gamma_{dt} > 6\Delta_{em} \quad or \quad t_{dt} < 1/6\Delta_{em} \tag{1.19}$$

While the criterion of $t_{dt} < 1/6\Delta_{em}$ serves as a good guidance for estimating required emitter linewidth for a reasonable entanglement fidelity, sometimes a simple inverse relation is also used. For example, a total linewidth limit of 100MHz is proposed by [28] based on a detector resolution of 300ps.

Of course, the usage of optical cavities is not compulsory and the results hold if κ_{eff} is replaced with the free-space rate γ. Although cavity enhanced emission does provide another degree of control to improve entanglement fidelity.

1.1.5 Entanglement Success Probability

As demonstrated at the start of section (1.1), measurement-based entanglement schemes have a probabilistic nature hence the entanglement success probability is a crucial parameter to achieve large-scale quantum networks. In a double-heralding scheme where two rounds of measurement are performed, the entanglement success rate scales quadratically

with an efficiency term η [26]:

$$P_{\text{succ}} = \frac{1}{2}\eta^2 \qquad \text{(eq. (1.5) revisit)}$$

The factor of $1/2$ represents the population of odd parity subspace in the prepared product state in eq. (1.1). The original definition of η given by [10, 26] only includes the photon collection and detection efficiencies. This definition is expanded by [12] to include the efficiencies through all the photon generation and detection processes:

$$\eta = \eta_{\text{ex}} \times \eta_{\text{em}} \times \eta_{\text{co}} \times \eta_{\text{tr}} \times \eta_{\text{dt}} \tag{1.20}$$

where η_{ex} is the excitation efficiency, η_{em} is the indistinguishable photon emission efficiency, η_{co} is the collection efficiency, η_{tr} is the transmission efficiency and η_{dt} is the detection efficiency.

An expression for η_{ex} has been given in eq. (1.14) to account for excitation laser detuning caused by transition energy drifts. η_{em} concerns the likely-hood of an useful photon being emitted after a successful excitation event. Competing processes include non-radiative decay, phonon-assisted radiative decay and non-spin-conserving transitions. η_{co} mostly depends on the morphology of the host material and the surrounding photonic structure. Regarding η_{tr}, work by [29] demonstrated that entanglement distillation protocol is an viable option to support kHz with lossy links between network nodes. Given existing single photon counting technology, η_{dt} is up to 70% in the visible-infrared wavelengths.

1.2 NV Centres in Diamond

The nitrogen-vacancy (NV) centre is the most widely studied optical defect in diamond, and it consists of a substitutional nitrogen atom located next to a vacancy defect. The NV centre has two charge-stats, NV^0 and NV^-. In particular, the negative charge-state has a more interesting electronic level structure that is well-suited as a solid-state spin qubit. Hence in this work, we will generally use 'NV' to refer to the NV^- charge-state unless specified otherwise.

As illustrated in fig. (1.4)(a) (more details in section (2.1)), the NV centre has a spin-triplet ground-state $^3A_2$ which is characterised by a 2.88GHz zero-field splitting between the $m_s = \pm 1$ and $m_s = 0$ sub-levels. The ground-state sub-levels are connected to the corresponding triplets in the ^3E excited-state, which is 1.945eV above the ground-state, via spin-dependent optical transitions. In addition, there also exists a pair of singlet states which couples to the triplet state in a spin-selective manner. The $m_s = \pm 1$ sub-levels of the excited-state have higher decay rates into the singlet states, while the single states decay preferentially back to the $m_s = 0$ ground-state sub-level.

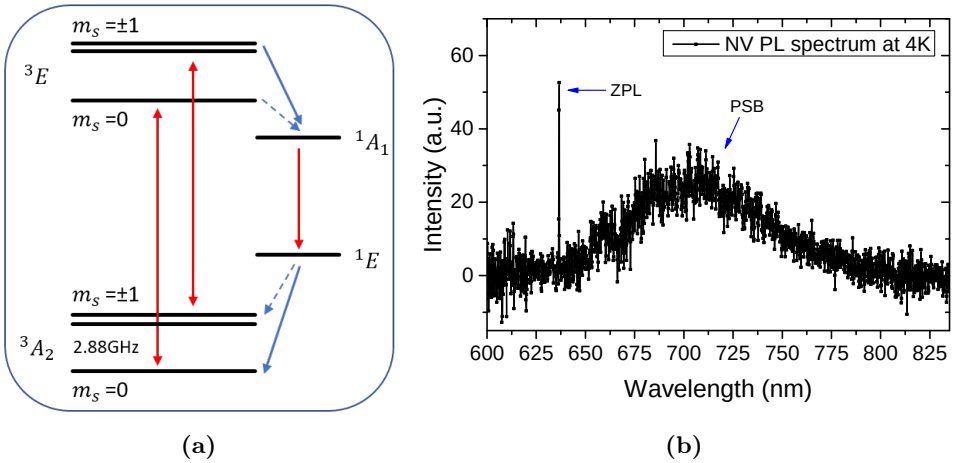

(a) **(b)**

Figure 1.4: **(a)** An illustration of NV's optical transitions between its $^3A_2$ ground-state and the ^3E excited-state. Red lines mark the radiative transitions, and blue lines mark the strong (solid) and weak (dashed) non-radiative transitions. Adapted from [30]. **(b)** A typical NV PL spectrum at 4K where only ≈4% of the photon is branched into the ZPL transition.

Recalling the DiVincenzo's criteria of a qubit mentioned at the start of this chapter, NV centre satisfies a majority of them thanks to the unique electronic structure as described above. Firstly, due to the existence of the singlet states, most of the population in the ground-state is easily polarised into the $m_s = 0$ sub-levels after a few optical cycles. Secondly, the 2.88GHz ground-state splitting between spin sub-levels can be driven and manipulated with a standard microwave field [31]. Thirdly, again thanks to the strong coupling between the singlet states and the excited-state $m_s = \pm 1$ sub-levels, the optical transitions between the $m_s = \pm 1$ levels are non-cyclic and hence appear much dimmer than the $m_s = 0$ cyclic transition. This provides a convenient readout capability via optical measurements. Moreover, NV electronic spin coherence time is on the order of hundreds of microseconds, which can be extended to over one second with dynamic decoupling

techniques [32]. These promising characteristics render the NV centre an excellent testbed for many quantum applications, including the measurement-based entanglement schemes.

Despite the promising properties mentioned above, NV also possesses several drawbacks which need to be addressed before it can compete with more mature qubit systems:

- The free-space branching ratio ζ^0 (the Debye-Waller factor) into the ZPL emission is only about 4% of total photon emission, as shown in fig. (1.4)(b). The ZPL branching ratio ζ is directly related to the indistinguishable photon emission efficiency η_{em}.
- Collecting photon from a high index material like diamond tends to be difficult due to the internal reflection. Hence the photon collection efficiency η_{co} can be limited.
- Due to the spectral diffusion of ZPL transition, the excitation efficiency η_{ex} can be compromised under resonant excitation at a fixed frequency.
- NV^- tends to be photo-ionised to NV^0 under resonant excitation at 637nm. Charge-state stability is also one of the concerns.
- Currently there lacks scalable fabrication techniques that support reliable on-demand creation of coherent NV centres in large quantities.

Fortunately, most of the listed problems have relatively clear solutions. For example, the ZPL branching ratio ζ can be boosted by coupling the NV ZPL with a resonant cavity mode to enhance ZPL emission. More efficient photon collection efficiency is achievable by implementing collection enhancing photonic structure such as a solid immersion lens (SIL). Novel fabrication method such as the laser-writing technique demonstrated coherent NV fabrication with reasonably good charge-state stability.

Although implementing all the advancements as a compact qubit still requires further material and device engineering, the diamond community is certainly working towards this goal collectively in a promising pace.

1.2.1 Entanglement Generation with NVs

Towards the goal of using NVs as network nodes, indistinguishable photon emission from independent NV centres has to be demonstrated. The Delft group [33] first demonstrated HOM interference [25] from two NV centres separated by 10µm in the same sample. Given that the maximum expected contrast of 72% due to background contribution, the obtained contrast of 66% is quite remarkable. The Harvard group [34] also demonstrated indistinguishable photon emission of 35% contrast with two remote NVs that are 2m apart. In both experiments, solid immersion lens are fabricated over native (grown-in) NVs in chemical vapour deposition (CVD) diamond to improve photon collection efficiency. Stark tuning of NV ZPL is implemented to minimize the detuning between different NV centres.

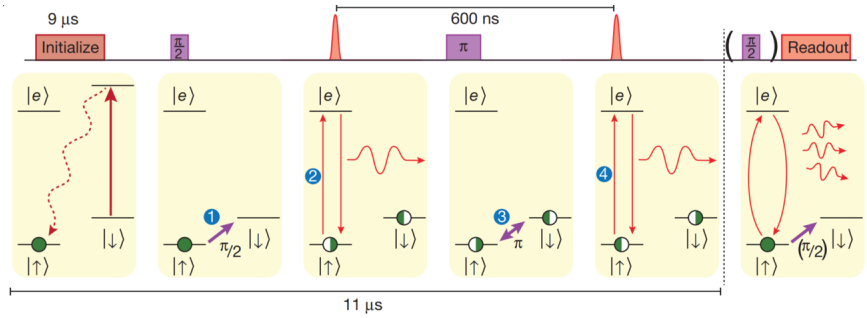

Figure 1.5: An illustration of entanglement generation under the Barrett & Kok scheme using NV centres in diamond. The two spin-dependent ZPL transitions used in the procedure are the non-cyclic A_1 transition for spin-polarisation, and the cyclic E_y transition for optical readout (more details about NV electronic structure in section (2.1)). Reprinted with permission from [22].

The experimental setup of two-photon interference measurement is essentially same with that required for entanglement generation under the Barrett-Kok scheme. Hence following the demonstration of indistinguishable photon in [33], the Delft group published another seminal work [22] in which they reported successful entanglement between two NVs separated by 3m. The detailed experimental sequence and the choice of NV transitions are illustrated in fig. (1.5) and fig. (1.6) respectively.

To setup the experiment, an excited-state $|e\rangle$ and two ground-state sub-levels $|\uparrow\rangle/|\downarrow\rangle$ are chosen to form a λ-scheme. In the context of NV centres, $|\uparrow\rangle/|\downarrow\rangle$ correspond to the m_s= 0 and m_s= -1 spin manifolds of NV centre's triplet ground-state. The $|e\rangle$ level also has m_s= 0 to form a cyclic transition with $|\uparrow\rangle$. More details about NV's energy level structure is given in section (2.1).

To initialise the process, the $|\downarrow\rangle$ level is pumped resonantly to its corresponding m_s= -1 excited-state from which the population relaxes indirectly down to the $|\uparrow\rangle$ level (m_s= 0) via inter-system crossing. This spin polarisation process is a feature of NV centre's level structure. Then, a $\pi/2$ pulse between $|\uparrow\rangle$ and $|\downarrow\rangle$ is applied to prepare the system into a coherent superposition state of $\frac{1}{\sqrt{2}}(|\uparrow\rangle+|\downarrow\rangle)$. The m_s= 0 transition between $|\uparrow\rangle$ and $|e\rangle$ is then used as readout photon to execute the double-heralding scheme as outlined in section (1.1).

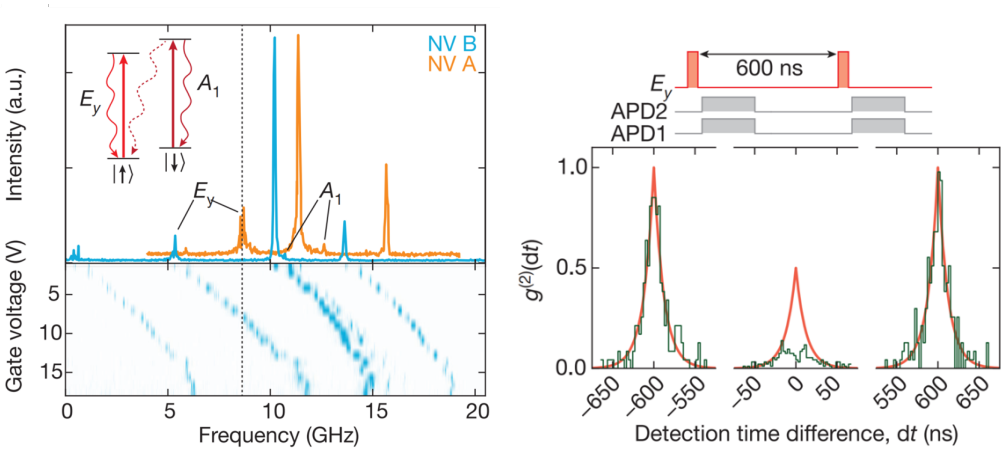

Figure 1.6: **(a)** The transition frequency tuning of the ZPL transitions between two NV centres. The depicted A_1 and E_y transitions (more details in section (2.1)) are selected for entanglement generation as illustrated in fig. (1.5). **(b)** Demonstration of indistinguishable photon generation. Reprinted with permission from [22].

This demonstration of entanglement generation features an attempt rate of 20kHz which produced an entanglement generation rate of 1.7×10^{-3} per second. The overall resonant photon detection efficiency was found to be η= 4×10^{-4} corresponding to an entanglement successful rate of P_{succ}=1×10^{-7}. In a follow-up demonstration of quantum teleportation [35] from the same group, the efficiency η was improved by an order of magnitude by implementing a charge-state recovery scheme.

More impressively, the same setup is later used to demonstrate loophole-free violations of Bell's inequalities with NVs separated by 1.3km via single-mode fibre connections [36] which sets a new record for distribution entanglement. The demonstration of indistinguishable photon over long-range fibre-network is especially encouraging given the signal attenuation of fibre and the demand on interferometric stability between two heralding events.

1.2.2 Optical Coherence of NV ZPL Transitions

On-demand fabrication of coherent NV centres is absolutely crucial in order to improve the technology readiness of the NV centre as quantum network nodes. Despite the remarkable achievement demonstrated by the above-mentioned indistinguishable photon and entanglement experiments, all of them relies on naturally occurring NVs during CVD growth. Although much progress has been made with these native defects, material engineering of diamond has come a long way in pursuit of deterministic creation of coherent NV centres.

Papers	Diamond	NV fab	Depth	δ_{hom} MHz	δ_{inhom} MHz	Notes
[18]	natural	native	-	13	-	
[37]	CVD	grown-in	-	≈25	≈100	
[38]	CVD	grown-in	-	-	<200	
[20]	CVD	grown-in	-	46	≈300	
[39][40]	CVD	grown-in	100nm	66	116	
[41]	CVD	grown-in		≈30	≈300	
[33]	CVD	grown-in		37	320	
[38]	CVD	ion	-	-	>5000	
[42]	CVD	ion	100nm	<37	<500	
[43]	CVD	ion	100nm	64	140	Native ^{14}N.
	CVD	ion	100nm	860	3100	Implanted ^{15}N.
[44]	CVD	ion	68nm	-	100	
	CVD	ion	68nm	-	1000	t<1µm.
[28]	CVD	e-beam	-	39	122	t>10µm.
	CVD	e-beam	-	86	189	t<3µm.
[45]	CVD	-	-	-	4000	t=0.2µm, [N]<1ppm.
[46]	CVD	grown-in	-	393	>5000	t=0.2µm.
[19]	CVD	laser	50µm	13	33	

Table 1.1: Summary of PLE results from previous literature works. Most linewidth estimates are taken from the best presented figures in each work. Micro-structured diamond samples are listed next to each other and the their thicknesses are given as t in the notes column.

In the past decade, several NV generation techniques have been tested, including electron irradiation, ion-implantation and laser-writing technique. One can refer to [47] for a complete review of NV fabrication methods. The optical coherence of created NVs varies to a large extend as summarised in table (1.1).

Early demonstration of ion-implanted technique [42] reported coherent NV generation

but the reproducibility was not ideal. It was later discovered that there exists two kinds of NVs in the ion-implanted diamond samples [43]. Due to the implantation ion damage, the NVs formed with native nitrogen impurities tends to exhibit much better optical coherence than the ones formed with implanted nitrogen. Work by [28] demonstrated coherent NV generation via electron radiation. The observed NV ZPL linewidths are very close to the native NVs. The NV fabricated with the novel laser-writing technique [19] reported an even better NV coherence with lifetime-limited homogeneous linewidth being observed in multiple NVs.

It seems like a trend is clear where the NV coherence is correlated to the intrusiveness of the fabrication method. The ion-implantation involves the strongest lattice damage due to the size of the ions. In contrary, the laser-writing technique modifies the crystal with no sizeable particles but only photons. The lattice defects are usually correlated to NV linewidth broadening effect such as homogeneous broadening due to non-radiative decay pathways and inhomogeneous due to dephasing in the form of spectral diffusion.

1.2.3 Charge-State Stability Under Resonant Excitation

The charge-state stability of NV centre under resonant excitation is an important factor to consider especially for entanglement generation. The NV centre tends to be photo-ionized by the 637nm excitation and switches charge-state from NV^- to NV^0. The NV^0 state requires a lower wavelength repump laser pulse to restore NV^- charge-state. Although this is a bi-directional conversion cycle, the high energy repump photons rearrange the local electric field configuration which leads to the spectral diffusion of ZPL transition. This complicates the ZPL tuning process and decreases the rate at which entanglement operation can be attempted.

Referring back to the entanglement demonstration by the Delft group [22], an initialization sequence is dedicated to prepare both NVs in the NV^- state before the entanglement measurement sequence is carried out. As shown in fig. (1.7), a 532nm pulse is first applied to prepare NV in the NV^- charge-state. Next, two resonant pulses corresponding to the E_y and A_1 transitions are applied. Only if the photon emission intensity passes a certain threshold, the entanglement generation sequence is executed.

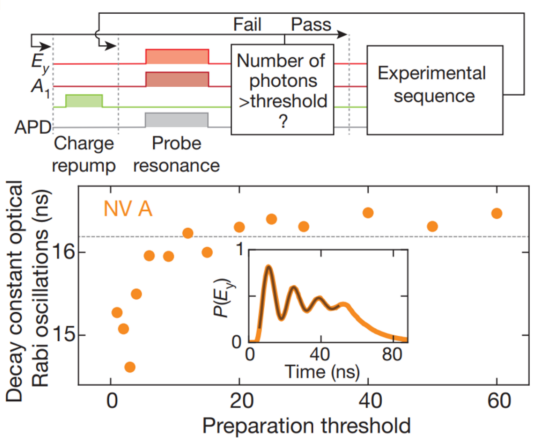

Figure 1.7: The charge-state and post-selection procedures before attempting for entanglement generation operations. Reprinted with permission from [22].

We note that the charge-state preparation by the 532nm pulse has a success probability. Moreover, the charge-state stability at 532nm is not necessarily transferable to that under the 637nm excitation. The actual probability of an NV passing the preparation step as NV^- is a balance between the ionization and recharge processes. To describe the efficiency of this charge-state preparation process, we modify the entanglement efficiency η in eq. (1.20) by adding the charge-state preparation efficiency η_{cs}:

$$\eta = \eta_{cs} \times \eta_{ex} \times \eta_{em} \times \eta_{co} \times \eta_{tr} \times \eta_{dt} \tag{1.21}$$

where η_{cs} indicates the probability of NV being in the NV^- charge-state after the probe resonant excitation.

In this work, we quantify η_{cs} using the PLE validation rate p_{val} obtained from PLE measurement statistics (details in section (3.6)):

$$p_{val} = \frac{\text{Number of validated PLE scans from } NV^-}{\text{Total number of PLE scans performed}} \tag{1.22}$$

In principle, p_{val} represents the probability of the NV staying in the NV^- charge-state under constant 637nm excitation across the ZPL transition which resembles η_{cs} quite closely. In addition, we also introduce the ionization p_{ion} and recharge probabilities p_{rec} to describe the bi-directional NV^-/NV^0 conversion processes. The value of p_{val} is dependent on the relative magnitude between p_{ion} and p_{rec}. Our data in section (5.3.5)

also show that some high quality NVs exhibits long-lived bright states which is described by a larger measured p_{val} than p_{rec}.

1.3 NV Centres in Optical Resonators

In addition to the material engineering considerations for coherent NV generation, device engineering is another crucial factor to enhance light-matter interaction and improve photon collection. Unlike the traditional silicon industry, the fabrication of the diamond-based device is less mature, and the scale of fabrication is limited to the laboratory level. Nevertheless, a variety of photonic structures have been developed to address the shortcomings of the NV centre. In this section, a review of diamond-based photonic devices is presented. The focus is placed on the optical resonator devices while some collection enhancing structures will also be mentioned.

Incorporation of NV centre in optical resonators is a widely adopted strategy to improve NV emission rate. Discussion in this section is limited to the weak coupling regime of cavity quantum electrodynamics because the strong coupling regime is unnecessary for entanglement generation and is generally difficult to realise with diamond photonic structures.

In the weak coupling regime, the spontaneous emission rate of a cavity-coupled NV is altered in response to the modification of the local density of photonic states (LDoS) due to the presence of the cavity structure. This effect is quantified by the Purcell factor F [48], and it benefits the entanglement generation in mainly two aspects.

Firstly, by coupling the NV ZPL to a cavity mode, the branching ratio of NV emission into the ZPL transitions is improved according to:

$$\zeta_{\mathrm{zpl}}^{\mathrm{cav}} = \frac{\zeta_{\mathrm{zpl}}^{0} F_{\mathrm{zpl}}}{\zeta_{\mathrm{zpl}}^{0} F_{\mathrm{zpl}} + (1-\zeta_{\mathrm{zpl}}^{0}) F_{\mathrm{psb}}} \qquad \text{(derivation in eq. (2.28))}$$

where F_{zpl} and F_{psb} are the emission enhancement in the ZPL and PSB spectral regions and ζ_{zpl}^{0} is the free-space ZPL branching ratio ($\approx 4\%$). The improved probability of ZPL emission for each optical cycle contributes directly to the entanglement success rate via the emission efficiency η_{em} in eq. (1.20).

Secondly, the cavity-coupled NV centre experiences a reduction in excited-state lifetime due to the increased spontaneous emission rate $\kappa_{\text{eff}} = 2g^2/\kappa$. The ZPL transition linewidth is therefore broadened proportional to $1/\kappa_{\text{eff}}$. If the cavity-NV interaction is strong enough, the dephasing effect at low-temperature might be overcome by increasing κ. A detailed discussion of cavity-funnelled indistinguishable photon generation is reported by [16].

To date, a variety of diamond-based and hybrid optical resonators has been developed, and the relevant cavity metrics have been summarised in table (1.2). The more popular structures include the microring/microdisk whispering gallery mode resonators, the thin-film 1D and 2D photonic crystal cavities and Fabry-Perot type open cavities. To cross-compare different photon systems, we refer to a number of important cavity metrics including the quality factor Q, the mode volume V in $(\lambda/n)^3$, the spontaneous emission rate F_{zpl} and modified ZPL branching ratio ζ^{cav}.

Papers	Resonator	Q	V $(\lambda/n)^3$	F_{zpl}	ζ^{cav}
[49]	Microring	5,000	17-32	12	25%
[50]	GaP microdisk	8,200	3.5	26	-
[45]	2D PCC	3,000	0.88	70	75%
[51]	1D PCC	3,300	1.05	62	54%
[52]	ND in FP	3,000	4.7	10	-
[44]	Membrane in FP	58,500	125	30	46 %

Table 1.2: A summary of cavity metrics from note-able literature demonstrations of cavity-coupled NV experiments.

Earlier demonstration of whispering gallery mode resonators was reported by [53] where microdisk structures were fabricated using FIB in nano-crystalline diamond [53]. The observed Q near 637nm was limited to 100 due to grain boundary and surface roughness scattering. The first resonant enhancement of NV ZPL was realised using a microring resonator fabricated by electron-beam lithography and dry etching [49]. The supported whispering gallery modes shows $Q \approx$4,000, and a ZPL emission enhancement of F_{zpl}=12 is observed.

A hybrid approach using a GaP-on-Diamond construction was also actively explored by [54, 55] where only moderate F is observed due to the weak emitter-field overlap. Recent work by [50] has demonstrated high-quality GaP-on-Diamond structure where a small

mode volume and F=26 is observed. The presented GaP disk also couples to waveguide structure with an efficiency of 0.09.

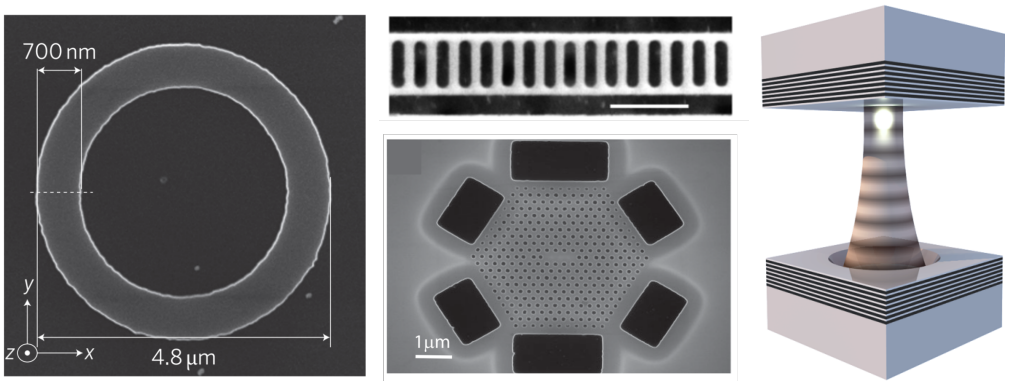

(a) **(b)** **(c)**

Figure 1.8: **(a)** A microring resonator, reprinted with permission from [49]. **(b)** The 1D and 2D photonic crystal cavitiesm, reprinted with permission from [45, 51].**(c)** The Fabry-Perot microcavities.

The photonic crystal cavity (PCC) consists of a periodic dielectric structure which creates a photonic band-gap for the designed wavelength. Local confined of the light field is achieved by modifying or removing some part of the periodic nodes. Both 1D and 2D PCCs have been developed for coupling to NV centres in diamond. The initial demonstration follows a hybrid approach where 2D-PCCs were fabricated from GaP, and the NV-containing nano-diamonds are placed at the desired locations to facilitate deterministic coupling [56]. Following the development of single-crystal diamond fabrication technique, more monolithic all-diamond structures have been demonstrated.

Recent work by [51] demonstrated high emission enhancement of a single NV coupled to a 1D PCC at 18K. The fabricated device features a Q up to 9,900 and mode volume down to $1.05(\lambda/n)^3$. The resultant 54% ZPL branching ratio is obtained by coupled the NV to a Q=3,300 PCC. Moreover, the 2D PCC fabricated by [45] exhibits an even higher F up to 70, and the inferred ZPL branching ratio reaches 75%. The demonstrated device has a mode volume of $0.88(\lambda/n)^3$ and Q=3,000. These are certainly the smaller mode volumes among all microcavity structure.

The Fabry-Perot type cavity is most commonly constructed with two dielectric DBR mirror in a planar-concavity configuration. Because the two mirrors are decoupled against each other, FP type cavities offer both lateral and resonance tuning capabilities such that maximum overlap between the emitter and the resonant field is routinely achieved.

In the proof of principle work by [52], NV centres in nano-diamonds are coupled to FIB-milled microcavities with a radius of curvature $\mathcal{R}$=7.6μm at 77K. With a small V at $4.7(\lambda/n)^3$ and a moderate Q at 3,000, the cavity-coupled NV ZPL experiences an emission enhancement of F_{zpl}=10 and a factor of 6.25 enhancement in ZPL intensity is observed. A more recently adaption of the FP cavity is reported by [44] where a membrane-in-cavity setup is adopted. The NV centres are hosted in the 200nm-thick diamond membrane and coupled to a high finesse FP cavity with $\mathcal{R}$=16μm at 4K. The quantified emission enhancement at NV ZPL is about F_{zpl}=30, which boosted the ZPL branching ratio to 46%.

Another actively explored open-cavity geometry uses DBR-coated fibre tips as cavity mirrors. Earlier demonstration of such construction demonstrated an impressive measured cavity finesse $\mathcal{F}$ at 130,000 with cavity feature fabricated with CO_2 laser machining [57]. This approach is promising in the build-up of fibre-based network although the photon collection can be limited by the low numerical aperture of single mode fibres (typically NA=0.1).

To summarise, the whispering gallery mode cavities has a larger mode volume and moderate cavity quality factor limited to surface roughness. By utilising the maturing chip-based fabrication methods, both all-diamond and hybrid approach has promising application within integrated diamond photonics. The PCC system is capable of supporting resonant modes with ultra-small mode volume, and the expected quality factor is also high. The 1D PCC cavity in particular also provides some extend of guiding capability for integrated photonic applications. However, the real-world performance is highly dependent on the surface quality and side-wall straightness of the periodic structure. Similar to the whispering gallery mode cavities, the tuning is also a slight complicated. The Fabry-Perot type resonator has the best tunability to match the emitter with the field maximum of the resonant cavity mode. Compared to the all-diamond approaches, it is still limited by the fabrication technology of nm-scale diamond structure which is situated between the mirrors.

1.4 Project Goals and Thesis Outline

The proof-of-principle work by [52] demonstrated promising emission enhancement of cavity-coupled NV in nano-diamond using a Fabry-Perot type micro-cavity. To further develop this methodology, two improvements are made in this project. Firstly, a membrane-in-cavity setup is adopted to replace nanodiamonds with an ultra-thin diamond membrane (fig. (1.9)(a)). By hosting the NV centre in a μm-thick membrane, improved coherence properties can be expected. Secondly, novel laser-writing technique of NV centres [19] is used as an alternative to the conventional ion-implantation method. Laser-written NVs have shown very promising coherence properties, and the fabrication capability is well-suited for large scale device fabrication.

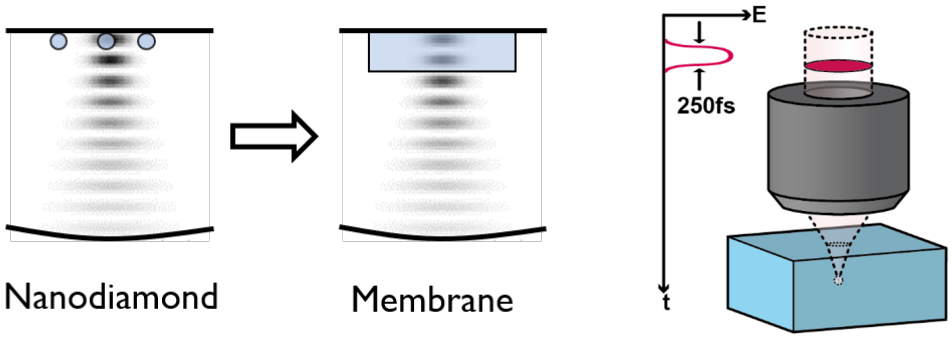

Figure 1.9: Illustration of project goals including **(a)** the realisation of membrane-in-cavity setup and **(b)** the usage of laser-writing technique for coherent NV generation in diamond membranes.

Instead of using high-R mirrors, the planar mirror in our setup is kept to a moderate reflectivity of 0.998. This compromise is primarily made to deal with cavity instability because our cavity setup only features passive stabilisation measures. The reduction in R improves the robustness of emission coupling and also allows an efficient collection of photons from the planar mirror transmission. As much as high emission enhancement is preferred to boost the ZPL branching ratio, we also value the change in photon collection efficiency. Both aspects contribute to the performance of the cavity device for entanglement generation applications.

There also exist additional issues associated with the membrane-in-cavity approach. With a high index material in a membrane morphology, lateral photon channelling via the

diamond membrane could be a dominant cavity loss mechanism in the membrane-in-cavity setup. We will quantify how such effect affects the emission enhancement and collection efficiency of our cavity device. Also, in comparison to NVs in bulk diamond, the optical coherence of NVs in ultra-thin membranes can be expected due to the increased exposure to surface trap states.

Throughout this thesis we will constantly refer back to the analysis framework established in sections (1.1.5) and (1.2.3) to quantify how our experimental results contribute towards efficient and high fidelity entanglement generation under the double-heralding entanglement scheme. The thesis chapters are structured as follows:

Chapter 2 - Theoretical Background

The essential theoretical tools required to describe the NV-cavity interaction in a membrane-in-cavity device is provided in this chapter. Firstly, we give an overview of the NV centre in diamond with the focus on the optical coherence of the ZPL transitions. Next, an introduction of basic cavity quantum electrodynamics concepts is followed by a discussion of the Purcell effect in the weak coupling regime. The cavity metrics of a single-medium Fabry-Perot cavity are reviewed both analytically and numerically with a 1D transfer matrix model. The same methodology is extended to the discussion of the hybrid-medium membrane-in-cavity device, where the distinction between air-like and diamond-like cavity mode is made. Finally, the theoretical background of the Finite-difference Time-domain (FDTD) simulation is covered.

Chapter 3 - Experimental Methods

The fabrication procedure towards NV-containing ultra-thin diamond membranes is demonstrated in a two-step process, including NV generation and membrane thinning. Sample preparation considerations are presented along with an introduction of necessary material processing and characterisation techniques. The setup and detailed analysis methodology of relevant optical measurements are demonstrated.

Chapter 4 - Finite-difference Time-domain Simulations

FDTD numerical simulation is carried out to provide insights into the dependence cavity performance on various cavity parameters. With the emphasis on accurately

quantifying device performance in terms of ZPL photon output, we propose a rigorous analysis protocol which combines the commonly used emission enhancement analysis with a detailed collection analysis. Basic understanding of cavity operation is established based on single-medium cavity simulations. Subsequent simulations with diamond-air hybrid-medium cavities are then conducted to provide experimental guidance.

Chapter 5 - NV Centre in Diamond Membranes

We first present the fabrication of earlier iterations of fabricated membranes with ion-implanted NVs. The encountered fabrication challenges are highlighted, and our solution to establish a reliable fabrication flow is demonstrated. The yield and spectral quality of implanted NVs are examined, and their evolution throughout the fabrication process is tracked. An on-going effort towards implementing laser-written NVs into the membrane is also presented. Finally, the optical coherence of NV centres from a variety of samples is probed with PLE measurement. A comparison between ion-implanted and laser-written NVs is made.

Chapter 6 - Low-temperature Cavity-coupling of NV Centre

Results from cavity-coupling experiments of the NV centre at 4K is presented in this chapter. To form the basis of comparison against cavity-coupling data, optical properties of a target NV centre are first measured in the on-mirror configuration. Most importantly, the orientation of emission dipole is determined, and the excited-state lifetime and power-saturated photon output are recorded. Moving on to the cavity-coupled configuration, model tuning across an NV ZPL is demonstrated and the in-cavity ZPL photon output is again quantified via lifetime and power saturation measurements. A primitive emission rate analysis is conducted with available information which concluded that FDTD simulation is required to fully explain the observed device performance.

Chapter 7 - FDTD Analysis of Cavity-coupling Results

Cavity-coupling data from chapter (6) is matched with FDTD simulations in this chapter using experimentally-measured cavity parameters. The single-frequency analysis model of FDTD simulation established in chapter (4) is further developed

into a multi-frequency integration approach to account for the structured NV emission spectrum. Calibrations between different experimental configurations are also required to accommodate the change in the local density of photonic states due to the dielectric structure. An excellent agreement between FDTD simulation and experimental data is reached by reducing the simulated mirror reflectivities, confirming the presence of an unidentified hidden loss in the experiment.

Chapter 8 - Conclusions and Outlook

The main outcomes of the work presented in this thesis are summarised. The limitations of current experimental setup and routes of potential improvement are listed to help further development of the cavity-coupled NV setup.

Chapter 2

Theoretical Background

In this chapter, we present the relevant theoretical backgrounds required for describing the experimental results in the following chapters. Firstly, an introduction of the NV centre in diamond is given with the focus placed on the optical coherence of ZPL transitions. Next, some relevant cavity quantum electrodynamics concepts are discussed to describe light-matter interaction. The basic optical resonator metrics are introduced following the analytical description of a single-medium Fabry-Perot cavity. The cavity discussion is then extended to the hybrid-medium cavities, which resembles the target membrane-in-cavity setup of this work. Lastly, the theoretical background of finite-different time-domain simulation is presented.

2.1 Nitrogen-Vacancy Centre in Diamond

First and foremost, the properties of NV center will be introduced with more details. The NV centre is a point defect in diamond which consists of a pair of substitutional nitrogen and vacancy defect orientated along the [111] lattice direction (fig. (2.1)(a)). The NV centre exhibits two fluorescent charge-states namely the NV^- and the NV^0 states. Both states are often observed to co-exist under 532nm excitation and a typical time-averaged NV spectrum is plotted in fig. (2.1)(b). The presences of NV^0 and NV^- are identified by the 575nm and the 637nm zero-phonon line (ZPL) respectively plus the phonon-assisted sideband (PSB) emission towards longer wavelengths. This work primarily concerns the negatively-charged state while some aspects of NV^0 will also be touched, for example in the discussion about charge-state switching.

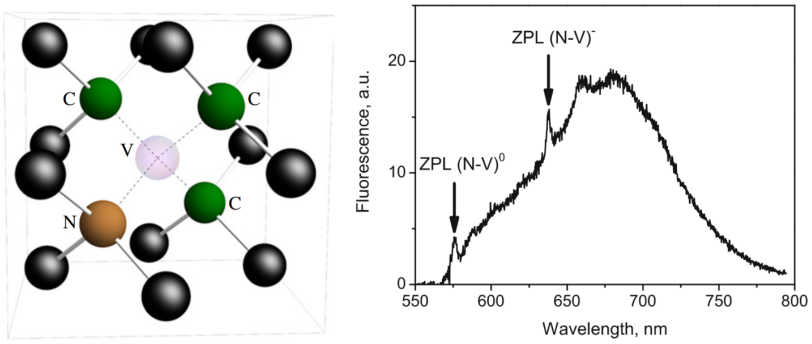

(a) **(b)**

Figure 2.1: **(a)** The nitrogen-vacancy centre in diamond. Reprinted with permission from [30]; **(b)** A typical NV spectrum containing both NV^0 and NV^-. Reprinted with permission from [58].

2.1.1 Electronic Structure of Negatively-Charged NV

The NV centre has a C_{3v} symmetry and there are four one-electron orbitals including two degenerate orbitals of E symmetry (e_x and e_y) and two orbitals of A_1 symmetry (a_1 and a_1'). The a_1' orbital is always occupied in the conduction band and thus can be ignored. The NV electronic structure is thus governed by the intra-band orbitals.

The NV^- charge-state possesses 6 electrons in total where 2 of them are in the a_1' orbital. The rest four electrons occupies a_1 and two e orbital as shown in fig. (2.2)(a) where three configurations are formed in order of increasing energy: $a_1^2e^2$, a_1e^3 and e^4. The corresponding multi-electron energy levels are $({}^3A_2, {}^1E, {}^1A_1)$, $({}^3E, {}^1E)$ and $({}^1A_1)$. These energy levels shift according to the corrections given by two-electron Coulomb repulsion where the final states of interest are marked in the green box.

Given that the ground triplet state ${}^3A_2$ of $a_1^2e^2$ configuration has a total spin angular momentum S=1 and the electric dipole transition requires spin-conservation, the matching triplet state in the excited-state is the ${}^3E$ level of a_1e^3 configuration. Hence the electric dipole transition corresponding to the 637nm ZPL emission is assigned to the ${}^3A_2(a_1^2e^2)$-${}^3E(a_1e^3)$ transition. The transition between the intermediate singlet states ${}^1A_1(a_1^2e^2)$-${}^1E(a_1e^3)$ is also allowed yielding an infrared transition at 1042nm.

Moreover, NV^- state is also identified by the ground-state zero-field splitting of 2.88 GHz at room-temperature. Due to the spin-spin interaction, the spin projections of both ${}^3A_2$ and ${}^3E$ triplet states are split into an m_s=0 and a degenerate m_s=± one sub-levels.

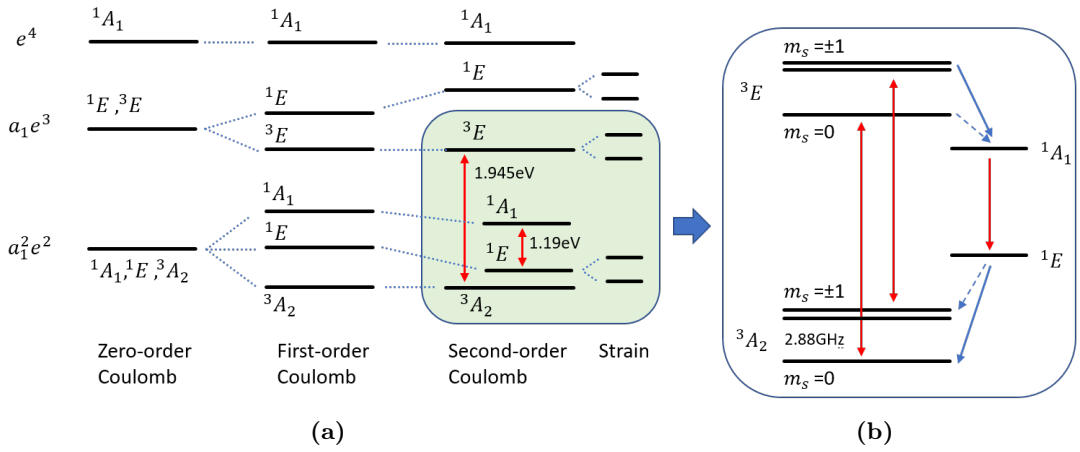

Figure 2.2: **(a)** The energy level structure of NV^- charge-state where the green box shows the states of interest. Adapted from [59]; **(b)** The spin-polarization process between the NV ground- and excited-states at room temperature. The red lines mark the radiative transitions and solid (dashed) blues lines represent strong (weak) non-radiative transitions. Adapted from [30].

In addition to the marked radiative decays, the population in ^3E also decays to $^3A_2$ via intermediate singlet states through non-radiative channels. Because of the relative strength of transition from ^3E to singlet states favours the m_s=0 spin projections, over a few optical cycles the majority of the population occupies the m_s=0 sub-levels. This process is referred to as optical spin-polarisation, which enables the spin-state process in most quantum information applications.

2.1.2 Excited-State Fine Structure at Low-Temperature

In addition to the simplified level structure in fig. (2.2)(b), the excited-state fine structure is further splitted due to a combination of spin-orbit and spin-spin interactions as illustrated in fig. (2.3)(a). The orbital-doublet spin-triplet ^3E excited-state consists of 6 states where the m_s= 0 states are labelled as (E_x, E_y) and the m_s= ±1 states are labelled as (A_1, A_2) and (E_1, E_2). Discussion in this section follows the group theory approach demonstrated by [60].

Firstly, the axial spin-orbit interaction splits the states with different total angular momentum into three two-fold degenerate levels: (E),(E') and (A_1, A_2) which are separated by the interaction strength of λ_z. The transverse spin-orbital interaction is generally weak and is ignored here.

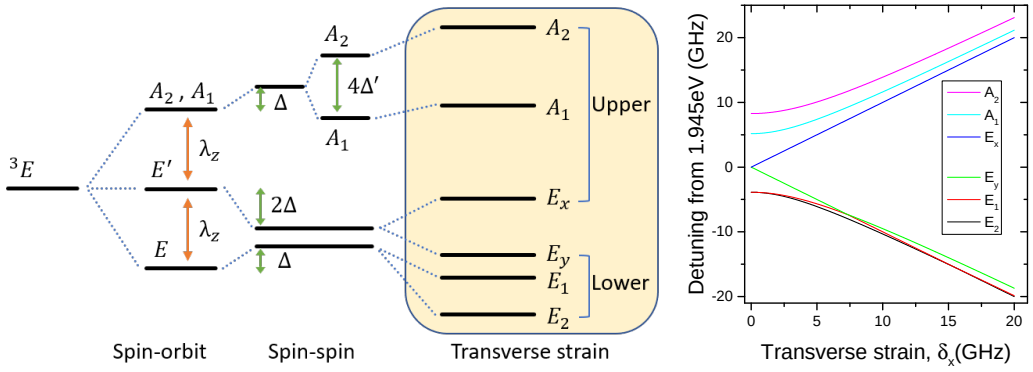

Figure 2.3: **(a)** The evolution of excited-state sub-levels under the influences of spin-orbit, spin-spin and transverse strain Adapted from [61]; **(b)** Excited-states fine structure plotted as a function of transverse strain δ_x. In addition to the parameters shown in **(a)**, a spin mixing term Δ'' is also included in the spin-Hamiltonian. Calculation based on the model established by [60].

Next, the spin-spin interaction shifts up the m_s=±1 states (E, A_1, A_2) by Δ and shifts down the m_s=0 states (E') by 2Δ. It also splits the states with different spin-projections hence A_1 and A_2 are separated by $4\Delta'$. The states in E and E' are mixed which is described by a spin-mixing term Δ'' [60].

Lattice strain also plays role where the longitudinal strain induces an overall energy shift of all levels (ignored here) and the transverse strain (δ_x/δ_y) splits the E_x and E_y levels [30]. At zero strain, the degenerate sub-levels in both E symmetry states are indistinguishable.

To summarise effects of above-mentioned interactions, the overall spin Hamiltonian whose energy eigenstates corresponding to all six transitions is written as:

$$\boldsymbol{H} = \boldsymbol{H}_{\mathrm{so}} + \boldsymbol{H}_{\mathrm{ss}} + \boldsymbol{H}_{\mathrm{strain}} = \tag{2.1}$$

$$= \begin{bmatrix} \lambda_z + \Delta - \Delta' & 0 & 0 & 0 & \delta_x & -i\delta_y \\ 0 & \lambda_z + \Delta + \Delta' & 0 & 0 & i\delta_y & -\delta_x \\ 0 & 0 & -2\Delta + \delta_x & \delta_y & \delta_x & i\Delta'' \\ 0 & 0 & \delta_y & -2\Delta - \delta_x & \Delta'' & 0 \\ \delta_x & -i\delta_y & 0 & \Delta'' & -\lambda_z + \Delta & 0 \\ i\delta_y & -\delta_x & -i\Delta'' & 0 & 0 & -\lambda_z + \Delta \end{bmatrix} \tag{2.2}$$

where λ_z= 5.5GHz, 3Δ= 1.42GHz, and Δ'= 1.55GHz [61, 62]. The value of Δ'' is taken

as 0.1GHz from [60]. Since the transverse strain δ_x and δ_y are equivalent, a plot of energy levels as a function of transverse strain δ_x is illustrated in fig. (2.3).

Combining with the triplet $^3A_2$ ground-state, in principle, a total of 6 transitions should be observable. However, due to the spin-polarization process introduced in fig. (2.2)(b), only E_{x} and E_{y} are good cyclic transitions. In fact due to the mixing between E_{y} and E_1 at $\delta_{\mathrm{x}} \approx$ 7GHz and thermal fluctuation, E_{y} is not always present in a PLE spectrum. In order to observe all six transitions under strain, either a microwave field at 2.88GHz or a side-band laser modulation [63] is required to mix the population in the grounds state. This way the non-cycling transitions can be maintained and observed.

2.1.3 Line-Broadening Effects of NV ZPL Transitions

Recalling the single-cycle linewidth expression of an optical transition in a solid:

$$\delta v_{\mathrm{hom}} = \frac{1}{\pi T_2} = \frac{1}{2\pi T_1} + \frac{1}{\pi T_2^*} = \frac{1}{2\pi}\left(\frac{1}{\tau_{\mathrm{rad}}} + \frac{1}{\tau_{\mathrm{nrad}}}\right) + \frac{1}{\pi T_2^*} \qquad \text{(eq. (1.10) revisit)}$$

where $\tau_{\mathrm{rad/nrad}}$ are the radiative and non-radiative lifetime and T_2^* is the pure dephasing time which accounts. In a time-averaged measurement, the total linewidth v_{tot} is obtained as a convolution between v_{hom}, and v_{inhom} processes related to slow dephasing process such as spectral diffusion.

In the following discussions, two main broadening mechanisms of NV ZPLs are reviewed. The power broadening of transition linewidth due to excitation laser will be neglected here.

2.1.3.1 Temperature Broadening

At room-temperature the NV ZPL transition is massively broadened due to temperature broadening. This is a T_1-type decoherence effect which is induced by the interaction between the NV excited-states and the phonon modes of the diamond lattice. The temperature dependence of ZPL linewidth was investigated by [37]. For $T < 100$K, a T^5

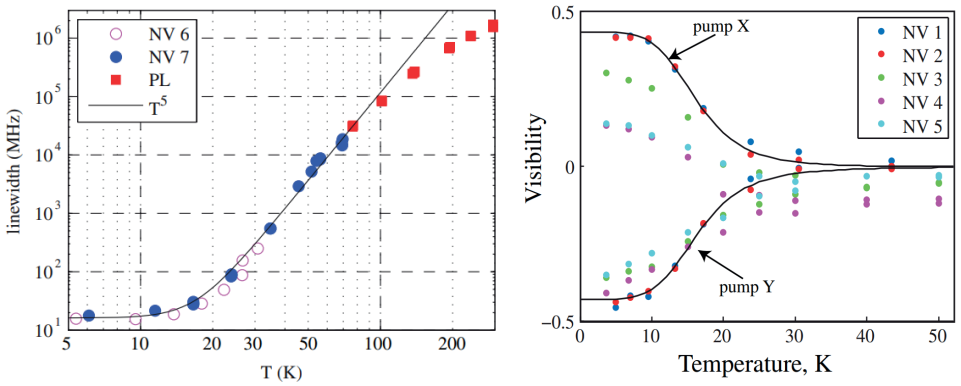

(a) **(b)**

Figure 2.4: The temperature dependence of ZPL linewidth. Reprinted with permission from [37].

relationship is found in the linewidth data shown in fig. (2.4)(a) by fitting the corresponding transition rates with:

$$\gamma(T) = \gamma_0 + crT^5 \tag{2.3}$$

where γ_0= $2\pi\times$16.2MHz, c=9.2$\times10^{-7}$K^{-}5 and r= $(12.5ns)^{-1}$.

Another finding by the authors is the temperature dependence of polarisation visibility between the strain-splitted orbital doublet as shown in fig. (2.4)(b). At T<30K the polarisation decay rate is comparable to the radiative decay rate while for T>30K the thermalisation process dominates. The authors assign both evidences to the dynamic Jahn-Teller effect below 100K. In order to quantify lifetime-limited NV ZPL linewidth and couple ZPL transition to cavity modes, measurements in this work are performed at 4K.

2.1.3.2 Spectral Diffusion

One of the prominent issue with NV ZPL transitions is the spectral stability. Due to the Stark effect [18], the ZPL transition frequency drifts as local electric field fluctuates. This is a T_2^*-type dephasing and is referred to as spectral diffusion.

As shown in fig. (2.5), between successive PLE scans (scan 50 to 150 for example), only minor drifts of ZPL position are observed. The more prominent spectral jumps often occur after a repump laser pulse is applied to recharge the NV centre from NV^0 to NV$^-$. In this case, the local charge configuration is shuffled completely, and the ZPL position

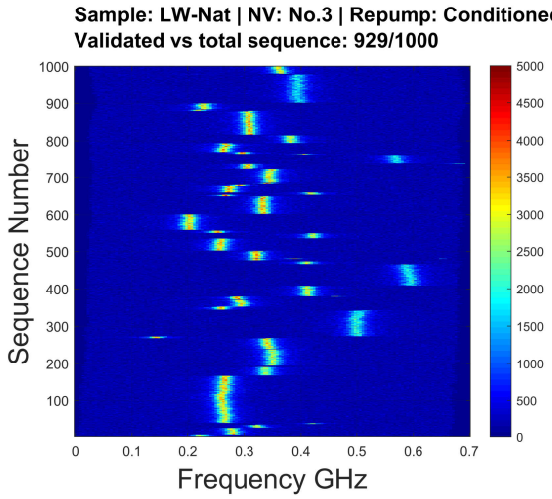

Figure 2.5: A PLE dataset taken from a laser-written NV centre to demonstrate the effect of spectral diffusion.

ends up far from the initial position. Under resonant excitation, spectral diffusion causes detuning between the driving field and the ZPL frequency, resulting in a faster oscillation damping and reduced contrast in two-photon interference measurement [20].

The charge fluctuation can be caused by a range of lattice imperfections. The most common candidates are the single substitutional nitrogen (P1), the single vacancy centres (GR1) and surface trap-states. Recent work [64] demonstrated the identification of a single defect trap around an NV using charge-state dynamics. Assuming that each ZPL position corresponds to one local charge configuration, the NV in fig. (2.5) most likely has a limited number of defects nearby. Later in section (5.3), we show that NVs with a low concentration of local charge-traps is routinely fabricated using the laser-writing technique. This is not normally achievable using the conventional ion-implantation technique.

2.1.4 Photo-Induced Charge-State Switching

Charge-state control of the NV centre is crucial for any quantum information applications that rely on the ZPL emission of NV^- charge-state. It is often observed [20, 38] that under prolonged resonant excitation, NV^- emission can be easily suppressed and the NV centres enter a long-lived dark state which is later identified as NV^0 [66, 67]. The bi-directional charge-state conversion process as a function of excitation wavelength is best summarised in fig. (2.6). The conversion loop is broken at blue wavelengths due to the lack of NV^-

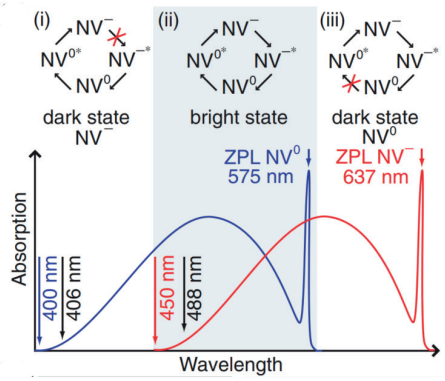

Figure 2.6: Wavelength dependent conversion cycle between NV^0 and NV^-. Reprinted with permission from [65].

absorption in the region and the same goes for the longer red wavelengths where NV^0 absorption is absent. The bi-directional conversion loop is only complete when exciting in the overlapping region.

The commonly accepted charge-state switching mechanism is established by [41] as depicted in fig. (2.7). The conversion from NV^- to NV^0 is initiated by absorbing two photons which promotes an electron from the a_1 orbital to the valance band via the excited-state. The promoted electron then relaxes back down to the ground-state via an Auger process which promotes the other excited-state electron into the valance band. The second electron gains enough energy to escape NV proximity and the NV centre relaxes back to NV^0 state.

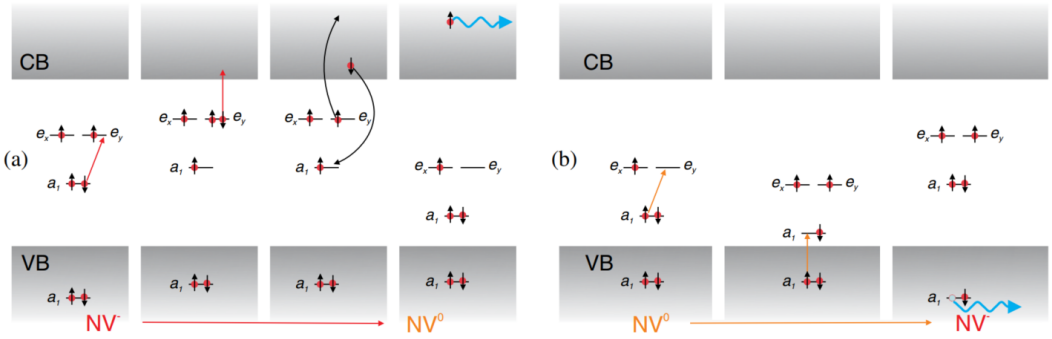

Figure 2.7: Illustration of the bi-directional charge-state conversion processes of NV centres: **(a)** NV^- is converted to NV^0 by absorbing two photons in succession which is followed by an Auger process to leave a free-moving electron in the conduction band; **(b)** NV^0 is converted to NV^- by absorbing two photons in succession which leaves a free-moving hole in the conduction band. Reprinted with permission from [41].

The conversion from NV^0 to NV^- starts with exciting an a_1 electron by absorbing one

photon. A second photon excitation then follows to promote a valence electron to the vacant a_1 orbital. This leaves a deep hole in the valence band which has enough energy to leave the NV centre such that it relaxes into the NV^- state.

As a result, charge-states switching, a repump laser is usually required during resonant excitation to convert NV^0 back into the NV^- state. Considering the relative absorption cross-sections, the commonly used repump wavelength is at 532nm. The 575nm repump at NV^0 ZPL wavelength has also been demonstrated [41, 42] which is claimed to be more efficient and less disruptive in theory but is slightly more difficult to implement in experimental conditions.

2.2 Cavity Quantum Electrodynamics

One of the key topics of this work is the light-matter interaction in an optical resonator which is a well-studied subject in the field of cavity quantum electrodynamics (CQED). In this section relevant CQED concepts will be introduced following the approach set out by [13].

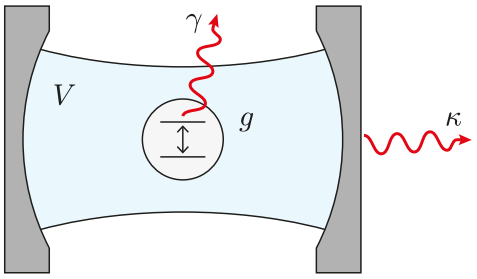

Figure 2.8: Illustration of a two-level atom in an optical resonator. Adapted from [13].

Taking for example a simple two-level atom in a cavity as illustrated in fig. (2.8), the atom-cavity interaction is mainly described by three parameters:

- κ - the cavity photon decay rate:

$$\kappa = \frac{\omega}{Q} = \delta\omega \tag{2.4}$$

where ω is the cavity resonant frequency, Q is the cavity quality factor and $\delta\omega$ is the cavity mode linewidth.

- γ - the non-cavity photon decay rate:

$$\gamma = \frac{1}{2T_1} = \frac{1}{2}\left(\frac{1}{\tau_{\text{rad}}} + \frac{1}{\tau_{\text{nrad}}}\right)\left(1 - \frac{\Delta\Omega}{4\pi}\right) \tag{2.5}$$

where T_1 is the population relaxation rate,$\tau_{\text{rad/nrad}}$ is the radiative and non-radiative lifetime, and $\Delta\Omega$ is the solid angle subtended by the cavity mode. The is not pure dephasing contribution T_2^* in the context of an isolated atom.

- g_0 - the atom-cavity coupling parameter:

$$g_0 = \left(\frac{\mu_{12}^2\omega}{2\epsilon_0\hbar V}\right)^{\frac{1}{2}} \tag{2.6}$$

where μ_{12} is the electric dipole matrix element of the transition, ϵ_0 is the dielectric constant and V is the volume of the photonic mode.

Distinction between the strong and the weak coupling regime is made depending on the relative sizes of κ, γ and g_0. In the strong coupling regime where $g_0 \gg (\kappa,\ \gamma)$, the atom-photon interaction happens faster than the loss of photon. The photon emission becomes a reversible process that the photons are re-absorbed by the atom before escaping the cavity. On the contrary in the weak coupling regime where $g_0 \ll (\kappa,\ \gamma)$, the photon emission event is an irreversible process dominated by photon loss out of the cavity mode.

In generally very high Q and low V are required to achieve strong coupling. In this work we aim to enhance NV ZPL emission in the weak coupling regime by using cavities with moderate Q and small V.

2.2.1 Free-Space Spontaneous Emission

The phenomena of spontaneous emission was initially regarded as an inherent property of the matter until the extension of quantum mechanics to the quantum field theory which the electromagnetic field is quantized. The zero-point energy state of this quantized field

is called the vacuum field whose magnitude is $\mathcal{E}_{\text{vac}}$:

$$\mathcal{E}_{\text{vac}} = \left(\frac{\hbar w}{2\epsilon_0 V}\right)^{\frac{1}{2}} \tag{2.7}$$

The electronic transition from the excited-state to the ground-state of an atom can be viewed as a mixing with the electromagnetic field transition from the ground-state to an excited-state plus one photon. Due to the infinitely large number of one-photon states to which the vacuum field can be excited, the spontaneous emission is an irreversible process. Consequently the electronic transition is treated with perturbation theory and the transition rate is given by Fermi's golden rule:

$$\gamma = \frac{2\pi}{\hbar^2}|M_{12}|^2 g(\omega) \tag{2.8}$$

where M_{12} is the transition matrix element:

$$M_{12}^2 = \frac{1}{3}\mu_{12}^2 \mathcal{E}_{\text{vac}}^2 = \frac{\mu_{12}^2 \hbar\omega}{6\epsilon_0 V} \tag{2.9}$$

and $g(\omega)$ is the density of photonic states. For free-space emission $g(\omega)$ takes the form of:

$$g^0(\omega) = \frac{\omega^2 V}{\pi^2 c^3} \tag{2.10}$$

Substituting both terms into eq. (2.8) the free-space spontaneous emission rate is given by:

$$\gamma^0 = \frac{\mu_{12}^2 \omega^3}{3\pi\epsilon\hbar c^3} \tag{2.11}$$

2.2.2 In-Cavity Spontaneous Emission

In the weak coupling regime the transition is also treated by perturbation theory. Due to the presence of an optical cavity, the density of photonic states is modified which either enhances or suppresses the spontaneous emission process. The density of photonic states of a single cavity mode is given by:

$$g^{\text{cav}}(\omega) = \frac{2}{\pi\delta\omega_{\text{cav}}} \frac{\delta\omega_{\text{cav}}^2}{4(\omega - \omega_{\text{cav}})^2 + \delta\omega_{\text{cav}}^2} \tag{2.12}$$

where ω_{cav} is the resonance frequency and $\delta\omega_{\text{cav}}$ is the mode linewidth. On coupling the atomic transition to the cavity mode where $\omega = \omega_0 = \omega_{\text{cav}}$, the density of photonic states reduces to:

$$g^{\text{cav}}(\omega_0) = \frac{2}{\pi\delta\omega_{\text{cav}}} = \frac{2Q}{\pi\omega_0} \tag{2.13}$$

The in-cavity transition matrix element M_{12} has the form of:

$$M_{12}^2 = \xi^2\mu_{12}^2\mathcal{E}_{\text{vac}}^2 = \xi^2\frac{\mu_{12}^2\hbar\omega}{2\epsilon_0 V} \tag{2.14}$$

where the $\frac{1}{3}$ term in eq. (2.9) is replaced with a more generalized dipole orientation factor ξ^2:

$$\xi = \frac{|\boldsymbol{p}\cdot\mathcal{E}|}{|\boldsymbol{p}||\mathcal{E}|} \tag{2.15}$$

where $\boldsymbol{p}$ is the emitter dipole and $\mathcal{E}$ is the cavity electric field. Substituting eqs. (2.13) and (2.14) into eq. (2.8) again, the spontaneous emission rate of the cavity-coupled emitter at ω_0 is given by:

$$\gamma^{\text{cav}} = \xi^2\frac{2Q\mu_{12}^2}{\hbar\epsilon_0 V} \tag{2.16}$$

2.2.3 The Purcell Factor

Comparing the in-cavity and free-space emission rate from eqs. (2.10) and (2.16), the spontaneous emission enhancement of a cavity-coupled emitter is given by:

$$F = \frac{\gamma^{\text{cav}}}{\gamma^0} = \xi^2\frac{3}{4\pi^2}\frac{Q}{V}\left(\frac{\lambda}{n}\right)^3 \tag{2.17}$$

where F is also called the Purcell factor [48]. We note that not all of the initial dipole emission interact with the cavity. Hence, F is only applicable to the part of initial emission that couples into the cavity modes, referred to as the cavity photons. The emission rate of the other part, i.e. the non-cavity photons, is unaffected. This distinction has implications in photon collection analysis of a cavity-emitter system, which is reflected in the setup of numerical simulations in section (4.3).

Up till now we assumed a maximum overlap between the positions of the electric field

maxima and the emitter dipole. To account for any spatial mismatch, eq. (2.17) is modified with an additional scaling factor:

$$\frac{n_{\mathrm{dp}}^2|\mathcal{E}_{\mathrm{dp}}|^2}{\max\left(n^2|\mathcal{E}|^2\right)} \tag{2.18}$$

where n_{dp}^2 and $|\mathcal{E}_{\mathrm{dp}}|^2$ are the refractive index and the electric field intensity at the dipole position. We note that some work use a scaling factor which only concerns the electric field intensity $|\mathcal{E}|^2$. This is valid for a single-medium cavity but causes problem for a hybrid-medium cavity (more in section (2.4.2)). In this work scaling according the energy density product $n^2|\mathcal{E}|^2$ is used.

In conclusion, the final form of the Purcell factor F for cavity-coupled emitter is given by:

$$F = \xi^2 \frac{3}{4\pi^2}\frac{Q}{V}\left(\frac{\lambda}{n_{\mathrm{dp}}}\right)^3 \frac{n_{\mathrm{dp}}^2|\mathcal{E}_{\mathrm{dp}}|^2}{\max\left(n^2|\mathcal{E}|^2\right)} \tag{2.19}$$

The expression of the cavity mode volume V follows the same the scaling convention:

$$V = \frac{\int \epsilon(\mathbf{r})|\mathcal{E}(\mathbf{r})|^2 d^3\mathbf{r}}{\max\left(\epsilon(\mathbf{r})|\mathcal{E}(\mathbf{r})|^2\right)} \tag{2.20}$$

2.2.4 Emission Enhancement of Cavity-Coupled NVs

For cavity-coupled emitters one of the more convenient tools to quantify the emission enhancement is the excited-state lifetime measurement. The Purcell enhancement experienced by the emitter is given by the ratio between the emitter lifetimes in free-space and in the cavity:

$$F = \frac{\tau^0}{\tau^{\mathrm{cav}}} = \frac{\gamma^{\mathrm{cav}}}{\gamma^0} \tag{2.21}$$

where γ^{cav} and γ^0 are the relevant relaxation rates. The free-space relaxation rate γ^0 consists of both radiative and non-radiative channels. For NV centres, the radiative emission is coarsely approximated as the sum of ZPL and PSB emissions:

$$\gamma^0 = \gamma_{\mathrm{rad}} + \gamma_{\mathrm{nrad}} = \gamma_{\mathrm{zpl}} + \gamma_{\mathrm{psb}} + \gamma_{\mathrm{nrad}} \tag{2.22}$$

When the NV ZPL is coupled to a cavity mode, the non-radiative relaxation rate is assumed to be unchanged. The ZPL and PSB emissions are modified by F_{zpl} and F_{psb} respectively:

$$\gamma^{\text{cav}} = \gamma_{\text{zpl}} F_{\text{zpl}} + \gamma_{\text{psb}} F_{\text{psb}} + \gamma_{\text{nrad}} \tag{2.23}$$

Two additional parameters, namely the free-space ZPL branching ratio (or the Debye-Waller factor) ζ^0_{zpl} and the quantum efficiency η_{qe}, are defined as following:

$$\begin{aligned} \zeta^0_{\text{zpl}} &= \frac{\gamma_{\text{zpl}}}{\gamma_{\text{rad}}} = \frac{\gamma_{\text{zpl}}}{\gamma_{\text{zpl}} + \gamma_{\text{psb}}} \\ \eta_{\text{qe}} &= \frac{\gamma_{\text{rad}}}{\gamma^0} = \frac{\gamma_{\text{zpl}} + \gamma_{\text{psb}}}{\gamma^0} \end{aligned} \tag{2.24}$$

Using eq. (2.24), all the γ terms in eq. (2.23) can be expressed in terms of γ^0:

$$\begin{aligned} &\gamma_{\text{zpl}} = \gamma^0 \eta_{\text{qe}} \zeta^0_{\text{zpl}}\,, \quad \gamma_{\text{psb}} = \gamma^0 \eta_{\text{qe}} (1 - \zeta^0_{\text{zpl}})\,, \quad \gamma_{\text{nrad}} = \gamma^0 (1 - \eta_{\text{qe}}) \\ &\Rightarrow \gamma^{\text{cav}} = \gamma^0 \left[\eta_{\text{qe}} \zeta^0_{\text{zpl}} F_{\text{zpl}} + \eta_{\text{qe}} (1 - \zeta^0_{\text{zpl}}) F_{\text{psb}} + (1 - \eta_{\text{qe}}) \right] \end{aligned} \tag{2.25}$$

As a result, the full-spectrum Purcell factor F_{full} experienced by a cavity-coupled NV centre is given by:

$$F_{\text{full}} = \frac{\gamma^{\text{cav}}}{\gamma^0} = 1 + \eta_{\text{qe}} \left[\zeta^0_{\text{zpl}} F_{\text{zpl}} + (1 - \zeta^0_{\text{zpl}}) F_{\text{psb}} - 1 \right] \tag{2.26}$$

Assuming a quantum efficiency of 1, eq. (2.26) reduces to:

$$F_{\text{full}} = \zeta^0_{\text{zpl}} F_{\text{zpl}} + (1 - \zeta^0_{\text{zpl}}) F_{\text{psb}} \tag{2.27}$$

The modified in-cavity ZPL branching ratio is thus given by:

$$\zeta^{\text{cav}}_{\text{zpl}} = \frac{\zeta^0_{\text{zpl}} F_{\text{zpl}}}{F_{\text{full}}} = \frac{\zeta^0_{\text{zpl}} F_{\text{zpl}}}{\zeta^0_{\text{zpl}} F_{\text{zpl}} + (1 - \zeta^0_{\text{zpl}}) F_{\text{psb}}} \tag{2.28}$$

Taking for example a moderate estimation where ζ^0_{zpl}=4%, F_{zpl}=5 and F_{psb}=0.95, eq. (2.27) yields a F_{full}= 1.11. This is equivalent to a 11% change in NV excited-lifetime and an in-cavity ZPL branching ratio $\zeta^{\text{cav}}_{\text{zpl}}$= 17%.

2.3 Single-Medium Fabry-Perot Cavity

In this section, a thorough discussion of a single-medium Fabry-Perot cavity is presented. In addition to an analytical description, the transfer matrix model is also introduced as a numerical tool to calculate cavity parameters. Contents in this section are fully transferable to the discussion of a hybrid-medium cavity in section (2.4) which resembles our target membrane-in-cavity device.

2.3.1 Resonance Condition

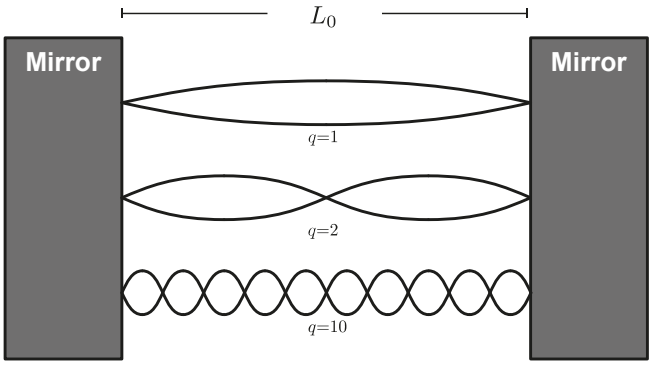

Figure 2.9: An illustration of a planar-planar Febry-Perot cavity with supported resonant modes with a mode index of q=1, 2, 10.

An illustration of a typical Febry-Perot cavity formed by two parallel planar mirrors is shown in fig. (2.9). For now the transverse field is not considered. The physical mirror separation is L_0 and the mirror reflectivities are R_1 and R_2. Assuming no absorption and scattering loss inside the cavity, the cavity transmission is given by [68]:

$$T_{\text{cav}} = \frac{1}{1 + F_{\text{c}} \sin^2(\phi/2)} \tag{2.29}$$

where F_{c} is the coefficient of finesse defined as:

$$F_{\text{c}} \equiv \left(\frac{2(R_1 R_2)^{\frac{1}{4}}}{1 - (R_1 R_2)^{\frac{1}{2}}} \right)^2 \tag{2.30}$$

and ϕ is the round-trip phase shift:

$$\phi = \frac{4\pi L}{\lambda} \tag{2.31}$$

with L being the optical cavity length $L = nL_0$. It is obvious that the cavity transmission is at its maximum when $\phi/2 = 2\pi q$, where q is an integer referred to as the cavity mode index. Substituting this condition back in eq. (2.31), the cavity resonance condition is obtained as:

$$\lambda = \frac{2L}{q} \quad \text{or} \quad v = q\frac{c}{2L} \tag{2.32}$$

Hence the cavity exhibits a sequence of resonance frequencies v with a constant mode spacing Δv (or free spectral range FSR) given by:

$$\Delta v = (q+1)\frac{c}{2L} - q\frac{c}{2L} = \frac{c}{2L} = \frac{v}{q} \tag{2.33}$$

where c is the speed of light in vacuum. A typical cavity transmission spectra in frequency domain is plotted in fig. (2.10)(a).

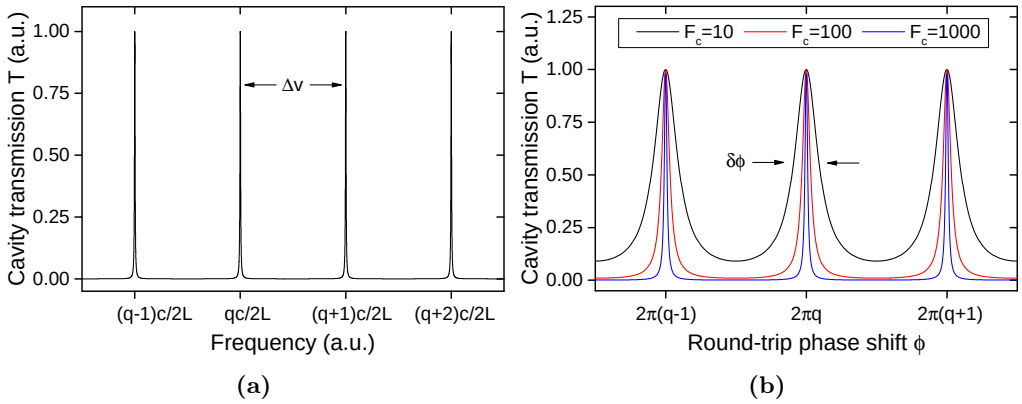

Figure 2.10: Cavity transmission spectrum: **(a)** in frequency units; **(b)** in phase units with varying coefficient of finesse F_c showing cavity linewidth variation.

2.3.2 Finesse and Quality Factor

The performance of an optical cavity device is often quantified by its capability to store photon energy. For this purpose two cavity figure of merits are often used to describe cavity performance: the cavity finesse $\mathcal{F}$ and the quality factor Q.

The cavity finesse $\mathcal{F}$ is defined by [68] as:

$$\mathcal{F} \equiv \frac{2\pi}{\delta\phi} \equiv \frac{\Delta v}{\delta v} \tag{2.34}$$

where $\delta\phi$ and δv are the FWHM of the cavity resonance in phase and frequency units respectively. In practice it is also useful to express $\mathcal{F}$ in terms of mirror reflectivities R_i. By referring back to eq. (2.29), $\delta\phi$ is found by equating $T_{\rm cav}$ to $\frac{1}{2}$:

$$\delta\phi = 4\arcsin\left(1/\sqrt{F_{\rm c}}\right) \tag{2.35}$$

which gives an exact solution of $\mathcal{F}_{\rm exa}$:

$$\mathcal{F}_{\rm exa} = \frac{\pi}{2\arcsin\left(\frac{1-(R_1R_2)^{\frac{1}{2}}}{2(R_1R_2)^{\frac{1}{4}}}\right)} \tag{2.36}$$

In the limit of high mirror reflectivities $F_{\rm c}$ is usually large. Hence $\arcsin\left(1/\sqrt{F_{\rm c}}\right) \approx 1/\sqrt{F_{\rm c}}$ and $\delta\phi$ becomes:

$$\delta\phi = 4/\sqrt{F_{\rm c}} \tag{2.37}$$

Combining with eq. (2.30) and eq. (2.34), a commonly quoted form of cavity finesse $\mathcal{F}_{\rm ana}$ is given by:

$$\mathcal{F}_{\rm ana} = \frac{\pi(R_1R_2)^{\frac{1}{4}}}{1-(R_1R_2)^{\frac{1}{2}}} \tag{2.38}$$

The arcsin approximation is validated by comparing the value of $\mathcal{F}_{\rm exa}$ and $\mathcal{F}_{\rm ana}$ as a function of mirror reflectivity as plotted in fig. (2.11)(a). Negligible deviation between the two is observed for R>0.3 suggesting good validity of eq. (2.38) for most R values.

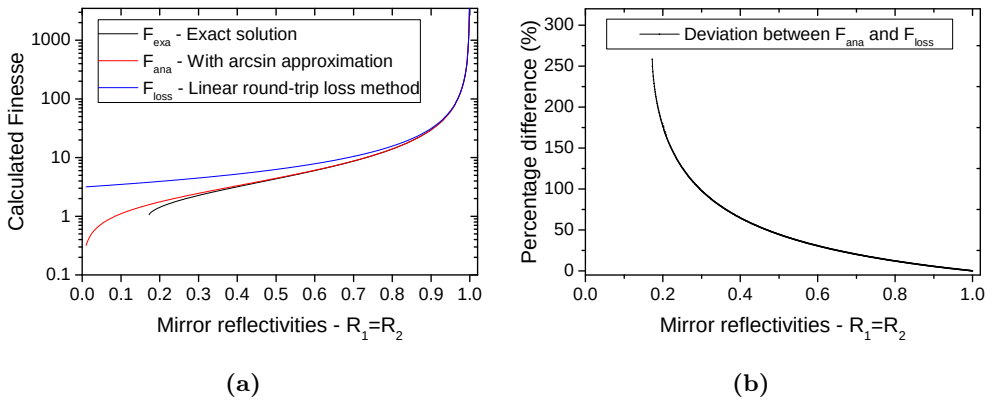

(a) **(b)**

Figure 2.11: **(a)** Calculated $\mathcal{F}$ using eqs. (2.36), (2.38) and (2.39). **(b)** The percentage difference between $\mathcal{F}_{\rm exa}$ (eq. (2.36)) and $\mathcal{F}_{\rm loss}$ (eq. (2.39)). At R= 0.95 the error is 2.5%.

Another commonly used finesse expression $\mathcal{F}_{\rm loss}$ [57, 69] is given by replacing the phase linewidth $\delta\phi$ in eq. (2.34) with a linear combination of round-trip losses $\mathcal{L}_{\rm lin}$= T_1+T_2=

$2-R_1-R_2$ (ignoring absorption and scattering):

$$\mathcal{F}_{\text{loss}} = \frac{2\pi}{\mathcal{L}_{\text{lin}}} \tag{2.39}$$

Again, calculated $\mathcal{F}_{\text{loss}}$ is shown in fig. (2.11)(a) which deviates massively from $\mathcal{F}_{\text{exa}}$ and $\mathcal{F}_{\text{ana}}$ for $R<0.9$. At $R= 0.95$ the difference between $\mathcal{F}_{\text{loss}}$ and $\mathcal{F}_{\text{exa}}$ falls to 2.5% (fig. (2.11)(b)). The $\mathcal{F}_{\text{loss}}$ expression is only a good approximation when all the contributing terms in $\mathcal{L}_{\text{lin}}$ are much smaller than 1.

The other important cavity parameter, the cavity quality factor Q of the resonant mode, is defined as [13]:

$$Q = \frac{v}{\delta v} = \frac{\omega}{\delta\omega} \tag{2.40}$$

where the mode linewidth in angular frequency δw is also equivalent to cavity photon decay rate κ in CQED terms (more in section (2.2)). Using eqs. (2.33) and (2.34) it is easy to find that Q is related to $\mathcal{F}$ by:

$$Q = \frac{\omega}{\delta\omega} = \frac{2\pi v}{2\pi\delta v} = \frac{q\Delta v}{\delta v} = q\mathcal{F} \tag{2.41}$$

Note that Q has a cavity length dependence because it concerns cavity loss per optical cycles. In contrary $\mathcal{F}$ concerns cavity loss per round-trips. We note that the length-scaling of Q only applies when mirror transmission losses dominate cavity loss. This certainly holds true under current 1D planar wave treatment where absorption and scattering losses are neglected.

In real experimental settings where the dipole emitter is located between the mirrors, the Q length-scaling often falls short due to various real-world loss mechanisms. For example the non-cavity photon loss depicted by γ in section (2.2) scales with the cavity length i.e. the larger the gap between cavity mirrors the less initial photon emissions are coupled into the cavity mode.

2.3.3 The Transfer Matrix Model

The basic analytical description in previous sections provides a good starting point for cavity analysis. However, such an approach assumes a singular reflective interface at

both ends of the cavity. In practice, distributed Bragg reflectors (DBRs) are commonly adopted to achieve high mirror reflectivity R. When dealing with multi-layer dielectric structures, the transfer matrix model (TMM) is a desirable numerical tool to calculate cavity parameters accurately. Such topics are routinely covered by textbooks [68, 70] and our discussion follow the layout and naming conventions in [71].

The core idea of TMM is to describe the electric field propagation through a dielectric structure using two types of matrices:

- **The propagation matrix** M_{p} - which describes the field propagation through a homogeneous dielectric medium.
- **The matching matrix** M_{m} - which relates field components on both sides of a dielectric interface.

The derivation of both matrices is presented in following sub-sections.

2.3.3.1 Field Propagation and the Propagation Matrix

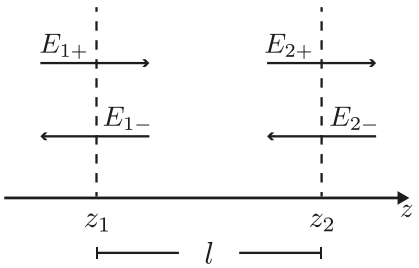

Figure 2.12: Illustration of field propagation through a lossless homogeneous medium.

Firstly, to derive M_{p} we consider an uniform plane wave travelling in a lossless dielectric medium along the z-axis as illustrated in fig. (2.12). The forward and backward propagating electric fields at z_1 and z_2 are written as:

$$E_{1+} = E_{0+}e^{-ikz_1}, \quad E_{2+} = E_{0+}e^{-ikz_2}$$
$$E_{1-} = E_{0-}e^{ikz_1}, \quad E_{2-} = E_{0-}e^{ikz_2}$$

where k=$2\pi/\lambda$ is the propagation constant. The electric fields at two positions are related by:

$$\begin{aligned} E_{1+} &= E_{2+}e^{ik(z_2-z_1)} = E_{2+}e^{ikl} \\ E_{1-} &= E_{2-}e^{-ik(z_2-z_1)} = E_{2-}e^{-ikl} \end{aligned}$$

where l is the distance between z_1 and z_2. Expressing these relationships in matrix form gives yields the propagation matrix M_p:

$$\begin{bmatrix} E_{1+} \\ E_{1-} \end{bmatrix} = \begin{bmatrix} e^{ikl} & 0 \\ 0 & e^{-ikl} \end{bmatrix} \begin{bmatrix} E_{2+} \\ E_{2-} \end{bmatrix} = M_\mathrm{p} \begin{bmatrix} E_{2+} \\ E_{2-} \end{bmatrix} \tag{2.42}$$

It is also useful to define the reflection coefficient Γ and wave impedance Z as:

$$\Gamma = \frac{E_-}{E_+} = \frac{\frac{1}{2}(E-\eta H)}{\frac{1}{2}(E+\eta H)} = \frac{Z-\eta}{Z+\eta} \tag{2.43}$$

$$Z = \frac{E}{H} = \frac{E_+ + E_-}{\frac{1}{\eta}(E_+ - E_-)} = \eta\frac{1+\Gamma}{1-\Gamma} \tag{2.44}$$

where H is magnetic component of the field, η=η_0/n is the material impedance and η_0 is the impedance of free space. Consequently the propagation of Γ and Z between z_1 to z_2 are written as:

$$\begin{aligned} \Gamma_1 &= \frac{E_{1-}}{E_{1+}} = \frac{E_{2-}e^{-ikl}}{E_{2+}e^{ikl}} = \Gamma_2 e^{-2ikl} \\ Z_1 &= \eta\frac{1+\Gamma_1}{1-\Gamma_1} = \eta\frac{1+\Gamma_2 e^{-2ikl}}{1-\Gamma_2 e^{-2ikl}} \end{aligned} \tag{2.45}$$

One useful application of eq. (2.45) for the purpose of this work is when l=$\frac{1}{4}\lambda$. This converts eq. (2.45) to:

$$\begin{aligned} \Gamma_1 &= -\Gamma_2 \\ Z_1 &= \frac{\eta^2}{Z_2} \end{aligned} \tag{2.46}$$

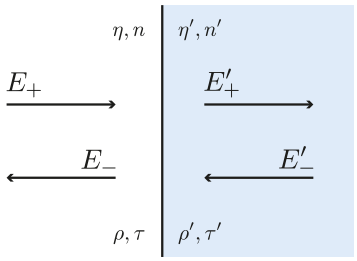

Figure 2.13: Illustration of field scattering at the interface between two different dielectric media.

2.3.3.2 Interface Scattering and the Matching Matrix

Next, to derive M_m we consider the electric field scattering at the interface between two dielectric media with refractive indices of n and n' respectively. An illustration is shown in fig. (2.13). The corresponding Fresnel coefficients are defined as:

$$\begin{aligned} \rho &= \frac{n - n'}{n + n'}, \quad \tau = \frac{2n}{n + n'} \\ \rho' &= \frac{n' - n}{n + n'}, \quad \tau' = \frac{2n'}{n + n'} \end{aligned}$$

where some convenient relationships between ρ and τ terms are given by:

$$\begin{aligned} \tau &= 1 + \rho, \quad \rho = -\rho' \\ \tau' &= 1 + \rho', \quad \tau\tau' = 1 - \rho^2 \end{aligned} \tag{2.47}$$

The relationship between electric fields propagating towards and away from the interface are thus:

$$\begin{aligned} E'_+ &= \rho' E'_- + \tau E_+ \\ E_- &= \rho E_+ + \tau' E'_- \end{aligned}$$

Expressing in matrix form and rearranging using eq. (2.47), the matching matrix M_m at this interface is then given by:

$$\begin{bmatrix} E_+ \\ E_- \end{bmatrix} = \begin{bmatrix} 1/\tau & \rho/\tau \\ \rho/\tau & 1/\tau \end{bmatrix} \begin{bmatrix} E'_+ \\ E'_- \end{bmatrix} = M_\mathrm{m} \begin{bmatrix} E'_+ \\ E'_- \end{bmatrix}$$

The boundary condition requires the total E and H field to be continuous across the interface. Hence Z and Γ on both sides of the interface are related by:

$$\Gamma = \frac{E_-}{E_+} = \frac{\frac{1}{\tau}(\rho E'_+ + E'_-)}{\frac{1}{\tau}(E'_+ + \rho E'_-)} = \frac{\rho + \Gamma'}{1 + \rho\Gamma'}$$
$$Z = Z' \tag{2.48}$$

2.3.4 Distributed Bragg Reflector

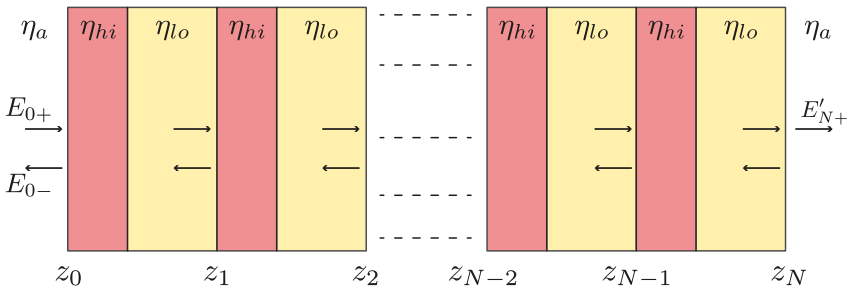

Figure 2.14: Illustration of a DBR stack with a normal incident plane wave propagating from left to right. All layer thicknesses are $\frac{1}{4}\lambda$.

Distributed Bragg reflectors (or dielectric mirrors) are made of alternating $\lambda/4$ layers of high (n_{hi}) and low (n_{lo}) index dielectric layers. The most commonly used coating combination is the Ta_2O_5- SiO_2 system where $n_{Ta_2O_5}$= 2.12 and n_{SiO_2}= 1.46. A DBR structure with N pairs of high/low index layers is illustrated in fig. (2.14) with a rightward-propagating normal incident plane. By making use of M_{p} and M_{m} the field propagation from z_0 to z_1 is described as:

$$\begin{bmatrix} E_{0+} \\ E_{0-} \end{bmatrix} = M_{\mathrm{m}}^{\mathrm{a/hi}} \begin{bmatrix} E'_{0+} \\ E'_{0-} \end{bmatrix} = M_{\mathrm{m}}^{\mathrm{a/hi}} (M_{\mathrm{p}}^{\mathrm{hi}} M_{\mathrm{m}}^{\mathrm{hi/lo}} M_{\mathrm{p}}^{\mathrm{lo}} M_{\mathrm{m}}^{\mathrm{lo/hi}}) \begin{bmatrix} E'_{1+} \\ E'_{1-} \end{bmatrix}$$

In analogy the field propagation through the whole stack is described as:

$$\begin{bmatrix} E_{0+} \\ E_{0-} \end{bmatrix} = M_{\mathrm{m}}^{\mathrm{a/hi}} \frac{(M_{\mathrm{p}}^{\mathrm{hi}} M_{\mathrm{m}}^{\mathrm{hi/lo}} M_{\mathrm{p}}^{\mathrm{lo}} M_{\mathrm{m}}^{\mathrm{lo/hi}})^N}{M_{\mathrm{m}}^{\mathrm{lo/hi}}} M_{\mathrm{m}}^{lo/a} \begin{bmatrix} E'_{N+} \\ 0 \end{bmatrix} \tag{2.49}$$

By dividing the structure into even smaller segments a field propagation profile can be visualized. The field profile of a DBR mirror with 5 pairs of Ta-Si coating designed for λ=637nm is shown in fig. (2.15)(a). Alternatively by computing eq. (2.49) for a range of

wavelengths, the transmission spectrum of DBR mirrors with increasing N are plotted in fig. (2.15)(b). It can be observed that as N increases the mirror reflectivity improves and the mirror stopband edge becomes sharper.

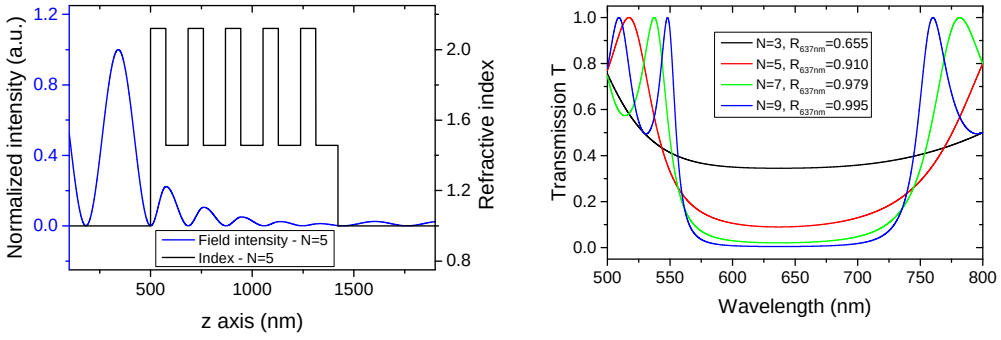

(a) **(b)**

Figure 2.15: **(a)** Field propagation profile through a N=5 DBR stack; **(b)** The mirror transmission spectrum with increasing N.

To quantify the mirror reflectivity, we first calculate the impedance propagation Z by using eqs. (2.46) and (2.48):

$$Z_0 = \frac{\eta_{\text{hi}}^2}{\eta_{\text{lo}}^2} Z_1 = \left(\frac{\eta_{hi}^2}{\eta_{\text{lo}}^2}\right)^N Z_N = \left(\frac{\eta_{hi}}{\eta_{\text{lo}}}\right)^{2N} \eta_a \tag{2.50}$$

Substituting into eq. (2.43) we find the reflectivity coefficient Γ as:

$$\Gamma_0 = \frac{Z_0 - \eta_a}{Z_0 + \eta_a} = \frac{\left(\frac{\eta_{hi}}{\eta_{\text{lo}}}\right)^{2N} - 1}{\left(\frac{\eta_{hi}}{\eta_{\text{lo}}}\right)^{2N} + 1} \tag{2.51}$$

Replacing $\eta_{hi}/\eta_{\text{lo}}$ with $n_{\text{lo}}/n_{\text{hi}}$ and rearranging gives:

$$\Gamma_0 = \frac{1 - \left(\frac{n_{\text{hi}}}{n_{\text{lo}}}\right)^{2N}}{1 + \left(\frac{n_{\text{hi}}}{n_{\text{lo}}}\right)^{2N}} \tag{2.52}$$

It is obvious that the larger the index contrast ($n_{\text{hi}}/n_{\text{lo}}$), the closer Γ_0 is to -1 i.e. 100% reflectivity. Same can also be achieved by increasing the number of DBR pairs N which was demonstrated in fig. (2.15)(b). Further distinction can be made between high- and low- termination DBR mirrors. In this work we work exclusively with high-termination DBRs such that the first anti-node is located in the diamond membrane for a hybrid-medium cavity.

2.3.5 Solving for Single-Medium DBR Cavity

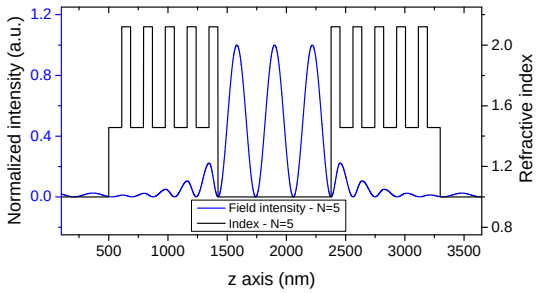

Figure 2.16: The electric field profile along z-axis calculated using the transfer matrix model.

The 1D transfer matrix model is also applicable when analyzing Fabry-Perot cavities formed by DBR mirrors. The electric field intensity profile of a q=3, N=5 cavity is shown in fig. (2.16) with three anti-nodes present between the DBR mirrors. By fixing q=3, increasing N yields narrower cavity transmission linewidth (fig. (2.17)(a)) due to an increase in cavity finesse (fig. (2.17)(b)). Compared to $\mathcal{F}_{\text{tmm}}$ calculated by fitting the transmission spectrum, other analytical finesse expressions such as $\mathcal{F}_{\text{ana}}$ and $\mathcal{F}_{\text{loss}}$ show an underestimation by 30-50%.

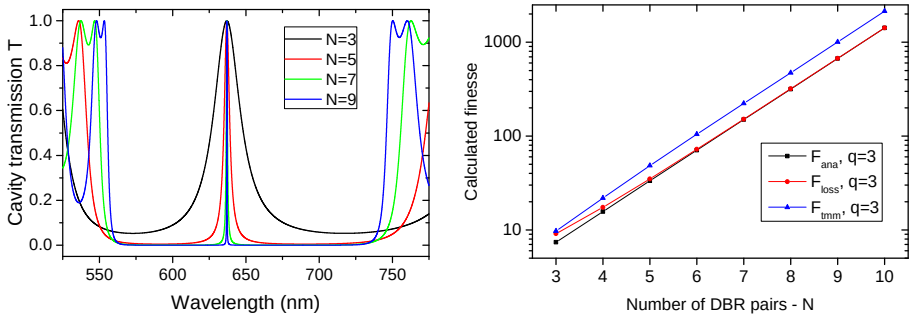

(a) **(b)**

Figure 2.17: Calculated **(a)** cavity transmission spectrum and **(b)** cavity finesse $\mathcal{F}$ as a function of DBR pair number N. The transfer matrix results $\mathcal{F}_{\text{tmm}}$ are compared to $\mathcal{F}_{\text{ana}}$ from eq. (2.38) and $\mathcal{F}_{\text{loss}}$ from eq. (2.39).

The cavity behaviour as a function of cavity mode index q is also investigated using TMM and the results are shown in fig. (2.18). With increasing q, both the cavity mode linewidth and the mode spacing decreases. More interestingly, both $\mathcal{F}_{\text{tmm}}$ and Q_{tmm} exhibit large deviations from analytical expressions ($\mathcal{F}_{\text{ana}}$ and $\mathcal{F}_{\text{loss}}$) at low q limit. As cavity length increases, the TMM results converges towards the analytical solutions.

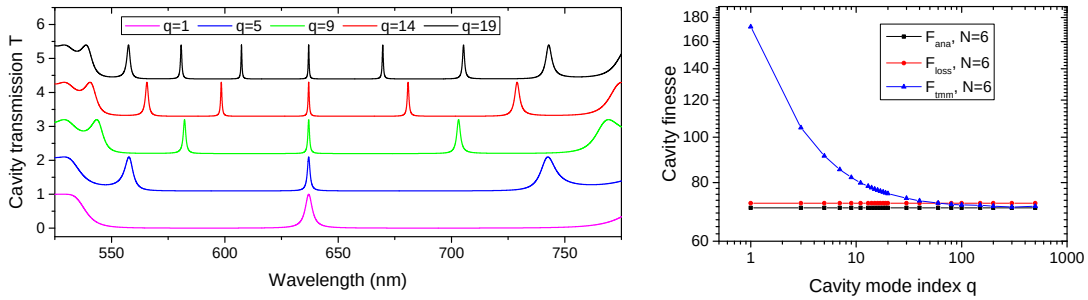

(a) **(b)**

Figure 2.18: Calculated **(a)** cavity transmission spectrum and **(b)** cavity finesse $\mathcal{F}$ as a function of cavity mode index q. The transfer matrix results $\mathcal{F}_{\text{tmm}}$ are compared to $\mathcal{F}_{\text{ana}}$ and $\mathcal{F}_{\text{loss}}$ from section (2.3.2).

In summary, among all variants of finesse expressions introduced by now, $\mathcal{F}_{\text{tmm}}$ is the most accurate one for analyzing multi-stack dielectric structures. The analytical approximation $\mathcal{F}_{\text{ana}}$ holds true against the exact solution $\mathcal{F}_{\text{exa}}$ for most R. The finesse $\mathcal{F}_{\text{loss}}$ obtained using linear round-trip loss only converges to $\mathcal{F}_{\text{ana}}$ for R>0.9.

2.3.6 Gaussian and Hermite-Gaussian Modes

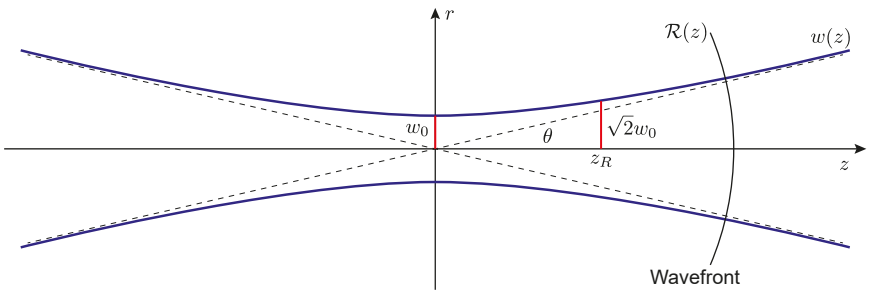

Figure 2.19: The schematic drawing of the Gaussian beam expression.

Up till this point only the longitudinal field propagation was considered under planar-planar cavity setup. In practice a planar-concave setup is often adopted to provide field confinement in the lateral dimensions required for reduced cavity mode volume V and increased cavity-emitter interaction (more in section (2.2)). The cavity modes formed in this type of resonator is well-described by the Gaussian beam expressions. Briefly speaking, the Gaussian beam is a solution to the Helmholtz's equation under the paraxial approximation (small divergence angle θ). Without going through the detailed derivations (available in standard textbooks [70, 72]), we quote the lowest-order (fundamental)

Gaussian solution as:

$$\begin{aligned}
\mathcal{E}(r) = \mathcal{E}_0 \frac{w_0}{w(z)} & \quad \text{amplitude reduction along } z \\
\times e^{-ikz} & \quad \text{beam propagation along } z \\
\times e^{-\frac{r^2}{w(z)^2}} & \quad \text{Gaussian profile with spot size } w(z) \\
\times e^{\frac{-ikr^2}{2\mathcal{R}(z)}} & \quad \text{wavefront radius of curvature at } z \\
\times e^{i\zeta(z)} & \quad \text{additional Guoy phase shift along } z
\end{aligned} \tag{2.53}$$

where w_0 and $\mathcal{E}_0$ are the beam waist and the field amplitude at z=0. Other beam parameters in fig. (2.19) are defined as:

$$\begin{aligned}
z_R = \frac{\pi w_0^2}{\lambda} & \quad \text{Rayleigh range} \\
w(z) = w_0 \sqrt{1 + \frac{z^2}{z_R}} & \quad \text{beam waist at } z \\
\mathcal{R}(z) = z + \frac{z_R^2}{z} & \quad \text{wavefront radius of curvature at } z \\
\zeta(z) = \arctan\left(\frac{z}{z_R}\right) & \quad \text{Guoy phase shift at } z
\end{aligned} \tag{2.54}$$

A fundamental Gaussian mode supported by a planar-concave cavity is illustrated in fig. (2.20). Here we define the mirror g factor as g_i= 1-$\frac{L}{\mathcal{R}_i}$, where L is the optical cavity length $\mathcal{R}_i$ is the mirror radius of curvature. Because the planar mirror has an infinitely large $\mathcal{R}_1$, g_1 equals to 1. The beam waist w at each mirror for the planar-concave cavity is given by:

$$\begin{aligned}
w_1^2 &= \frac{\lambda L}{\pi} \sqrt{\frac{g_2}{g_1(1 - g_1 g_2)}} = \frac{\lambda L}{\pi} \sqrt{\frac{\mathcal{R} - L}{L}} \\
w_2^2 &= \frac{\lambda L}{\pi} \sqrt{\frac{g_1}{g_2(1 - g_1 g_2)}} = \frac{\lambda L}{\pi} \sqrt{\frac{\mathcal{R}^2}{L(\mathcal{R} - L)}}
\end{aligned} \tag{2.55}$$

which yields the cavity stability criteria: $\mathcal{R} - L$>0. The mode volume is given by:

$$V_{\text{ana}} = \frac{\pi w_0^2}{4} L \tag{2.56}$$

The Gaussian beam solution in eq. (2.53) assumes a transverse profile with a lowest-order Gaussian shape. There also exists a set of Hermite-Gaussian solutions where the

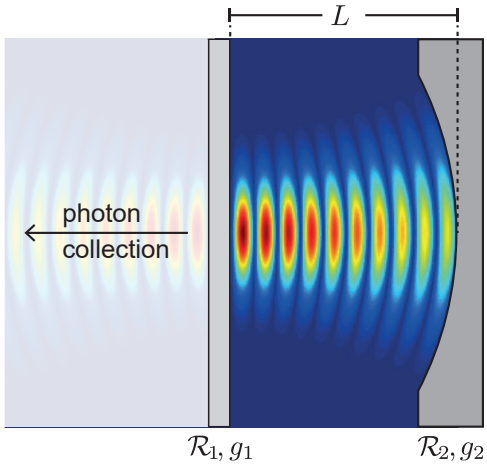

Figure 2.20: A fundamental Gaussian mode supported by a planar-concave cavity. Additional phase shift of $\pi/2$ is applied to create a node at the surface of the planar mirror. $\mathcal{R}$ is the mirror radius of curvature.

transverse profile takes a different form:

$$\mathcal{E}(x,y) = \mathcal{E}_0 \frac{w_0}{w(z)} \times e^{-ikz} \times e^{-\frac{x^2+y^2}{w(z)^2}} \times e^{\frac{-ik(x^2+y^2)}{2\mathcal{R}(z)}} \times e^{i\zeta(z)(m+n+1)} \times H_m\left[\frac{\sqrt{2}x}{w_0}\right] H_n\left[\frac{\sqrt{2}y}{w_0}\right] \tag{2.57}$$

where the additional H terms are the Hermite polynomials and m/n are the transverse mode indices representing the order of H in each lateral direction. The cavity mode resonance condition is:

$$L = \frac{\lambda}{2n}\left[q + \frac{1}{\pi}(m+n+1)\arccos\left(\sqrt{\frac{\mathcal{R}-L}{\mathcal{R}}}\right)\right] \tag{2.58}$$

where q is the longitudinal index and modes. The Hermite-Gaussian modes with none-zero m/n are also called higher-order transverse-electromagnetic modes which can be expressed as $\text{TEM}_{q,m,n}$. When $m{+}n{=}$ 0, eq. (2.57) reduces to the fundamental mode ($\text{TEM}_{q,0,0}$) expression in eq. (2.53).

2.3.7 Transverse-Mode Coupling

The higher-order TEM modes are generally unfavourable due diffraction losses related strong transverse field components and subsequent. The fundamental modes couple more efficiently into external optics. According to eq. (2.58), the higher-order TEM modes of

smaller q can couple to the fundamental modes and deteriorate cavity performance [73]. For example the resonance conditions for the $\mathrm{TEM}_{q,0,0}$ and the $\mathrm{TEM}_{q-1,m,n}$ modes are given by:

$$\begin{aligned} L_q &= \frac{\lambda}{2n}\left[q + \frac{1}{\pi}\arccos\left(\sqrt{1-\frac{q\frac{\lambda}{2}}{\mathcal{R}}}\right)\right] \\ L_{q-1,m,n} &= \frac{\lambda}{2n}\left[(q-1) + \frac{1}{\pi}(m+n+1)\arccos\left(\sqrt{1-\frac{(q-1)\frac{\lambda}{2}}{\mathcal{R}}}\right)\right] \end{aligned} \tag{2.59}$$

Setting L_q=$L_{q-1,m,n}$, the solution to m+n are:

$$m+n = \frac{\frac{1}{\pi}\arccos\left(\sqrt{1-\frac{q\frac{\lambda}{2}}{\mathcal{R}}}\right)+1}{\frac{1}{\pi}\arccos\left(\sqrt{1-\frac{(q-1)\frac{\lambda}{2}}{\mathcal{R}}}\right)} - 1 \tag{2.60}$$

Figure (2.21) shows mode profile of the $\mathrm{TEM}_{5,0,0}$ and the $\mathrm{TEM}_{4,2,4}$ modes where q=5 and m+n= 6 is a solution of eq. (2.60). It can be observed that the optical cavity lengths of the two modes are roughly equal, suggesting the $\mathrm{TEM}_{5,0,0}$ mode is likely to be leaky due to transverse-mode coupling with the $\mathrm{TEM}_{4,2,4}$ mode.

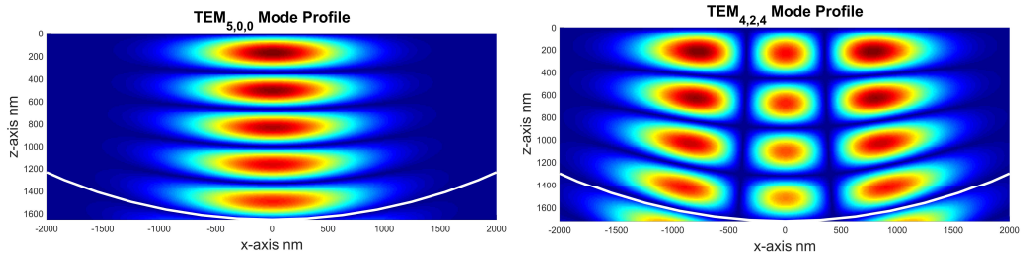

(a) **(b)**

Figure 2.21: Mode profile of **(a)** the $\mathrm{TEM}_{5,0,0}$ and **(b)** the $\mathrm{TEM}_{4,2,4}$ modes. These two modes are both supported by a cavity length of $L_q \approx L_{q-1}$, suggesting coupling interaction between the two is likely.

It is possible to selectively support only the fundamental modes by restricting the cavity feature size. However, this might also cause clipping loss at the edge of the cavity feature if the beam waist is larger than the feature size. In practice, a trade-off between the two has to be made.

2.4 Hybrid-Medium Fabry-Perot Cavity

After having established basic concepts and tools in the context of a single-medium cavity in section (2.3), we proceed to analyze the hybrid-medium cavity by introducing a diamond membrane in the cavity.

2.4.1 Analytical Description

To describe the hybrid diamond-air cavity, we again start with a schematic drawing in fig. (2.22) where $t_\mathrm{a}/t_\mathrm{d}$ are the physical dimensions of the diamond and the air portion. The reflection and transmission Fresnel coefficients at the diamond-air interface are $\rho = \frac{n_\mathrm{a}-n_\mathrm{d}}{n_\mathrm{a}+n_\mathrm{d}}$ and $\tau = \frac{2n_\mathrm{a}}{n_\mathrm{a}+n_\mathrm{d}}$ respectively.

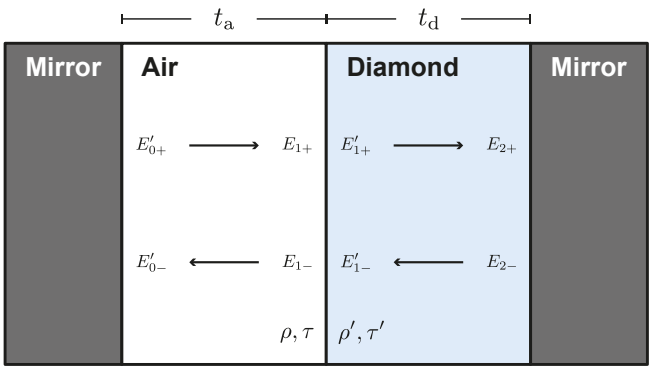

Figure 2.22: An illustration of a planar-planar Fabry-Perot with two different media.

Using the transfer matrices M_p and M_m, the E'_0 field components at the air-mirror interface are related to the E_2 field components at the diamond-mirror interface by:

$$\begin{aligned}
\begin{bmatrix} E'_{0+} \\ E'_{0-} \end{bmatrix} &= M_\mathrm{p}^\mathrm{a} M_\mathrm{m}^\mathrm{a/d} M_\mathrm{p}^\mathrm{d} \begin{bmatrix} E_{2+} \\ E_{2-} \end{bmatrix} \\
&= \begin{bmatrix} e^{ikt_\mathrm{a}} & 0 \\ 0 & e^{-ikt_\mathrm{a}} \end{bmatrix} \begin{bmatrix} 1/\tau & \rho/\tau \\ \rho/\tau & 1/\tau \end{bmatrix} \begin{bmatrix} e^{ikn_\mathrm{d}t_\mathrm{d}} & 0 \\ 0 & e^{-ikn_\mathrm{d}t_\mathrm{a}} \end{bmatrix} \begin{bmatrix} E_{2+} \\ E_{2-} \end{bmatrix} \\
&= \frac{1}{\tau} \begin{bmatrix} e^{ikL} & \rho e^{ikL'} \\ \rho e^{-ikL'} & e^{-ikL} \end{bmatrix} \begin{bmatrix} E_{2+} \\ E_{2-} \end{bmatrix}
\end{aligned} \tag{2.61}$$

where $L = t_a + n_d t_d$ is the optical cavity length and $L' = t_a - n_d t_d$ is the optical length difference. To support a resonant mode, the total electric fields at both mirror interfaces need to be zero to forming a node:

$$\begin{aligned} E'_{0+} + E'_{0-} &= 0 \\ E_{2+} + E_{2-} &= 0 \end{aligned} \tag{2.62}$$

By solving eqs. (2.61) and (2.62) simultaneously the transcendental equation describing the resonant cavity modes in terms of t_a and t_d is obtained:

$$\begin{aligned} \sin(kL) &= \rho \sin\big(kL'\big) \\ \sin\left(\frac{2\pi}{\lambda}(t_a + n_d t_d)\right) &= \frac{1 - n_d}{1 + n_d} \sin\left(\frac{2\pi}{\lambda}(t_a - n_d t_d)\right) \end{aligned} \tag{2.63}$$

Two sets of solutions can be obtained by solving eq. (2.63):

$$\begin{aligned} kL &= 2\pi m + \arcsin\left(\rho \sin\big(kL'\big)\right) \\ kL &= 2\pi m + \left(\pi - \arcsin\left(\rho \sin\big(kL'\big)\right)\right) \end{aligned} \tag{2.64}$$

where m is an integer. With some rearrangement the above solutions is written as:

$$\begin{aligned} kL &= \pi(2m) + (-1)^{2m} \arcsin\left(\rho \sin\big(kL'\big)\right) \\ kL &= \pi(2m+1) + (-1)^{2m+1} \arcsin\left(\rho \sin\big(kL'\big)\right) \end{aligned} \tag{2.65}$$

which are combined into a singular expression by replacing $2m$ and $2m+1$ by the longitudinal index q:

$$kL = q\pi + (-1)^q \arcsin\left(\rho \sin\big(kL'\big)\right) \tag{2.66}$$

The $(-1)^q \arcsin\left(\rho \sin(kL')\right)$ takes the value of -1 to 1 which is small compared to the $q\pi$ term. Therefore k on the left-hand side is expressed as $2\pi v/c$ and k on the right-hand side is expressed as $q\pi/L$. The solution to resonance frequency v is a function of q, t_a and t_d:

$$v = \frac{c}{2\pi(t_a + n_d t_d)} \left\{ q\pi + (-1)^q \arcsin\left[\frac{n_a - n_d}{n_a + n_d} \sin\left(q\pi \frac{t_a - n_d t_d}{t_a + n_d t_d}\right)\right]\right\} \tag{2.67}$$

When n_a=n_d, eq. (2.67) reduces to the resonance condition of a single-medium cavity given by eq. (2.32). Both L and t_d are experimentally measurable quantities, a slightly more useful form of eq. (2.67) for data fitting purpose is can be obtained by replacing t_a with $L-n_d t_d$:

$$v = \frac{c}{2\pi L}\left\{q\pi + (-1)^q \arcsin\left[\frac{n_a - n_d}{n_a + n_d}\sin\left(q\pi\frac{L-2n_d t_d}{L}\right)\right]\right\} \tag{2.68}$$

2.4.2 Air-Like and Diamond-Like Modes

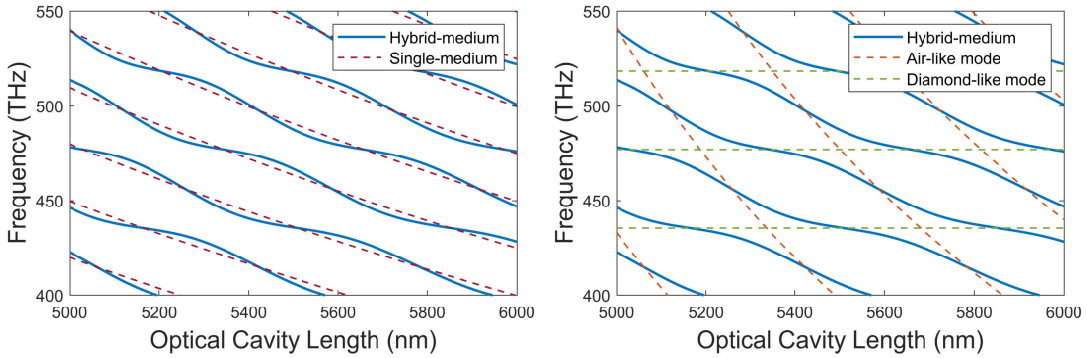

(a) **(b)**

Figure 2.23: Cavity mode structure of a hybrid-medium cavity visualized as **(a)** a deviation from a single-medium cavity or **(b)** the hybridization of the diamond-like and air-like modes in each sub-cavity medium. Diamond membrane thickness t_d is set to 1500nm.

There are two ways to visualize the mode structure of a hybrid-medium cavity given by eq. (2.68). Firstly the mode map of a hybrid-medium cavity is compared to that of a single-medium cavity as plotted in Figure (2.23)(a). The hybrid-medium modes exhibit a modulated deviations from that of the single-medium cavity due to the presence of the diamond membrane. The modulation period is determined by the sin(...) term in eq. (2.67) and it takes the value of 0 to π. The magnitude and direction of the deviation is set by the combined $(-1)^q \arcsin(...)$ term.

The second visualization incorporates the concepts of diamond-like and air-like modes as plotted in fig. (2.23)(b). By considering the each media in the cavity as a sub-cavity, it is desirable for standing waves to form within each sub-cavity. The resonant mode supported by the air sub-cavity requires a node at the air-diamond interface while the diamond sub-cavity mode requires an anti-node at the interface. As a result, the two types of modes hybridize and show anti-crossing behaviour. Depending on the relative

size between t_a and $n_d t_d$, the overall cavity modes are referred to as either a diamond-like or air-like mode.

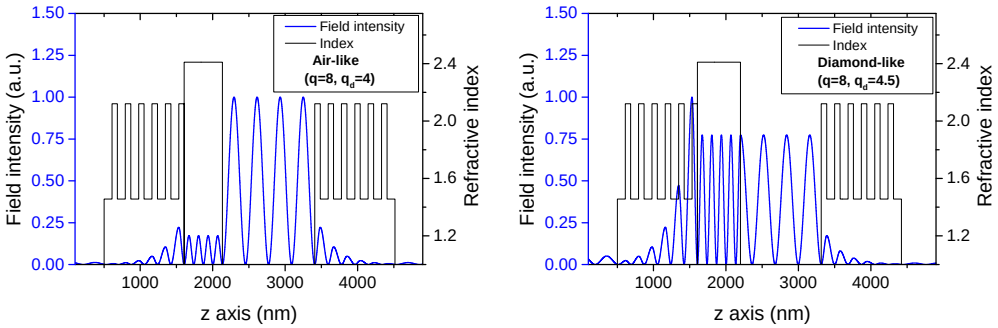

(a) Air-like mode. **(b)** Diamond-like mode.

Figure 2.24: The field intensity profiles of **(a)** an air-like mode cavity and **(b)** an diamond-like mode cavity. Both graphs are calculated using 1D TMM.

The diamond-like mode has a diamond mode index q_d of m+0.5 while the air-like mode has a q_d of m, where m is a integer. The electric field intensity profiles of both types of modes are plotted in fig. (2.24). The diamond-like mode shows a levelled field intensity maxima across the diamond-air interface.

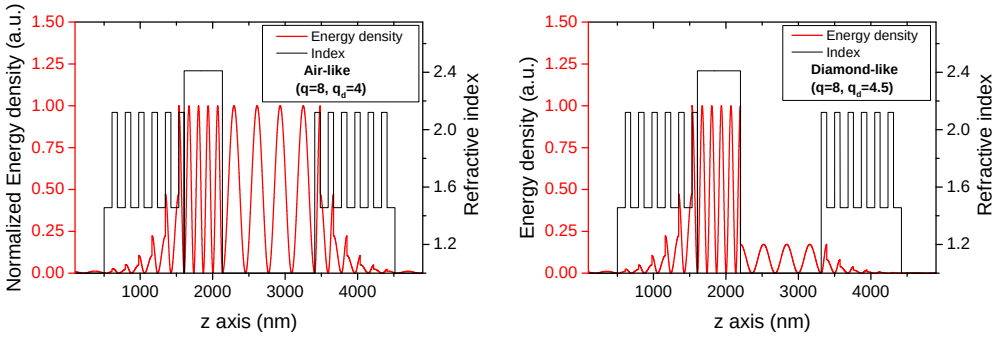

(a) Air-like mode. **(b)** Diamond-like mode.

Figure 2.25: The energy density profiles of **(a)** an air-like mode cavity and **(b)** an diamond-like mode cavity. Compared to fig. (2.24), the energy density profile gives a better visualization of the spatial extend of the cavity mode.

However, we note that field intensity $|\mathcal{E}^2|$ profiles are not the most best way to visualize energy distribution and mode volume V of the cavity mode. One common definition of V in literature work is given as:

$$V = \frac{\int \epsilon(\mathbf{r})|\mathcal{E}(\mathbf{r})|^2 d^3\mathbf{r}}{\max\left(\epsilon(\mathbf{r})\right)\max\left(|\mathcal{E}(\mathbf{r})|^2\right)} \tag{2.69}$$

which is valid for a single-medium cavity. But in the context of a hybrid-medium cavity this definition becomes problematic because the spatial locations of maximum field intensity and maximum refractive index can be different, as observed in fig. (2.24)(b). Therefore, it only makes sense to analyze $n^2|\mathcal{E}^2|$ together as the energy density of the mode using the V expression we introduced in section (2.2.3):

$$V = \frac{\int \epsilon(\mathbf{r})|\mathcal{E}(\mathbf{r})|^2 d^3\mathbf{r}}{\max\left(\epsilon(\mathbf{r})|\mathcal{E}(\mathbf{r})|^2\right)} \qquad \text{(eq. (2.20) revisit)}$$

Following this line of thought, it is more preferable to look at the distribution of energy density $n^2|\mathcal{E}^2|$ of the cavity mode, as plotted in fig. (2.25). This visualisation is fully compatible with both expressions of mode volume V and Purcell factor F as introduced in section (2.2.3).

2.4.3 Expected Finesse and Cavity Enhancement

The addition of the diamond membrane can be regarded as one additional layer on the planar mirror. As a result, the effective planar mirror reflectivity R_{plan} drops for q_{d}= m+0.5 (diamond-like mode) as shown in table (2.1), and the cavity finesse will also be affected.

	N_{plan}	q_{d}	R_{plan}
Single-medium - Reference	6	0	0.961
Hybrid-medium - Air-like	6	m	0.961
Hybrid-medium - Diamond-like	6	m+0.5	0.792

Table 2.1: The planar mirror reflectivity R_{plan} modification for different diamond membrane thickness. The coating pairs is set to 6 for demonstration and m is a positive integer.

Here, we calculate the expected cavity finesse in two ways: using eq. (2.38) to find the analytical approximation $\mathcal{F}_{\text{ana}}$ with the modified R_{plan}; using the numerical TMM treatment to find $\mathcal{F}_{\text{tmm}}$ via spectrum analysis. To compare the diamond-like and air-like modes, q_{tot} is fixed 4 and q_{d} is varied. The two DBR mirrors are constructed with 10/17 ($N_{\text{plan}}/N_{\text{feat}}$) pairs Ta-Si and both mirrors have a high-index termination.

The calculated $\mathcal{F}_{\text{ana}}$ and $\mathcal{F}_{\text{tmm}}$ are plotted in fig. (2.26)(a). Both $\mathcal{F}_{\text{ana}}$ and $\mathcal{F}_{\text{tmm}}$ have a similar oscillation corresponding to the competition between the resonance conditions of

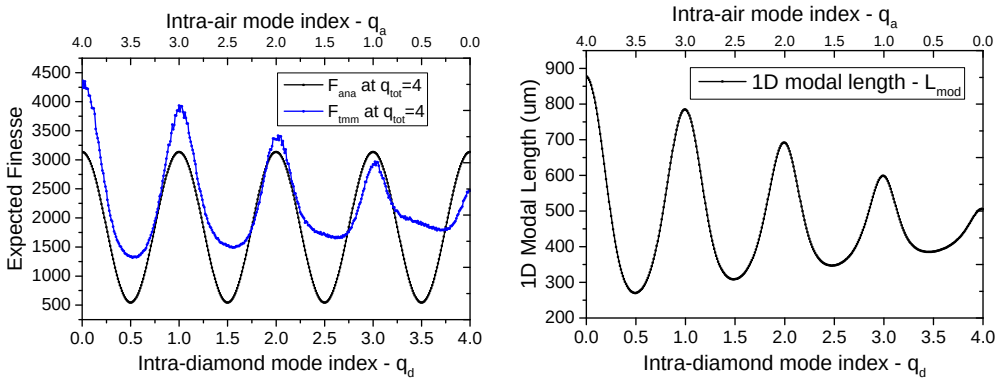

(a) **(b)**

Figure 2.26: **(a)** A comparison between expected cavity finesse calculated using analytical and numerical TMM descriptions. **(b)** The numerical 'modal length' L_{mod} calculated using TMM treatment.

air and diamond sub-cavities. In addition, the $\mathcal{F}_{\mathrm{tmm}}$ plot exhibits a damping behaviour towards larger q_{d}. This is explained by the fact that the index of diamond (n_{d}= 2.41) is larger than that of Ta_2O_5 (n_{ta}=2.12). In the extreme case of q_{d}=q_{tot}, i.e. the whole cavity is filled with high-index diamond, the effective DBR mirror reflectivities on both cavity mirrors drops. As a result, the cavity finesse at q_{d}=q_{tot} is much smaller than that at q_{d}=0.

To quantify the trend of expected cavity enhancement, in analogy to the 3D 'modal volume' V, we define the 1D 'modal length' L_{mod} as:

$$L_{\mathrm{mod}} = \frac{\int \epsilon(\mathbf{r})|\mathcal{E}(\mathbf{r})|^2 d\mathbf{z}}{\max\left(\epsilon(\mathbf{r})|\mathcal{E}(\mathbf{r})|^2\right)} \tag{2.70}$$

which is essentially the normalized 1D energy distribution of the cavity mode. Combining L_{mod} with the Gaussian beam description, a 3D cavity mode volume can be inferred by substituting L_{mod} into eq. (2.56):

$$V_{\mathrm{ana}} = \frac{\pi w_0^2}{4} L_{\mathrm{mod}} \tag{2.71}$$

As shown in fig. (2.26)(b), the calculated L_{mod} using TMM treatment also has a damping oscillation. More importantly, the diamond-like modes have much smaller modal length thanks to the high energy density in the high-index diamond layer (fig. (2.25)).

Because the expected cavity enhancement is $\sim \mathcal{F}_{\mathrm{tmm}}/L_{\mathrm{mod}}$, whose trend is plotted in

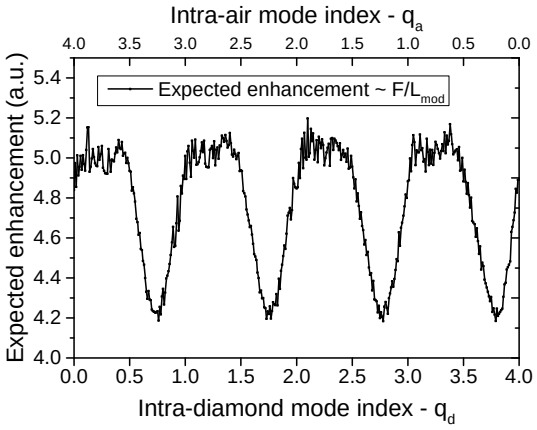

Figure 2.27: Calculated expected cavity enhancement F which is proportional to $q\mathcal{F}_{\mathrm{tmm}}/L_{\mathrm{mod}}$.

	Mode position	$T_{\mathrm{plan+memb}}$	$\mathcal{F}_{\mathrm{tmm}}$	L_{mod}	$\mathcal{F}_{\mathrm{tmm}}/L_{\mathrm{mod}}$
q_{d}=1.0	636.985nm	0.0198	3,932	785	5.01
q_{d}=1.25	624.134nm	0.0047	2,213	443	5.00
q_{d}=1.5	637.012nm	0.0034	1,524	309	4.94
q_{d}=1.75	650.423nm	0.0057	1,816	430	4.22

Table 2.2: The detailed cavity parameters for a number of key q_{d} values.

fig. (2.27). Interestingly, the diamond-like and air-like mode are expected to have a similar performance. Although the diamond-like modes have low expected $\mathcal{F}$, the spatial extend of the diamond-like mode is also much smaller.

The 16% drop of enhancement at q_{d}=m+0.75 is attributed to the discrepancy in mirror transmission $T_{\mathrm{plan+memb}}$ for different q_{d}. The detailed parameters at a number of key q_{d} values are shown in table (2.2). The q_{d}=1.75 row features a mirror transmission $T_{\mathrm{plan+memb}}$ of 0.0057 which yields a 20% lower $\mathcal{F}_{\mathrm{tmm}}$ than for example that of q_{d}=1.25. This disadvantage in $\mathcal{F}_{\mathrm{tmm}}$ is only compensated by 2.3% overhead in L_{mod} which leads to the 16% drop in enhancement.

2.4.4 Scattering Loss at Diamond Membrane Surfaces

The cavity scattering loss due to surface roughness requires particular attention for a hybrid-medium cavity. Due to fabrication limits, the best achievable surface roughness of a micro-structured diamond membrane is on the scale of nano-meter. Here we introduce two ways to incorporate surface scattering loss in our cavity analysis.

Firstly, we define an universal round-trip parameter $\mathcal{U}_0$ to replace $(R_1R_2)^{\frac{1}{2}}$ in eq. (2.38):

$$\mathcal{U} = (R_1R_2 \times (1-S)^4)^{\frac{1}{2}} \tag{2.72a}$$

$$\mathcal{F}_{\text{ana,scat}} = \frac{\pi\mathcal{U}^{\frac{1}{2}}}{1-\mathcal{U}} \tag{2.72b}$$

where S is the scattering loss at one membrane surface which is raised to power of 4 to account for a total of 4 passes in one round-trip. A widely used expression for S in terms of the RMS surface roughness σ is given by [57, 74]:

$$S = \left(\frac{4\pi\sigma}{\lambda}\right)^2 \tag{2.73}$$

Alternatively one can also use $\mathcal{F}_{\text{loss}}$ expression in eq. (2.39) by linearly incorporating S in $\mathcal{L}_{\text{lin}}$:

$$\mathcal{L}_{\text{lin,scat}} = 2 - R_1 - R_2 + 4 \times S \tag{2.74a}$$

$$\mathcal{F}_{\text{loss,scat}} = \frac{2\pi}{\mathcal{L}_{\text{lin,scat}}} \tag{2.74b}$$

A comparison between $\mathcal{F}_{\text{ana,scat}}$ and $\mathcal{F}_{\text{loss,scat}}$ are plotted in fig. (2.28). As expected a

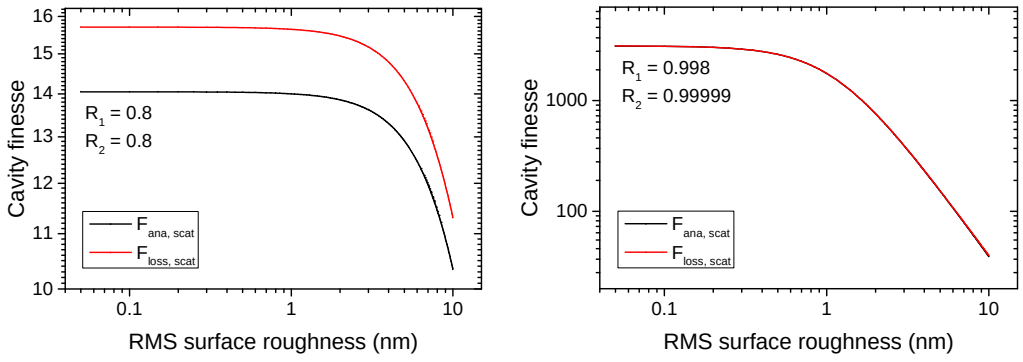

Figure 2.28: Calculated $\mathcal{F}_{\text{ana,scat}}$ and $\mathcal{F}_{\text{loss,scat}}$ for **(a)** a low-R and **(b)** a high-R cavity as a function of RMS surface roughness σ, both in log-log scales. The R= 0.998/0.99999 mirror pair is also the specification used in our experimental setup.

good agreement between the two is observed for the high-R cavity while for the low-R cavity $\mathcal{F}_{\text{loss,scat}}$ exhibits overestimation. Nevertheless a same conclusion can be drawn from both graphs: σ<1nm is desirable for close-to-optimal cavity operation especially for a high-finesse cavity.

Lastly, it is possible to modify the interface matching matrix M_{m} in TMM to include field incoherence due to scattering or absorption losses [75]. However this only works for analyzing R of DBR mirrors which concerns field intensity changes. In a single-mode analysis such as TMM, incoherent M_{m} also changes the phase expression of the propagating field. For a cavity structure where phase matching is required to establish cavity resonance, incoherent M_{m} inevitably shifts resonance position which is not desirable.

Chapter 3

Experimental Methods

In this chapter, the experimental methodologies used in this work will be introduced in detail. Firstly, the preparation of NV-containing bulk diamond samples is demonstrated. The generation yield and basic optical properties of ion-implanted NV centres are measured. The fabrication procedure of the ultra-thin diamond membrane with dry-etching techniques will also be presented. Next, the experimental apparatus used for sample characterization is introduced. This includes the XPS technique for surface characterization, as well as the scanning confocal microscope for optical characterization. Finally, the methodology and data analysis protocols of different optical characterizations are presented. Emphasis is given to the PLE measurement, where particular attention is paid to establish a thorough data process algorithm to ensure data quality.

3.1 NV Generation and Membrane Fabrication

In this work, NV centres are created using two methods: the conventional ion-implantation method and the novel laser-writing technique. Despite of the differences in annealing conditions, the two techniques share a similar fabrication flow as shown in fig. (3.1). Details of each step is given as following:

(a) For quantum network applications single crystal diamond with low defect concentration is preferred. The Element Six (E6) 'electronic grade' diamond grown by chemical vaper deposition (CVD) in {100} orientation has a low concentration of boron and nitrogen (<5ppb). Hence these plates are chosen as the standard stock sample

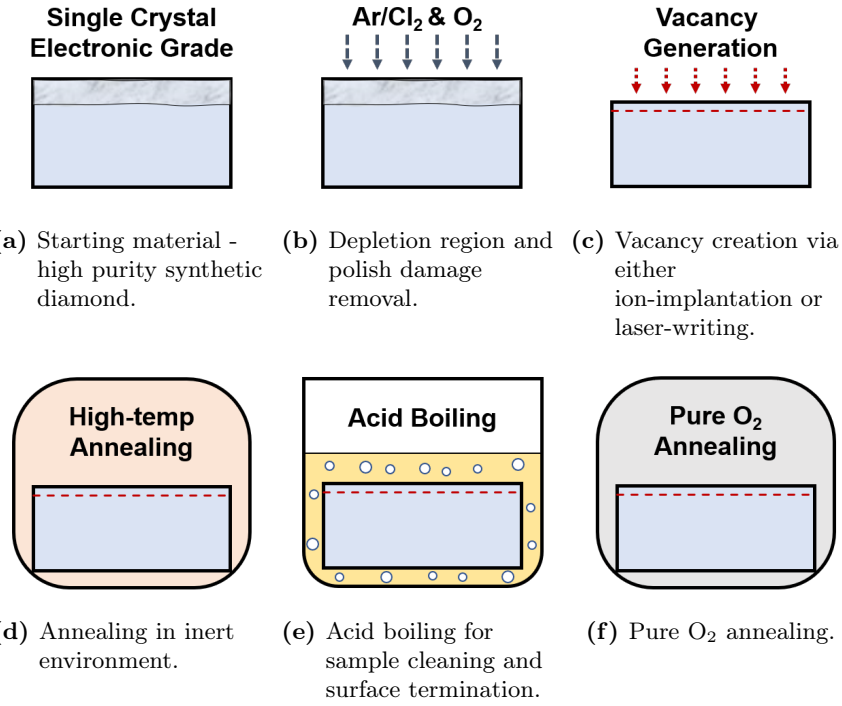

(a) Starting material - high purity synthetic diamond.

(b) Depletion region and polish damage removal.

(c) Vacancy creation via either ion-implantation or laser-writing.

(d) Annealing in inert environment.

(e) Acid boiling for sample cleaning and surface termination.

(f) Pure O_2 annealing.

Figure 3.1: A flow chart of sample preparation and NV fabrication steps in bulk diamond plates.

for this project. Single crystal {110} diamond plate grown by high-pressure high-temperature (HPHT) method from the New Diamond Technology (NDT) is also explored for its alternative crystal orientation. These samples also have [N]<5ppb with the added benefit of low lattice strain thanks to HPHT growth process.

(b) Previous work by [40, 76] reported that the as-received CVD diamond often contains a sub-surface depletion region up to 20µm deep due to hydrogen incorporation during the CVD growth process. In these regions, NV fluorescence can be quenched due to the formation of NVH complex.

To mitigate such effect, surface layers of CVD samples are removed with an ICP/RIE dry etch consist of an Ar/Cl_2 recipe with 10µm removal and an O_2 recipe with 5µm removal. The HPHT sample is treated similarly to remove polish marks and sub-surface polish damage.

(c) NV centre in this work is primarily fabricated using conventional ion-implantation followed by annealing. The implantation ion energy is around 50-70KeV with a target NV depth at 60-80nm which corresponds to the first anti-node position of the cavity mode. The stopping and range of ions in matter(SRIM) simulation suggest a

stopping depth of 65.5(15.2)nm for a 52KeV implantation. The ion fluence is set at 10^9ions/cm^2 for a better chance to generate confocal resolvable single NV defects.

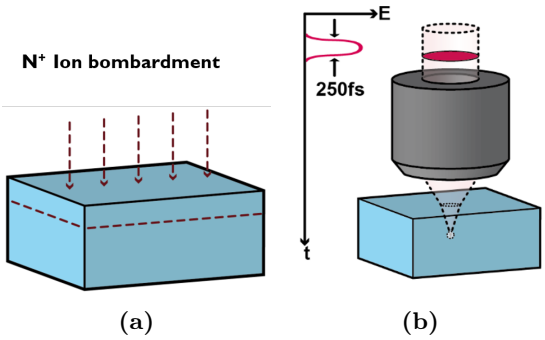

Figure 3.2: Illustration of different vacancy creation methods: **(a)** conventional ion-implantation followed by annealing; **(b)** single-pulse laser-writing technique followed by annealing.

Following the development of novel laser-writing technique [19, 77], diamond membranes with laser-written NVs are also fabricated. An illustration of the laser-writing technique is shown in fig. (3.2)(b) where single fs laser pulses are focused into the diamond to create lattice damage. Thanks to the strong non-linear effect, vacancies are created within a volume that is below the diffraction limit. As a result, minimal lattice damage is induced, and coherent NV generation has been demonstrated in [19]. The laser-writing of NV centre in this work is carried out by Dr.Patrick Salter.

(d) After vacancy creation, high-temperature annealing is performed to mobilize vacancy to form NV centre. The ion-implanted samples are treated with a multi-stage high-temperature annealing [42] in an inert atmosphere which consists of a 4hr step at 400°C, a 2hr step at 800°C and a 2hr step at 1200°C with 1hr ramp-up time between steps. The laser-writing samples are treated with a 3hr 1000°C annealing [19].

(e) Acid boiling is a widely used diamond treatment for sample cleaning and surface termination with oxygen species. In this work, acid boiling is carried out by heating a pre-mixture of acid and nitrate salt to avoid acid spillage. A glass thimble is used to cage the sample in acid solution, as shown in fig. (3.3) such that post-treatment sample handling is simplified.

In practice, an excess amount of KNO_3 is added to about 10mL of conc. H_2SO_4 to immerse the sample. The solid-liquid mixture is then heated with a heat plate until

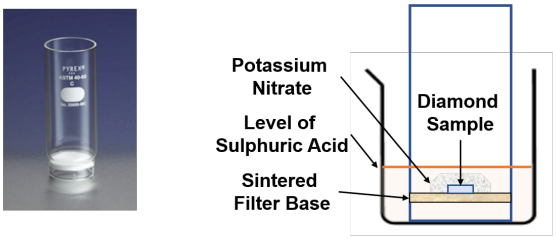

Figure 3.3: Experimental apparatus designed for acid boiling treatment. The diamond sample is placed in the glass thimble, which has a porous filtering base, and nitrate salt is added into the thimble. The thimble is then placed in a standard beaker where the acid is added to immerse the sample and nitrate salt.

>150°C. Bubbles of oxygen are released to clean and terminate the sample surface, and this process is left for >10min. Lastly, the sample is rinsed with de-ionized water to remove salt precipitation and dried with a blow-dryer.

(f) It has been reported [78] that the oxygen-terminated surface degrades over time, especially in air moisture. Hence an O_2 annealing at 465°C [38] is set up to refresh the sample surface as needed.

In practice, the vacuum annealing chamber is slowly heated up to 465°C. Next, a gentle flow of grade 5 oxygen gas is fed into the chamber, and the sample is kept in the oxidative environment for a couple of hours. It is important to not over-shoot above 465°C because sp^3 carbon starts to oxidize at higher temperature [79]. This is equivalent to thermally etching the diamond in the oxygen-rich environment which roughens sample surfaces.

3.1.1 Membrane Fabrication

Following the creation of NV centre in diamond as illustrated in fig. (3.1), the membrane fabrication procedure used to prepare μm-thick membrane are shown in fig. (3.4)(a)-(d). All the membrane samples in this work are made from CVD starting material.

Firstly, bulk diamond samples containing active NV are sent to a commercial laser-machining company (Delaware Diamond Knives) where the top implantation surfaces are sliced into 30μm-thick stock samples. These thin-plate samples are then capillary bonded on a silicon wafer with the implanted surface facing towards the substrate. Bulk

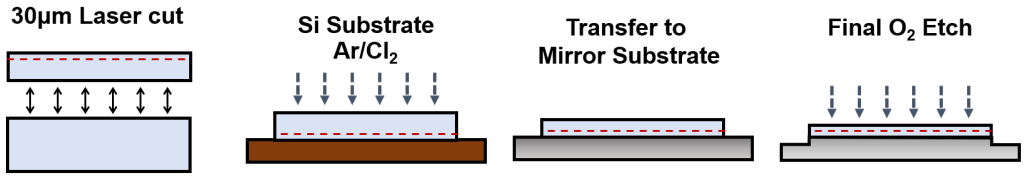

(a) Top surface laser cutting.

(b) Bulk removal with Ar/Cl_2 on a Si substrate.

(c) Transfer to the DBR mirror substrate.

(d) Final O_2 etch on DBR mirror.

Figure 3.4: The diamond membrane fabrication workflow, starting the bulk sample contains a layer of fabricated NVs near surface. Detailed description in text.

material removal is carried out using the Ar/Cl_2 ICP/RIE etching recipe for high etch rate and smooth surface finish.

At the thickness of about 5μm, the sample is transferred onto a DBR mirror substrate with the same sample facing. The final thinning is performed using a pure O_2 etching recipe to remove chlorine damage from previous etching steps. At this stage, the sample surface should have been terminated with oxygen-rich species but additional pure O_2 annealing at 465 °C is usefully used to ensure maximal oxygen coverage. The same annealing recipe is also used to refresh surface termination periodically because oxygen termination tends to degrade over time in the presence of moisture in the atmosphere [78].

3.2 Dry Etching protocols

Material thinning is a crucial fabrication step toward ultra-thin diamond membrane. To achieve precise control of etching depth and premium surface quality, inductively-coupled reactive-ion Etching (ICP/RIE) is adopted as the main material removal technique. An illustration of the ICP/RIE equipment is shown in fig. (3.5). All dry-etching in this work is carried out by our collaborator at University of Strathclyde.

Compared to conventional capacitive RIE, the plasma generation and DC bias in ICP/RIE system are controlled by separate power sources: the coil power and the platen power respectively. The ICP coils inductively couple the plasma with the RF antenna to generate high-density plasma up to 10^{13} cm^{-3}. The platen power then creates a DC bias to direct plasma towards sample surfaces.

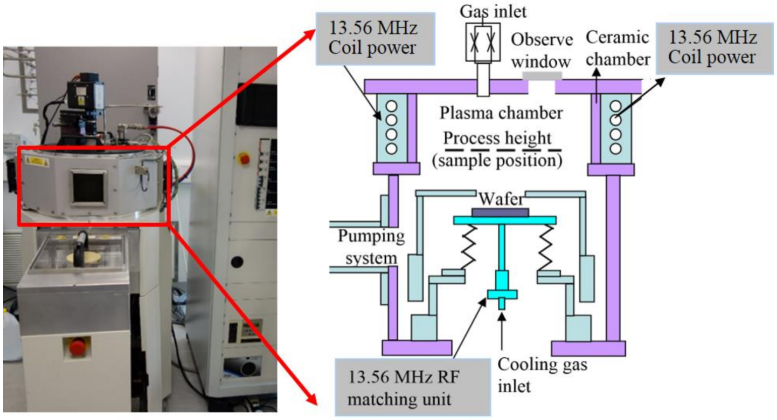

Figure 3.5: The ICP/RIE dry etching equipment. Photon and illustration in courtesy of Hangyu Liu.

This work utilizes two etching recipes involving Ar/Cl_2 and O_2 where typical etching parameters are shown in table (3.1). Estimated etch rate is not included due to large variance. Recipes containing Ar/O_2 is avoided due to sub-surface ion damage reported by [80].

	Pressure (mTorr)	Gas flow (sccm)	Platen power (W)	Coil power (W)
Ar/Cl_2	5	25(Ar), 40(Cl_2)	350	400
O_2	10	40(O_2)	100	700

Table 3.1: Typical etching parameters of the Ar/Cl_2 and O_2 etching recipes used in this work.

Generally ICP/RIE etching consists of a physical and a chemical etching component. During the Ar/Cl_2 etch, argon ion provides strong ion bombardment and the chlorine radicals react with sample surface and bombardment debris. As a result, high quality surface and fast etch rate is routinely achieved. The O_2 recipe involves little ion bombardment and is dominated by chemical etching. Consequently the etching process is more isotropic and the surface quality is not as good.

3.3 X-Ray Photoelectron Spectroscopy

X-ray photoelectron spectroscopy (XPS) is a surface-sensitive spectroscopic technique that allows the measurement of elemental composition down to an accuracy of parts per thousand (ppt) or 0.1%. Surface analysis by XPS involves irradiating the target

sample surface *in vacuo* with monoenergetic X-rays and analyzing the energy of the detected electrons. The XPS spectrum is plotted as the number of detected electrons per energy interval versus their kinetic energy (E_{k}). Different elements are associated with characteristic peak positions and spectral features where a quantitative measure of element fraction can be obtained from peak heights and peak areas. The typical detection range of XPS is the top 10nm of the surface due to the small mean free path of electrons in solids.

The emitted electrons after the X-ray irradiation have measured kinetic energies given by:

$$E_{\mathrm{k}} = hv - E_{\mathrm{b}} - \phi_{\mathrm{s}} \tag{3.1}$$

where hv is the photon energy, E_{k} is the binding energy of the atomic orbital of the electron and ϕ_{s} is the work function of the spectrometer. The binding energy is the energy difference between the initial and final states after the photoelectron has left the atom. Each type of atom has a variety of possible final states; therefore, the emitted electrons for a specific element will have a set of possible kinetic energies. Combined with the probability or cross-section associated with the final states, XPS is capable of identifying element concentrations in surface layers.

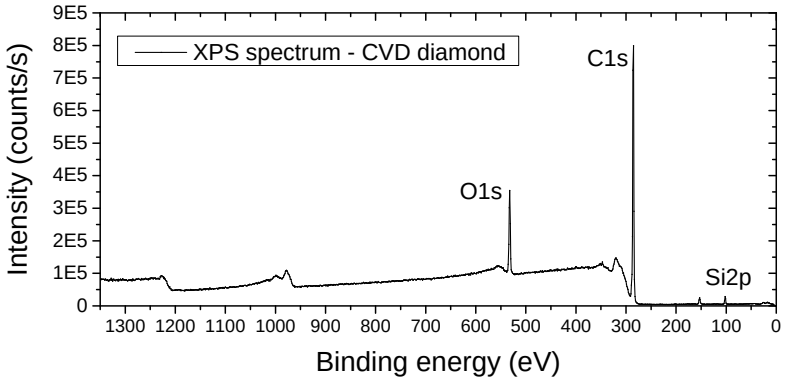

Figure 3.6: An example of XPS spectrum obtained from the as-received CVD diamond sample.

In this work, we are interested in verifying the effectiveness of the oxygen termination treatments applied to the diamond samples, and detecting any potential sub-surface damage caused by chlorine-based RIE etching recipes. The primary XPS signals of carbon, oxygen and chlorine are the C1s peak at ≈286eV, the O1s peak at ≈532eV and the Cl2p peak at ≈200eV. A typical XPS spectrum obtained from an oxygen-terminated CVD

diamond is shown in fig. (3.6).

We noted that XPS is not capable of detecting hydrogen, which is a common termination type of CVD diamond. Assuming that the amount of carbon is relatively constant within the sampling volume, the coverage of surface oxygen species can be inferred using carbon peaks as reference. A larger oxygen/carbon signal ratio is a good indication of a better oxygen surface termination.

XPS in this work is carried out with a Thermo Scientific K-alpha XPS machine at the Oxford Materials Characterisation Service with the kind help from Phil Holdway. More about XPS operation and reference data used for XPS spectrum interpretation can be found in [81].

3.4 Scanning Confocal Microscopy

All the fluorescence characterization in this work is carried out with a home-built confocal microscope whose main components and light paths are illustrated in fig. (3.7). The 532nm excitation is switched between an 80MHz pulsed PicoQuant DPSS laser and a continuous wave (CW) LaerQuantum Gem532 laser. A tunable 637nm external cavity diode laser (Topica DL-pro) is also available for PLE experiments. All the lasers have individual polarization and power controls

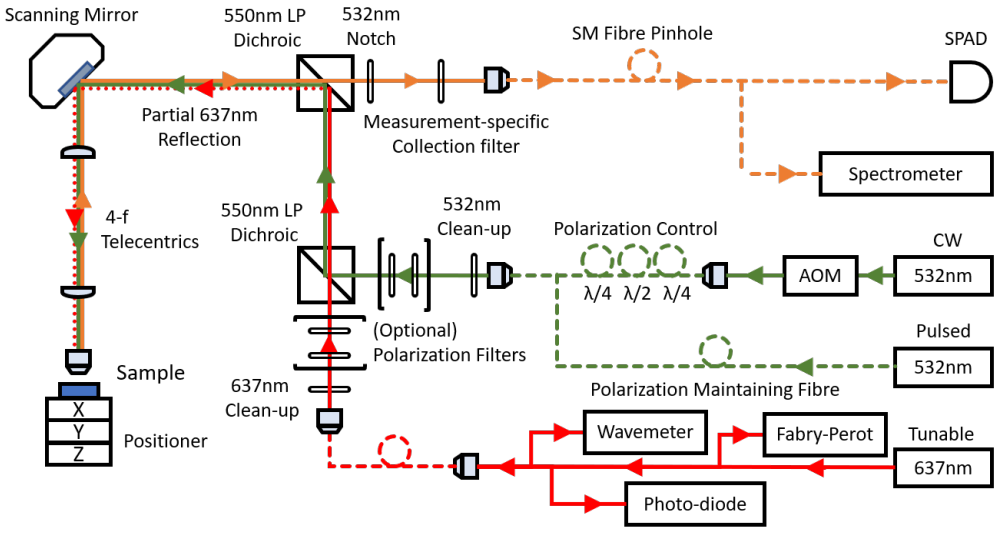

Figure 3.7: A schematic drawing of the beam scanning confocal microscope used in this work.

The light path is steered by a scanning mirror (Newport FSM300) and relayed with a set of 4-f telecentric lenses onto the sample stage. The photoluminescence (PL) from defects is collected through a NA=0.8 low-temperature objective which has a diffraction-limited resolution of about 300nm. The collection photons are analyzed with either single-photon avalanche detector (SPAD) or a spectrometer.

For experiments at cryogenic temperatures, the room-temperature 4-f telecentric lenses are swapped out for a pair of 4-f singlets with longer focal length to match the length of the vacuum tube. Both the sample stage and the 4-f system are situated in the vacuum tube and inserted into a bath cryostat (Wessington Cryogenics-CH100) which filled with cryogenic liquids. The vacuum tube contains 50mBar of He gas for heat exchange.

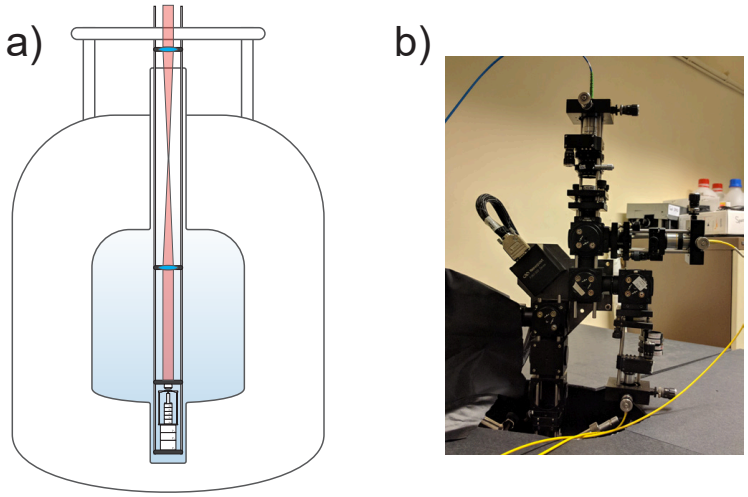

Figure 3.8: **(a)** The experimental apparatus for low-temperature experiments. **(b)** An photo of the confocal microscope on top of the bath cryostat in the enclosure box.

For vibration isolation, the cryostat is placed in an enclosure box build on a 150kg metal platform. The platform is supported with four passive isolation mounts (Thorlabs PWA075), and the enclosure box is surrounded by sound-proofing sidewalls.

3.4.1 Cavity-Coupling Assembly

The cavity assembly used in this work is illustrated in fig. (3.9)(a). The relative position and tip-tilting angles between the planar and featured cavity mirrors are controlled by the top five mini-piezo positioners in a secondary cage system. The featured mirror is

mounted on top of a LED. The three long-range piezo positioners at the bottom are capable of moving the whole secondary cage system in relation to the objective lens for sample navigation.

Membrane samples are mounted on the planar mirror with capillary bonding. Towards the preparation of the cavity-coupling experiments, the sample is firstly characterized by the planar mirror mounted facing upwards. After identifying target NVs, the planar mirror is flipped to face downwards. Due to the mirror reflectivity, confocal imaging in this geometry is difficult. The defect relocation relies on the FIB-milled registration marks on the planar mirror (fig. (3.9)(b)). Once the target NVs are located again, the featured cavity mirror (fig. (3.9)(c)) is brought in using mini-piezos to form the cavity.

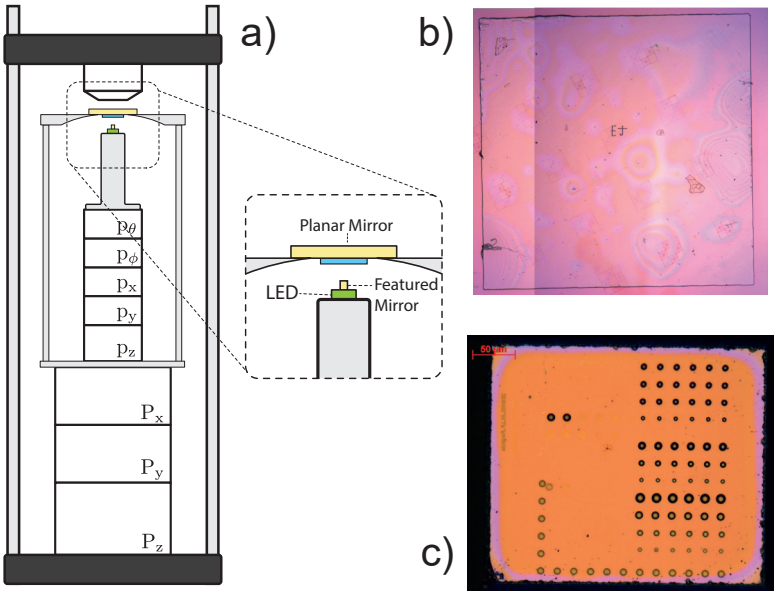

Figure 3.9: **(a)** An illustration of the cavity assembly used in this work where all the piezo positioners are from Attocube. The top five mini-piezos are ANGt50, ANGp50, ANPx51 (x2) and ANPz51. The bottom long-range piezos are ANPx100 (x2) and ANPz100. The low-temperature objective lens is LT-ASWDO/0.82. **(b)** An image of a 4x4mm diamond membrane on the planar mirror. **(c)** An image of a 300x300µm featured mirror.

The cavity features are fabricated using FIB-milling which is developed by Dr.Philip Dolan and Dr.Aurelien Trichet [82, 83]. The cavity plinth used in this work is fabricated by Dr.Lucas Flatten and coated by a commercial coating company.

3.5 Optical Characterizations

3.5.1 Lineshape Fitting

Due to the large amount of spectral line-shape fitting involved in this work, different line-shape functions are clarified in this section including the Lorentzian, the Gaussian and the Voigt functions:

$$\text{Lorentzian}: \quad f_{\mathrm{L}}(x) = A\frac{2}{\pi}\frac{w_{\mathrm{L}}}{4(x-x_{\mathrm{c}})^2 + w_{\mathrm{L}}^2} \tag{3.2}$$

$$\text{Gaussian}: \quad f_{\mathrm{G}}(x) = A\frac{2}{w_{\mathrm{G}}}\sqrt{\frac{\ln 2}{\pi}}e^{-\frac{4\ln 2}{w_{\mathrm{G}}^2}(x-x_{\mathrm{c}})^2} \tag{3.3}$$

$$\text{Voigt}: \quad f_{\mathrm{V}}(x) = A\frac{2\ln 2}{\pi^{\frac{3}{2}}}\frac{w_{\mathrm{L}}}{w_{\mathrm{G}}^2}\int_{-\infty}^{\infty}\frac{e^{-t^2}}{\ln 2(\frac{w_{\mathrm{L}}}{w_{\mathrm{G}}})^2 + (\sqrt{4\ln 2}\frac{x-x_{\mathrm{c}}}{w_{\mathrm{G}}} - t)^2}dt \tag{3.4}$$

where the w terms are the corresponding FWHM linewidths and the x_{c} terms are the peak positions. A comparison of these line-shapes is given in fig. (3.10)(right).

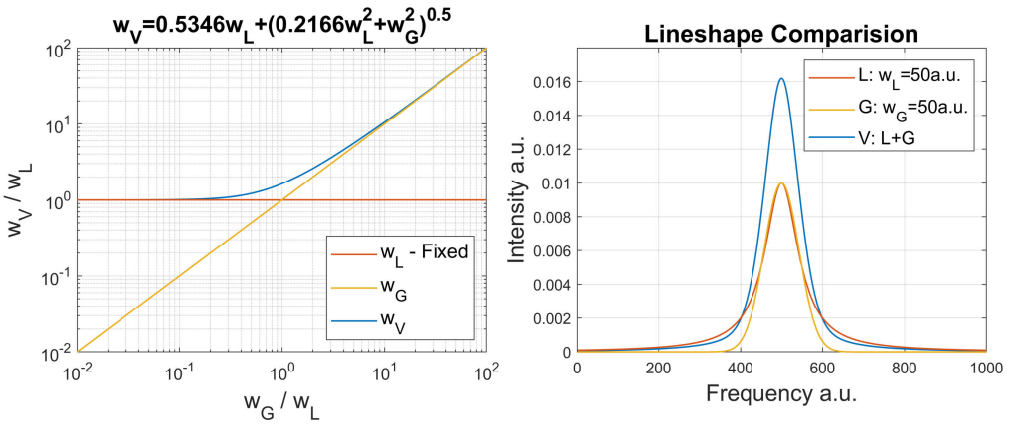

Figure 3.10: Left: Calculated Voigt linewidth w_{V} given a fixed Lorentzian linewidth w_{L} and a varying Gaussian linewidth w_{G}. **Right:** Plots of a pure Lorentzian profile, a pure Gaussian profile and a Voigt profile obtained by convoluting the former two functions. The broadening effect due to the Gaussian contribution is better visualized as the difference between the Voigt profile and the Lorentzian profile $w_{\mathrm{V}} - w_{\mathrm{L}}$ instead of w_{G}.

Generally speaking, the Lorentzian function is used to fit homogeneous NV ZPL transitions and intrinsic cavity mode shapes. The Gaussian line-shape resembles inhomogeneous broadening effects such as spectral diffusion of NV ZPL and broadening of cavity mode due to mechanical instability. The Voigt function is a convolution of Lorentzian and Gaussian lineshapes. It is often used when the magnitudes of homogeneous and

inhomogeneous effects are comparable.

An alternative way to find the Voigt function linewidth w_V is using an empirical approximation given by [84]:

$$w_V = 0.5346 w_L + \sqrt{0.2166 w_L^2 + w_G^2} \tag{3.5}$$

which holds true in the limit of a pure Gaussian profile and has a negligible error in the limit of a pure Lorentzian profile. A visualization of eq. (3.5) is shown in fig. (3.10)(left). It is observed that when w_G and w_L differs by two orders of magnitude, the dominating line-shape is obviously the better fit. The Voigt profile is preferred when w_G and w_L are within one order of magnitude difference.

The above lineshape discuss is perhaps most relevant to PLE data analysis in section (3.6) where the homogeneous ZPL transition (Lorentzian w_L) is broadened by spectral diffusion (Gaussian w_G). The overall ZPLlinewidth is given by the Voigt function linewidth w_V. For simplicity w_G is not usually de-convoluted from w_V. Instead, the linewidth broadening due to spectral diffusion is quantified by $w_V - w_L$ which is much easier to visualize with PLE data.

3.5.2 Excited-State Lifetime

The excited-state lifetime measurement is taken with a pulsed laser excitation at 532nm. The detected fluorescence signal is sent to a time-correlated single photon counting (TCSPC) device and correlated against the pulse trigger signal from the laser head.

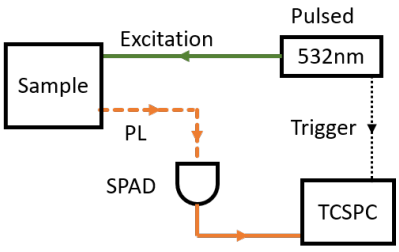

Figure 3.11: A schematic drawing of excited-lifetime measurement setup. The dashed orange line represents the fibre connections.

The lifetime measurement taken at the defect location is referred to as the 'total signal' dataset I which composes of three components:

$$I = I_{\text{def}} + I_{\text{bg}} + I_0 \tag{3.6}$$

where I_{def} is the pure defect signal, I_{bg} is the background contribution and I_0 is the instrument response. Each of these terms has a exponential decay form: $Ae^{-t/\tau}$, where A is a weighting factor and τ is the time-constant associated.

Assuming the background fluorescence is spatially uniform, the 'total signal' dataset is subtracted by an off-defect 'spatial background' dataset which contains I_{bg} and I_0. This yields the 'defect signal', I_{def}, which is fitted with a mono-exponential decay function to extract the defect excited-state lifetime. In the case where the background fluorescence is modulated at different locations, the 'total signal' is directly fitted with a tri-exponential decay function to represent all three terms in eq. (3.6).

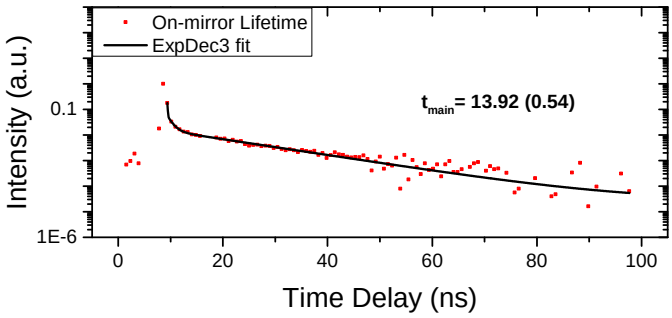

Figure 3.12: An example of lifetime data which is fitted with a tri-exponential decay function. The fitted lifetimes in the are t_{def}= 13.92ns, t_{bg}= 0.96ns and t_0= 0.07ns.

An example of lifetime data fitting is shown in fig. (3.12) where a tri-exponential decay function is used. Counting from the highest data point, the first few data points following the highest point are always neglected during the fitting process. This increases fitting accuracy of the longer lifetime component I_{def} by reducing the weighting factor of I_{bg} and I_0, which both have short lifetimes.

3.5.3 Power Saturation Measurement

The power saturation measurement records the defect fluorescence intensity I as a function of excitation laser power P. Assuming no background contribution, the fitting function is given by:

$$I = \frac{I_{\text{sat}} P}{P + P_{\text{sat}}} \tag{3.7}$$

where I_{sat} is the saturation intensity and P_{sat} is the saturation power.

In practice, some background contribution is inevitable. A main source of background signal in our experiments is the fluorescence from the DBR mirror coating which is particularly strong at low-temperature. Further complication is introduced by the presence of diamond membrane which causes intensity variation both spectrally and at a different spatial location.

In the very ideal case where a spatially uniform background fluorescence is present, two sets of power saturation measurements are usually taken: one at the defect location as the 'total signal' dataset and one at a nearby off-defect location as the 'spatial background' dataset. Subtracting the two yields the 'defect signal' dataset which is then fitted with eq. (3.7).

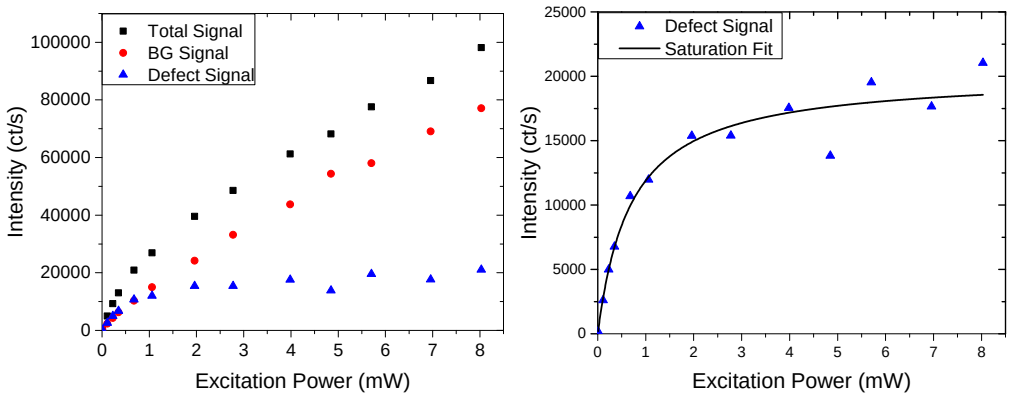

(a)

(b) Fitted I_{sat}=20,157ct/s and P_{sat}=0.70mW.

Figure 3.13: A P_{sat} measurement with spatially uniform background fitted with a simple saturation function.

An example of this fitting protocol is illustrated in fig. (3.13) where a good saturation fit is obtained. This protocol is usually applicable to defects in bulk material or fluorescent particles on an uniform substrate.

3.5.3.1 Dealing with Spatially Modulated Background

In this work most of the samples are thin membranes. In this case, both the spectral composition and the signal intensity of background fluorescence is modulated by a thin membrane. As a result, a direct subtraction between the 'spatial background' and the 'total signal' does not yield the true 'defect signal' accurately.

Hence for membrane samples, the 'total signal' dataset is decomposed into three components:

$$I = I_{\text{def}} + I_{\text{bg}} + I_0 \tag{3.8}$$

where I_{def} is the defect signal which follows eq. (3.7), I_{bg} is the background term and I_0 is the detector dark count (100-300ct/s). The I_{bg} term is usually approximated to scale linearly with P,

$$I_{\text{meas}} = \frac{I_{\text{sat}} P}{P + P_{\text{sat}}} + A_{\text{lin}} \times P + I_0 \tag{3.9}$$

where A_{lin} is the linear scaling factor. Unfortunately, fitting results using eq. (3.9) is usually not accurate enough in practice.

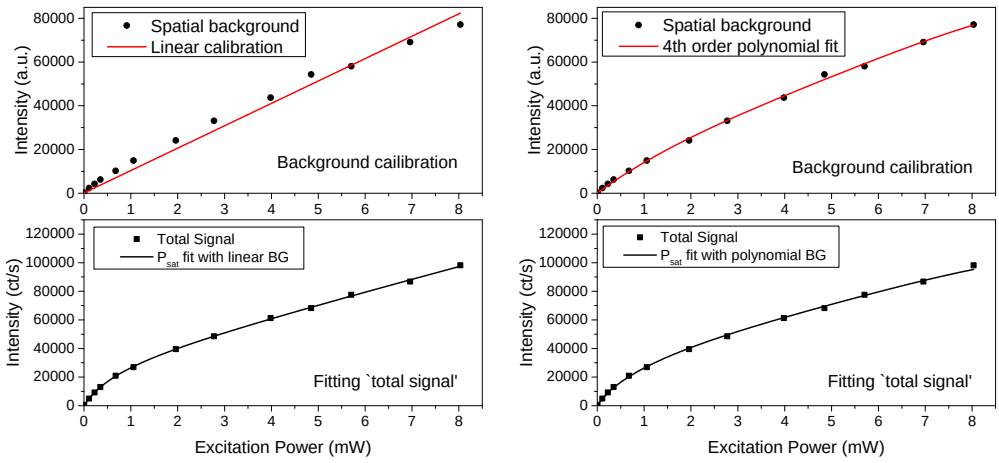

(a) Fitted I_{sat}=31,778ct/s and P_{sat}=0.78mW. **(b)** Fitted I_{sat}=19,743ct/s and P_{sat}=0.61mW.

Figure 3.14: **(a)** The linear I_{bg} fitting scheme. In the bottom panel A_{lin} is left as a free parameter. **(b)** The polynomial I_{bg} fitting scheme. The fit in bottom panel utilized the analytically extracted H_{bg} in the top panel and the scaling factor A_{pol} is left as a free parameter.

Instead, we assume that the power dependence of background fluorescence (in terms of a polynomial function H_{bg}) is identical at all positions irregardless of the spectral modulation. Under this assumption, H_{bg} can be calibrated using the off-defect 'spatial

background' dataset and substitute into I_{bg} with a free-fitting scaling factor A_{pol}. The fitting function eq. (3.8) is then given by:

$$I_{\mathrm{tot}} = \frac{I_{\mathrm{sat}} P}{P + P_{\mathrm{sat}}} + A_{\mathrm{pol}} \times H_{\mathrm{bg}} + I_0 \tag{3.10}$$

Figure (3.14) presents a comparison of the fitting results with the linear and the polynomial I_{bg} methods using the same 'total signal' dataset from fig. (3.13). It is observed that the polynomial I_{bg} method yields comparable I_{sat} and P_{sat} results compared to that in fig. (3.13)(b). In contrary, the linear $_{\mathrm{bg}}$ fit massively overestimated I_{sat} data by more than 50%. Therefore, in this work, most of the NV power measurement in membrane samples adopt the polynomial fitting protocol, especially for the in-cavity measurements.

3.5.4 Hanbury Brown-Twiss Measurement

Hanbury Brow-Twiss (HBT) measurement is a useful tool to confirm single photon emission properties and its experimental setup is shown in fig. (3.15). A 665/150nm band-pass filter is inserted between two SPADs to eliminate fluorescence cross-talk between photodetector chips. In this work all HBT are taken with CW excitation.

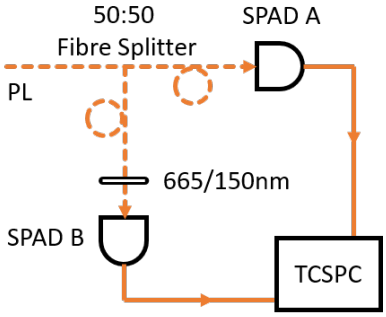

Figure 3.15: A schematic drawing of the experimental setup of HBT measurement. The dashed line represents fibre connections.

The collected photons are directed onto two SPADs (A/B) through a 50:50 fibre beamsplitter. The time-correlated single photon counting (TCSPC) device registers each photon detection event as an A- or B-channel tick and the time delay τ between them are recorded. The gathered correlation data is then built up as an intensity histogram of τ which is referred to as the second-order correlation function $G^{(2)}(\tau)$:

$$G^{(2)}(\tau) = \langle I_{\mathrm{A}}(t) I_{\mathrm{B}}(t+\tau) \rangle \tag{3.11}$$

where $I_{\mathrm{A}}(t)$ is the signal intensity on SPAD A at time t and $I_{\mathrm{B}}(t+\tau)$ is the signal intensity on SPAD B at time $t+\tau$. The degree of second-order coherence $g^{(2)}(\tau)$ is then written as:

$$g^{(2)}(\tau) = \frac{\langle I_{\mathrm{A}}(t) I_{\mathrm{B}}(t+\tau)\rangle}{\langle I_{\mathrm{A}}(t)\rangle \langle I_{\mathrm{B}}(t+\tau)\rangle} \tag{3.12}$$

The denominator in eq. (3.12) is also referred to as the normalization A_{hbt}:

$$A_{\mathrm{hbt}} = \overline{I}_{\mathrm{A}} \times \overline{I}_{\mathrm{B}} \times \delta t \times t_{\mathrm{tot}} \tag{3.13}$$

where δt is the time bin width and t_{tot} is the total integration time. The values of $\overline{I}_{\mathrm{A/B}}$ are not directly measurable with TCSPC. But for a steady defect signal with little fluctuations, $\overline{I}_{\mathrm{A/B}} \approx I_{\mathrm{A/B}}$.

The value of $g^{(2)}(\tau)$ is obviously dependent on the probability of detection events on SPAD A at t and on SPAD B at $t+\tau$. For a single photon emitter with a finite radiative lifetime, it is impossible for two photons to strike both SPADs at the same time (τ=0). Therefore, in the ideal case with no background signal contribution, a $g^{(2)}(0)$=0 dip can be expected for a single photon emitter.

In practice, the NV level structure is approximated with a simple three-level model and $g^{(2)}(\tau)$ is fitted with [85]:

$$g^{(2)}(\tau) = 1 + c_1 e^{-\frac{\tau}{\tau_1}} + c_2 e^{-\frac{\tau}{\tau_2}} \tag{3.14}$$

We note that in most cases background fluorescence is inevitable, especially for low-temperature experiments where the mirror fluorescence is particularly strong. Hence in this work we also include the expected HBT dip $g^{(2)}(0)_{\mathrm{exp}}$ as a baseline to present the background contributions in $g^{(2)}(\tau)$. By writing the total count rate I as S+BG where S is the defect signal and BG is the background intensity, $g^{(2)}(0)_{\mathrm{exp}}$ is given by:

$$g^{(2)}(0)_{\mathrm{exp}} = 1 - \frac{S_{\mathrm{A}}}{I_{\mathrm{A}}} \times \frac{S_{\mathrm{B}}}{I_{\mathrm{B}}} \tag{3.15}$$

or in terms of signal-to-noise ratio SNR= S/BG:

$$g^{(2)}(0)_{\mathrm{exp}} = 1 - \frac{SNR_{\mathrm{A}}}{SNR_{\mathrm{A}}+1} \times \frac{SNR_{\mathrm{B}}}{SNR_{\mathrm{B}}+1} \tag{3.16}$$

Again, the above equations assume a steady signal level with little fluctuations.

3.5.4.1 Dealing with Fluctuating Signal

There are occasions where the input signal intensity varies over time and this has implications on how HBT analysis should be done. This is applicable to the cavity-coupled NV emission if the cavity system exhibits some instability. In this case, HBT measurement is best taken with a time-tagging device which is capable of recording the signal evolution over the acquisition period. Although such apparatus is not available in this project, a discussion is still included as following.

Given that $I_{\mathrm{A/B}}$ are functions of t, the normalization factor A_{hbt} also has a t dependence. By writing $t_{\mathrm{tot}}= N\times\delta t$ where N is the number of time bins, eq. (3.13) is changed to:

$$A_{\mathrm{hbt}} = \overline{I}_{\mathrm{A}} \times \delta t \times \overline{I}_{\mathrm{B}} \times \delta t \times N \tag{3.17}$$

By expressing $I \times \delta t$ terms with summation notations:

$$A_{\mathrm{hbt}} = \frac{\sum_{i=1}^{N} I_{\mathrm{A}}(N)}{N} \times \delta t \times \frac{\sum_{i=1}^{N} I_{\mathrm{B}}(N)}{N} \times \delta t \times N \tag{3.18}$$

Using the above A_{hbt} expression, $g^{(2)}(\tau)$ can be properly normalized for a fluctuating signal and then fitted with eq. (3.14) as normal.

A proper estimation of $g^{(2)}(0)_{\mathrm{exp}}$ is more difficult because even a time-tagging device does not distinguish between defect and background signals. One's best bet is probably assuming a constant background level and estimating the average signal levels $\overline{S}$ using time bin summations:

$$\overline{S} = \frac{\sum_{i=1}^{N} I_{\mathrm{A}}(N)}{N} - BG \tag{3.19}$$

The expected background baseline is then given by:

$$g^{(2)}(0)_{\mathrm{exp}} = 1 - \frac{\overline{S}_{\mathrm{A}}}{I_{\mathrm{A}}} \times \frac{\overline{S}_{\mathrm{B}}}{I_{\mathrm{B}}} \tag{3.20}$$

3.5.5 Dipole Orientation Determination

The polarization measurement of NV centre is usually performed by rotating the polarization of the excitation laser with a half-wave-plate and monitoring the intensity change of dipole emissions. Because most samples in this work have {100} crystal orientation, a slightly different approach is used. By placing a linear polarizer is in the collection path, the intensity of strain-splitted NV ZPLs is monitored as a function of polarizer angle. .

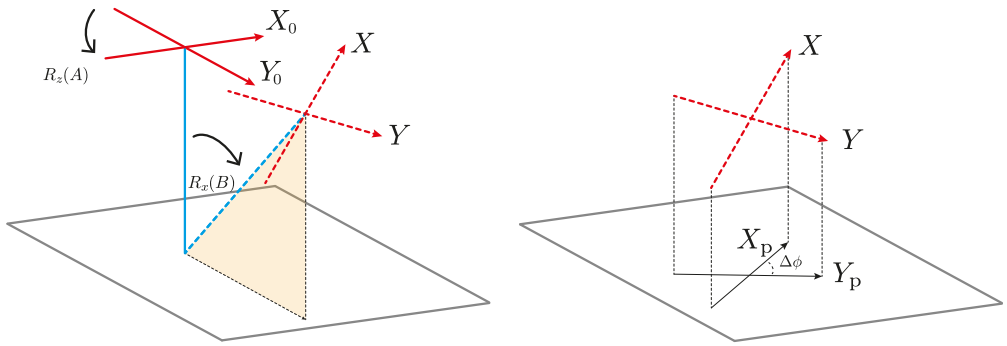

Figure 3.16: Illustration of dipole **(a)** rotation and **(b)** projection on to the x-y plane.

A schematic drawing of NV dipole orientations is shown in fig. (3.16). Starting with a set of unit vectors X_0, Y_0 and Z_0 where E_x/E_y represents the strain-splitted NV ZPL dipoles and Z_0 is the NV axis:

$$X_0 = \begin{bmatrix} 1 \\ 0 \\ 0 \end{bmatrix}, \quad Y_0 = \begin{bmatrix} 0 \\ 1 \\ 0 \end{bmatrix}, \quad Z_0 = \begin{bmatrix} 0 \\ 0 \\ 1 \end{bmatrix}$$

The actual NV orientation can be derived from this set of unit vectors with two rotation matrices as shown in fig. (3.16)(a): rotation R_z around the z-axis and rotation R_x around

the x-axis:

$$R_{\mathrm{z}}(A) = \begin{bmatrix} \cos A & -\sin A & 0 \\ \sin A & \cos A & 0 \\ 0 & 0 & 1 \end{bmatrix} \tag{3.21a}$$

$$R_{\mathrm{x}}(B) = \begin{bmatrix} 1 & 0 & 0 \\ 0 & \cos B & -\sin B \\ 0 & \sin B & \cos B \end{bmatrix} \tag{3.21b}$$

where A and B are the rotation angles. The combined transformation matrix is found to be:

$$R_{\mathrm{tot}} = R_{\mathrm{x}}(B)R_{\mathrm{z}}(A) = \begin{bmatrix} \cos A & -\sin A & 0 \\ \cos B \sin A & \cos B \cos A & -\sin B \\ \sin B \sin A & \sin B \cos A & \cos B \end{bmatrix} \tag{3.22}$$

Applying R_{tot} to X and Y:

$$X = \begin{bmatrix} \cos A \\ \cos B \sin A \\ \sin B \sin A \end{bmatrix}, \quad Y = \begin{bmatrix} -\sin A \\ \cos B \cos A \\ \sin B \cos A \end{bmatrix} \tag{3.23}$$

Projecting X and Y on to the x-y plane (fig. (3.16)(b)), the projected vectors are obtained by omitting the z components:

$$X_{\mathrm{p}} = \begin{bmatrix} \cos A \\ \cos B \sin A \\ 0 \end{bmatrix}, \quad Y_{\mathrm{p}} = \begin{bmatrix} -\sin A \\ \cos B \cos A \\ 0 \end{bmatrix} \tag{3.24}$$

Using the dot product expression we can write the angle $\Delta\phi$ between the two projections as:

$$\begin{aligned}\cos(\Delta\phi) = \frac{X_\mathrm{p}\cdot Y_\mathrm{p}}{|X_\mathrm{p}||Y_\mathrm{p}|} &= \frac{(-\sin A\cos A+\cos^2 B\sin A\cos A)}{\sqrt{(\cos^2 A+\cos^2 B\sin^2 A)(\sin^2 A+\cos^2 B\cos^2 A)}} = \\ &= \frac{(-\frac{1}{2}\sin 2A\sin^2 B)}{\sqrt{(1-\sin^2 B\sin^2 A)(1-\sin^2 B\cos^2 A)}} = \\ &= \frac{(-\frac{1}{2}\sin 2A\sin^2 B)}{\sqrt{(\cos^2 B+\frac{1}{4}\sin^2 2A\sin^4 B)}}\end{aligned} \tag{3.25}$$

By rearranging we obtain:

$$\begin{aligned}\sin 2A &= \frac{2}{\sin B\tan B\tan\Delta\phi} \\ A &= \frac{1}{2}\arcsin\left(\frac{2}{\sin B\tan B\tan\Delta\phi}\right)\end{aligned} \tag{3.26}$$

Provided that the sample has a {100} orientation, all four possible NV orientations along [111] directions have the same angle against the optical z-axis i.e. B= arccos ($\frac{1}{\sqrt{3}}$)=0.955rad. From the measurement, X_p and Y_p are recorded as a function of polarizer angle. The dataset for each dipole is fitted with a Malus-law function:

$$I(\phi) = I_0 + I_1\cos^2(\phi_{\mathrm{x/y}}+\phi) \tag{3.27}$$

The relative angle $\Delta\phi$ between X_p and Y_p is simply $|\phi_\mathrm{x}-\phi_\mathrm{y}|$. Substituting B= 0.955rad and the measured $\Delta\phi$ back to eq. (3.25), the rotation angle A can be obtained. The rotated vector X/Y and their projections $X_\mathrm{p}/Y_\mathrm{p}$ can be written in terms of A and B using eq. (3.23) and eq. (3.24). The orientation factor ξ in terms of $\theta_{\mathrm{x/y}}$ for both vectors can be calculated using the dot product expressions:

$$\begin{aligned}\xi_\mathrm{x} = \cos(\theta_\mathrm{x}) &= \frac{X\cdot X_\mathrm{p}}{|X||X_\mathrm{p}|} = \sqrt{1-\sin^2 B\sin^2 A} \\ \xi_\mathrm{y} = \cos(\theta_\mathrm{y}) &= \frac{Y\cdot Y_\mathrm{p}}{|Y||Y_\mathrm{p}|} = \sqrt{1-\sin^2 B\cos^2 A}\end{aligned} \tag{3.28}$$

3.6 Photoluminescence Excitation Measurement

Photoluminescence excitation (PLE) measurement is a high-resolution spectroscopic measurement which is used to probe the linewidth of the NV ZPL transition in this work.

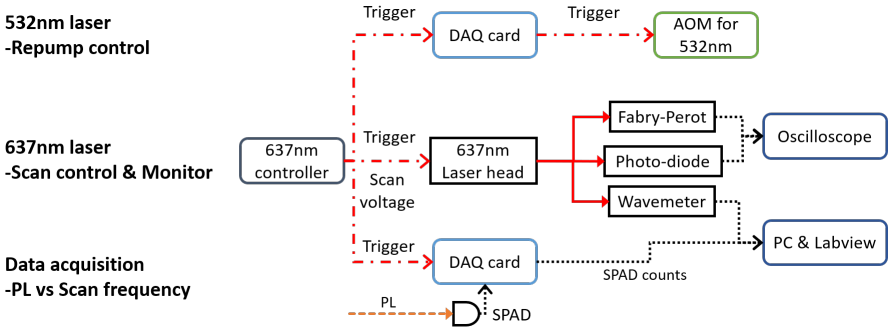

Figure 3.17: Workflow diagram of PLE measurement. Most of the device control units and data acquisition sequences are synchronized against a trigger pulse from the 637nm laser control unit.

A resonant 637nm excitation laser (Toptica DL-100/DL-pro) is scanned across the ZPL frequency, and the PSB emission (>650nm) is collected. The resultant data is an excitation spectrum as a function of laser scanning frequency whose resolution is in principle only limited by the linewidth of the scanning laser. The PSB photons are detected with a standard SPAD while the laser frequency is recorded using a wavemeter (Highfinesse WSU). A workflow diagram of PLE measurement is illustrated in fig. (3.17).

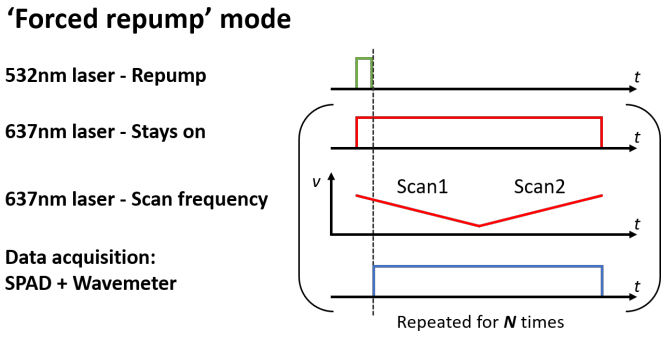

Figure 3.18: An illustration of PLE measurement sequence in the 'force repump' mode.

PLE measurement is typically carried out at 4K to eliminate phonon-assisted broadening of ZPL [37]. The 637nm excitation laser is usually set to circular polarization and a high optical density filter at 637nm is used in the collection arm to block 637nm leakage. Repump laser pulses of 50ms are applied to switch NV^0 to NV^- charge-state. An alternative repump wavelength at 575nm (Fianium SuperChrome) is also briefly explored. The basic PLE measurement sequence is shown in fig. (3.18).

3.6.1 Post-Analysis Protocol and PLE Validation Rate

Bulk analysis of PLE data can be difficult due to mid-scan photo-ionization events which leads to 'half-peak' signals as plotted in fig. (3.19)(b). Inclusion of these half-peak signal in the final database causes significant underestimation of ZPL linewidth. Unfortunately the half-peak data can not be distinguished from the full-peak data (fig. (3.19)(a)) using simple peak-finding gadgets.

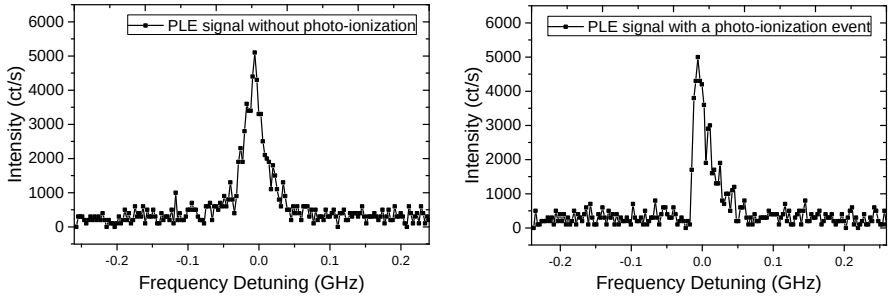

(a) **(b)**

Figure 3.19: Examples of PLE scans of NV ZPL transitions **(a)** when no photo-ionization took place, and **(b)** where a half-peak signal was recorded due to mid-scan photo-ionization.

In this work, a two-scan measurement sequence (fig. (3.18)) is adopted where each target scan (scan1) is followed by a charge-state validation scan (scan2). In the post-analysis procedure, a target scan is considered as valid if the validation scan shows a PLE signal regardless of the peak shape. This is generally true because the validation scan of a photo-ionized target scan will not show any PLE signal. This way, the defective target scans with half-peak PLE signals can be picked out with simple peakfind functions and data quality is ensured. In practice, user input is still requested at different stages of the analysis flow chart as shown in fig. (3.20).

During this process, the PLE validation rate p_{val} is given by:

$$p_{\text{val}} = \frac{\text{Number of validated PLE scans from NV}^-}{\text{Total number of PLE scans performed}} = \eta_{\text{cs}} \tag{3.29}$$

where p_{val} is equivalent to the charge-state preparation efficiency η_{cs} as introduced in section (1.2.3). An improvement in p_{val} can quadratically boost the entanglement efficiency by enabling easier preparation of NV^- charge-state.

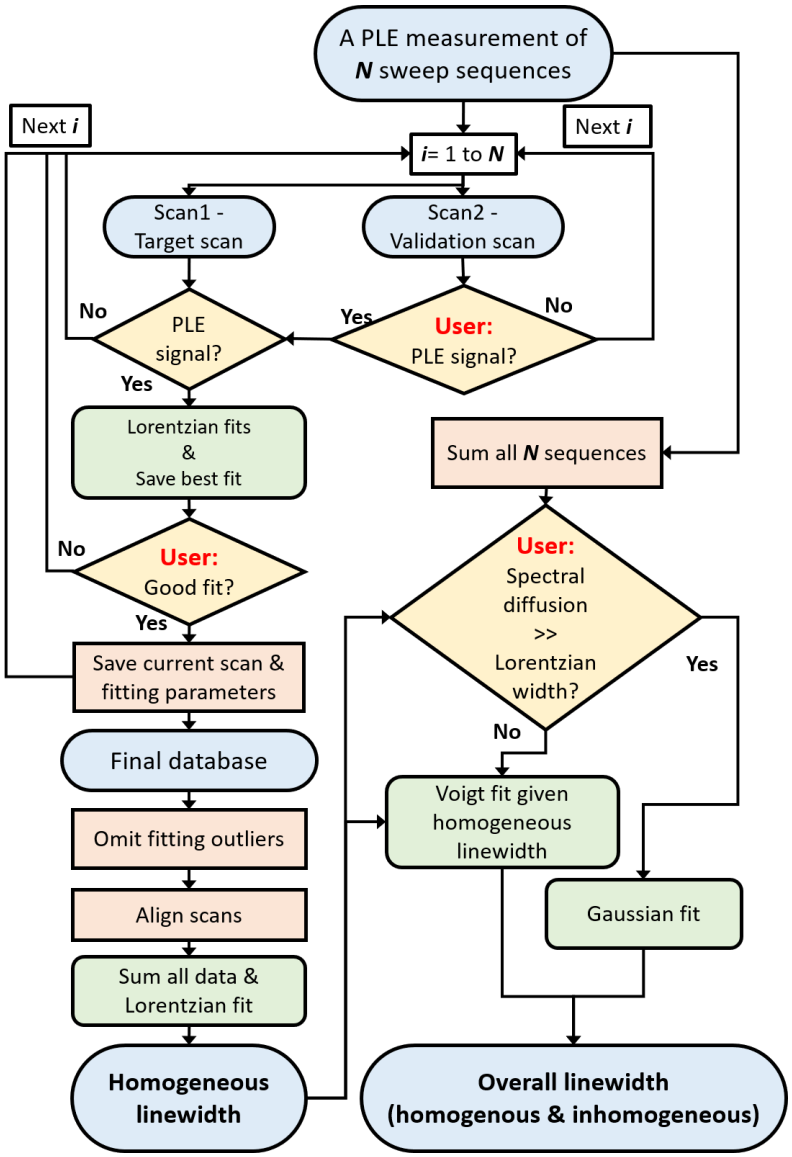

Figure 3.20: PLE data post-analysis algorithm for obtaining reliable measurement of homogeneous linewidth of NV ZPL transition.

3.6.2 Determination of ZPL Linewidths

After the validation process, each validated scan1 data is fitted with a Lorentzian function and the fitting statistics is recorded (fig. (3.21)(b)). According to the fitted peak positions, the validated scan1 data are aligned and summed to find the homogeneous ZPL linewidth $\delta\nu_{\mathrm{hom}}$ again with a Lorentzian function (fig. (3.21)(a)).

The overall ZPL linewidth $\delta\nu_{\mathrm{tot}}$ is obtained by processing the summation of all scan1 data regardless of validation status (fig. (3.21)(a)). The photo-ionized scan1 data are also included because they contributes towards the observed linewidth in long acquisition measurements. Normally a Gaussian or a Voigt function fit is used to find $\delta\nu_{\mathrm{tot}}$. When the

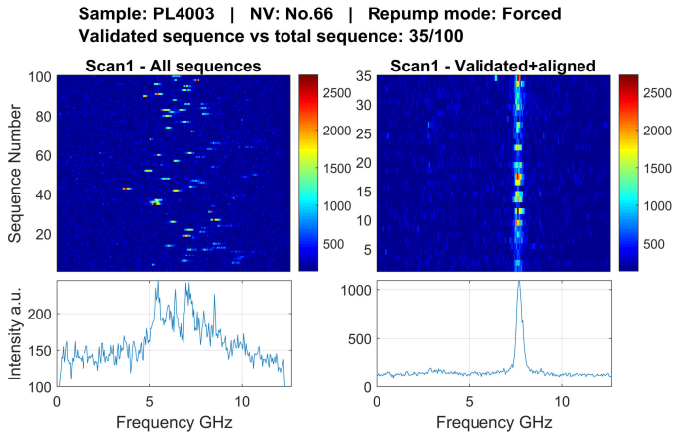

(a)

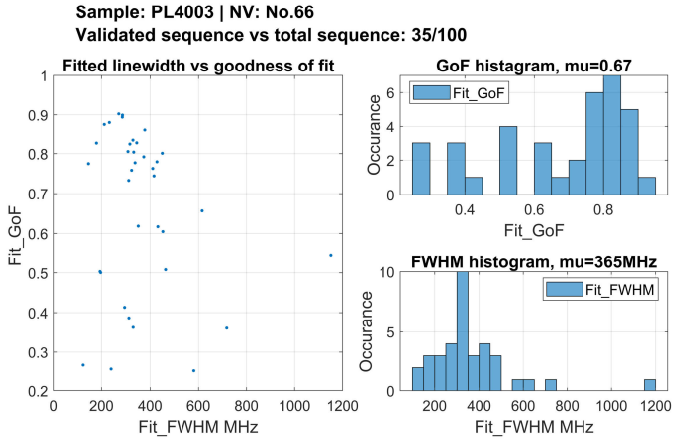

(b)

Figure 3.21: The overall ZPL linewidth is obtained by fitting the summation of all scan1 data and the homogeneous ZPL linewidth is obtained by fitting a Lorentzian function to the summation of all validated scan1 data.

summation data consist of well-defined sub-peaks, δv_{tot} is taken as the distance between the furthest peaks.

For entanglement generation, a δv_{hom} close to ≈13MHz indicates minimal optical decoherence due to non-radiative decay and a small δv_{tot} suggests minimal dephasing due to spectral diffusion. Both δv_{hom} and δv_{tot} contributes towards entanglement success rate via the excitation efficiency η_{ex}:

$$\eta_{\text{ex}} = \frac{\delta v_{\text{hom}}}{\delta v_{\text{tot}}} \qquad \text{(eq. (1.14) revisit)}$$

3.6.3 Charge-State Conversion Probabilities

The conversion probability of the bi-directional charge-state switching between NV^0 and NV^- is available from measurement statistics. After each scan1 data is validated, the validation status is recorded as 'true' or 'false'. For two neighbouring scan1 data, a false-to-true conversion represents a recharge event from NV^0 to NV^- and vice versa. This way, the recharge probability p_{rec} is obtained by fitting a histogram of number of scans between two successive recharge events (fig. (3.22)(a)). The same is done to obtain the ionization probability p_{ion} (fig. (3.22)(b)). Both histograms are fitted with a geometric distribution with probability p:

$$H(x) = p(1-p)^{(x-1)} \tag{3.30}$$

where x is the N-th repump to restore NV^- for p_{rec} fit and the N-th consecutive validated PLE scan for p_{ion} fit.

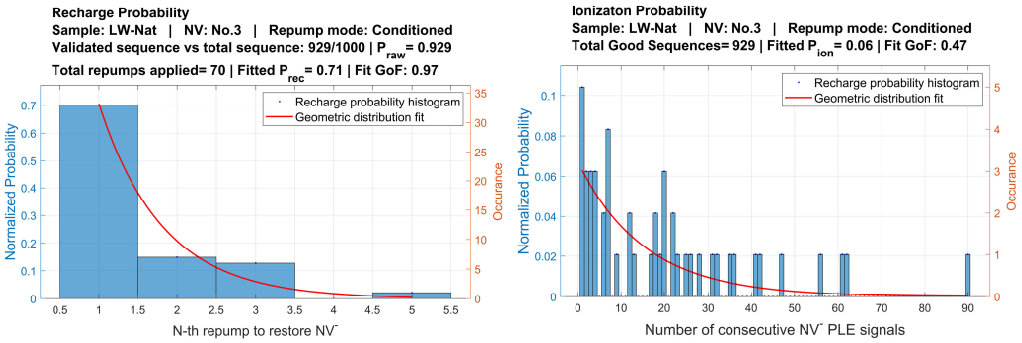

(a) **(b)**

Figure 3.22: Histograms and geometric distributions fits to obtain **(a)** the recharge probability p_{rec}=0.71 and **(b)** the ionization probability p_{ion}=0.06. Given that p_{val}=0.93 which is larger than p_{rec} and p_{ion} is very small, this laser-written NV is very favourable for entanglement generation.

We note that the validation rate p_{val} is determined by the balance between p_{ion} and p_{rec}. When $p_{\text{val}}>p_{\text{rec}}$, there likely exists a long-lived bright state (for example the x=90 column in fig. (3.22)(a)). In contrary, $p_{\text{val}}<p_{\text{rec}}$ suggests a lot repumps have been applied with no successful recharge event i.e. there exists a long-lived dark state. More discussion of $p_{\text{ion}}/p_{\text{rec}}$ analysis is presented in section (5.3).

3.6.4 'Forced' and 'Conditioned' Repump Modes

Depending on the NV charge-state stability, two different repump modes are used in this work. For NVs with a strong ionization tendency, the repump pulse is applied continuously to improve measurement efficiency because the NV is unlikely to maintain NV^- charge-state anyway. This is referred to as the 'forced' repump mode (fig. (3.18)) which is usually the default mode to start with.

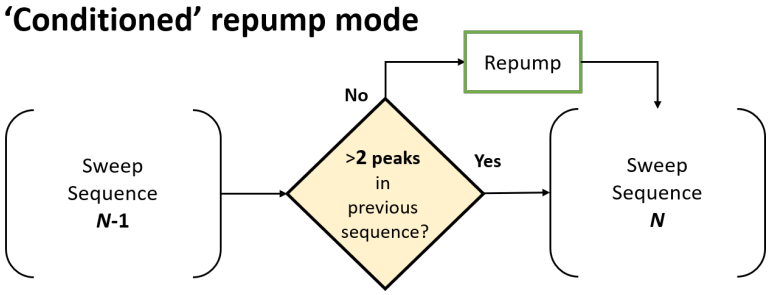

Figure 3.23: Measurement sequence with 'conditioned repump'.

For NVs with relatively stable ZPL frequency and high p_{val}, the 'conditioned' repump mode is used where the repump pulse is only applied if the previous scan shows no PLE signal (fig. (3.23)). This conditional decision is made *in situ* by a simple peak find function in the data acquisition program. Hence relatively high PLE signal intensity is preferable, which fortunately is usually the case for charge-state stable NVs.

We note that the p_{ion} calculation is only available from 'conditioned' repump mode because NV^- is allowed to evolve freely and 'spontaneous' ionization event is allowed to take place. In the 'forced' repump mode, even the NV is in NV^- it is still excited with excessive repump pulses. The recharge probability p_{rec} is available in both cases.

In practice, ion-implanted NVs are usually treated with 'forced' repump and laser-written NVs support 'conditioned' repump mode.

Chapter 4

Finite-Difference Time-domain Simulation

Although the analytical and TMM descriptions of optical resonators in chapter (2) provide a good starting point to predict cavity performance, the cavity loss analysis is largely limited to 1D in both cases. The more powerful numerical FDTD simulation (Lumerical), which accounts for the complete 3D dielectric environment, provides a fuller picture of photon emission rate and emission pattern.

In this work, we use a combination of time-dependent emission analysis to distinguish cavity and non-cavity photons, and spatially-resolved collection analysis to quantify cavity collection performance. In addition to the commonly used emission enhancement (Purcell factor) calculation, the importance of collection analysis is emphasized here. Particular attention is paid to the cavity loss through 2D guided modes, which is absent in the 1D analytical descriptions. Single-medium cavities are first examined to understand the influences of various cavity parameters. Then cavities with a diamond-air hybrid-medium are simulated to mimic the real device, and the difference between the so-called air-like and diamond-like cavity modes is investigated.

We noted that all simulations in this work are ran with a broadband dipole source instead of a narrowband one which yields two benefits. Firstly, this approach saves simulation time as the broadband source has a much shorter pulse duration. Secondly, it allows easier cavity mode tuning towards the target frequency of the NV ZPL transition at 637nm. Particularly, in this chapter, the obtained broadband cavity mode spectrum is analyzed

at a single-frequency near 637nm (exact frequency determined by the simulated fundamental mode), assuming perfect cavity-emitter coupling and narrow emitter linewidth. For real cavity-coupling experiments where both ZPL emission and PSB emission are considered, analysis is extended to a multi-frequency integration approach with the help of an analytical emitter spectrum. This will be demonstrated in chapter (7).

The naming convention of variables is as following: single superscripts represent each individual measurement configurations, e.g. γ^0, γ^{mir} and γ^{dev}; double superscripts mark the relative properties between two configurations, e.g. $F^{\mathrm{on/mir}}$ is the emission enhancement of the in-cavity on-resonance configuration with respect to the on-mirror configuration; the usage of subscripts is varied, e.g. spectral compositions are denoted as F_{ful}, F_{zpl} and F_{psb}, or channel compositions are denoted as P_{feat}, P_{plan} and P_{lat}.

4.1 Theoretical Background

Finite Difference Time Domain (FDTD) is numerical simulation technique where electromagnetic field propagation within a dielectric structure is solved using Maxwell's curl equations. The FDTD software packaged used in this work is a commercially available software (Lumerical).

By making use of the electric displacement $\mathcal{D}$ and the magnetic field strength $\mathcal{H}$, the Maxwell's curl equations in an isotropic medium are given by:

$$\frac{\partial \mathcal{B}}{\partial t} = -\boldsymbol{\nabla} \times \mathcal{E} \tag{4.1a}$$

$$\frac{\partial \mathcal{D}}{\partial t} = \boldsymbol{\nabla} \times \mathcal{H} + \mathcal{J} \tag{4.1b}$$

$$\mathcal{D} = \epsilon(w)\mathcal{E} \tag{4.1c}$$

$$\mathcal{B} = \mu(w)\mathcal{H} \tag{4.1d}$$

where $\epsilon(w)$ and $\mu(w)$ are the frequency-dependent permittivity and permeability of the medium respectively. The $\epsilon(w)$ term is generally complex to represent material absorption while the $\mu(w)$ is equated to unity for non-magnetic medium.

In a Cartesian coordinate system, eqs. (4.1a) and (4.1b) are equivalent to a set of six scalar

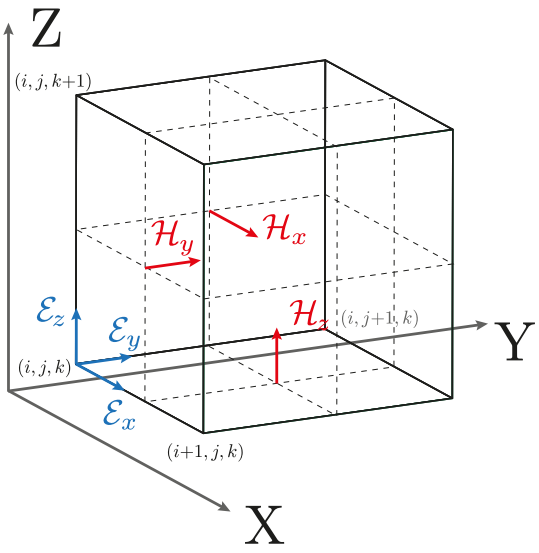

(a)

Figure 4.1: An illustration of the Yee cell: the electric field components are calculated along the edges and the magnetic field components are calculated perpendicular to the faces.

partial differential equations as shown in eq. (4.2). The J term is dropped assuming no free current within the region. It can be seen that the change in the electric field in time is dependent on the curl of the magnetic field. As a result, the electric field at one time instant is calculated using the stored value of the electric field and the curl of the magnetic field in the previous time instant. The same goes for the magnetic field calculation, which uses the stored value of the magnetic field and the curl of the electric field. This forms the basic time-stepping relationship that FDTD calculation utilizes.

$$\frac{\partial \mathcal{B}_x}{\partial t} = \frac{\partial \mathcal{E}_y}{\partial z} - \frac{\partial \mathcal{E}_z}{\partial y} \tag{4.2a}$$

$$\frac{\partial \mathcal{B}_y}{\partial t} = \frac{\partial \mathcal{E}_z}{\partial x} - \frac{\partial \mathcal{E}_x}{\partial z} \tag{4.2b}$$

$$\frac{\partial \mathcal{B}_z}{\partial t} = \frac{\partial \mathcal{E}_x}{\partial y} - \frac{\partial \mathcal{E}_y}{\partial x} \tag{4.2c}$$

$$\frac{\partial \mathcal{D}_x}{\partial t} = \frac{\partial \mathcal{H}_z}{\partial y} - \frac{\partial \mathcal{H}_y}{\partial z} \tag{4.2d}$$

$$\frac{\partial \mathcal{D}_y}{\partial t} = \frac{\partial \mathcal{H}_x}{\partial z} - \frac{\partial \mathcal{H}_z}{\partial x} \tag{4.2e}$$

$$\frac{\partial \mathcal{D}_z}{\partial t} = \frac{\partial \mathcal{H}_y}{\partial x} - \frac{\partial \mathcal{H}_x}{\partial y} \tag{4.2f}$$

To solve these equations numerically, both space (x, y, z) and time (t) are discretised. The simulation region is divided into discrete cuboidal Yee Cells [86] such that each

grid position is labelled as $(i\Delta x, j\Delta y, k\Delta z)$, where Δx, Δy and Δz are the cell dimensions. An illustration of a Yee Cell is shown in fig. (4.1) where the electric field components are calculated along the cell edges and the magnetic field components are calculated perpendicular to the cell faces. The simulation timeline is also discretised into finite $n\Delta t$ steps. Combining the two we can write any function of space and time as $F(i\Delta x, j\Delta y, k\Delta z, n\Delta t)$=$F^n(i, j, k)$.

Using a central difference approach the partial derivatives of each variable in function $F^n(i, j, k)$ can be written in the form of (only $\frac{\partial F}{\partial x}$ is shown):

$$\left[\frac{\partial F}{\partial x}\right]_{j,k,n} = \frac{F^n(i+\frac{1}{2}, j, k) - F^n(i-\frac{1}{2}, j, k)}{\Delta x} + O((\Delta x)^2) \tag{4.3}$$

where $O((\Delta x)^2)$ is the error in this approximation derived by the Taylor's theorem. The error term is negligible if the variable step is sufficiently small. Because the electric and magnetic field is calculated at staggered coordinates in the Yee cell as shown in fig. (4.1), the time-evolution of electric field and the magnetic field can be assessed numerically in a leapfrog manner for spatial variables $(\Delta x, \Delta y, \Delta z)$ in half-time steps $\frac{\Delta t}{2}$. By applying eq. (4.3) in eq. (4.2) the $\mathcal{B}$ and $\mathcal{D}$ field calculations now have the following numerical forms (only $\mathcal{B}_x$ and $\mathcal{D}_x$ are shown):

$$\begin{aligned}
&\frac{B_x^{n+\frac{1}{2}}(i,j,k) - B_x^{n-\frac{1}{2}}(i,j,k)}{\Delta t} = \\
&\qquad \frac{E_y^n(i,j,k+\frac{1}{2}) - E_y^n(i,j,k-\frac{1}{2})}{\Delta z} - \frac{E_z^n(i,j+\frac{1}{2},k) - E_z^n(i,j-\frac{1}{2},k)}{\Delta y} \\
&\frac{D_x^{n+\frac{1}{2}}(i,j,k) - D_x^{n-\frac{1}{2}}(i,j,k)}{\Delta t} = \\
&\qquad \frac{H_z^n(i,j+\frac{1}{2},k) - H_z^n(i,j-\frac{1}{2},k)}{\Delta y} - \frac{H_y^n(i,j,k+\frac{1}{2}) - H_y^n(i,j,k-\frac{1}{2})}{\Delta z}
\end{aligned} \tag{4.4}$$

These are referred to as the update equations. Combining the update equations with eqs. (4.1c) and (4.1d), all $\mathcal{E}, \mathcal{B}, \mathcal{D}, \mathcal{H}$ fields can be calculated accordingly. It should be noted that the field quantities in eq. (4.4) are function of time while both $\epsilon(w)$ and $\mu(w)$ are function of frequency. In practice, FDTD software uses analytical approximations of ϵ and μ and Fourier transforms to avoid computationally-heavy convolution calculations.

For the FDTD simulations to yield meaningful results, the choices of variable step sizes

$(\Delta x, \Delta y, \Delta z, \Delta t)$ must be such that over one increment in each variable the electromagnetic field does not change significantly. This means that the spatial and time step sizes must be small enough to resolve the field propagation which travels at the maximum speed of light within the simulation region. The stability criterion is given by eq. (4.5) which is referred to as the Courant-Friedrichs-Levy stability criterion.

$$\sqrt{\Delta x^2 + \Delta y^2 + \Delta z^2} > c\Delta t \tag{4.5}$$

After solving the update equations, the numerical results of the electric and the magnetic fields are stored in a 4D matrix as a function of (x, y, z, t) referred to as the time-domain data. The frequency-domain data is then obtained by a Fourier Transform, and its accuracy depends heavily on the choice of simulation length. Early termination is equivalent to applying a rectangular time window which introduces a convolution of sinc function in the frequency-domain. In this work, for the accuracy of Purcell factor analysis, most calculations are run until a cut-off field intensity of 10^{-5} within the simulation region is reached. Note that this is not a requirement for Q factor calculation since it depends only on the rate of field decay. More details of cavity analysis will be shown in section (4.4) .

4.2 Simulation Setup

In this work, the cavity length is often described in the unit of cavity mode index q instead of the optical cavity length L in SI units. The two quantities are related by the cavity resonance condition:

$$L = q\frac{\lambda}{2} \qquad \text{(eq. (2.32) rearranged)}$$

where $L{=}nL_0$ is the optical cavity length and L_0 is the physical cavity length.

The usage of q emphasizes the fact that the simulation methodology introduced in this work is widely applicable to any emitter wavelength. It also avoids the complication of refractive index scaling of optical cavity length when multiple cavity medium are involved. For reference, a conversion table of L against q is given as following in table (4.1):

Cavity mode index q	1	2	3	4	5	6
Optical cavity length L (nm)	318.5	637	955.5	1274	1592.5	1911
Physical L in diamond (nm)	132.7	265.4	398.1	530.8	663.5	796.25

Table 4.1: Conversion table from cavity mode index q to optical cavity length L for a single-medium air cavity constructed for NV ZPL wavelength at 637nm. The conversion to the corresponding physical cavity length for a single-medium diamond cavity is also given.

4.2.1 Simulation Objects and Cavity Mirrors

The simulated cavity structure consists of a planar mirror (top) and a patterned mirror (bottom) with FIB-milled hemispherical cavity features (fig. (4.2)). The cavity shape is defined by the cavity depth L_{depth} and the radius of curvature $\mathcal{R}$. The cavity length L is calculated using the Gaussian beam expression to account for the Guoy phase shift. The mirror separation is denoted as L_{2D} to indicate their ability to support 2D guided modes.

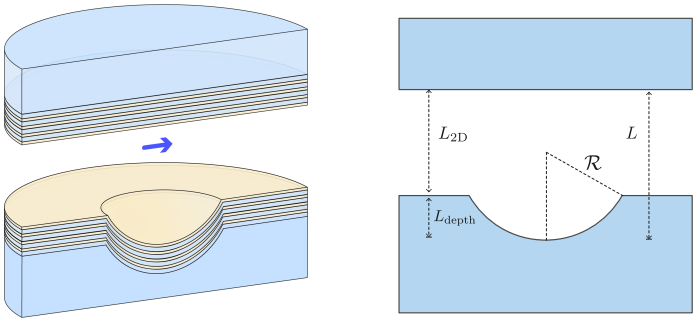

(a) **(b)**

Figure 4.2: **(a)** An illustration of simulated cavity structure including both the planar and the featured mirrors. The blue arrow represents the electric dipole source. **(b)** An schematic drawing showing the main geometric variables: cavity length L, depth of cavity feature L_{depth}, cavity radius of curvature $\mathcal{R}$ and mirror separation L_{2D}.

Table (4.2) shows the parameters for several DBR coating setups used in our simulations. The Ta_2O_5-SiO_2 coating system has an index contrast of 2.12/1.46 and is prioritized due to better film quality and lower material absorption. The TiO_2-SiO_2 system is also simulated for its higher refractive index contrast of 2.58/1.46. The high-Q coating setups resemble the mirror specifications in experiments. However, high-Q simulations usually take too long to compute. Hence the majority of work in this chapter uses the low-Q versions.

	Planar Mirror			Featured Mirror			
	N_{plan}	$t_{\text{sub,plan}}$ (nm)	T_{plan} (ppm)	N_{feat}	$t_{\text{sub,feat}}$ (nm)	T_{feat} (ppm)	$\mathcal{F}_{\text{tmm}}$ at q=1
Ta/Si High-Q	10	22	2000	17	27	10	7855
Ti/Si High-Q	6	98	2000	11	43	10	5871
Ta/Si Low-Q	6	22	39300	13	27	200	385
Ti/Si Low-Q	4	11	39300	8	110	200	291

Table 4.2: DBR coating parameters: number of coating pairs N, substrate thickness t, mirror transmission T and expected finesse $\mathcal{F}_{\text{tmm}}$. The value of $\mathcal{F}_{\text{tmm}}$ is calculated using TMM for a q= 1 cavity. The value of T is also calculated using TMM and fine-tuned with substrate thickness t_{sub}.

4.2.2 Monitor Placement

The simulation region is bounded by Perfectly-Matched-Layer (PML) which strongly absorbs the outgoing waves without reflecting them back into the simulation region. To avoid undesirable absorption, simulation boundaries are kept at least half-wavelength away from the main cavity modes. The setup of data collection monitors is shown in the fig. (4.3).

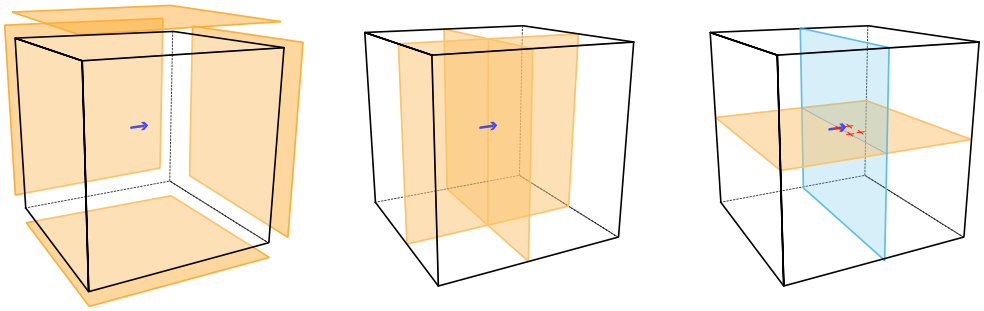

(a) **(b)** **(c)**

Figure 4.3: Illustration of simulation monitor setup: **(a)** the f-domain edge monitors; **(b)** the f-domain cross-section monitors; **(c)** the index monitor, f-domain beam profile monitor and t-domain field decay monitors. The f-domain monitors are marked in orange, the t-domain monitors are marked as red cross, the index monitor is in blue and dipole source is marked as the blue arrow.

Three main types of data monitors in FDTD simulation are the frequency-domain (f-domain) monitor, the time-domain (t-domain) monitor and the refractive index monitor. According to specific analysis demands, the monitors used in our simulations are illustrated in fig. (4.3):

- The f-domain edge monitors in fig. (4.3)(a) capture photon loss in all orthogonal directions and the results feed into collection analysis in section (4.3.2).
- The f-domain cross-section monitors in fig. (4.3)(b) and the index monitor in fig. (4.3)(c) contributes to mode volume calculation in section (4.4.4). The f-domain data is collected in both x-z and y-z planes to account for the two-fold dipole symmetry.
- The t-domain monitors in fig. (4.3)(c) are placed at an node position of the cavity mode and they record the electric field decay over all frequencies. The data collected is used for quality factor calculation section (4.4.2).

In addition, the dipole source simulation object has a set of built-in monitors referred to as the 'Purcell monitors'. The Purcell monitors monitor the dipole power emission with and without the simulation structure, as expressed by the sourcepower(f) and the dipolepower(f) functions, respectively. By comparing the dipolepower P^{dev} emitted in the simulation structure to the sourcepower P^0 in a homogeneous medium, the emission enhancement F is calculated using eq. (4.6) (more in section (4.4.1)).

$$F = \frac{P^{\text{dev}}}{P^0} \tag{4.6}$$

In principle, the Purcell monitors behave like the f-domain power monitors which record the photon emission as the simulation runs. Hence the data from the Purcell monitors are only accurate if the simulation run-time allows a complete decay of the electromagnetic field inside the simulation region (see section (4.1)).

4.2.3 Yee Cell Meshing Accuracy

Refining the average size of the Yee Cell (fig. (4.4)(b)) reduces the artificial scattering at curved surfaces at the cost of increasing simulation time and resource with a cubic scaling. Without going through the detailed calculations right here, some key cavity parameters are plotted in fig. (4.5) as a function of mesh size. A 10% improvement in Q and a convergence behaviour of the mode volume integral V_{int} are observed towards finer mesh settings.

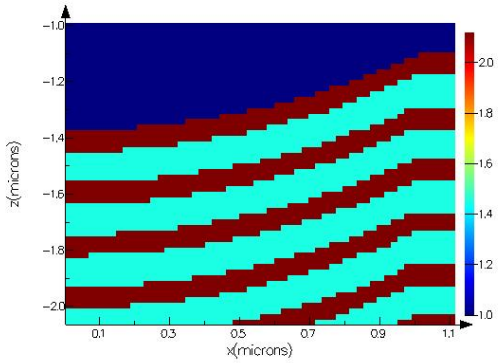

(a)

Setting	Cell size (nm)	Mode position (nm)
2	27.2	637.18
3	19.5	635.06
4	15.2	634.49
5	12.5	634.16
6	10.6	633.72
7	9.2	633.64

(b)

Figure 4.4: **(a)** The rendered 'step' geometry of the cavity feature at accuracy setting 3. **(b)** Various mesh accuracy settings and the corresponding average cell sizes and simulated mode positions.

Following the convergence test, we decided to use mesh accuracy 3 (fig. (4.4)(a)) in this work for the trade-off between data accuracy and simulation time. This setting provides a factor of 8 reduction in computation resources at the cost of a 10% error in Q. This is very tolerable in most situations.

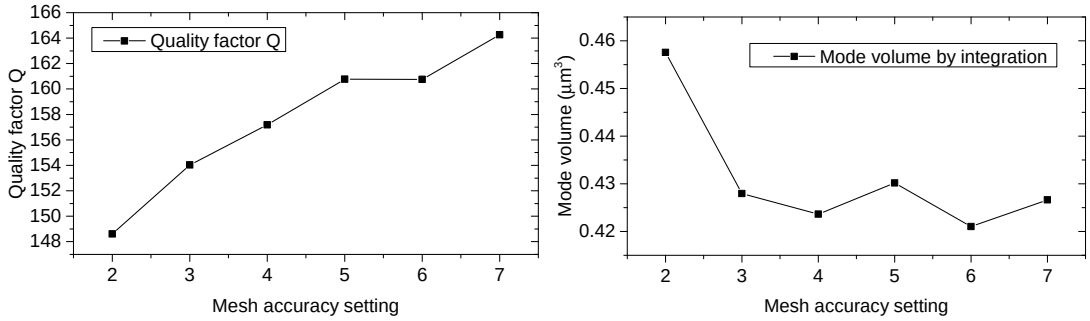

(a) The quality factor Q.

(b) The mode volume calculated by integration V_{int}.

Figure 4.5: Mesh cell size convergence test.

4.3 Analysis Methodology

Just like real experiments, FDTD simulation has a wide parameter space, and it produces an overwhelmingly large amount of data. Hence it is crucial to establish a comprehensive analysis protocol to pinpoint key bench-mark figures.

In most literature works, analysis of cavity-coupled NV experiments is limited to the Purcell enhancement that is derived from emitter lifetime reduction. However, the obtained

enhancement factor often does not agree with the observed increase in ZPL photon output due to a change in photon collection efficiency. Experimental determination of collection enhancement of cavity devices is usually tricky because a comparison between free-space and device-enhanced emission is often less straightforward.

Fortunately, this is not an issue for FDTD simulations because an emission rate comparison with a free-space dipole is always possible. To fully utilize this feature, our analysis protocol combines a time-dependent emission analysis and a spatially-resolved collection analysis.

4.3.1 Time-Dependent Emission Analysis

It was illustrated in fig. (2.8) that some cavity-coupled dipole emission is not channeled into the cavity modes. This part of emission is referred to as the 'non-cavity photon' as opposed to the 'cavity photon' in the resonant modes.

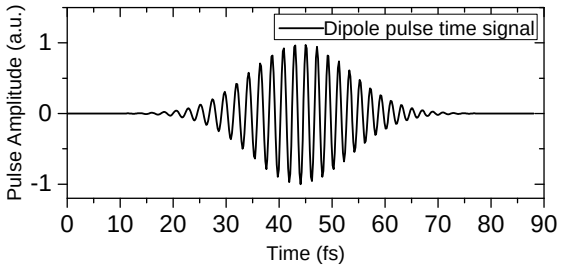

(a) The initial dipole pulse signal.

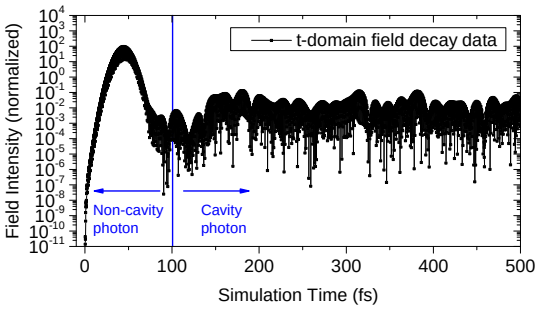

(b) T-domain data from a q=16 cavity where the cavity and non-cavity photon groups has a clear separation.

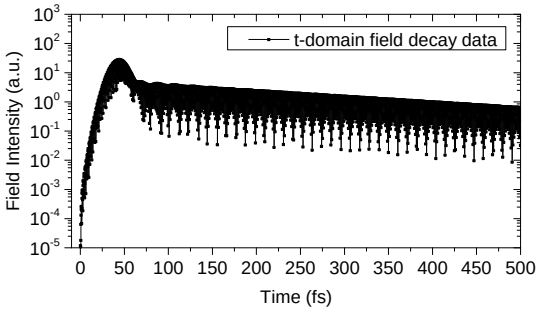

(c) T-domain data from a q=2 cavity where the cavity and non-cavity portion overlaps each other.

Figure 4.6: Illustration of the dividing line between the 'cavity photon' and the non-cavity photon' temporal groups: **(a)** the time signal of the initial dipole pulse; the corresponding t-domain data from **(b)** a q=16 long cavity and **(c)** a q=2 short cavity. The actual field decay time is much longer than the plotted time axes.

These two photon groups have a same emission rate determined by the LDoS modification

but their emission pattern differs massively. Hence they should be treated with two separate sub-simulations where the two are distinguished in t-domain as illustrated in fig. (4.6)(b). The cut-off threshold of t= 100fs is chosen to be slightly larger than the 90fs dipole pulse.

In fact, the cut-off threshold is often not clear especially for short cavity lengths. Figure (4.6)(b) is extracted from a q=16 cavity with a 68fs round-trip time which is longer than half of the dipole pulse. As a result, a small revival peak at t= 45+68 ≈ 110fs and the start of main cavity decay at t= 45+68×2 ≈ 170fs are observed in fig. (4.6)(b). In contrary, fig. (4.6)(c) is extracted from a q=2 cavity with a 9fs round-trip time. Hence overlap between the two photon groups is inevitable.

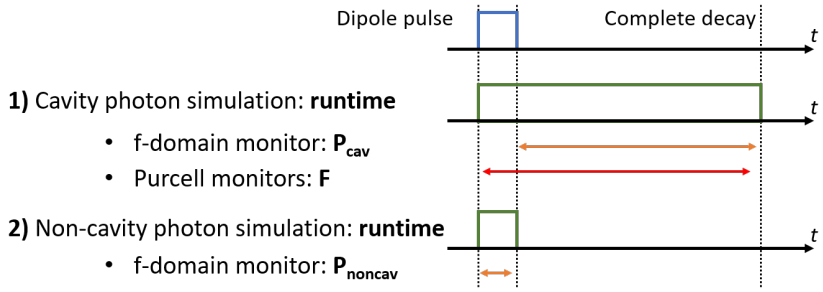

Figure 4.7: The simulation timeline comparison between the cavity and non-cavity sub-simulations.

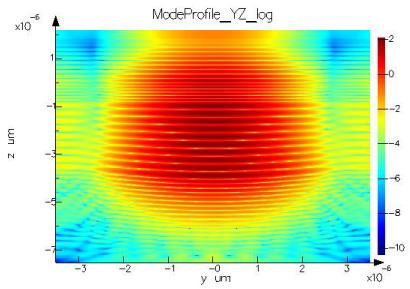

(a) Field profile of the cavity photon group.

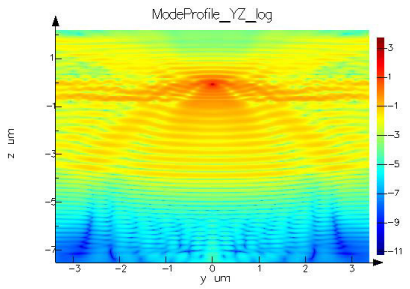

(b) Field profile of the non-cavity photon group.

Figure 4.8: Field profile of the simulation region for **(a)** the cavity photon group from the main simulation and **(b)** the non-cavity photon group from the secondary simulation.

The simulation timelines for each sub-simulation is illustrated in fig. (4.7). The cavity-photon sub-simulation is ran till a complete field decay within the simulation region. The f-domain monitors are time-gated for t>100fs to record the emission pattern of the resonant mode as shown in fig. (4.8)(a). The Purcell monitors does not need to be time-gated. The obtained emission enhancement F^{dev} represents LDoS modification imposed

by the cavity structure and it applies to both cavity and non-cavity photons alike. The non-cavity photon sub-simulation is ran until t=100fs and the emission pattern by the f-domain monitors is shown in fig. (4.8)(b) where the dipole location is visible at the center of the cavity.

4.3.2 Spatially-Resolved Collection Analysis

The photon loss mechanism from the simulation region is analyzed by dividing the photon emission into three spatial loss channels as illustrated in fig. (4.9): transmission through the planar mirror, transmission through the featured mirror and 2D guided mode loss in lateral directions.

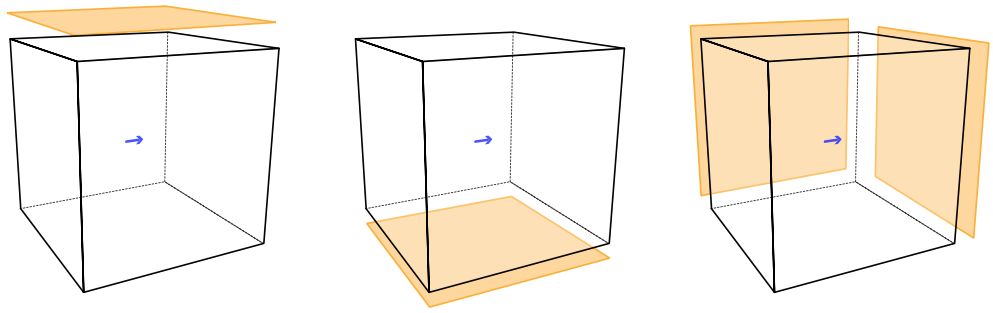

(a) Planar mirror transmission.

(b) Featured mirror transmission.

(c) 2D guided mode loss in lateral directions.

Figure 4.9: Monitors associated with each spatial loss channels.

The channel-dependent photon losses can be written either as a percentage of device dipolepower η_{ch} (unit: $\%P^{\text{dev}}$), or as an absolute power term P_{ch} (unit: $\%P^0$). The sourcepower P^0 and the dipole power P^{dev} are related by eq. (4.6).

This loss channel approximation is deemed reasonable because most of the photonic modes of interest propagate in orthogonal directions with respect to the cavity axis. A template of collection efficiency η analysis is shown in table (4.3). Because the 'useful' photons are collected via the planar mirror transmission, η_{plan} shall be maximized.

To reflect the external collection optics in experiment (an NA=0.8 air objective lens), the far-field data of the planar mirror monitor in fig. (4.9)(a) is analyzed to yield a far-field collection efficiency $\eta_{\text{plan}}^{\text{NA}}$. The ZPL collection efficiency $\eta_{\text{zpl}}^{\text{dev}}$ for a given device is then

written as:

$$\eta_{\text{zpl}}^{\text{dev}} = \sum \eta_{\text{plan}} \times \eta_{\text{plan}}^{\text{NA}} \tag{4.7}$$

where the summation includes the contribution from both the cavity and non-cavity photon groups whenever applicable.

	All η	η_{guid}	η_{feat}	η_{plan}	$\eta_{\text{plan}}^{\text{NA}}$	$\eta_{\text{zpl}}^{\text{dev}}=\eta_{\text{p}}\eta_{\text{p}}^{\text{NA}}$	$F_{\text{zpl}}^{\text{dev/0}}$	$P_{\text{out}}^{\text{dev}}$
Unit:	($\%P^{\text{dev}}$)				($\%\eta_{\text{plan}}$)	($\%P^{\text{dev}}$)	(P^{dev}/P^{0})	($\%P^{0}$)
Non-cav	14.02	12.18	0.00	1.84	76.11	1.40	-	-
Cav	85.98	52.56	0.30	33.12	100	33.12	-	-
Sum	100	64.74	0.30	34.96	-	34.52	2.524	87.12

Table 4.3: A template of collection analysis and emission analysis for a given simulation structure. The contributions from both cavity photon and non-cavity photon are considered. The emission enhancement F and ZPL photon output P are also included.

Among the three spatial loss channels, particular attention is paid to the 2D guided mode loss (see fig. (4.8)) because its information is not available from 1D analytical approaches. In order for the energy in the fundamental mode to leak through the 2D guided modes, some transverse coupling is required. One likely scenario of this kind has been demonstrated in fig. (2.21) where the fundamental mode of index q family couples to the higher-order TEM modes of index $q-1$ family when their resonance conditions match. These TEM modes of index $q-1$ family has strong transverse components, hence they couples to 2D guided loss modes efficiently. The involvement of these TEM modes can be suppressed by reducing the width of cavity feature, but this can undermine the lateral confinement of the fundamental mode as will be shown in section (4.5.1).

The relative magnitudes between η_{ch} terms are very sensitive to a number of cavity geometric parameters combined. This makes it very difficult to analytically analyze the spatial distribution of photon loss. For exactly this reason, numerical method like FDTD simulation is well-suited for the purpose.

4.3.3 Predicting Observable Enhancement of Photon Output

In cavity-coupled NV experiments, the performance of the membrane-in-cavity device is quantified by comparing the NV ZPL emission in- and out-cavity. To avoid the confusion

when using the term 'free-space', the three main characterization configurations are illustrated in fig. (4.10). In our experiments, the ZPL photon output are compared between the on-mirror and in-cavity configurations.

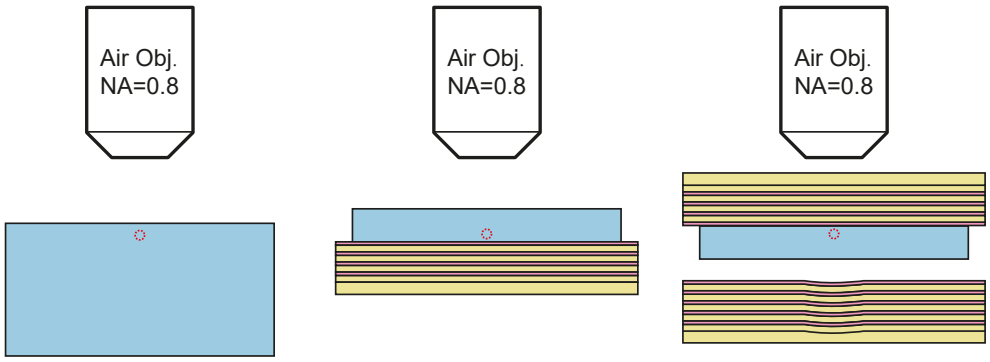

(a) Free-space. **(b)** On-mirror. **(c)** In-cavity.

Figure 4.10: Experimental configurations corresponding to different dielectric environment: (a) the free-space bulk configuration; (b) the membrane-on-mirror configuration; (c) the membrane-in-cavity configuration (including the on and off-resonance scenarios).

To unify the emission analysis and the collection analysis as set out in previous sections, we write the ZPL photon output power $P_{\text{out}}^{\text{dev}}$ of a given simulated structure as:

$$P_{\text{out}}^{\text{dev}} = \eta_{\text{zpl}}^{\text{dev}} \times P^{\text{dev}} = \eta_{\text{zpl}}^{\text{dev}} \times P^{0} \times F^{\text{dev}} \tag{4.8}$$

Using eq. (4.8), the on-mirror and in-cavity ZPL output are written as:

$$\begin{aligned} P_{\text{out}}^{\text{dev}} &= P^{0} \times F^{\text{dev}} \times \eta_{\text{zpl}}^{\text{dev}} \\ &= P^{0} \times F^{\text{dev}} \times (\eta_{\text{cav,plan}} \times \eta_{\text{cav,plan}}^{\text{NA}} + \eta_{\text{noncav,plan}} \times \eta_{\text{noncav,plan}}^{\text{NA}}) \end{aligned} \tag{4.9a}$$

$$\begin{aligned} P_{\text{out}}^{\text{mir}} &= P^{0} \times F^{\text{mir}} \times \eta_{\text{zpl}}^{\text{mir}} \\ &= P^{0} \times F^{\text{mir}} \times \eta \times \eta^{\text{NA}} \end{aligned} \tag{4.9b}$$

The relative ZPL output enhancement $P_{\text{out}}^{\text{dev/mir}}$ between the on-mirror and the in-cavity configurations is simply given by:

$$P_{\text{out}}^{\text{dev/mir}} = \frac{P_{\text{out}}^{\text{dev}}}{P_{\text{out}}^{\text{mir}}} = \frac{F^{\text{dev}}}{F^{\text{mir}}} \left(\frac{\eta_{\text{cav,plan}} \times \eta_{\text{cav,plan}}^{\text{NA}} + \eta_{\text{noncav,plan}} \times \eta_{\text{noncav,plan}}^{\text{NA}}}{\eta_{\text{bot}} \times \eta_{\text{bot}}^{\text{NA}}} \right) \tag{4.10}$$

Although $P_{\text{out}}^{\text{mir}}$ is generally a constant for a given membrane thickness and DBR mirror

design. Therefore, the trend in $P_{\text{out}}^{\text{dev}}$ is usually representative of the trend in $P_{\text{out}}^{\text{dev/mir}}$ unless changes are made to the dielectric environment. To maximize $P_{\text{out}}^{\text{dev/mir}}$, we focus on improving $P_{\text{out}}^{\text{dev}}$ which comes down to increasing the emission enhancement F^{dev} and the collection through the planar mirror η_{plan} .

4.4 Simulation Figure of Merits

4.4.1 Emission Enhancement Factor

In this work, the dipole emission enhancement F is quantified in two ways. The first method utilizes the device-dependent dipolepower P^{dev} and the free-space dipole source-power P^0 given by the Purcell monitors:

$$F_{\text{pow}} = \frac{P^{\text{dev}}}{P^0} \qquad \text{(eq. (4.6) revisit)}$$

. Because the Purcell monitors directly record the dipole emission powers, F_{pow} is reliable as long as the simulation runs till a complete field decay.

The second method of obtaining F uses the Purcell equation introduced in section (2.2.3) in a semi-analytical way:

$$F_{\text{semi}} = \xi^2 \frac{3}{4\pi^2} \frac{Q}{V} \left(\frac{\lambda}{n_{\text{dp}}} \right)^3 \frac{n_{\text{dp}}^2 |\mathcal{E}_{\text{dp}}|^2}{\max\left(n^2 |\mathcal{E}|^2\right)} \qquad \text{(eq. (2.19) revisit)}$$

where ξ^2 is the dipole orientation factor, Q is the cavity quality factor, V is the mode volume, n_{dp} and $\mathcal{E}_{\text{dp}}$ are the refractive index and electric field amplitude at the dipole position. In this work, the dipole is always placed at the anti-node position and parallel to x-y plane hence ξ^2 equals to unity. All the other contributing terms in eq. (2.19) can be obtained numerically.

Between F_{pow} and F_{semi}, F_{pow} is usually the one quoted as F in this work due to its reliability. The calculation of F_{semi} has a major drawback in its accuracy due to the various contributing terms. The largest error comes from the numerically integrated mode volume V_{int} which is typically an overestimation (more in section (4.4.4)). As a

result, F_{semi} is often an underestimation of the true enhancement factor. That being said, F_{semi} is still routinely calculated as a reference for troubleshooting.

4.4.2 Cavity Quality Factor

A standard definition of cavity quality factor Q for a resonant mode is given by:

$$Q = \frac{\omega_0}{\delta\omega} \qquad \text{(eq. (2.41) revisit)}$$

where ω_0 is the centre frequency and $\delta\omega$ is the FWHM linewidth. In principle, $\delta\omega$ can be obtained from either the f-domain data or the Fourier-transformed t-domain data. However, the f-domain data in FDTD is defined by a coarse frequency axis which is incapable of resolving linewidth of high-Q cavity mode without exhausting computational resources. The accurate determination of $\delta\omega$ from Fourier-transformed t-domain data (fig. (4.11)(c)) is also not straightforward and is inefficient under large workload.

Alternatively, the definition of Q as the power dissipation rate of the system ([87]) is used. Satring with t-domain signal $\mathcal{E}(t)$, its Fourier-transformed f-domain form is written as:

$$\mathcal{E}(t) = e^{-t(\alpha - i\omega_0)} \tag{4.11a}$$

$$|\mathcal{E}(\omega)|^2 = \frac{1}{\alpha^2 + (\omega - \omega_0)^2} \tag{4.11b}$$

where α is the decay constant. From eq. (4.11b) it is easy to obtain the FWHM of the resonance in f-domain as $\delta\omega = 2\alpha$. Substitute this into eq. (2.41) we find $\alpha = \omega_0/2Q$. Re-writing the t-domain expression from eq. (4.11a) in log form and substitute α in terms of Q:

$$\log_{10}(|\mathcal{E}(t)|) = \frac{-\omega_0 t}{2Q}\log_{10}(e) = mt \tag{4.12}$$

where m is the linear slope fitted to $\log_{10}(|\mathcal{E}(t)|)$ the simulated t-domain data. With some rearrangement the expression for Q in terms of m is given by:

$$Q = \frac{-\omega_0 \log_{10}(e)}{2m} \tag{4.13}$$

In practice, the raw t-domain data is firstly Fourier-transformed to f-domain. The target resonance peak is picked out using a Gaussian filter with a width that is larger than a coarsely estimated mode width $\delta\omega$. This ensures that the cavity mode spectrum in f-domain is not over-cropped and the real width of the cavity mode can be extracted. The data is then inversely Fourier-transformed back to the t-domain. The slope of $\log_{10}(|\mathcal{E}(t)|)$ is then extracted to obtain the quality factor Q. The full process are plotted in fig. (4.11)(a)-(c).

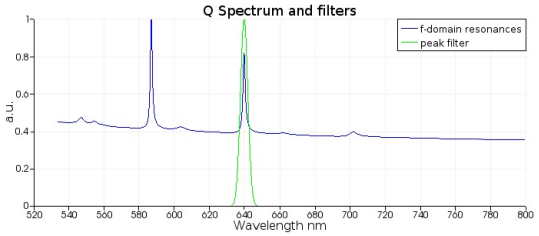

(a) The f-domain data and the Gaussian peak filter.

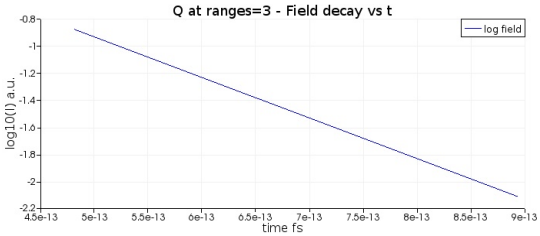

(b) The $\log_{10}(|\mathcal{E}(t)|)$ plot of the selected portion of t-domain data in log scale.

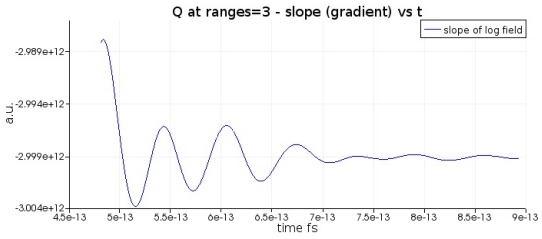

(c) The slope of $\log_{10}(|\mathcal{E}(t)|)$ showing a beating behavior.

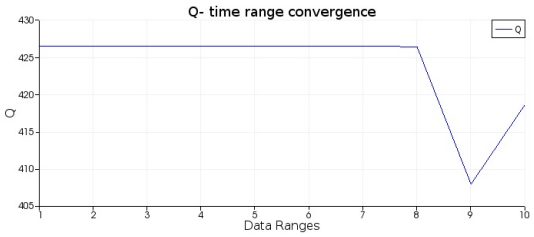

(d) The convergence behaviour of Q as a function of data range setting.

Data Range Setting	1	2	3	4	5	6	7	8	9	10
Lower Bound (%)	45	40	35	30	25	20	15	10	5	0
Upper Bound (%)	55	60	65	70	75	80	85	90	95	100

(e) Processing ranges of the t-domain data which is included in the analysis after the application of the Gaussian filter.

Figure 4.11: An example of a stable Q convergence test on the t-domain data range.

The Gaussian filtering inherently includes some undesirable modes which induce a beating behaviour, as shown in fig. (4.11)(c). The Gaussian filter also introduces error at the end of the t-domain signal after the inverse Fourier-transform. To address these problems, a convergence test of the processing range of t-domain data is always in place to make sure a sufficiently large proportion of t-domain data is used to overcome the beating frequency, but not so large that the errors at the end of the time signal are included.

The data range settings of the Q convergence test are listed in fig. (4.11)(e) and an

example of Q convergence is plotted in fig. (4.11)(b). An unstable Q convergence curve might occur when there are multiple strong resonant modes in close vicinity, leading to a difficulty in overcoming the beating effect just by changing the data range.

The Q calculations in this work are all treated with the slope calculation method due to its reliability. In this method, the FWHM linewidth of the resonance peak is not directly used to obtain Q but as a parameter of the Gaussian filter. This removes the requirement of obtaining accurate FWHM data and improves the robustness of Q. This method is also advantageous in early-stage simulations where only Q is of interest, and it can be obtained without the need to run the simulation till a complete decay.

4.4.3 Cavity Finesse and Round-Trip Loss

Another parameter that is closely related to Q is the cavity finesse $\mathcal{F}$:

$$\mathcal{F} = \frac{Q}{q} \qquad \text{(eq. (2.34) revisit)}$$

where q is the cavity mode index. Compared to Q, $\mathcal{F}$ is more closely related to emission enhancement because in the Purcell equation, both Q and V scale with cavity length.

Given $\mathcal{F}$, the round-trip cavity loss $\mathcal{L}_{\text{lin}}$ is coarsely estimated as:

$$\mathcal{L}_{\text{lin}} = \frac{2\pi}{\mathcal{F}} \qquad \text{(eq. (2.39) revisit)}$$

Combining with the channel-dependent collection efficiency η_{ch}, the channel-dependent ppm loss is obtained as $\mathcal{L}_{\text{ch}} = \mathcal{L}_{\text{lin}} \times \eta_{\text{ch}}$. We do note again that eq. (2.39) should be used with caution due to its compromised accuracy for low-Q cavities (see fig. (2.11)(a)).

4.4.4 Calculating Mode Volume

Mode volume V is the other key parameter in the Purcell equation and one of its standard definitions is given by:

$$V = \frac{\int \epsilon(\mathbf{r})|\mathcal{E}(\mathbf{r})|^2 d^3\mathbf{r}}{\max\left(\epsilon(\mathbf{r})|\mathcal{E}(\mathbf{r})|^2\right)} \qquad \text{(eq. (2.20) revisit)}$$

where $\mathcal{E}(\mathbf{r})$ and $\epsilon(\mathbf{r})$=$n(\mathbf{r})^2$ are the electric field amplitude and the dielectric constant at the position $\mathbf{r}$. The normalization factor in the denominator follows the energy density product convention introduced in section (2.2.3).

It is possible to obtain the mode volume integral in eq. (2.20) by directly integrating a 3D f-domain monitor. However, such an integral is very computationally burdening because of the 4D matrix data. Instead, one can utilize the cylindrical symmetry (fig. (4.12)(a)) of the cavity device and convert eq. (2.20) into a double integral:

$$V_{\text{int2D}} = \frac{\int_0^{r_{max}} \int_{z_{min}}^{z_{max}} 2\pi r \epsilon(\mathbf{r,z}) |\mathcal{E}(\mathbf{r,z})|^2 dz dr}{max\left(\epsilon(\mathbf{r,z}) |\mathcal{E}(\mathbf{r,z})|^2\right)} \tag{4.14}$$

where dz and dr are the mesh cell sizes which do not necessarily follow a linear scale due to the build-in mesh optimization process by the FDTD software.

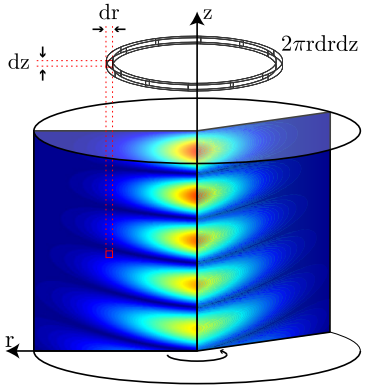

(a)

q	V_{int3D} (μm^3)	V_{int2D} (μm^3)	$\Delta\%$
1	0.136	0.133	1.9
2	0.205	0.202	1.8
3	0.298	0.288	3.2
4	0.447	0.429	4.0
5	0.672	0.665	1.1

(b) V_{int} as a function of the cavity mode number q.

Figure 4.12: Illustration of cylindrical symmetry used for mode volume approximation.

To account for the two-fold dipole symmetry, an averaged 2D profile from both x-z and y-z cross-sections is used to calculate V_{int2D}. Figure (4.12)(b) shows a validation test within our computational power to compare V_{int3D} and V_{int2D} as a function of q. A decent agreement between the two is observed.

We note that V_{int} is always an overestimation because it concerns all modes at a given frequency without spatially discriminating between resonant and non-resonant modes. This is especially problematic if the planar part of the cavity extends further because of the associated 2D guided modes. In addition to V_{int}, one can also substitute the calculated

F and Q into the Purcell equation in eq. (2.19) to reversely estimate the effective mode volume V_{eff} that is responsible for the enhancement observed.

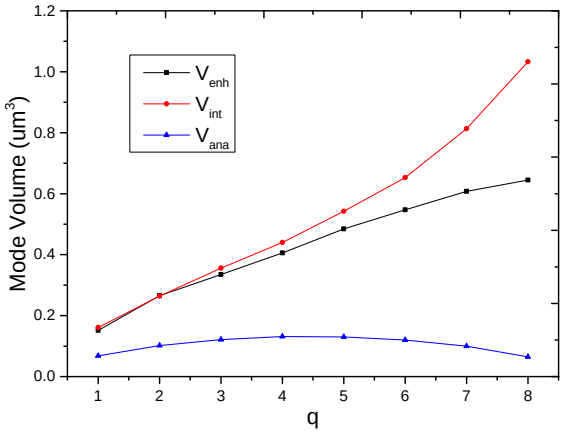

Figure 4.13: A comparison between mode volume by integration V_{int}, mode volume by enhancement V_{eff} and mode volume by Gaussian mode analysis V_{ana} for a $\mathcal{R}$=3µm cavity.

The simulated V_{int} and V_{eff} are plotted in fig. (4.13) along with the analytical mode volume V_{ana} from section (2.3.6). V_{int} and V_{eff} matches well for small q but diverges for larger q due to the growing contribution from 2D modes. V_{ana} has much lower values because it does not consider mirror penetration depth. Generally speaking, V_{int} is more useful for visualizing the spatial extend of the mode while V_{eff} gives more precise estimate of the DBR penetration.

4.5 Single-Medium Air Cavity

In this section, the established analysis protocol is applied to single-medium air cavities, and the influence of cavity parameters on cavity performance is investigated. The conclusions from this section are transferable to the discussion of membrane-in-cavity setup in section (4.6).

4.5.1 Depth of Cavity Feature: 0D-2D Interaction

The cavity depth L_{depth} determines the smallest achievable cavity length. It also modulates the interaction between the on-axis 0D modes and 2D guided modes between the planar part of the cavity mirrors. L_{depth} is usually minimized in fabrication in order to

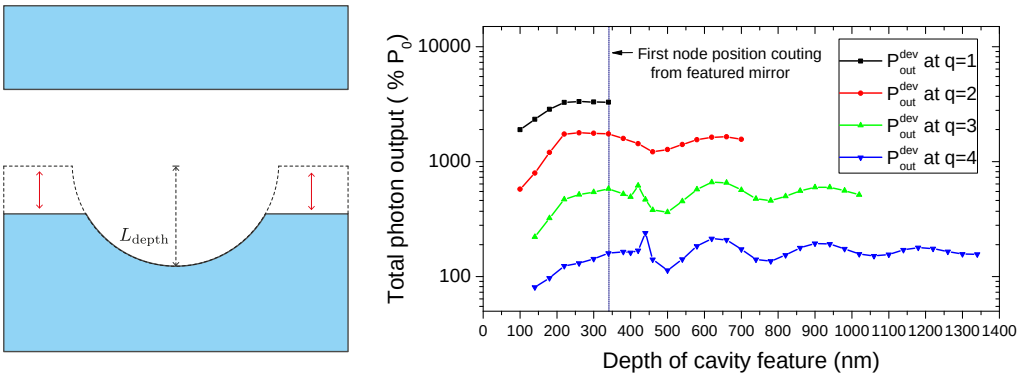

(a) **(b)**

Figure 4.14: **(a)** A schematic illustration of L_{depth} dependence investigation. **(b)** Summary of data obtained from a radius of curvature $\mathcal{R}$=2µm cavity at cavity length of q=1 to 4 while varying L_{depth}. Plot is in log scale for better visualization.

achieve small V, but too shallow a cavity feature can obviously lead to insufficient lateral confinement which is not desirable either.

Figure (4.14)(b) shows the ZPL photon output $P_{\text{out}}^{\text{dev}}$ of a $\mathcal{R}$=2µm cavity as L_{depth} is varied from 100nm to the full cavity length for q from 1 to 4. Bad cavity performance is observed for L_{depth}<200nm due to the reason mentioned above.

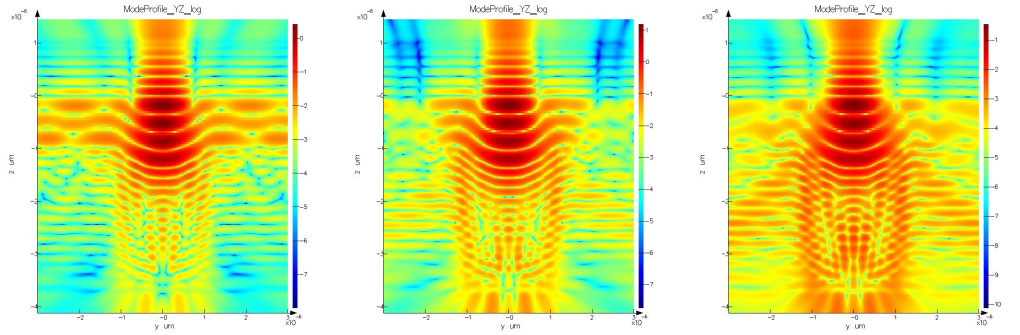

(a) Profile at L_{depth}= 380nm. **(b)** 0D-2D hybridization at L_{depth}= 420nm. **(c)** Profile at L_{depth}= 480nm.

Figure 4.15: The cavity mode cross-section profile for the $\mathcal{R}$=2µm q=4 cavity at **(a)** the short-cavity and **(b)** the long-cavity limit.

At $L_{\text{depth}}\approx$ 420nm, $P_{\text{out}}^{\text{dev}}$ peaks are present in the q=3 and 4 dataset. This is attributed to a localized 0D-2D hybridization mode whose mode profile is plotted in fig. (4.15)(b). Although the hybridized mode induced some performance boost, it is a rather transient feature and its far-field emission pattern does not couple well into external optics.

Around the same L_{depth}, it is also observed that the cavity loss mechanism switches from

P_{lat}-dominant to P_{feat}-dominant with increasing L_{depth} as shown in fig. (4.15)(a)(c). Using this observation we distinguish between shallow/deep-cavity with a threshold L_{depth} at around 400nm.

In the region between L_{depth}= 300-400nm, $P_{\text{out}}^{\text{dev}}$ reaches its first local maxima (except the hybridization peaks). This corresponds to the first node position from the featured mirror whose exact position varies slightly for different q because of the Gaussian Guoy phase shifts. Given that $P_{\text{out}}^{\text{dev}}$ does not exhibit a significantly higher value for L_{depth} >400nm, we set L_{depth}= 325nm as a default for all other simulations in this chapter.

4.5.1.1 Modulation of 2D Guided Modes

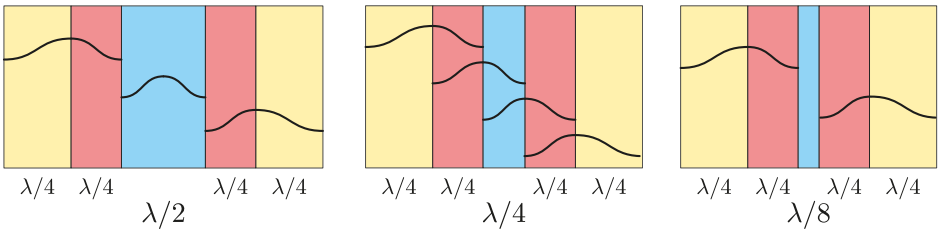

Figure 4.16: Illustration of the supported guided modes in a multi-layer structure for $L_{2\text{D}}$= $\lambda/2$, $\lambda/4$ and $\lambda/8$. The $\lambda/2$ intra-cavity layer supports the most guided modes whereas in the $\lambda/8$ case half of the guided modes are not supported. The $\lambda/4$ layer combines with DBR layers to support guided modes.

For L_{depth} >400nm, $P_{\text{out}}^{\text{dev}}$ in fig. (4.14)(b) shows a modulation behaviour which we attribute to the presence of 2D guided modes between the planar part of the cavity mirrors. The oscillation period of ≈317nm agrees with the planar-planar cavity resonance condition of $L_{2\text{D}}$=$q_{2\text{D}}\lambda/2$. More interestingly, the modulation maxima is found at the $\frac{1}{8}\lambda$ positions counting from the planar mirror. For example, for q=4 and L_{depth}= 650nm, the planar mirror separation is $L_{2\text{D}}$= 1373nm- 640nm= 753nm ≈ $1+\frac{1}{8}\lambda$.

	Period	Local max	Mid point	Local min	Mid point	Local max
$L_{2\text{D}}$	$\frac{1}{2}\lambda$	$(m+\frac{1}{8})\lambda$	$(m+\frac{1}{4})\lambda$	$(m+\frac{3}{8})\lambda$	$(m+\frac{1}{2})\lambda$	$(m+\frac{5}{8})\lambda$
$q_{2\text{D}}$	n	$n+\frac{1}{4}$	$n+\frac{1}{2}$	$n+\frac{3}{4}$	$n+1$	$n+1+\frac{1}{4}$

Table 4.4: A description of cavity performance modulation in terms of 2D planar separation $L_{2\text{D}}$ and 2D mode index $q_{2\text{D}}$. Both m and n are positive integers.

To explain this, we refer to the illustration in fig. (4.16) where the supported guided modes in a multi-layer structure are visualized. It is apparent that the multi-layer structure with a $\lambda/8$ intra-cavity layer supports less guided modes compared to those with a $\frac{1}{4}\lambda$ and $\frac{1}{2}\lambda$ intra-cavity layers. The $\frac{1}{4}\lambda$ layer forms guided modes with DBR layers and $\frac{1}{2}\lambda$ layer is an efficient guided loss channel on its own. Following this analysis, the modulation minima and maxima positions are given in table (4.4).

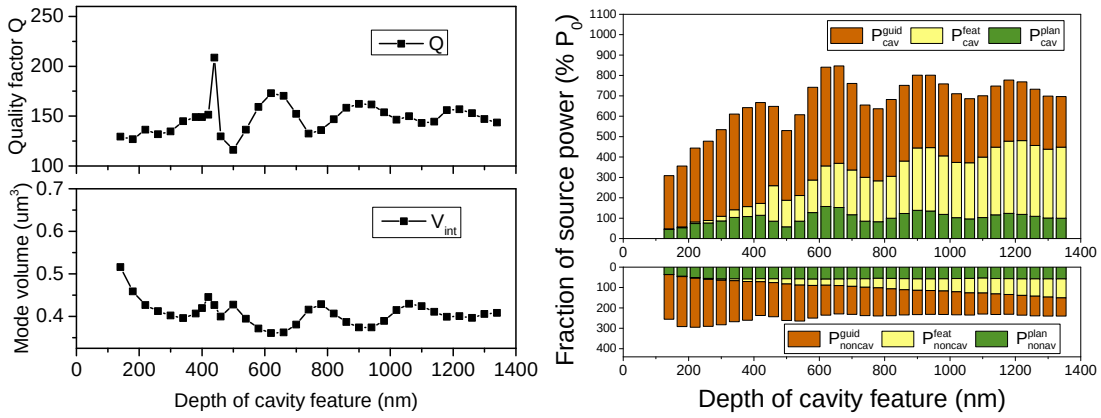

(a) Cavity figure of merits: quality factor Q and integrated mode volume V_{int}.

(b) Collection distribution -P_{ch}.

Figure 4.17: Plots showing the effect of mirror separation modulation extends to **(a)** cavity confinement capabilities and **(b)** photon collection distributions.

Plots in fig. (4.17) shows similar modulations as $P_{\text{out}}^{\text{dev}}$ in Q, V and most of the spatial loss channels. This confirms the particular importance of 2D guided modes in cavity analysis, especially for a DBR cavity. Such guided loss is expected to be even more prominent in a hybrid-medium cavities due to the channeling effect of the high-index diamond layer.

4.5.2 Cavity Length Tuning: Short- v.s. Long-Cavity Limit

The cavity length dependence investigation is perhaps most transferable to the daily operation of cavity experiments. Big efforts are often devoted to cavity mirror alignment such that a minimal cavity length can be achieved. The simulation results offer insights into the potential improvement in cavity performance that might be expected from for example pushing the cavity one q shorter. In this section we distinguish between short- and long-cavity based on differences in cavity performance.

Three cavities with $\mathcal{R}$=2, 3 and 4μm are simulated with q ranges from 1 to largest allowed

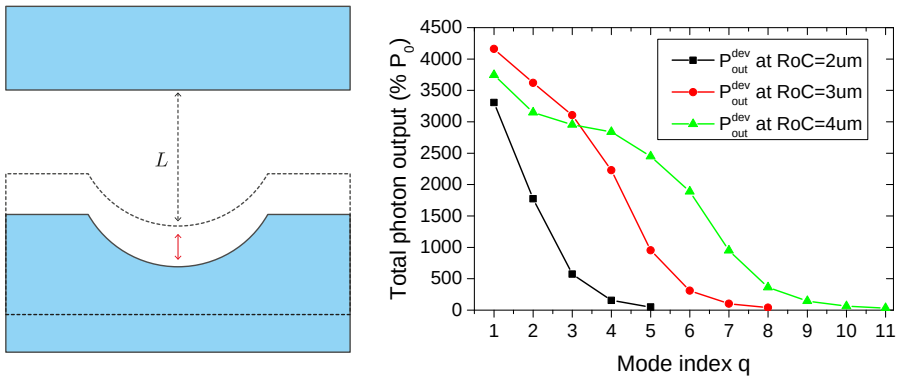

(a) **(b)**

Figure 4.18: **(a)** A schematic of cavity length q tuning and **(b)** the obtained $P_{\text{out}}^{\text{dev}}$ results.

cavity length q_{max}. The ZPL photon output $P_{\text{out}}^{\text{dev}}$ results are summarised in fig. (4.18)(b) where a peaking trend is observed.

The observed trend is best visualized by plotting Q and $\mathcal{F}$ in fig. (4.19) along with the expected values calculated using analytical description and TMM modeling (refer to section (2.3.5)). It is observed that Q peaks at $q_{\text{max}}/2$ and $\mathcal{F}$ is large than the $\mathcal{F}_{\text{ana}}$ for $q<q_{\text{max}}/2$. According to these characteristics, the cavity length of $q<q_{\text{max}}/2$ is assigned as the short-cavity limit (blue area) and $q>q_{\text{max}}/2$ is the long-cavity limit (pink area).

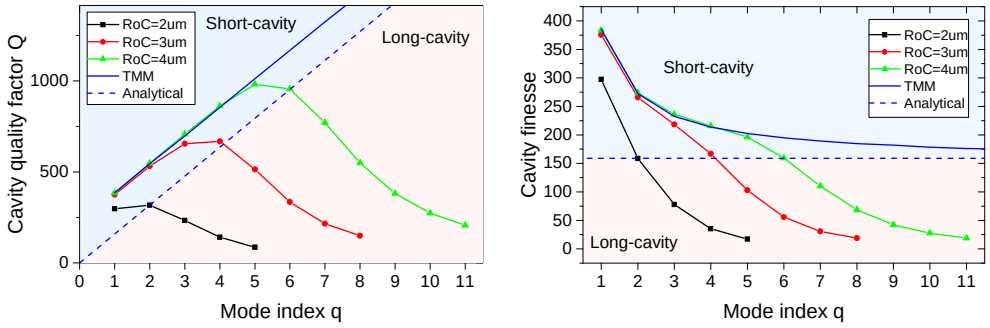

(a) Quality factor Q. **(b)** Cavity finesse $\mathcal{F}$.

Figure 4.19: The distinction between short- and long- cavity limit visualized in **(a)** cavity quality factor Q plot and **(b)** cavity finesse $\mathcal{F}$ plot. The TMM Q does converge towards the analytical Q in large q limit.

In the short cavity limit, the cavity performance is close to the lossless TMM model. For $q>q_{\text{max}}/2$ the guided mode loss starts to dominate over other loss mechanisms as shown in fig. (4.20)(a) and consequently the cavity performance start to degrade quickly. The trend in $P_{\text{out}}^{\text{dev}}$ in fig. (4.18)(b) certainly reflects the combined effect of the emission and the collection performance of the cavity.

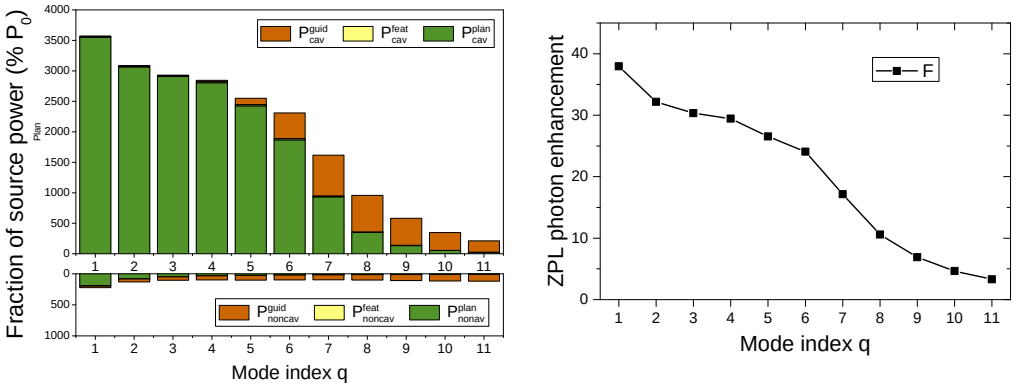

(a) Collection distribution -P_{ch}. **(b)** Emission analysis - F.

Figure 4.20: **(a)** Collection and **(b)** emission analysis of the $\mathcal{R}$=4μm cavity, as a function of mode index q.

In conclusion, we consider the distinction between short- and long-cavity a very practically useful finding. For experiments that requires high-Q, a cavity length of q= $q_{\mathrm{max}}/2$ is more desirable. For experiments that requires strong emission enhancement F^{dev}, short-cavity limit is always preferable.

We do also note that the $\mathcal{R}$=2μm cavity at q=1 is expected to outperform cavities with larger $\mathcal{R}$. Its under-performance is investigated in the next section.

4.5.3 Radius of Curvature: Beam Penetration and Coating Materials

4.5.3.1 Beam Focusing Effect in Short-Cavity Limit

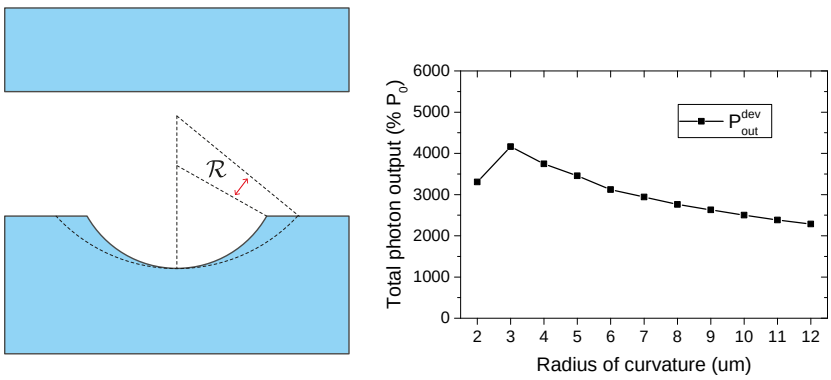

(a) **(b)**

Figure 4.21: **(a)** A schematic drawing of $\mathcal{R}$ and **(b)** the obtained $P_{\mathrm{out}}^{\mathrm{dev}}$ graph.

The total photon output $P_{\mathrm{out}}^{\mathrm{dev}}$ as a function of $\mathcal{R}$ from 2 to 12μm is plotted in fig. (4.21) for q=1 cavities. As expected, a general decreasing trend in $P_{\mathrm{out}}^{\mathrm{dev}}$ with increasing $\mathcal{R}$ is

observed due to weaker lateral confinement and increased mode volume. Most noticeably a 20% performance drop is observed for the $\mathcal{R}$=2µm cavity.

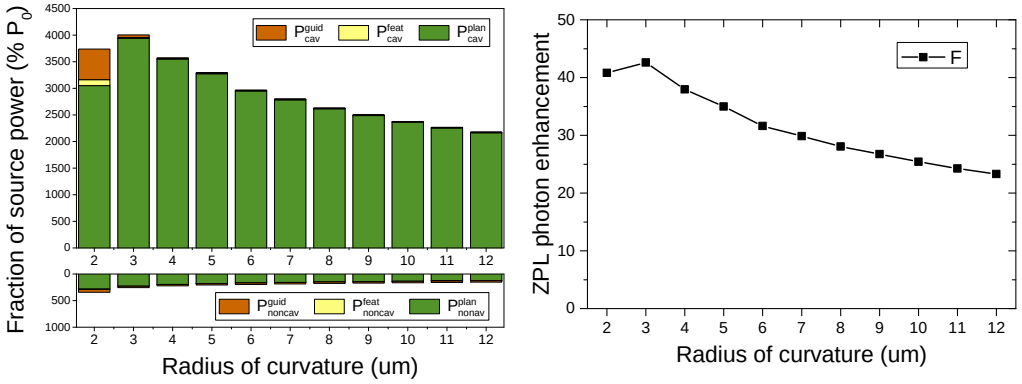

(a) Collection distribution -P_{ch}. **(b)** Emission analysis - F.

Figure 4.22: **(a)** The collection analysis in absolute photon collection P_{ch} and **(b)** the emission analysis F, both as a function of $\mathcal{R}$ for q=1 cavities.

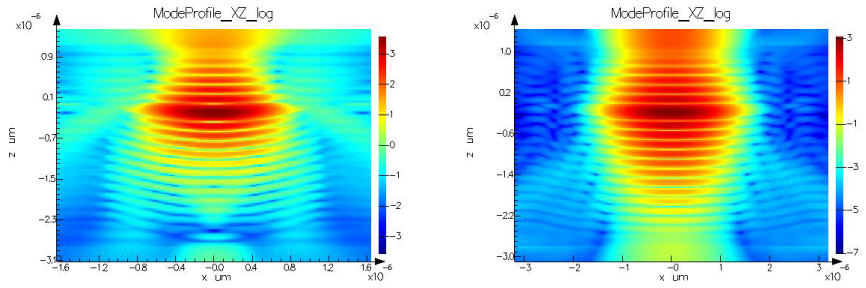

(a) Mode profile at $\mathcal{R}$=2µm. **(b)** Mode profile at $\mathcal{R}$=12µm.

Figure 4.23: The mode profiles of **(a)** the $\mathcal{R}$=2µm and **(b)** the 12µm cavities.

Detailed collection analysis shown in fig. (4.22) indicates that the $\mathcal{R}$=2µm cavity has extra cavity-photon loss through guided modes and its cavity emission enhancement is also lower. A stronger side-way scattering is observed for the $\mathcal{R}$=2µm compared to the 12µm cavities (fig. (4.23)). We attribute this observation at $\mathcal{R}$= 2µm, q=1 to a strong focusing effect which is best visualized by the energy density product profile in fig. (4.24).

Compared to the even energy distribution of the $\mathcal{R}$= 12µm simulation, the energy density maxima of the $\mathcal{R}$=2µm simulation is 'pushed' into the first pair of DBR coatings (red arrow in fig. (4.24)) which leads to two consequences. Firstly, it induces stronger lateral scattering due to the more efficient guiding in high-index DBR layers and the larger mode divergence angle at $\mathcal{R}$= 2µm. Secondly, it reduces the the energy density normalization

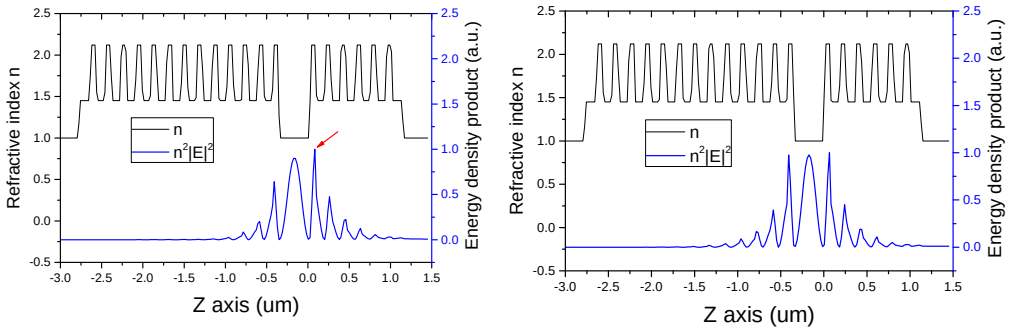

(a) Profile of $n^2|\mathcal{E}|^2$ at $\mathcal{R}$=2μm. **(b)** Profile of $n^2|\mathcal{E}|^2$ at $\mathcal{R}$=12μm

Figure 4.24: Comparison of the energy density product distribution for **(a)** $\mathcal{R}$=2μm and **(b)** 12μm. Note that the energy density maxima in the $\mathcal{R}$=2μm cavity is located within the DBR coating layers (red arrow).

factor in eq. (2.19):

$$\frac{n_{\text{dp}}^2|\mathcal{E}_{\text{dp}}|^2}{\max\left(n^2|\mathcal{E}|^2\right)}$$

This analysis essentially suggests that the Ta-Si coating system can not confine the field effectively at small $\mathcal{R}$ and q so a comparison is made against the Ti-Si system which has a higher index contrast. On-mirror simulations are first ran (data not shown) to calibrate the LDoS changes on different mirrors. The on-mirror ZPL photon output $P_{\text{out}}^{\text{mir}}$ are found to be $86.2\%P^0$ and $95.1\%P^0$ for Ta-Si and Ti-Si respectively. The difference is quite negligible.

The in-cavity results in fig. (4.25) confirmed that the Ti-Si system has a better performance compared to the Ta-Si system for all ranges of $\mathcal{R}$, especially at $\mathcal{R}$=2μm and q=1. The Ti-Si cavity does show slightly worse Q which is most likely due to stronger scattering at curved interfaces. But this is compensated by the small V thanks to the stronger field confinement.

The field penetration depth q_{pen} (in the unit of mode index q) is calculated by converging the simulated V to the analytical values V_{ana}:

$$V_{\text{ana}} = \frac{\pi w_0^2 L}{4} \qquad \text{(eq. (2.56) revisit)}$$

By adding q_{pen} worth of additional field penetration to L, V_{ana} is found to equal to V_{eff} when q_{pen} is $1.35q$ and $0.85q$ for the Ta-Si and Ti-Si cavities respectively. Note that these are guideline figures under the analytical Gaussian beam approximation to show

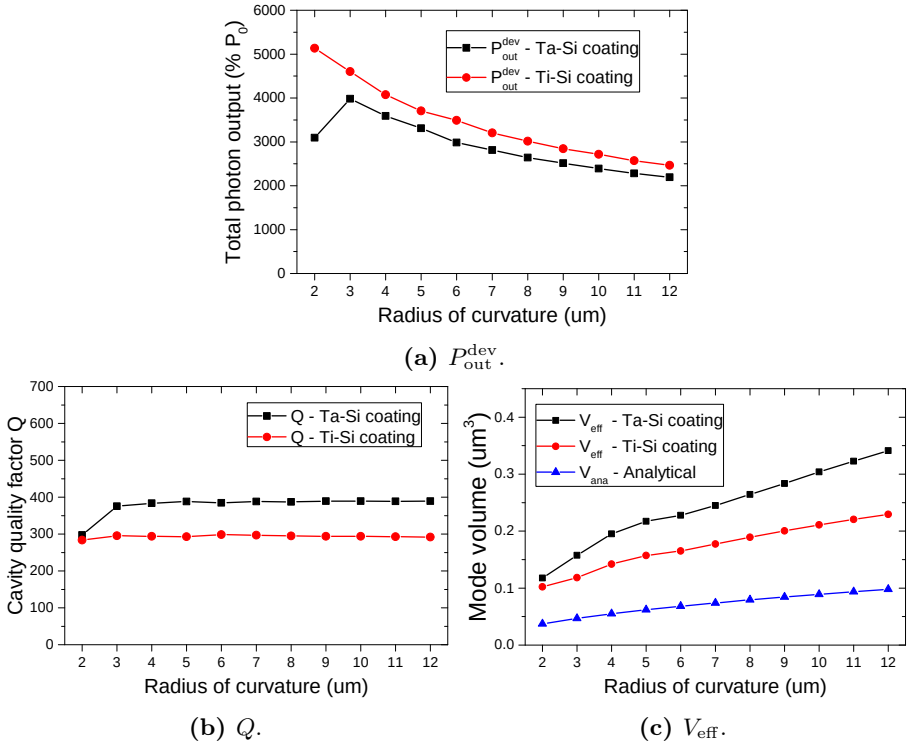

(a) $P_{\text{out}}^{\text{dev}}$.

(b) Q.

(c) V_{eff}.

Figure 4.25: Cavity simulation results of Ta-Si versus Ti-Si coating systems: **(a)** overall photon output $P_{\text{out}}^{\text{dev}}$, **(b)** quality factor Q and **(c)** mode volume V_{eff} in comparison with analytical model.

the relative size of field penetration between two coating systems. A better approach to find q_{pen} accurately is to analyze the field decay into the DBRs purely numerically in FDTD, which is not required here for the purpose of coating comparison.

Despite the promising properties of Ti-Si coating in theory, their real-world performance is limited by fabrication technology resulting in high absorption loss and sub-optimal index contrast.

4.5.3.2 Trends in Long-Cavity Limit

The $\mathcal{R}$ dependence investigation of a q=5 cavity in this section resembles experimental scenarios where the cavity length is limited by mirror clipping or an intra-cavity medium. An interesting trend is observed in fig. (4.26)(a) where $P_{\text{out}}^{\text{dev}}$ peaks at $\mathcal{R}$=4µm. This is explained if we recall the distinction we made between short/long-cavities by comparing q with $q_{\text{max}}/2$ for a given $\mathcal{R}$. The cavity is in the lossy long-cavity regime for $\mathcal{R}<$ 4µm because $q>$ $q_{\text{max}}/2$. This is confirmed by the extra collection loss (fig. (4.26)(b)) and lowered Q (fig. (4.27)(a)).

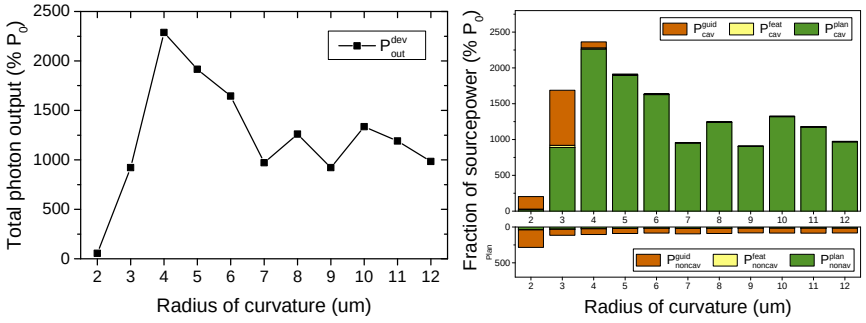

(a) **(b)**

Figure 4.26: **(a)** The ZPL photon output $P_{\text{out}}^{\text{dev}}$ and **(b)** the collection analysis P_{ch} for a medium/long cavity at q=5, as a function of $\mathcal{R}$.

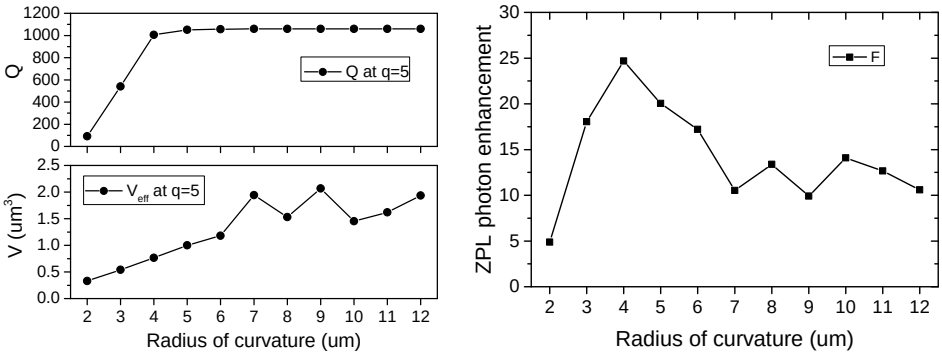

(a) **(b)**

Figure 4.27: **(a)** The cavity Q and V_{eff} and **(b)** the resulting emission enhancement F for a medium/long cavity at q=5, as a function of $\mathcal{R}$.

On the other hand, as $\mathcal{R}$ increases q_{max} becomes larger and the cavity enters the short-cavity regime. The quality factor saturates at intrinsic values but V continues to grow due to increasing $\mathcal{R}$. The combined trends of Q and V lead to a performance peak in $P_{\text{out}}^{\text{dev}}$ at $\mathcal{R}$= 4μm with $q_{\text{max}}/2 \approx 6$. This finding is especially useful in experimental conditions to determine the best choice of $\mathcal{R}$ for a given cavity length.

4.5.4 Mirror Reflectivity: Optimising Device Photon Output

Mirror reflectivity R tuning is the only intrinsic way to adjust the designed cavity finesse as pointed out by eq. (2.36). By adjusting R, the relative strength of loss channels changes accordingly. This affects both the cavity/non-cavity photon distribution as well as the channel-dependent loss distribution.

Firstly, the cavity ZPL output $P_{\text{out}}^{\text{dev}}$ is monitored as a function of the mirror DBR pairs

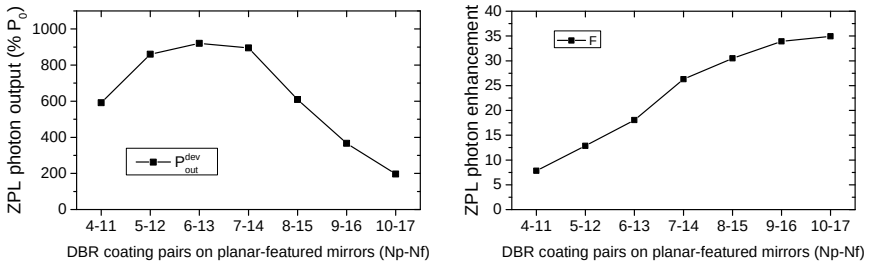

(a) **(b)**

Figure 4.28: **(a)** Device ZPL photon output $P_{\text{out}}^{\text{dev}}$ and **(b)** emission enhancement F analysis for a medium-sized (q=4 given q_{max}=9) $\mathcal{R}$=3μm cavity as a function of increasing DBR pairs N_{plan}-N_{feat}.

($N_{\text{plan}}/N_{\text{feat}}$) from 4/11 to 10/17 which corresponds to cavities with increasing Q. A medium-sized $\mathcal{R}$=3μm cavity at q=4 is used where the maximum supported mode index being q_{max}=9. It is observed that despite an increasing trend of emission enhancement F, $P_{\text{out}}^{\text{dev}}$ peaks at the 6-13 DBR pairs.

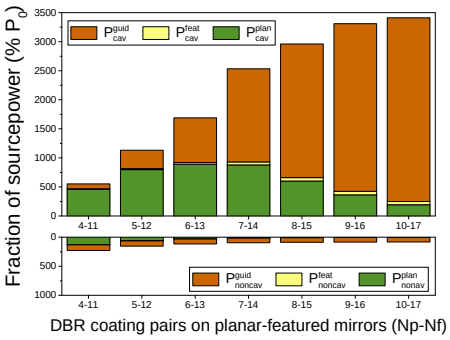

Figure 4.29: The channel-dependent cavity loss distribution in terms of absolute photon output P^{ch} for a medium-sized (q=4 given q_{max}=9) $\mathcal{R}$=3μm cavity as a function of increasing DBR pairs N_{plan}-N_{feat}.

This is explained by examining the channel-dependent loss distribution P^{ch} as plotted in fig. (4.29). Although the photon emission is greatly enhanced for the high-Q cavities, the amount of photon being collected through the planar mirror decreases drastically. This observation suggests that the benefit of emission enhancement is severely undermined when a strong loss channel such as P^{guid} is present. The photons that are rejected by the high-R mirrors are lost through the dominant 2D guided modes.

The cavity performance is also investigated by varying the mirror reflectivity asymmetry. The DBR pair on featured mirror is fixed at N_{feat}=13 and the planar DBR pair N_{plan} is varied from 2 to 12. Both a short-cavity (q=1) and a long-cavity (q=4) are simulated

and the ZPL output $P_{\text{out}}^{\text{dev}}$ are plotted in fig. (4.30)(a)(b). As expected, both cavity has a $P_{\text{out}}^{\text{dev}}$ peaking behaviour despite of the increasing F because of the collection distribution P_{ch} as shown in fig. (4.31).

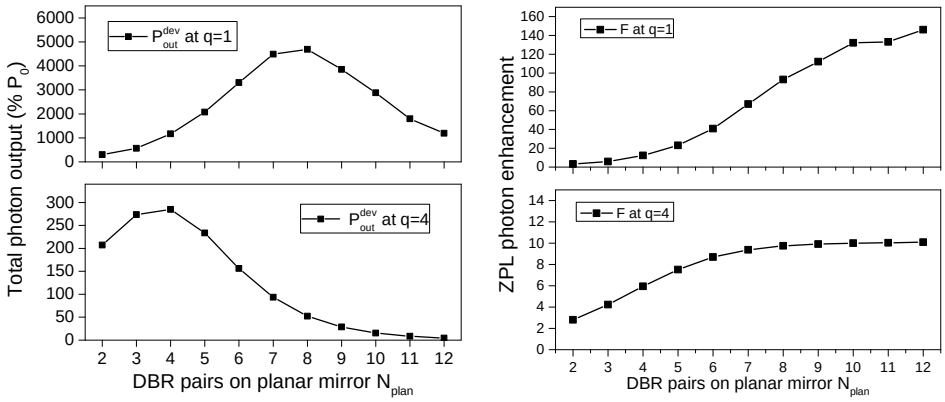

(a) $P_{\text{out}}^{\text{dev}}$ of both q=1 and 4 cavities. **(b)** F of both q=1 and 4 cavities.

Figure 4.30: Simulated **(a)** ZPL photon output $P_{\text{out}}^{\text{dev}}$ and **(b)** emission enhancement F from both the short- and long-cavity simulations as a function of N_{plan}.

More interestingly, $P_{\text{out}}^{\text{dev}}$ peaks at N_{plan}=8 for the q=1 cavity and N_{plan}=4 for the q=4 cavity. This can be explained by analyzing the relative strength of different loss channels. The q=4 cavity features a large mirror separation which supports a large amount of intra-cavity 2D guided modes. Therefore, the 2D guide mode loss becomes dominant for N_{plan}>5. On the contray, the q=1 cavity features limited intra-cavity 2D guided modes. Hence it relies on the intra-DBR 2D guided modes which is only switched on for high mirror R, i.e. N_{plan}>8.

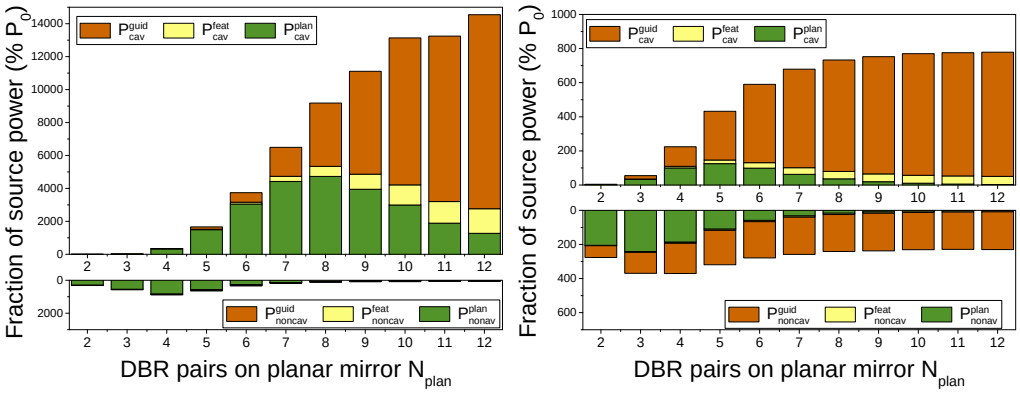

(a) P_{ch} distribution of a short-cavity. **(b)** P_{ch} distribution of a long-cavity.

Figure 4.31: Collection analysis in the **(a)** short-cavity and **(b)** long-cavity limit (q=4) while varying N_{plan}.

In conclusion, both investigations in this section demonstrate the importance of cavity

loss distribution analysis when optimizing cavity performance. Whenever a stronger loss mechanism is present, increasing cavity Q by increasing mirror R will reach a performance bottleneck due to increased channelling into the dominant loss mechanism (2D guided mode in our case).

In practice, the cavity loss through 2D guided modes is difficult to quantify experimentally. This again renders FDTD especially necessary for the analysis of Febry-Perot type cavities.

4.6 Hybrid-Medium Air-Diamond Cavity

The performance of the membrane-in-cavity setup is investigated. As established in section (2.4), depending on the membrane thickness t_d, a hybrid-medium cavity supports either a diamond-like mode ($q_\mathrm{d}= m+0.5$) or an air-like mode ($q_\mathrm{d}= m$) where q_d is the diamond mode index and m is an integer.

The focus is to firstly compare the cavity performance between the air-like and diamond-like modes. Most of the conclusions from single-medium cavity simulations in section (4.5) are transferable to the analysis of hybrid-medium cavities.

Next, the analytical resonance condition of the hybrid-medium cavity from section (2.4) is verified by fitting a simulated cavity mode map and t_d can be accurately determined. This is especially useful for real experiments because optical interferometry measurement is inaccurate when the membrane is placed on a DBR mirror, and profilometry measurement overestimates t_d since DBR mirror surrounding the membrane is also etched.

4.6.1 Dipole Emission in Free-Standing Membrane

Because the presence of a diamond membrane changes the local photonic density of states at the dipole location, on-mirror simulations are firstly ran to verify the change in dipole emission rate. Free-standing membranes with thickness of q_d=1 and q_d=1.5 are simulated and the dipole source is placed 66nm below the top surface. The collection and emission analysis are both summarised in fig. (4.32)(c). Compared to the free-space dipole emission demonstrated in section (4.5.3.1), the channeling effect of the diamond membrane greatly

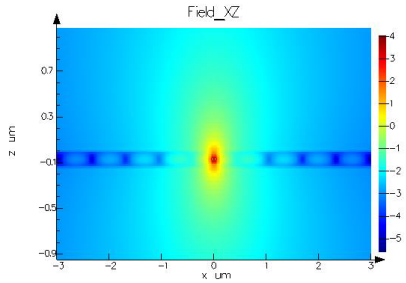

(a) Emission profile of a q_d=1 diamond membrane without DBR mirror.

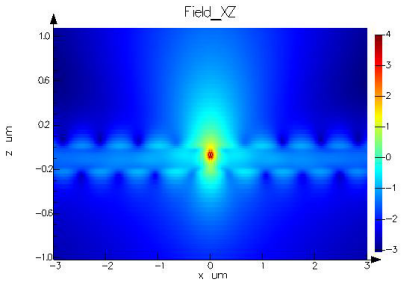

(b) Emission profile of a q_d= 1.5 diamond membrane without DBR mirror.

	Total	η_{guid}	η_{bot}	η_{top}	η_{bot}^{NA}	η_{top}^{NA}	F^{mir}	$P_{out,bot}^{mir}$	$P_{out,top}^{mir}$
Unit:		($\%P^0$)			($\%$)			($\%P^0$)	($\%P^0$)
q_d=1	100	93.65	3.27	3.08	77.79	83.50	0.907	2.20	2.22
q_d=1.5	100	90.82	2.00	7.18	67.72	88.24	1.038	1.25	5.86

(c) Collection and emission analysis at 637nm.

Figure 4.32: Free-standing membrane simulations with membrane thickness at q_d=1 and q_d=1.5. The total photon output P_{out} is calculated for both top and bottom collection.

reduced the photon collection in both the top and bottom directions. The photon output P_{out} is only around 2-5$\%P^0$ in both simulations which is way lower than that of an on-mirror free-space dipole (>80$\%P^0$). The difference between a q=1 and q=1.5 membrane is fairly negligible.

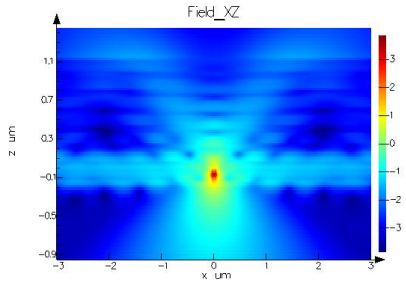

(a) Emission profile of a q_d=1 membrane on mirror.

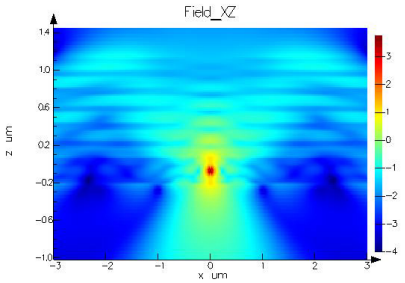

(b) Emission profile of a q_d= 1.5 membrane on mirror.

Figure 4.33: **(a)-(b)** The dipole emission profile of the q_d=1 and q_d=1.5 diamond membrane on a DBR mirror.

Next membrane-on-mirror simulation are carried out for both membrane thicknesses and the resultant emission profiles are shown in fig. (4.33)(a)(b). A clear difference in emission pattern is observed. The strongest loss channel for the q_d=1 membrane is the 2D guided mode in the diamond layer while in the q_d=1.5 simulation guided modes are supported mainly in the DBR layers. This observation is consistent with description in fig. (4.16).

	Total	η_{guid}	η_{bot}	η_{top}	$\eta_{\text{bot}}^{\text{NA}}$	F^{mir}	$P_{\text{out,bot}}^{\text{mir}}$
Unit:		($\%P_{0,\text{d}}$)			(%)		($\%P_{0,\text{d}}$)
q_{d}=1	100	90.07	8.78	1.16	91.68	0.907	7.30
q_{d}=1.5	100	76.58	20.84	2.58	97.94	1.038	21.18

Table 4.5: Membrane-on-mirror simulation results with membrane thickness at q_{d}=1 and q_{d}=1.5. The photon collection takes placed at the bottom of the simulation region.

Compared to the membrane-only simulation, the photon output $P_{\text{out}}^{\text{mir}}$ towards the bottom of the simulation region clearly improved thanks to the DBR mirror. The q_{d}=1 membrane has a lower $P_{\text{out}}^{\text{mir}}$ because of the much more dominant intra-diamond guided mode as shown in table (4.5). The emission enhancement F remains similar to that of the membrane-only simulations, suggesting the morphology of the membrane is the dominant source of LDoS modification instead of the DBR mirror.

We note that in the context of membrane-in-cavity device, the lateral channeling effect is likely to influence only the non-cavity photon branch. The emission pattern of the cavity photon is strongly modified by the cavity mode which propagates along the cavity axis.

4.6.2 Photon Output of Air-Like and Diamond-Like Modes

The hybrid-medium cavities are simulated with L_{depth}= 325nm and $\mathcal{R}$=3μm cavity features. The diamond-like and air-like modes are investigated by setting q_{d}=1.5 and 1 respectively. The dipole source is positioned at 66nm from the mirror-diamond interface.

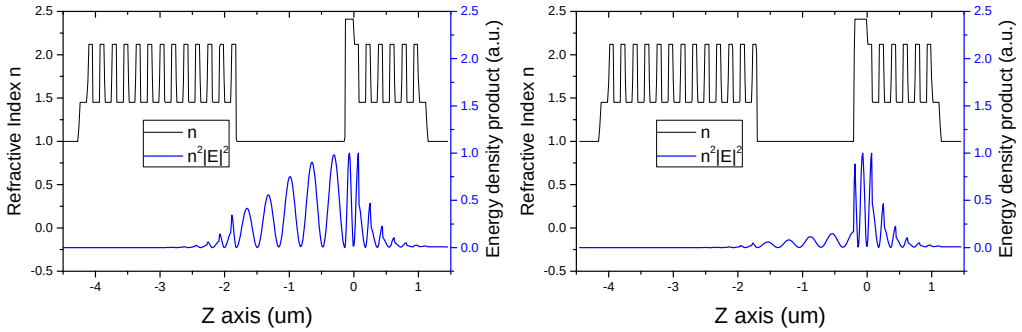

(a) Energy density profile $n^2|\mathcal{E}|^2$ at q=6 and q_{d}=1.

(b) Energy density profile $n^2|\mathcal{E}|^2$ at q=6 and q_{d}=1.5.

Figure 4.34: Simulated energy density profiles $n^2|\mathcal{E}|^2$ for **(a)** the air-like mode and **(b)** the diamond-like mode.

The profile of the energy density product $n^2|\mathcal{E}|^2$ along the cavity axis is plotted in

fig. (4.34). As expected, the energy distribution of the air-like mode is continuous across the air-diamond interface while the diamond-like mode has its energy concentrated within the membrane layer. This is in agreement with the analytical calculation presented in fig. (2.25) and a confirmation of the correct modes being supported in both simulations.

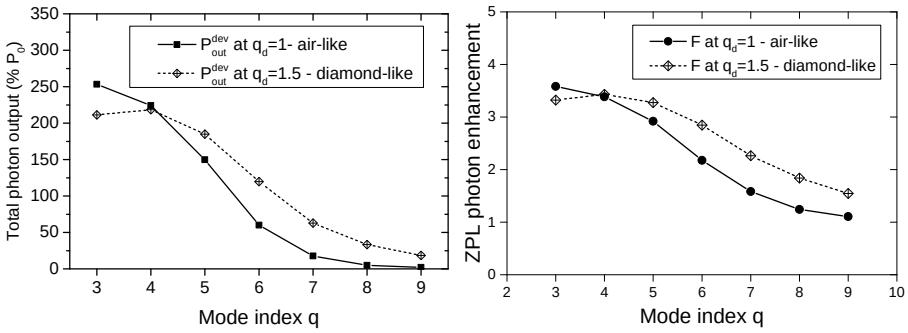

(a) Photon output P_{out} of both modes. **(b)** Emission analysis F of both modes.

Figure 4.35: Simulated **(a)** photon output P_{out} and emission enhancement F for both types of modes.

The photon output $P_{\text{out}}^{\text{dev}}$ and emission enhancement F of both devices are plotted in fig. (4.35). Due to the index down-scaling of n_{d}^3, F is low for both air-like and diamond-like modes. Despite of having a reduced mirror reflectivity due to the diamond membrane, performance of the diamond-like mode is surprisingly on par and even slightly better than that of air-like cavity at large q.

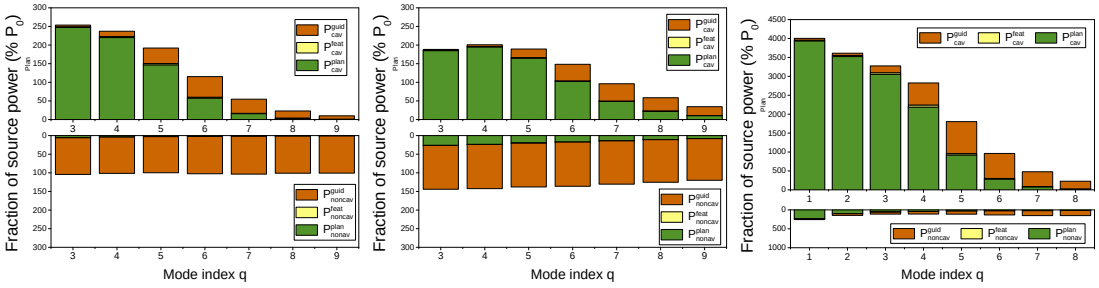

(a) Collection analysis P_{ch} of the air-like mode. **(b)** Collection analysis P_{ch} of the diamond-like mode. **(c)** Collection analysis P_{ch} of a single-medium cavity.

Figure 4.36: Simulated collection analysis: **(a)** the air-like hybrid-medium cavity; **(b)** the diamond-like hybrid-medium cavity; **(c)** the single-medium cavity.

Figure (4.36) compares the collection distribution of the hybrid-medium cavities with a single-medium cavity from section (4.5.2). It is apparent that both air-like and diamond-like modes suffer from a significant loss of non-cavity photon through the 2D guided modes P_{guid} due to the presence of membrane. However, the cavity photon collection is largely unaffected because the well-defined propagation directions of resonant cavity modes.

The collection behaviour of the air-like and diamond-like modes mainly differs in that the planar mirror reflectivity of the diamond-like mode is effectively reduced by the q_{d}=1.5 membrane. Therefore, the P_{plan} loss channel of the diamond-like mode is more competitive against the dominant guided mode loss channel P_{guid}. Hence the diamond-like mode slightly out-performs the air-like mode especially at larger q where P_{guid} is the strongest.

4.6.3 Other Cavity Figure of Merits

To further compare the hybrid-medium cavities with the single-medium cavities, both Q and V_{int} are plotted in fig. (4.37). To avoid confusion, the photon output P_{out} is not included in this discussion because the dipole is located in different dielectric mediums. Focus is placed on cavity loss and the collection characteristics of the corresponding cavity devices to quantify the influence of the addition of the diamond membrane to the cavity.

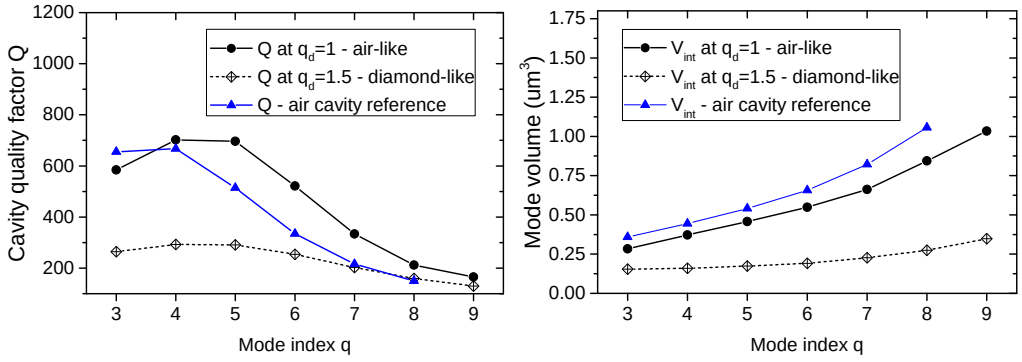

(a) Quality factor Q. **(b)** Mode volume by integration V_{int}.

Figure 4.37: Comparison of **(a)** cavity quality factor Q and **(b)** mode volume V_{int} between the hybrid-medium and the single medium cavity.

The air-like mode has a similar Q to that of the single-medium cavity because the resonance conditions are similar. The Q curve of air-like mode is shifted towards positive q due to the addition of the membrane. The diamond-like mode exhibit much lower Q due to the reduced effective planar mirror reflectivity. However, because the energy density of diamond-like mode is highly concentrated in the diamond layer (fig. (4.34)), the diamond-like has a far smaller mode volume V_{int} than the other two cavities. The air-like mode also benefits from this effect as its V_{int} is slightly smaller than that of the single-medium cavity. Considering both trends in Q and V_{int}, the performance of diamond-like mode is able to keep up with that of the air-like mode such similar emission enhancements F is observed between the two (fig. (4.35)(b)).

4.6.4 Fitting Simulated Cavity Mode Map with Analytical Model

Recalling the analytical resonance condition for a hybrid-medium cavity established in section (2.4.1), the resonant frequency is given as a function of mode index q, membrane thickness t_d and optical cavity length L:

$$v = \frac{c}{2\pi L}\left\{q\pi + (-1)^q \arcsin\left[\frac{n_\mathrm{a}-n_\mathrm{d}}{n_\mathrm{a}+n_\mathrm{d}}\sin\left(q\pi\frac{L-2n_\mathrm{d}t_\mathrm{d}}{L}\right)\right]\right\} \qquad \text{(eq. (2.68) revisit)}$$

Two sets of simulations are ran for cavities supporting an air-like mode and a diamond-like mode with L being varied to cover three mode families. The simulation variables are summarised in table (4.6). The resultant cavity mode maps are plotted in fig. (4.38). Some high-order TEM modes are also visible but here we only concern the fundamental modes.

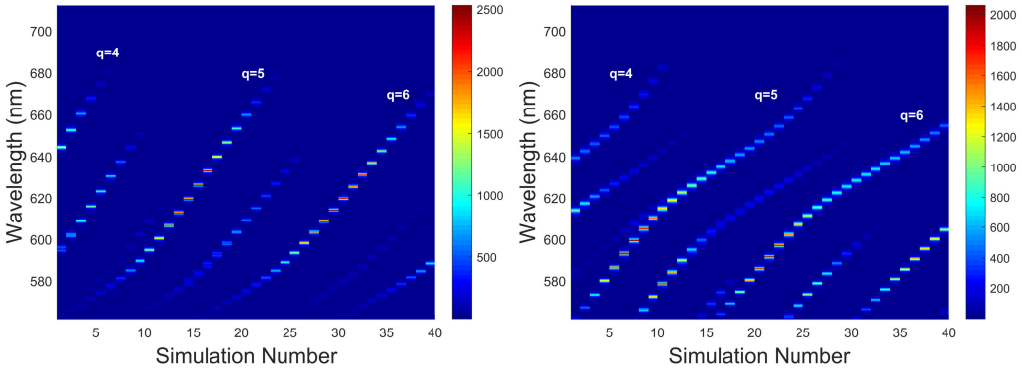

(a) Air-like mode map at q=4, q_d=2. **(b)** Diamond-like mode map at q=4, q_d=2.5.

Figure 4.38: Simulated cavity mode map for **(a)** the air-like mode and **(b)** the diamond-like mode. The x-axis is in frame-number instead of cavity length because a length re-scaling is required to adapt the numerical simulation to 1D analyitcal model.

	q	q_d	t_d (nm)	Physical Cavity Length (nm)
Air-like	4	2	264	976 - 1756
Diamond-like	4	2.5	330	882 - 1662

Table 4.6: Simulation variable used to generate the cavity mode maps.

Note that the simulated cavity mode follows the Gaussian mode propagation whereas eq. (2.68) is an 1D analytical model. Therefore, a length scale conversion is require to account for the Guoy phase shift in the Gaussian beam expression. By defining a set-point L_0 and a conversion ratio L_ratio, the new optical length axis is obtained from the

simulation frame number N_{frame}:

$$L_{\text{new}}=L_0+L_{\text{ratio}}\times N_{\text{frame}} \tag{4.15}$$

During the fit, L_0, L_{ratio} and t_{d} are all left as free-parameters while the residue in fitted mode position is minimized. The resulting fits for each mode family are plotted in fig. (4.39) and fig. (4.40) and the fitting parameters are listed in table (4.7). We note that fitting parameters are not shared between different mode families, again because of the length scaling discrepancies.

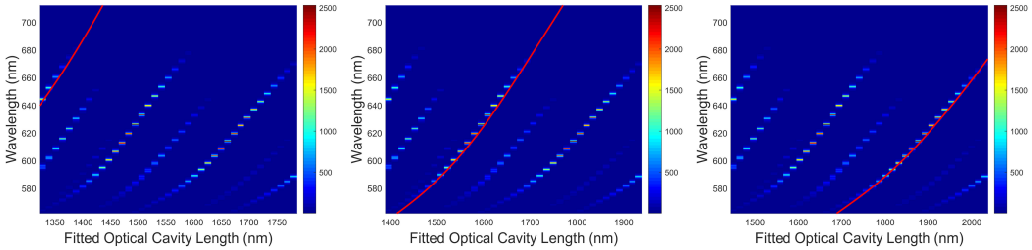

(a) q=4 mode family. **(b)** q=5 mode family. **(c)** q=6 mode family.

Figure 4.39: Fitting the cavity mode map of th air-like mode at q_{d}=2. Fitting is done separately for each mode family.

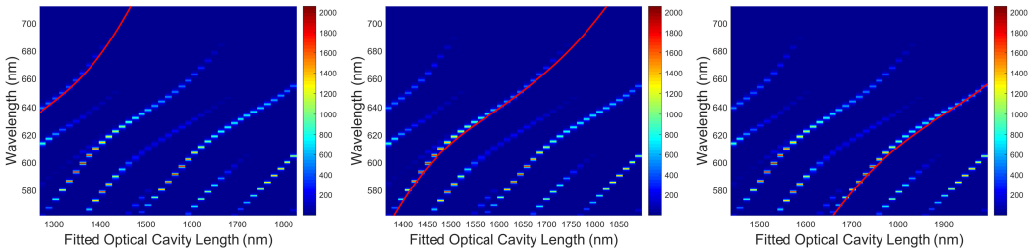

(a) q=4 mode family. **(b)** q=5 mode family. **(c)** q=6 mode family.

Figure 4.40: Fitting the cavity mode map of the diamond-like mode at q_{d}=2.5. Fitting is done separately for each mode family.

The fitting residues are of all fits are comparable to the 0.4THz f-domain resolution of the simulations. Comparing to the original simulation parameters in table (4.6), the fitted t_{d} of the diamond-like cavities agrees well with the simulated t_{d}=330nm. The fitted t_{d} of the air-like cavity shows about 30nm deviation from the simulated t_{d}=264nm which is within the $\lambda/2n_{\text{d}}$=33nm error of the analytical model [88].

In summary, the 1D analytical description of the resonance condition of a hybrid-medium cavity shows good agreement with the simulation data. We expect the fitting accuracy to improve for larger cavities where the beam propagation deviation is less prominent.

	q	Fitted L_0	Fitted L_{ratio}	Fitted t_{d}	Fitting Residue
		(nm)	(nm/frame)	(nm)	(THz/frame)
Air-like	4	1332	11.9	304	0.459
	5	1389	14.1	289	0.663
	6	1443	15.3	290	0.910
Diamond-like	4	1268	14.4	331	0.191
	5	1362	13.8	331	0.639
	6	1437	14.3	332	0.790

Table 4.7: The fitting results for each mode family in the air-like and diamond-like simulations. The simulated membrane thickness is t_{d}=264nm for the air-like cavity and t_{d}=330nm for the diamond-like mode. All the cavity lengths are in optical cavity length.

This fitting methodology is reasonably reliable in finding the membrane thickness given a cavity mode map and is especially useful in experimental conditions to determine t_{d} as shown later in section (6.3.4).

4.7 Conclusions

In this chapter, we proposed a comprehensive analysis methodology for simulating Fabry-Perot type cavity with FDTD. The analysis protocol consists of a time-dependent emission analysis and a spatially-resolved collection analysis. The dipole emission is divided in t-domain as cavity and non-cavity photons with different emission patterns. The overall photon loss is decomposed into spatial loss channels, including the mirror transmission losses ($P_{\text{plan}}/P_{\text{feat}}$) and 2D guided mode loss (P_{guid}). The overall cavity performance is bench-marked with the ZPL photon output P_{out}.

The dependence of P_{out} on each cavity variable is investigated with a single-medium cavity, and insights into basic cavity operation are obtained. In principle, the cavity performance is limited by its photon loss characteristics which affect both the emission rate enhancement F and photon collection P_{plan}. The changes in cavity parameters are often reflected in the relative photon coupling strengths into different loss channels. The goal is then to maximize useful photon extraction (P_{plan}) versus the dominant loss channel (P_{guid}).

One important conclusion from the single-medium cavity simulations is the distinction

between short- and long-cavity limits. The boundary of the two is found at $q_{\max}/2$ which is the maximum supported mode index for a given radius of curvature $\mathcal{R}$. Most obviously, the emission enhancement is the strongest for the smallest mode index q with high cavity finesse $\mathcal{F}$ due to limited P_{guid} losses. The cavity quality factor Q is maximized at q=$q_{\max}/2$ beyond which both emission enhancement and collection efficiency are deteriorated significantly as P_{guid} starts to dominate. This analysis helps to determine the optimal combination of q and $\mathcal{R}$ in experimental conditions.

For a lossy cavity with large P_{guid}, mirror reflectivity R down-tuning also shows decent cavity performance boost. By dropping R, some emission enhancement is sacrificed, but better P_{plan} to P_{guid} ratio ensures more efficient collections. Although R tuning is challenging to execute in practice, for a known structure, optimal R can be designed before carrying out the cavity experiments.

The most noticeable impact of a high-index diamond membrane in the Fabry-Perot cavity is the additional P_{guid} due to the intra-membrane 2D guided modes. As a result, the emission rate enhancement and the collection efficiency of non-cavity photons drops significantly compared to a single-medium cavity. The collection of cavity photon is relatively immune to the presence of the membrane because of the directionality of cavity resonant modes along the optical axis.

The cavity performance of the diamond-like and air-like mode of a hybrid-medium cavity is found to be quite comparable, which agrees with the TMM calculation in section (2.4.3). The lowered Q of the diamond-like mode is compensated by a smaller V because a substantial proportion of field energy resides in the diamond layer. Given current fabrication technology, precise control over membrane thickness is very difficult.

For the membrane-in-cavity setup, instead of focusing on which type of mode to support, we reckon it is more important to limit the contribution of the membrane P_{guid} such that higher emission and collection enhancement can be achieved. This might be realized by constructing a monolithic device with a thin layer of diamond with limited lateral dimensions. This way, the DBR coatings completely closes the intra-cavity gap in the planar part of the mirrors, and only minor P_{guid} is supported by the intra-DBR guided modes.

Chapter 5

NV Centre in Diamond Membranes

In this chapter, we present the optical characterisation results of diamond membranes with NV centres that are created by both the ion-implanted and the laser-writing technique. The main fabrication obstacles related to membrane thinning are highlighted, and our solution is demonstrated. The yield and spectral properties of ion-implanted NVs are bench-marked before and after membrane fabrication. By the end of this project, the membrane sample containing laser-written NVs is still half-way through the fabrication process; hence only the early-stage preliminary characterisation data will be shown.

The optical coherence properties of NV centres from a variety of sample geometries and identities are probed with PLE measurement at 4K. The ion-implanted and laser-written NVs are compared against each other. The ZPL transition linewidths and charge-state switching probabilities are obtained to quantify NV optical coherence.

5.1 Membranes with Ion-Implanted NVs

5.1.1 Ion-implanted NVs in Bulk Samples

The initial ion-implantation investigation is carried out on three E6 CVD {100} samples from Element Six and one NDT HPHT {110} sample. All samples are 'electronic grade' with [N]$<$5ppb with a 2mm lateral dimension.

The long-range strain distribution of each sample is examined with cross-polar images and

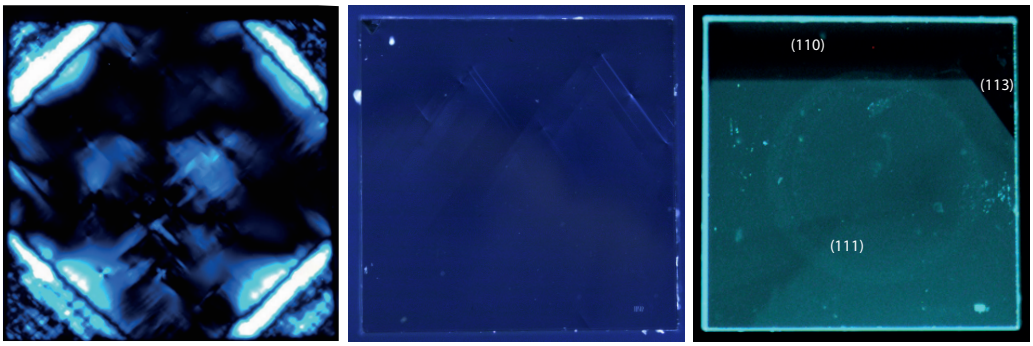

(a) **(b)** **(c)**

Figure 5.1: Cross-polar images revealing strain distribution in **(a)** a CVD and **(b)** a HPHT bulk sample; **(c)** A DiamondView image showing growth sector boundaries in the HPHT sample.

two of them from a CVD and a HPHT sample are shown in fig. (5.1)(a)-(b). The brightness contrasts indicate the presence of lattice strain.The CVD sample exhibits strong oblique strain bands at the corners while the HPHT sample shows much smaller strain variation across the sample. Both observations are characteristic of the respective sample growth technique. The DiamondView image in fig. (5.1)(c) shows the different growth sectors in the HPHT diamond..

5.1.1.1 Implantation Parameters

The implantation parameters for each sample are summarised in table (5.1). The ion fluence is chosen to be at the lower bound of that in [42] for a better chance of generating confocal resolvable single defects. The ion energy is chosen such that the estimated depth of implantation is equal to the location of the first diamond anti-node ($\lambda/2n_{\mathrm{d}}$=66.1nm) in the cavity. According to SRIM simulation (fig. (5.2)), the stopping ranges corresponding to ion energies of 75KeV and 52KeV are 89.9(18.7)nm and 65.5(15.2)nm respectively.

Sample	[N]	Growth Type [Orientation]	Fluence (ions/cm^2)	Energy (KeV)
A - ME309	<5ppb	CVD {100}	5×10^9	75
B - PL4003	<5ppb	CVD {100}	5×10^9	75
C - PL4505	<5ppb	CVD {100}	2.5×10^9	75
D - NDT110B	<5ppb	HPHT 110	2.5×10^9	52

Table 5.1: Sample identities and implantation parameters.

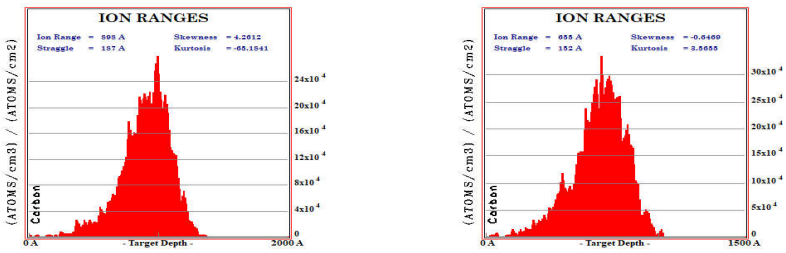

(a) **(b)**

Figure 5.2: SRIM simulation results showing the average ion stopping range for the ion energies at **(a)** 75KeV and **(b)** 52KeV.

Following the implantation and annealing processes, room-temperature characterization are carried out to confirm the creation of NV centres. Typical photoluminescence (PL) emission spectrum (fig. (5.3)(a)) from defects in sample A exhibits the characteristic NV^- ZPL emission at 637nm and the broadband PSB transition centered around 700nm. The measured excited-state lifetime of 13ns (fig. (5.3)(b)) is typical of literature quoted values. Both measurements confirms the successful creation of NV^- centres.

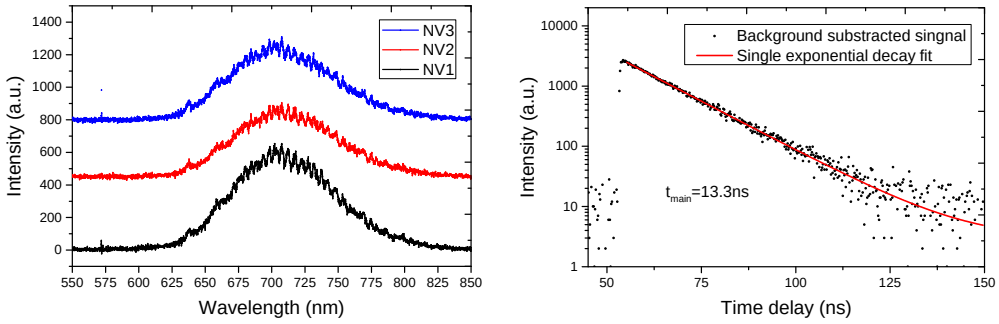

(a) Emission spectrum. **(b)** Excited-state lifetime.

Figure 5.3: Preliminary room-temperature characterizations to confirm the creation of NV centres after ion-implantation and annealing.

5.1.1.2 Defect Density and Implantation Yield

To further quantify the implantation yield and NV quality, samples are cooled down to 4K and the NV ZPL distribution are surveyed in each sample. Scanning confocal images are used to estimate NV generation efficiency as shown in fig. (5.4). The sample D is imaged in the (111) growth sector (refer to fig. (5.1)(c)). The observed defect 'network' is characteristic of NV layers created by ion-implantation.

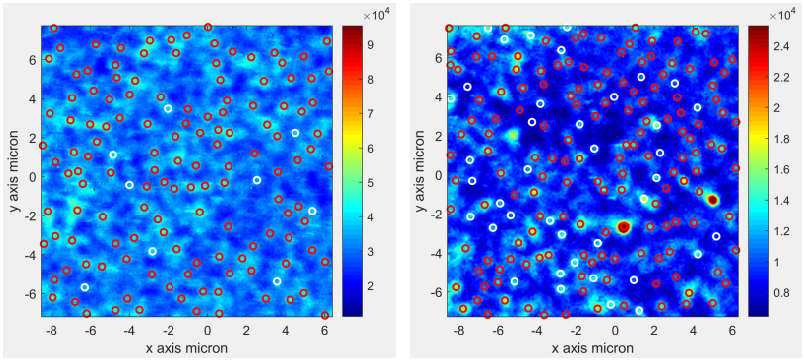

(a) Sample A - 15x15µm^2 **(b)** Sample B - 15x15µm^2

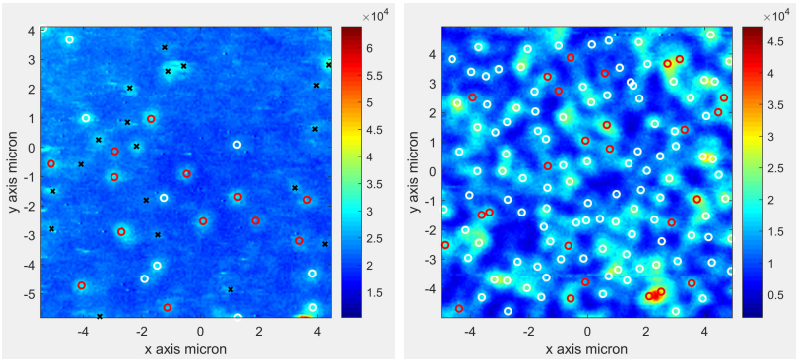

(c) Sample C - 10x10µm^2 **(d)** Sample D - 10x10µm^2

Figure 5.4: Low temperature confocal scans from all four samples: NVs with a single ZPL are circled in white; NVs with ≥2 ZPL are circled in red; non-NV defects or unstable NVs are marked with black crosses.

Due to large number of defects under investigation, identifying single emitters using HBT measurement is not realistic. Instead, high resolution PL spectrum with a 1200 grooves/mm grating (0.03nm/21GHz resolution) are used. Any confocal-resolvable NVs with a single ZPL transition are considered a single defect. The NVs showing two ZPL transitions could be either a double-NV site or a single NV with strain-splitted ZPLs. For simplicity defect sites with ≥2 ZPL transitions are all regarded as a double-NV in the counting process. The NV density per 10x10µm^2 (table (5.2)) are compared against the implantation ion fluence to give nitrogen conversion yield.

Sample	Total No. of NVs	No. Single ZPL NVs	Nitrogen Yield
A - ME309	63	10	1.26%
B - PL4003	63	11	1.26%
C - PL4505	23	10	0.92%
D - NDT110B	134	107	5.36%

Table 5.2: Number of NV centres per 10x10µm scan area. The nitrogen conversion rate is calculated by counting NVs with a single ZPL as a single defect and averaging all the other NVs with multiple ZPLs as a double defect site.

Sample A and B both show a higher NV density than sample C due to difference in ion fluence. The nitrogen conversion yield is comparable between sample A/B (1.26%) and sample C (0.92%). Variations of NV density are observed at different sample locations.

Sample D (HPHT) had the same ion fluence as sample C but shows a much denser NV population and higher nitrogen yield. To rule out batch-to-batch variance, a reference CVD {100} sample (data not shown) from the same implantation batch shows a nitrogen conversion yield of 1.6% which is much closer to that of sample C. This suggests the observation with sample D is associated with intrinsic sample properties. Two possible explanations considering crystal orientation and intrinsic [N] are discussed next.

Previous molecular dynamics simulation work [89] suggests a larger depth discrepancy between ion stopping range and vacancy creation when implanted along the {110} axis. Vacancies are created at shallower depths while implanted nitrogen concentrates at deeper locations. Assuming intrinsic [N] are equally low and NV formation relies on implanted nitrogen, {110} orientation is should yield less NV than {100} crystal which contradicts our observations.

On the other hand, multiple studies [90, 91] report growth sector dependent impurity concentration in NDT HPHT diamond. Provided that the (111) growth sector in fig. (5.4)(d) has a higher impurity incorporation efficiency, the observed high NV density is likely associated with high intrinsic [N]. In diamond lattice, a 1ppb concentration variation ($3.14\times10^9/\text{cm}^2$ atomic density) is on the same order of magnitude as the implantation ion fluence. This also suggests intrinsic nitrogen has a significant contribution towards NV formation. Later in section (5.3.4) more evidence from PLE measurement is shown to support this deduction.

5.1.1.3 ZPL Distribution of Implanted NVs

The PL spectrum from all measured NVs are summed in fig. (5.5) to investigate ZPL distribution in each sample. In this case no distinction is made between NVs with a single or multiple ZPLs. The data of sample A, B and D are fitted with a Gaussian distribution and the FWHM are found to be 0.086nm, 0.064nm and 0.045nm respectively. The narrow ZPL distribution in HPHT sample D is also partly because a large proportion (107 in

134) of measured NVs contain only one ZPL transition. In contrast, only 10 of the 63 measured NVs in CVD samples fall under this category.

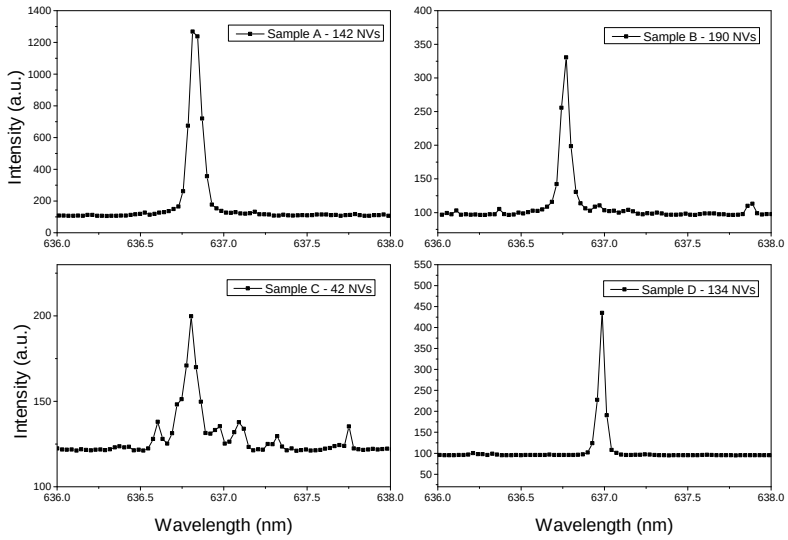

Figure 5.5: The summations of all NV spectrum (>100 on average) measured in each ion-implanted sample. The overall ZPL distribution of sample A, B and D are fitted with a Gaussian FWHM of 0.086nm, 0.064nm and 0.045nm respectively.

Changes in ZPL positions are usually associated with lattice strain: longitudinal strain along NV axis shifts the ZPL frequency, and transverse strain splits the E_x/E_y ZPL transitions. Much stronger strain in CVD samples was previously confirmed with cross-polar images, as shown in fig. (5.1). Our observations agree well with this explanation.

5.1.2 NV Quenching in First Generation Membranes

During the first membrane fabrication batch, the final etch in fig. (3.4)(h) is carried out with Ar/Cl_2 instead of O_2. It is later observed that these membranes (Gen1-m1 and Gen1-m2) do not host any active NV centres in either charge-state. The observed defect morphology in confocal images (fig. (5.6)) is very similar to those of the bulk ion-implanted samples (fig. (5.4)). However, the defects (e.g. the one circled in red) often disappear after a short period of 532nm excitation and no NV signature is observable with spectrometer either before or after the laser excitation.

Initially, we attribute the fluorescence quenching to surface termination degradation. Hence efforts are made to the re-established oxygen-terminated surface for Gen1-m1 sample by repeatedly annealing in pure O_2 at 465°C. The oxygen annealing did reduce overall

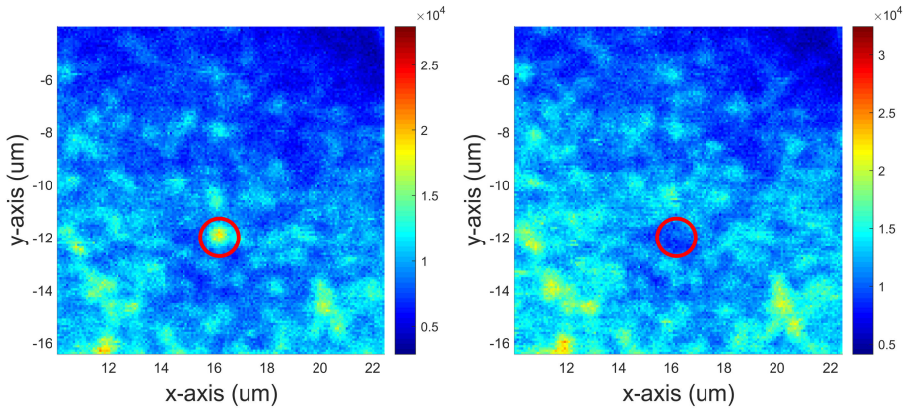

Figure 5.6: An example of observed defect quenching under laser exposure in the first generation samples.

background fluorescence, but the laser-induced defect quenching continues to happen. No defect is stable enough for any optical measurements after a total annealing time of 10hr.

After re-evaluating the fabrication procedure, we suspect that the Ar/Cl_2 etch is creating deep sub-surface damage which depletes electron from the NV centre. Chlorine-related quenching effect is previously reported in [78] where near-surface NV centres are de-activated following brief Ar/Cl_2 exposure. In our work, the implanted NV layer is on the opposite side of the etch-exposed surface. The observed NV quenching suggests that the ion damage might have extended deep through the membrane thickness (≈3μm)from the chlorine-exposed surface.

To verify this hypothesis, we carried out X-ray photoelectron spectroscopy (XPS) to characterise the surface elemental composition of unsuccessful Gen1 membranes. The element of interest is chlorine, oxygen and silicon.

5.1.2.1 XPS Investigation and Fabrication Optimization

In addition to Gen1-m1 and Gen1-m2, unprocessed bulk sample A is also included as a pre-fabrication reference and a summary of XPS data are listed in table (5.3).

Firstly, in chlorine-related region at binding energy E_b=200eV, signal is observed in both Gen1 membranes as plotted in fig. (5.7). Gen1-m2 contains 0.23% of chlorine and noticeable chlorine trace is also present in Gen1-m1. For reference XPS detection sensitivity is 0.1% element fraction (or 1ppt). Given the impurity level of [N]<5ppb, [Cl] near the

exposed surface is 3 order of magnitude higher than [N].

Unit: %	Gen1-m1		Gen1-m2		Bulk Sample A	
	Site 1	Site 2	Site 1	Site 2	Site 1	Site 2
C_{1s}	63.8	38.1	79.7	87.2	84.3	85.0
Cl_{2p}	0.1*	-	0.1	0.2	-	-
O_{1s}	26.4	41.7	15.9	11.0	13.0	12.7
Si_{2p}	8.6	15.4	4.4	1.5	2.6	2.3
Na_{1s}	0.7	1.0	-	-	-	-
K_{2p}	0.4	1.2	-	-	-	-
Ta_{4f}	0.2	2.6	-	-	-	-

* Limited by detection sensitivity of XPS.

Table 5.3: Summary of % element fraction on the surfaces of first generation membranes.

It is reported in other semiconductor system [92] that chlorine radical damage can quench emission of quantum dots 500μm away from radical-exposed surfaces. Although it is non-trivial to compare the radical penetration in different materials, their recipe and etching rate are similar to ours. Considering the ppt level [Cl] in our sample, it is reasonable to assume chlorine penetrated a few μm into the diamond lattice.

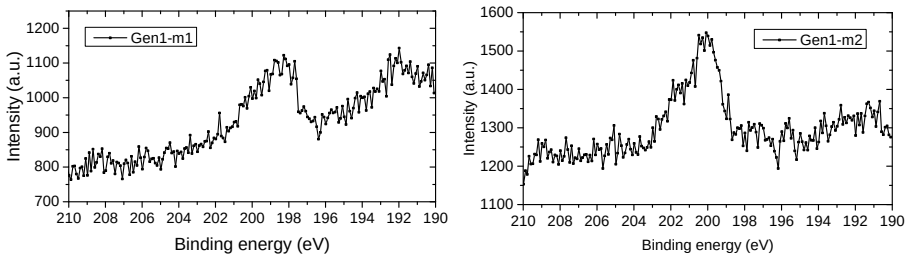

(a) **(b)**

Figure 5.7: The chlorine-related XPS trace at around 200eV binding energy measured from **(a)** Gen1-m1 and **(b)** Gen1-m2 membranes.

As a result of the 10hr O^2 annealing of Gen1-m1, its surface oxygen content is significantly higher than that of Gen1-m2 and sample A. Because sample A is only treated with acid boiling, this observation confirms the advantage in oxygen termination coverage of the O^2 annealing. Gen1-m1 also contains a higher level silicon and metallic elements. This is attributed to contamination caused by silicon wafer re-deposition and shared usages of RIE/ICP chamber.

In summary, XPS is proven to be a powerful tool to help optimizing the membrane fabrication process at early stages of this work. High concentration of chlorine content

is observed in both Gen1 membranes which suffer from NV fluorescence quenching. To address this issue, >2μm of O_2 etch (fig. (3.4)(h)) replaces Ar/Cl_2 as the finishing etch for later sample batches. In consequence active NV centres are successfully preserved in later batches of fabricated membranes.

XPS analysis also helps us to identify sources of contamination and extra chamber cleaning steps are added to eliminate the impurity species due to equipment sharing. It is possible to further limit substrate re-deposition by using a quartz etching mask [28]. Implementation of such techniques are discussed in chapter (8).

5.1.3 NVs in Second Generation Membranes

In this work a total of three Gen2 membranes are produced and their information are listed in table (5.4). Active NVs are observed in all three samples suggesting that the strategy of keeping the chlorine-exposed surface at least 2μ away from the NV layer has been successful. However on average only 0.65 NV is found per 10x10μm scan area and a typical confocal scan image in a 25x25μm area is shown in fig. (5.8)(a). Compared to the bulk samples right after ion-implantation in section (5.1.1.2), the NV density is significantly lower.

	Maximum thickness (μm)			Wedge angle (mrad)	
	Initial	Transfer	Final	Initial	Final
Gen2-m1	36.6	6.8	2.5	1.5	1.3
Gen2-m2	18.6	4.6	1.1	1.8	0.9
Gen2-m3	16.9	4.8	2.5	0.8	0.8

Table 5.4: Membrane morphologies at different stages of fabrication process.

A typical set of low-temperature optical characterization results of NV5 in membrane Gen2-m2 is shown in figs. (5.8) and (5.9). The emission spectrum exhibits a membrane-modulated PSB emission band and sharp ZPLs at 575nm and 637nm. Due to location-specific modulation pattern, spatial background subtraction is not a reliable way to obtain ZPL branching ratio and is included only for visual guidance. The measured lifetime of 11.40ns is typical of values reported in literature and the HBT measurement confirms that NV5 is a single photon emitter.

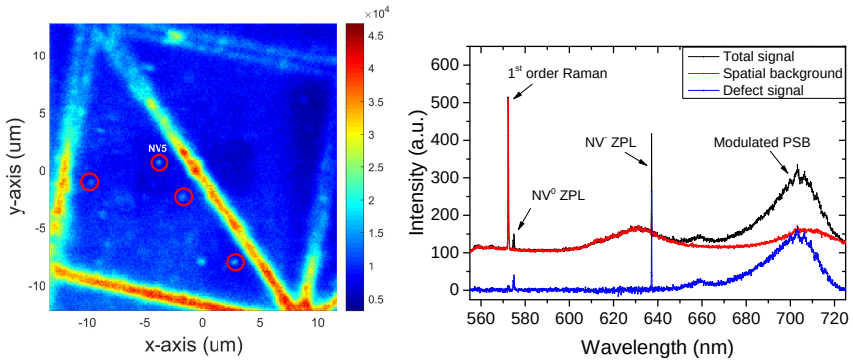

(a) **(b)**

Figure 5.8: **(a)** A typical confocal scan image of a 25x25µm area showing reduced NV density in membrane Gen2-m2; **(b)** PL emission spectrum of NV5 in the area. The background baseline in HBT data gives an estimate of the minimal $g^{(2)}(0)$ achievable given the background count rate at the NV location.

Although the resulting NV yield in membrane samples are relatively low, most of identified NVs exhibit stable charge-state under 532nm excitation and no blinking behaviour is observed. In later chapters low-temperature cavity-coupling data of NV centres in membrane samples will be presented.

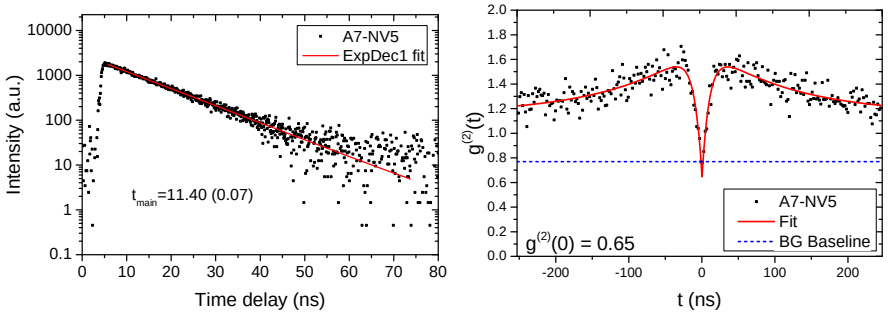

(a) **(b)**

Figure 5.9: **(a)** The excited-state lifetime and **(b)** HBT results of NV5 in the area. The background baseline in HBT data gives an estimate of the minimal $g^{(2)}(0)$ achievable given the background count rate at the NV location.

5.1.3.1 Surface Morphology of Second Generation Membranes

Next we go over basic thin-film characterization of Gen2 samples and comment on the surface morphology of the fabricated membranes. For cavity operations surface smoothness at dielectric interfaces are crucial due to cavity loss induced by surface scattering. Efforts are made to reduce membrane surface roughness to minimize surface scattering

loss. The surface roughness of all 3 samples are tracked throughout the thinning process using AFM measurement and the results are listed in table (5.5).

	RMS roughness (nm)			Etch removal on DBR	
	Initial	Transfer	Final	Ar/Cl_2	O_2
Gen2-m1	0.24	0.22	3.55	1.8µm	2.5µm, 2×20min, non-biased
Gen2-m2	1.14	0.89	0.77	-	3.5µm, 8×5min, biased
Gen2-m3	2.17	0.82	0.78	-	2.3µm, 4×10min, biased

Table 5.5: Membrane surface roughness evolution at different fabrication stages.

Figure (5.10) shows the optical microscope images of the Gen2-m3 membrane samples at different stages of the fabrication process. The initial stock plate shows strong white light optical interference fringes due to sample wedge. After some thinning and transferring onto the DBR mirror, inclusions at the membrane/mirror interface becomes more visible given the surrounding local optical fringes. The final membrane has its bottom-right corner completely etched off and color of the optical fringes corresponds to DBR mirror stopband in yellow-red wavelengths.

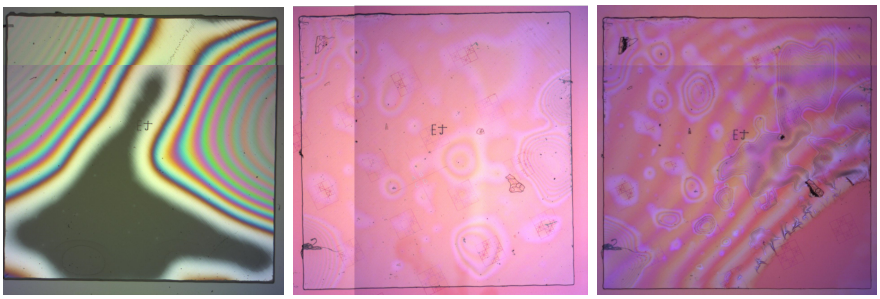

(a) At 30µm thickness on silicon wafer. **(b)** At 5µm thickness on DBR mirror. **(c)** Final membrane at 1µm thickness.

Figure 5.10: Optical microscope images of sample Gen2-m3: **(a)** stock plate as received from laser-slicing at 30µm thickness; **(b)** sample at 5µm transferred to the DBR mirror after bulk-thinning on a silicon wafer; **(c)** finished membrane after final pure O_2 etch on the DBR mirror.

Among three fabricated Gen2 membranes, Gen2-m1 has the lowest starting roughness at 0.24nm but its surface is greatly roughened to 3.55nm RMS after the final 2.5µm of O_2 etch. We reckon the cause here is two-fold. Firstly, after being transferred onto DBR mirror, the membrane is processed with a combination of Ar/Cl_2 and O_2 etch. Due to the aggressiveness of the Ar/Cl_2 recipe, surface re-deposition sites are formed and further developed by the subsequent O_2 annealing. Secondly, the O_2 etch on this sample is performed with 20min-segments which could raise the temperature of the sample holder.

Because the O_2 recipe has a strong chemical etch component, at increased temperature the etching process becomes even more isotropic, which results in significantly roughened surfaces.

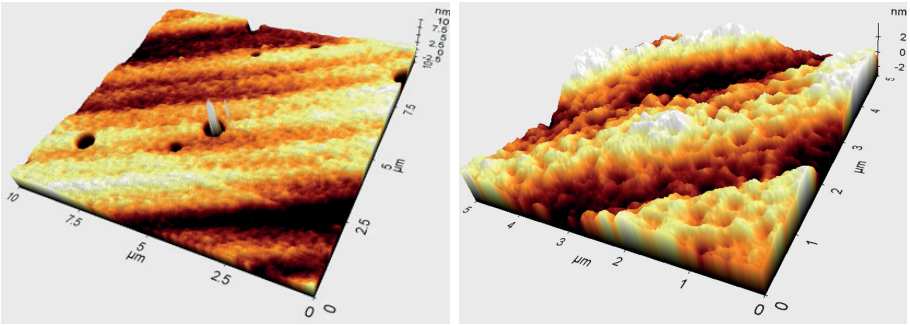

(a) Average roughness at 0.77nm. **(b)** Average roughness at 0.78nm.

Figure 5.11: AFM scans of **(a)** Gen2-m2 and **(b)** Gen2-m3 after the O_2 etching recipe adjustment where improvement in surface quality has been shown on both samples. Sparse etching pits as appeared in **(a)** remains a problem even with the improved O_2 etch recipe.

To improve the surface quality, we avoided the Ar/Cl_2 etch completely after the DBR transfer and O_2 etch are divided into shorter segments with 15min of sample cooling between each etch step. Also, an ICP platen power of 100W is used to improve the directionality of the O_2 etches. As a result, the surface roughness of Gen2-m2 and Gen2-m3 are well maintained below 1nm after the final etch. Examples of AFM data taken in a small region of interest are shown in fig. (5.11).

Although changes made to the final etch improved fabrication consistency, one outstanding issue remains as etching pits are present sparsely across O_2 exposed surface. We attribute the pitting behaviour to pre-existing or re-deposited surface particles which act as micro-mask in later etching steps. Due to different etching selectivity, a pillar structure starts to form, as shown in fig. (5.11)(a). When pillars become too tall, they break off to leave etch-pits as it is observed on the AFM images. A potential solution inspired by [28] will be presented in chapter (8).

5.2 Membranes with Laser-written NVs

Membrane fabrication with laser-written NVs is also attempted. Although by the end of this project, the laser-writing membrane (LW-M) is not yet finished, some preliminary

data will be presented here.

The fabrication procedure generally follows that in section (3.1) with the ion-implantation being replaced by single 300fs laser pulses at 790nm to create lattice damage. The writing plan is illustrated in fig. (5.12)(a) and the writing is carried out at five depths from 13 to 17µm in a stripe pattern laterally. Within each strip, two rows of high damage sites are fabricated as alignment marks which are followed by 20 rows of low damage site with decreasing laser pulse energy (fig. (5.13)(a)).

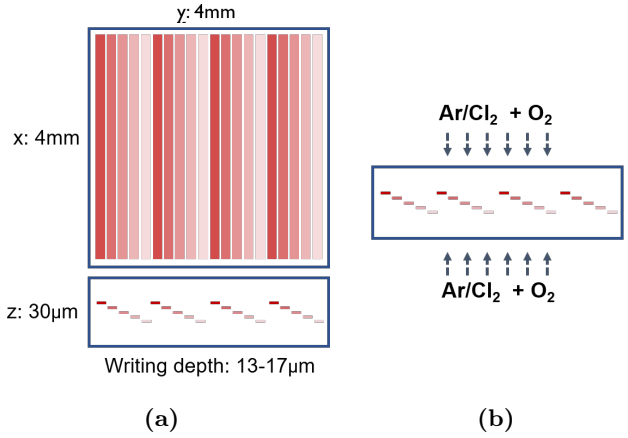

Figure 5.12: **(a)** The laser-writing fabrication plan. The writing is carried out at five depths indicated by different colours. **(b)** Because the writing is not carried out at near-surface locations, the 30µ post-slice sample has to be etched from both sides.

Compared to the original work in [19] where only a small area is fabricated, LW-M is written with a free-running method such that the whole sample area is covered. Given the sample size of 4x4mm and fabrication site spacing of 5µm, up to 640,000 sites are fabricated in this sample. The demonstrated fabrication capability with positioning control certainly shows promises in terms of scalability.

In previous work, the most coherent NVs are identified near the 'GR1 visibility threshold' beyond which no GR1 fluorescence is visible in confocal images. The corresponding pulse energy depends on a multitude of factors including sample purity, fabrication depth and equipment calibration status. To make sure GR1 visibility threshold is included, a pulse energy calibration is done in a separate sample on the same day to fine-tune the energy range. As a result, LW-M shows a GR1 visibility threshold at row11 as plotted in fig. (5.13)(a).

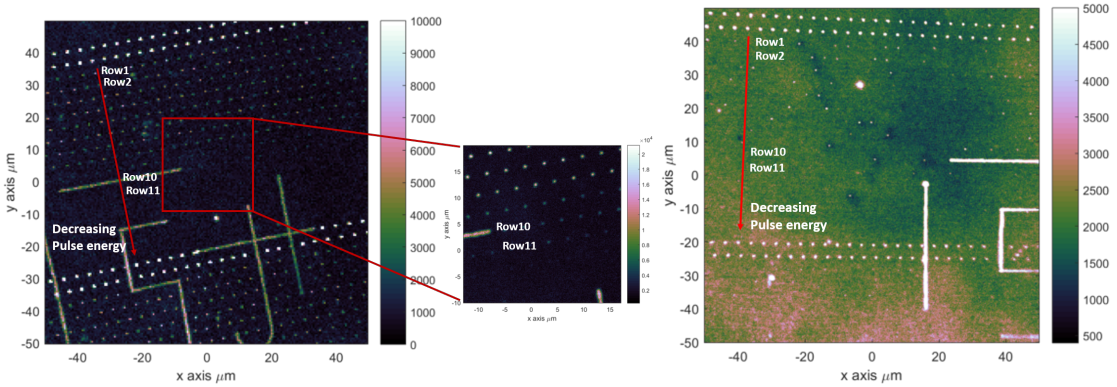

(a) **(b)**

Figure 5.13: Confocal scanning images **(a)** before annealing and **(b)** after annealing. The zoomed-in image in **(a)** shows the GR1 visibility threshold at row11. After annealing, the NVs formed beyond this row are expected to have the least lattice damage.

After a 3hr annealing at 1000°C, NVs are formed throughout the sample while most low energy damage sites are healed (fig. (5.13)). The NV emission signature is verified by spectrometer as shown in fig. (5.14). We note that some NVs are formed at row13, which is beyond the GR1 visibility threshold during the fabrication. These NVs are expected to have the least lattice damage and best coherence properties.

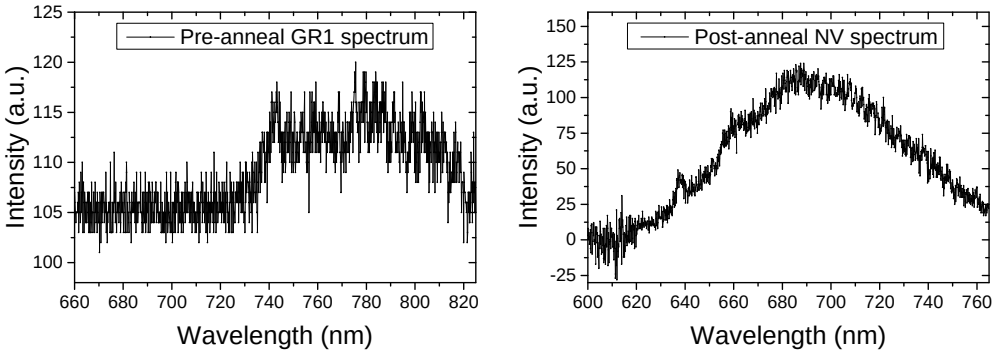

(a) **(b)**

Figure 5.14: The PL spectrum at laser-written sites: **(a)** clear GR1 feature at 740nm is observed before annealing; **(b)** NV ZPL is observed at 637nm after annealing.

The overall NV yield is 11% which is very good compared to ion-implantation results. It also comes with the added benefit of defect positioning accuracy within 200nm in lateral directions [19]. Single photon emission properties of the laser-written NVs are confirmed with HBT measurements (data not shown). Some of the NVs are also examined with PLE measurement and the data is shown in next section.

5.3 Optical Coherence of NV ZPL Transitions

The optical coherence of ion-implanted and laser-written NVs are probed using PLE measurements. The PLE measurement setup and analysis algorithm is discussed in section (3.6) in detail. Briefly speaking, each PLE measurement sequence consists of a target scan (scan1) and a charge-state validation scan (scan) to the exclude low-quality data due to mid-scan photon-ionization event. The main figure of merits are the homogeneous linewidth δv_{hom}, the overall linewidth δv_{tot}, the PLE validation rate p_{val} and the charge-start stability quantified by the ionization probability p_{ion} and recharge probability p_{rec}.

5.3.1 Sample Catalogue

PLE data in this work is gathered from a variety of samples whose information are summarised in table (5.6). Depending on different starting materials and sample morphologies, useful comparisons of optical coherence can be made.

Sample	CVD	HPHT	Bulk	Membrane	Shallow	Deep
Ion-implanted						
B - PL4003	✓		✓		✓60nm	
C - PL4505	✓		✓		✓60nm	
D - NDT110B		✓	✓		✓60nm	
E - Gen2-m2	✓			✓	✓60nm	
Laser-written						
F - LW-Nat*	✓		✓			✓50µm
G - LW-3D	✓		✓		✓10µm	
H - LW-M	✓		✓**		✓15µm	

* Data re-analyzed from [19].
** LW-M sample is prepared towards the membrane form, but is currently half-way through the process at 30µm-thick. Hence it is still a 'bulk" sample at this stage.

Table 5.6: A summary of samples information from which PLE data is gathered. A sample is considered a 'membrane" if its thickness is below 10µm. Above this thickness, the optical properties of NV centres are largely unaffected by the far-side surface [28].

In general, the ion-implanted NVs are located near sample surfaces and more susceptible to surface trap states. Work by [43] suggests a strong correlation between lattice damage caused by ion-implantation and ZPL decoherence. In contrary, laser-written NVs are

located deeper in the lattice (>10μm) and the fabrication creates minimal lattice damage. In general, ion-implanted NVs to exhibit wider homogeneous linewidth and worse spectral diffusion than the laser-written ones.

PLE data of deep laser-written NVs are re-analysed from a CVD bulk diamond sample (sample F, LW-Nat) in [19]. In the previous work, some of the homogeneous linewidth figures are extracted from single PLE scans which are slightly less representative. Here, more consistent results are obtained with the established analysis protocol in section (3.6) and more information about charge-state stability is extracted.

PLE data of shallower laser-written NVs are obtained from sample G (LW-3D) and sample H (LW-M). Sample G is a bulk CVD diamond where NVs are directly written at 10μm.

5.3.2 637nm Excitation Power Optimization

The linewidth estimates of PLE measurement relies on having a decent number of successful PLE scans. Increasing 637nm power can improve signal-to-noise ratio *SNR* but it also causes power broadening of the homogeneous linewidth $\delta\upsilon_{\text{hom}}$ and increases ionization probability p_{ion} which reduces the validation rate p_{val}. As a result, the measurement efficiency is lowered and the data quality is compromised.

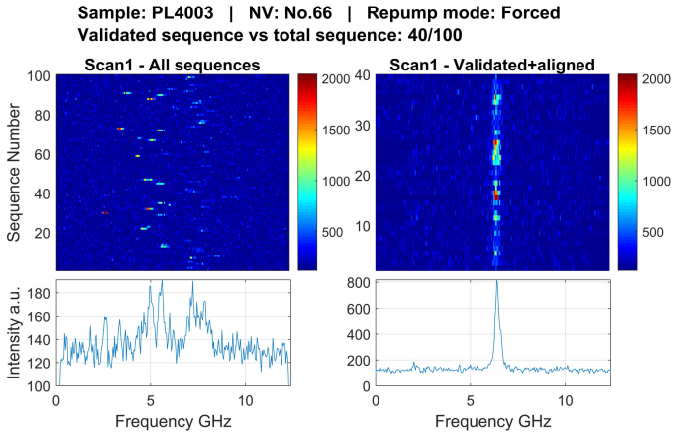

Figure 5.15: Example of ZPL linewidth extracted from PLE data of ion-implanted NV66 in sample B: **(left)** the raw scan1 dataset; **(right)** validated and aligned scan1 sequences.

To determine the working power at 637nm, a power dependence test is carried out using an ion-implanted NV66 in sample B under the 'forced' repump mode at 532nm. The result

of 100 PLE scans at 0.28μW of 637nm is shown in fig. (5.15) with fitted δv_{tot}=4.2GHz and δv_{hom}=247MHz. The averaged PLE signal intensity is 685ct/s above background.

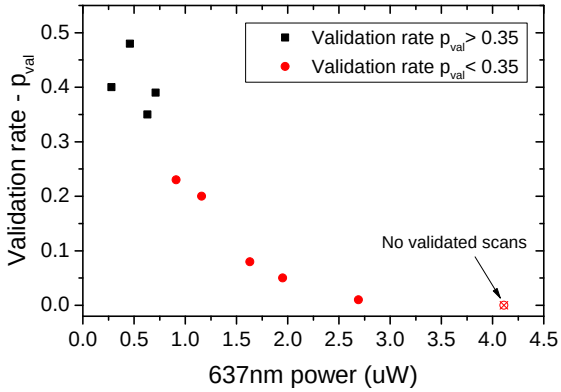

Figure 5.16: A dataset of raw PLE measurement validate rate p_{val} versus 637nm excitation power taken from NV66 in sample B. The power settings are coarsely divided into two groups.

The same is done while varying the 637nm power and the validation rate p_{val} is plotted in fig. (5.16). The dataset is coarsely divided into high-p_{val} and low-p_{val} groups. The data points in the low-p_{val} group are associated with large uncertainty due to lower amount of validated scans which makes other measured quantities from this group less reliable.

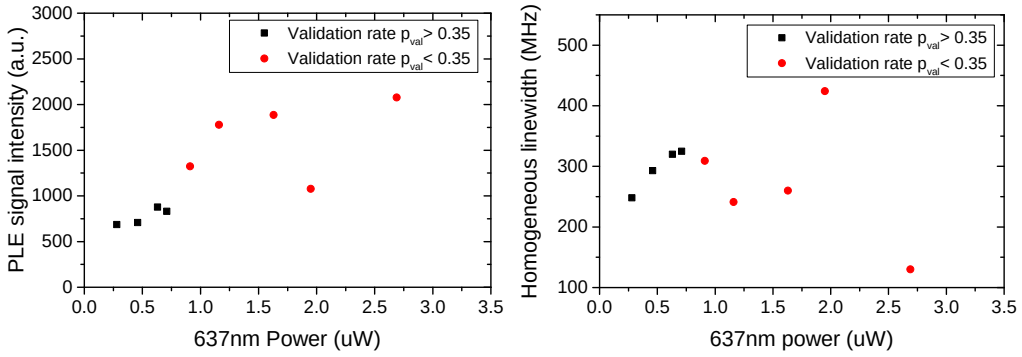

(a) **(b)**

Figure 5.17: **(a)** The averaged PLE signal intensity above background (≈140cts/s) and **(b)** the homogeneous linewidth δv_{hom} as a function of 637nm excitation power. Some power broadening is observable, but there is not enough data point to get a good fit.

The trends in averaged PLE signal intensity and δv_{hom} are plotted in fig. (5.17). Increases in 637nm power do lead to a better *SNR*, and the signal intensity more or less saturates at high power. More importantly, some power broadening of δv_{hom} is observed for the high-p_{val} data points but a power broadening fit is not attempted due to limited data points. A coarse visual extrapolation suggests that δv_{hom} is probably broadened by a factor of 2-3.

Although the power dependence of PLE results probably differs between different NVs, to ensure good data quality and high p_{val}, the 637nm excitation should be kept at sub-μW level.

5.3.3 575nm Repump and Long-Lived Dark State

The alternative repump wavelength at 575nm is also attempted and the narrowest emission bandwidth of the supercontinuum laser is 3000GHz (2nm) as shown in fig. (5.18). This bandwidth is much larger than the linewidth of NV^0 ZPL which ensures the resonant excitation of NV^0.

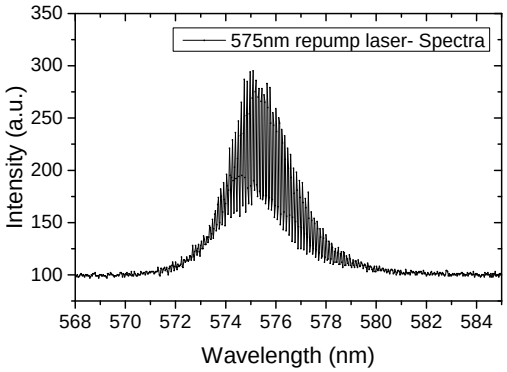

Figure 5.18: The emission spectrum of the supercontinuum laser when set to 575nm emission wavelength.

The measured 575nm power is 1μW at the back of objective lens. This is equivalent to a spectral power density of 0.33nW/GHz. For reference, previous literature work [41] used a sub-GHz single mode dye laser at 100nW, corresponding to a power density of 100nW/GHz. Although cross-system power comparison is non-trivial, our setup certainly has a lower spectral power density.

An ion-implanted NV in sample C is measured with both 575nm and 532nm repump where 4000 and 3000 PLE scans are acquired. The first 500 scans from both dataset are plotted in fig. (5.19). In total, 415 and 694 scans are validated for each dataset, corresponding to a validation rate of p_{val}=0.10 and 0.23 respectively.

To further quantify the effectiveness of both repump methods, the recharge probability p_{rec} is obtained by fitting measurement statistics histograms as shown fig. (5.20). It is found that p_{rec}=0.25 and 0.22 for 575nm and 532nm repumps which is fairly similar. This

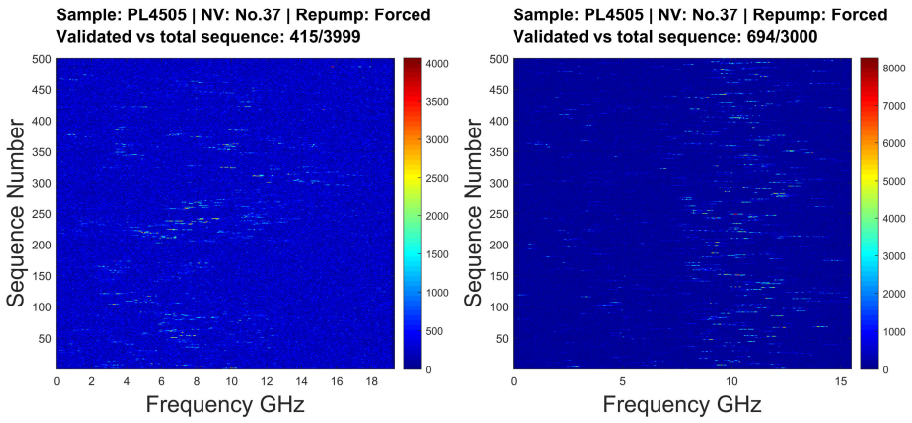

(a) With 575nm repump laser. **(b)** With 532nm repump laser.

Figure 5.19: 500 measurement sequences using **(a)** 575nm and **(b)** 532nm repump lasers. Both scan1 and scan2 data are shown before validation process.

suggests that despite the low spectral power density of 575nm excitation, both repump wavelengths is equally effective in converting NV^0 to NV^-. The main difference between the two is that the 575nm dataset has a lot more instances where >40 repumps pulses are required to restore NV^-. The longest gap between two validated PLE scan is about 140 scans.

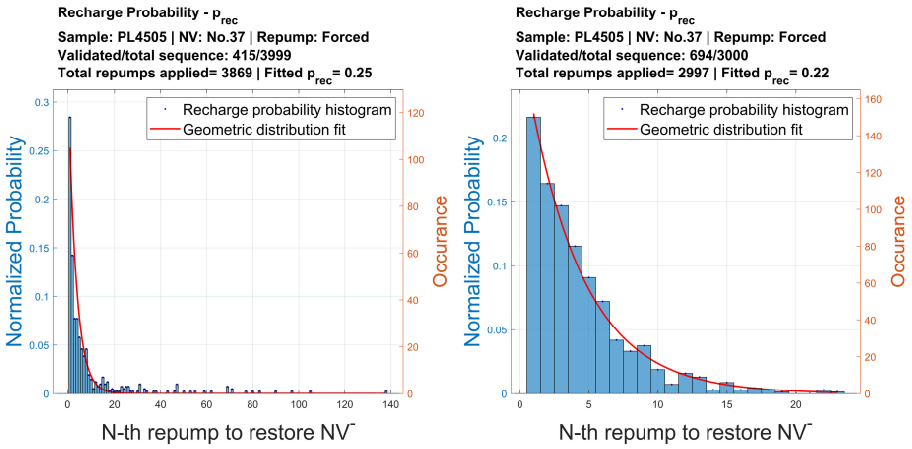

(a) With 575nm repump laser. **(b)** With 532nm repump laser.

Figure 5.20: Number of using **(a)** 575nm and **(b)** 532nm repump lasers.

We picture this intermittent turn-off behaviour as the NV centre entering a long-lived dark state ($p_{\text{val}}<p_{\text{rec}}$) that is difficult for 575nm repump laser to restore. The NV could be in the NV^0 charge-state or even non-fluorescing NV^+ state in an electron-depleted local environment. In both cases, the NV is taken out of NV^0/NV^- conversion cycle which leads to the ineffectiveness of 575nm repump at low power.

One of the most praised advantages of 575nm repump in literature [41, 42] is the reduced spectral diffusion and overall ZPL linewidth δv_{tot}. The results of linewidth analysis for above dataset are shown in fig. (5.21). The homogeneous linewidth are found to be δv_{hom}=260MHz and 400MHz for 575nm and 532nm. We reckon the difference in δv_{hom} is not intrinsic because neither of the post-alignment dataset shows a good Lorentzian fit. It is probably caused by slight misalignments between validated scan1 data.

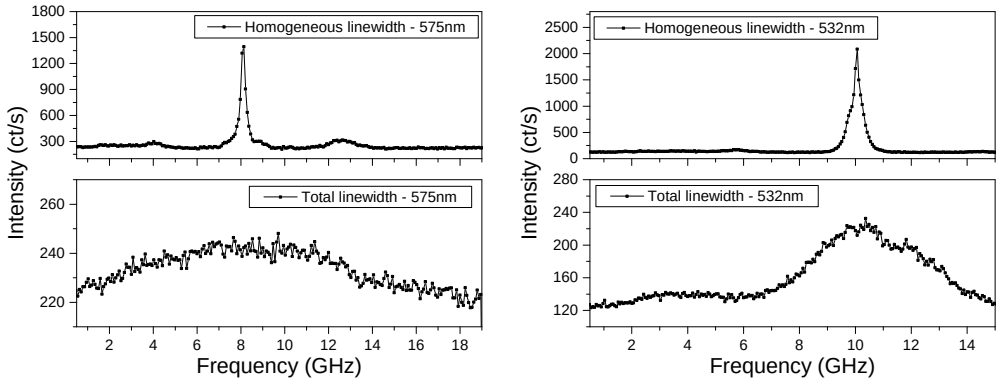

(a) With 575nm repump laser. **(b)** With 532nm repump laser.

Figure 5.21: Linewidth measurement using both 575nm and 532nm repump lasers. The homogeneous linewidths are fitted to be δv_{hom}=260/400MHz and the total linewidths are δv_{tot}=11.2/4.2GHz (575nm/532nm).

In contrary, the fitted total linewidth δv_{tot}=11.2GHz and 4.2GHz for 575nm and 532nm repumps should be intrinsic because δv_{tot} are obtained without data alignment. The 575nm repump induces more severe spectral diff fusion than the 532nm repump which disagrees with literature works.

Fundamentally, the spectral diffusion arises the Stark effect of ZPL transitions. The extend of inhomogeneous broadening is proportional to the total number of distinct local electric field configurations which is determined by the 637nm ionization pulse. It is possible that the 575nm photons are too weak to deplete electrons from certain charge-traps which always contribute towards additional electric field configurations. On the other hand, 532nm photon is strong enough to excite these defects such that they are effectively 'invisible' when considering the local electric field configuration. As a result, NV^- under 532nm repump interacts with less charged lattice site which gives less local electric field configurations and a smaller overall linewidth δv_{tot} is observed.

5.3.4 Transition Linewidths Comparison

The homogeneous and total linewidth data from all samples mentioned in section (5.3.1) are plotted in fig. (5.22). Some NVs are taken with high power 637nm excitation, but this does not affect the validity of the following discussions.

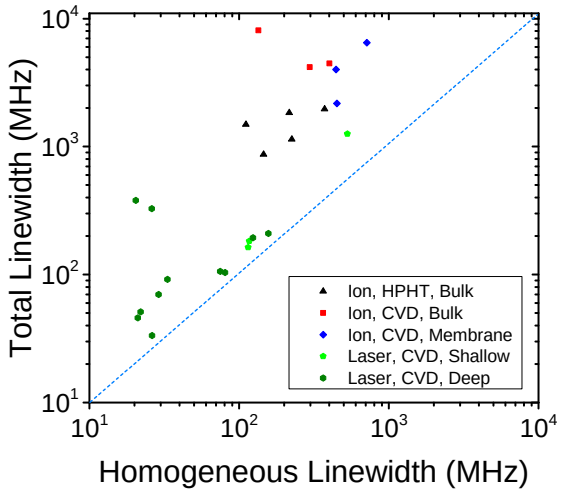

Figure 5.22: A scatter plot of total and homogeneous linewidth from all samples listed in table (5.6). Sample B/C are grouped together as 'ion-implanted CVD, bulk' and sample G/H are grouped together as 'laser-writing CVD, shallow'.

Most obviously, compared to the laser-written NVs, the ion-implanted NVs generally shows larger $\delta\nu_{\text{tot}}$ and $\delta\nu_{\text{hom}}$. The reason is two-fold. Firstly, the ion-implanted NVs are located near the sample surfaces such that they are more susceptible to surface charge states. A more inherent problem with ion-implantation is the unhealable ion damage in the lattice and its correlation with broadened $\delta\nu_{\text{tot}}$ and $\delta\nu_{\text{hom}}$ has been shown by [43]. Both surface charge states and lattice defects contribute additional non-radiative decay pathways which introduces T_1-type decoherence as $\delta\nu_{\text{hom}}$ broadening. As charge traps, they also induce T_2^*-type dephasing in the form of spectral diffusion leading to $\delta\nu_{\text{tot}}$ broadening.

Compared to the ion-implanted NVs in bulk samples, the ion-implanted NVs in μm-thick membranes experience a further $\delta\nu_{\text{hom}}$ deterioration. A similar observation is reported by [28], but no conclusion was drawn by the authors regarding the origin of the problem. We reckon that the broadened $\delta\nu_{\text{hom}}$ in the membrane is also caused by the exposure of NVs to surface charges states because the NV in the membrane is exposed to one additional

surface.

Moreover, the ion-implanted NVs in the HPHT sample (black marker) shows narrower linewidths comparing to their CVD counterparts. It is reported in [43] that following ion-implantation, NVs formed by native nitrogen show narrower linewidths compared to those formed by ion-implanted nitrogen because of the associated ion-implantation damage. Recall that from the NV yield analysis in section (5.1.1.2), we concluded that the HPHT sample has a higher native [N] in the {111} growth sector. Therefore, the observed narrower linewidth in this sample is probably obtained from NVs with native-nitrogen.

Last but not least, the laser-written NVs generally show excellent optical coherence of ZPL transitions with linewidth at δv_{hom}<100MHz and δv_{tot}<200MHz. Compared to the deep laser-written NVs as previously reported by [19], the 'shallower' (≈10μm-deep) NVs fabricated in this work show no significant decoherence except one data point. Of course, these NVs are located nowhere near diamond surfaces, and their optical coherence in membranes is subject to further investigation. Current dataset suggests the potential is indeed there.

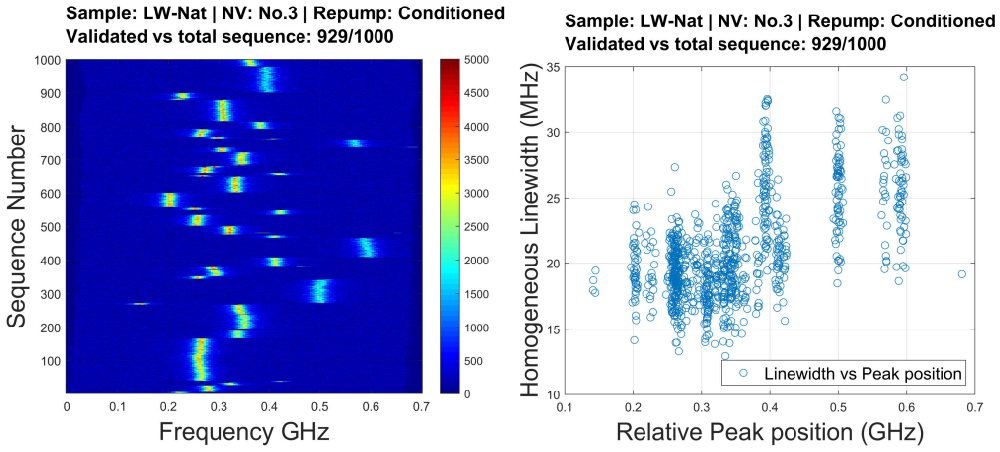

(a) **(b)**

Figure 5.23: A PLE dataset from NV3 in sample F: **(a)** summary of 1000 raw scans and **(b)** a scatter plot of single-scan linewidth versus relative resonance position. The data points that are closer to the blue dotted line suffers less from the spectral diffusion.

Also, we note an interesting observation of δv_{hom} dependence on ZPL frequency. A PLE dataset of a laser-written NV is plotted in fig. (5.23) where distinct ZPL positions can be identified. It is observed that the homogeneous linewidth δv_{hom} is slightly broader at

higher ZPL frequencies. Assuming that each ZPL position is related to a distinctive local charge configuration, it is probably not surprising that certain configurations contribute more non-radiative paths which broaden δv_{hom}. Recent work by [64] demonstrates the identification of an individual defect site near NV with blinking statistics. The observation in fig. (5.23) might also enable a similar capability to probe local NV environment in a deterministic way.

5.3.5 Switching Probabilities and Long-Lived Bright States

As mentioned in section (1.2.3), the PLE validation rate p_{val} is directly related to the charge-state preparation efficiency η_{cs} for entanglement generation with NV centres. Histograms of p_{val} is plotted in fig. (5.24) for both ion-implanted and laser-written NVs. Generally speaking, the laser-written NVs exhibit much better charge-state stability. The maximum observed p_{val} is 0.973 where only 27 repumps have to be applied in a 1000 scan measurement. In fact, the laser-written NVs with low p_{val} are measured with high 637nm excitation power >0.5μm. Further improvement of p_{val} can be expected at weak excitation regime.

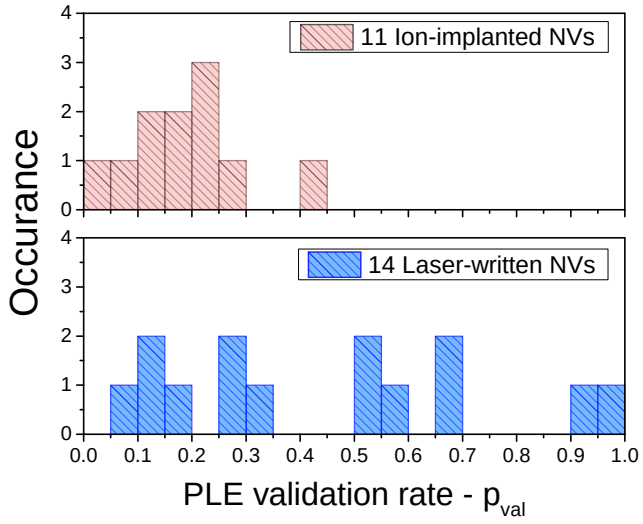

Figure 5.24: A comparison of PLE validation rate p_{val} for the ion-implanted and laser-written NVs.

In principle, the PLE validation rate p_{val} is dependent on the balance between the ionization probability p_{ion} and the recharge probability p_{rec}. A scatter plot p_{rec} versus p_{val} is presented in fig. (5.25) for all measured NVs. Imagine that the NV always starts as

NV^0 at the start of PLE scans, p_{rec} should be equal to p_{val} which corresponds to dashed blue line in fig. (5.25). Most of the ion-implanted NVs measured in this work falls on this line, suggesting that almost every 637nm scan converts the ion-implanted NV to NV^0. Apparently the charge-state equilibrium of ion-implanted NV strongly favours the NV^0 charge-state.

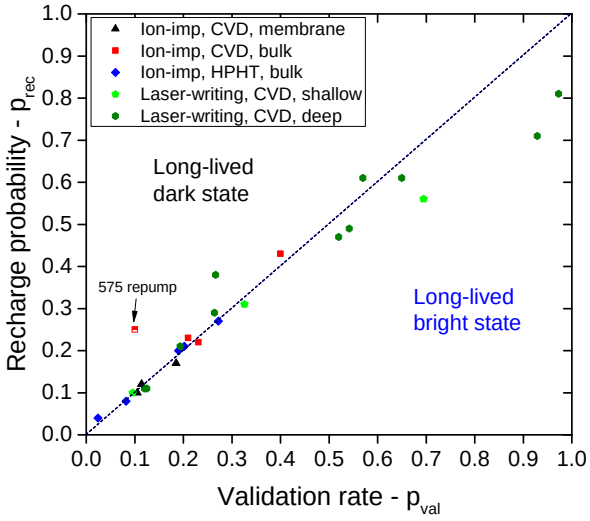

Figure 5.25: A scatter plot of the recharge probability p_{rec} against the validation rate p_{val}. Data from all NVs from all samples listed in table (5.6) are included.

Extending this analysis, the off-diagonal data points in fig. (5.25) suggests the presence of long-lived dark states ($p_{val}<p_{rec}$) and long-lived bright states ($p_{val}>p_{rec}$). The dark states exhibit consecutive dark PLE scans under non-stop repump excitation and an example of such behaviour is given in section (5.3.3). On the contrary, the bright states show consecutive bright PLE scans under non-stop 637nm excitation and such an NV is shown in fig. (5.23). This particular NV is capable of maintaining NV^- charge-state for more than 100 consecutive 637nm scans which is quite remarkable.

Next, a scatter plot of p_{rec} versus p_{ion} is shown in fig. (5.26). We note that only the data from laser-written NVs are included here because p_{ion} is exclusive to the 'conditioned' repump mode. Interestingly, a negative correlation between p_{rec} and p_{ion} is observed in fig. (5.26). For reference, these two terms are calculated based on independent recharge/ionization statistics hence this correlation should be intrinsic. Two example data plots from NV8 in sample F is shown in fig. (5.27).

In principle, the charge-state stability of a particular NV is determined by its local charge

environment. Therefore, it is perhaps not too surprising to observe a negative correlation between p_{rec} and p_{ion}.

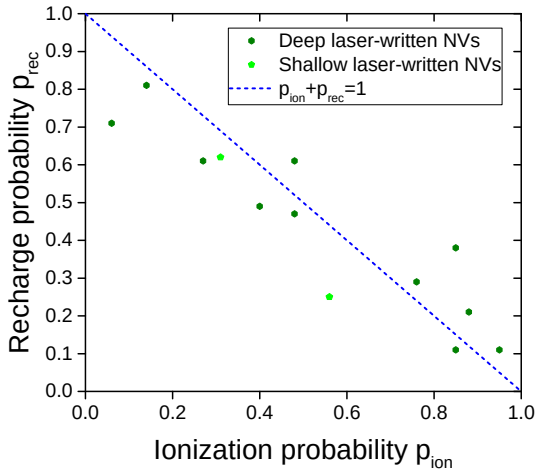

Figure 5.26: The recharge probability p_{rec} plotted against the ionization probability p_{ion}. Data of p_{ion} is only available from laser-written NVs under 'conditioned' repump mode. The blue dashed line is a visual guidance of p_{rec}+p_{ion}=1.

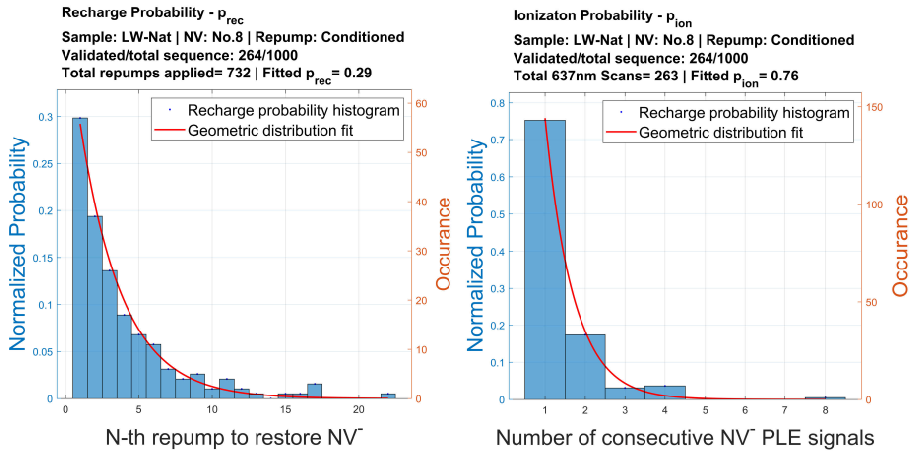

(a) Recharge probability. **(b)** Ionization probability.

Figure 5.27: Histograms of recharge/ionization probability calculation from a laser-written NV8 in sample F.

5.4 Conclusions

In this chapter, we first demonstrated the membrane fabrication procedures to produce ultra-thin diamond membranes with ion-implanted NVs. Following the observation of NV fluorescence quenching due to chlorine-related damage, the etching protocol is modified

to include a pure O^2 etch. Efforts are also made to improve membrane surface quality by dividing etches into smaller time intervals to lower the average temperature during the etch. The surface roughness improvement helps to reduce scattering loss in cavity experiments.

Membrane fabrication with laser-written NVs is also attempted, and a scalable fabrication technique to cover a large area of the sample surface is presented. As an on-going project, the preliminary data suggest a promising NV creation yield of 11% within the stochastic limit. Because the NVs are written at a depth of 15µm, fabrication challenges such as etching from two-sided etching remain to be addressed.

Characterisation of the optical coherence of NV centres is carried out with PLE measurements. In addition to conventional linewidth comparison, we also gained insight into the charge-state stability via measurement statistics analysis. Both aspects of PLE measurement proved that for coherent NV generation, laser-writing is a superior fabrication technique than conventional ion-implantation method.

Firstly, in terms of transition coherence, the laser-written NVs exhibits much better homogeneous linewidth δv_{hom} and total linewidth δv_{tot}. The narrow δv_{hom} is indicative of low non-radiative decay pathways contribution, leading to a short population relaxation T_1 time. Consequently, the degree of photon indistinguishability is improved according to:

$$I = \frac{T_2}{2T_1} \qquad \text{(eq. (1.8) revisit)}$$

It is shown in section (1.1.3) that I has the same expression as the excitation efficiency η_{ex} which directly contributes towards the entanglement success rate P_{succ}. The η_{ex} term is more conveniently written in linewdith terms as:

$$\eta_{\text{ex}} = \frac{\delta v_{\text{hom}}}{\delta v_{\text{tot}}} \qquad \text{(eq. (1.14) revisit)}$$

where v_{hom} is the lifetime-limited homogeneous linewidth. Assuming a moderate v_{hom}=100MHz, the averaged δv_{tot} of ion-implanted and laser-written NVs in fig. (5.22) are 3GHz and 100MHz respectively, suggesting a factor of 30 advantage in I and η_{ex} for laser-written NVs. However, we do note that to date, most advanced photon interference and entanglement experiments in literature are carried out with native or grown-in NVs [18, 22, 35,

36], not ion-implanted NVs. Hence, the linewidth advantage of laser-written NV discussed above does signify its strength, but it is not necessarily a fair comparison.

Secondly, the laser-written NVs also exhibits excellent charge-state stability in PLE measurements as quantified by the high PLE validation rate p_{val}. Due to similar resonance excitation condition at 637nm, p_{val} from PLE measurement is very translatable to the charge-state preparation probability η_{cs} in entanglement generation operations. The average measured p_{val} from a laser-written NV in this work is around 0.75. Compared to an averaged q_{val} of 0.25 for ion-implanted NVs, a factor of 3 improvement in η_{cs} and 9 times higher P_{succ} can be expected.

Additionally, the laser-writing technique also has the added benefit of high positioning accuracy [19] and long NV spin coherence time [93]. The development of laser-writing technique is certainly a crucial advancement towards the scalable fabrication of coherent NV centres for quantum network and computation applications.

Chapter 6

Low-Temperature Cavity-Coupling of NV ZPL

The low-temperature cavity-coupling data of an NV centre (A4-NV4) from membrane Gen2-m3 will be presented in this chapter. The optical properties of A4-NV4 are examined in both on-mirror (fig. (6.1)(b)) and in-cavity configurations (fig. (6.1)(c)).

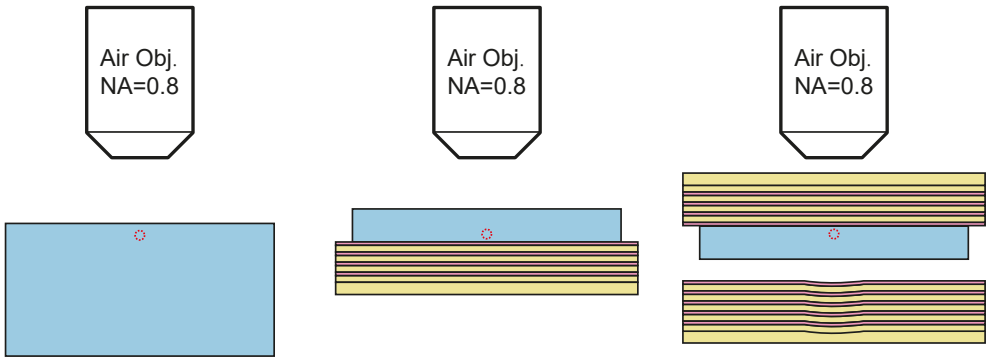

(a) 'Free-space' **(b)** 'Membrane-on-mirror' **(c)** 'Membrane-in-cavity'

Figure 6.1: Experimental configurations corresponding to different dielectric environment: **(a)** the free-space bulk configuration; **(b)** the membrane-on-mirror configuration; **(c)** the membrane-in-cavity configuration (including the on and off-resonance scenarios). The NV location is marked with red dotted circles.

The in-cavity configuration in this chapter is further divided into the on- and off-resonance sub-configurations to reflect the relative position between the cavity mode and the NV ZPL. Variable naming convention follows that in chapter (4).

6.1 On-Mirror Characterization

The target NV (A4-NV4) from Gen2-m3 is firstly characterized at 4K in the on-mirror configuration with the NV implanted surface facing towards the DBR mirror. Figure (6.2) shows an optical microscope image of Gen2-m3 on a DBR mirror and the areas scanned with the confocal microscope are marked in the zoomed-in image.

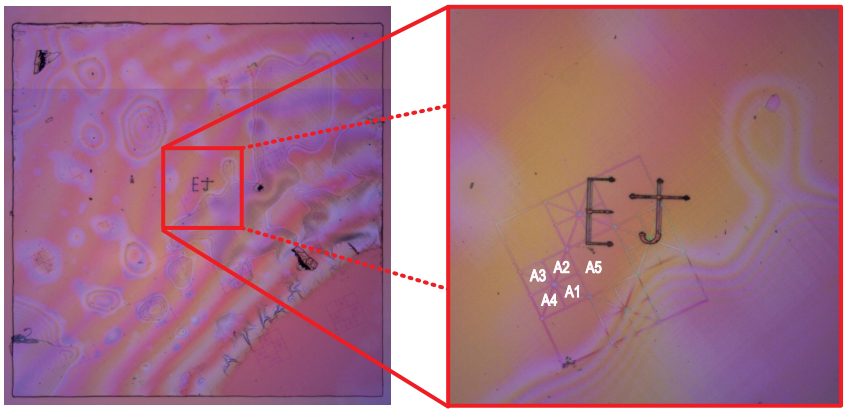

Figure 6.2: An optical microscope image of the Gen2-m3 membrane: **(left)** showing the whole membrane sample; **(right)** a zoomed-in image of the area of interest. The mirrored 't3' mark is a graphitic orientation marker engraved by laser-writing and the faint rectangular grids (150µm across) are the FIB-milled registration marks for defect relocation.

Two 30µm-ROI (region of interest) confocal PL images (no collection filter) of area A4 and A1 are shown in fig. (6.3). The active NV centres are marked in red circle. It was previously mentioned in section (5.1.3) that the yield of active NV centre in finished membrane samples is very low compared to the starting defect density. It is certainly no exception in these two areas. Among all six 30µm-ROI areas that has been characterized in fig. (6.2), the average NV density is about 1-4 per area. We suspect that most other visible point defects are also NV centres but in a different charge state. They also tend to get photo-bleached quickly under laser exposure which we attribute to either the residue etching damage or unfavourable surface termination.

Two close-up images of A4-NV4 with and without a narrow-band 638/3nm band-pass filter are shown in fig. (6.4). Due high mirror background fluorescence (ten times higher than defect signal) at low-temperature, suitable spectral filtering is often required to locate NV centres. While the 638/3nm filter emphasizes NV ZPL emission, a 709/167nm

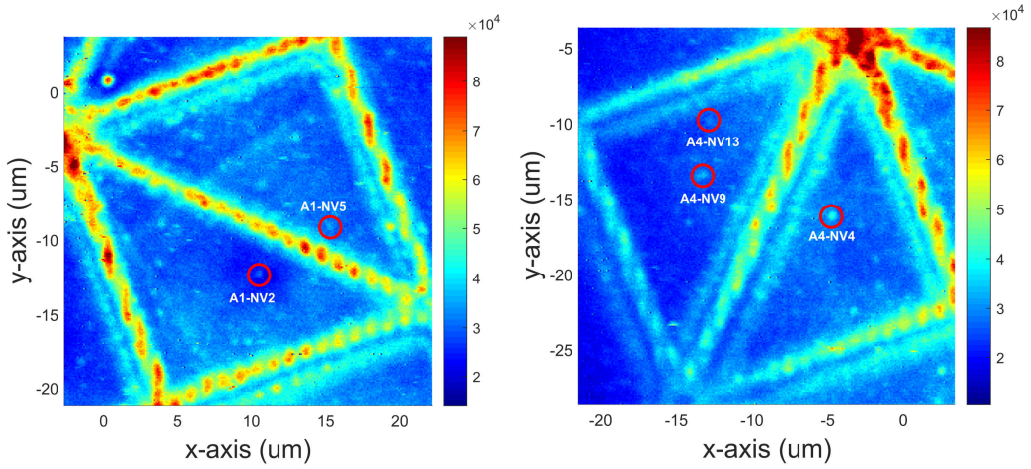

(a) **(b)**

Figure 6.3: On-mirror PL images of Gen2-M3 sample in area **(a)** A1 and **(b)** A4. All the spectrum-confirmed active NVs in the areas are marked with red circles. Excitation power of 532nm laser is around 1.5mW.

band-pass filter is used more routinely to improve general imaging quality. High background also means careful treatment of background subtraction is required in other optical measurements.

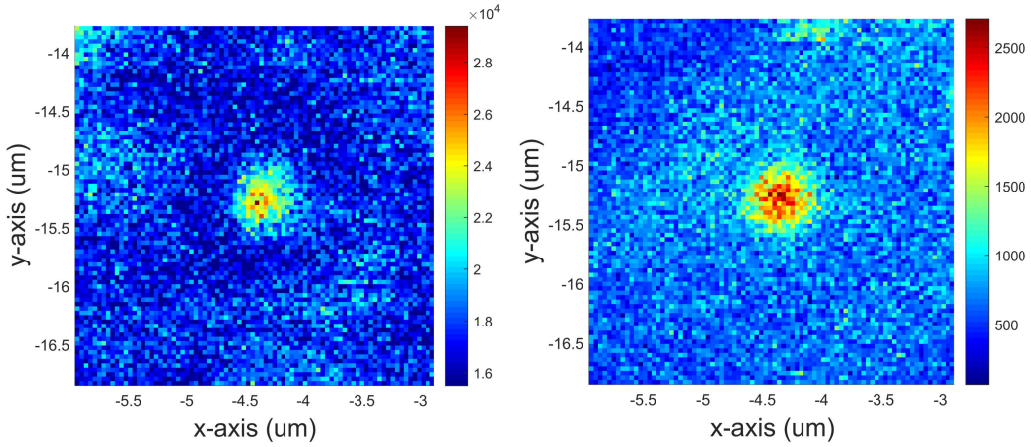

(a) No collection filter. **(b)** With a 638/3nm band-pass.

Figure 6.4: Zoomed-in PL images of A4-NV4 **(a)** without any collection filter and **(b)** with a narrow-band 638/3nm band-pass filter.

6.1.1 Spectrum Analysis and ZPL Branching Ratio

The PL spectrum of A4-NV4 are plotted in fig. (6.5)(a) where a strong NV^- ZPL is observed at 637nm. The shape of PSB shows a modulation due to the membrane. In principle, it is possible to fit the membrane thickness using this modulation with 1D transfer matrix. However, in fig. (6.5)(a) there only exists one modulated peak within

the mirror stopband, indicating that the membrane is <1.5μm at this location. A proper TMM fit can not be implemented due to the lack of modulation peaks. The membrane thickness is determined more accurately in section (6.3.4) using a cavity mode map.

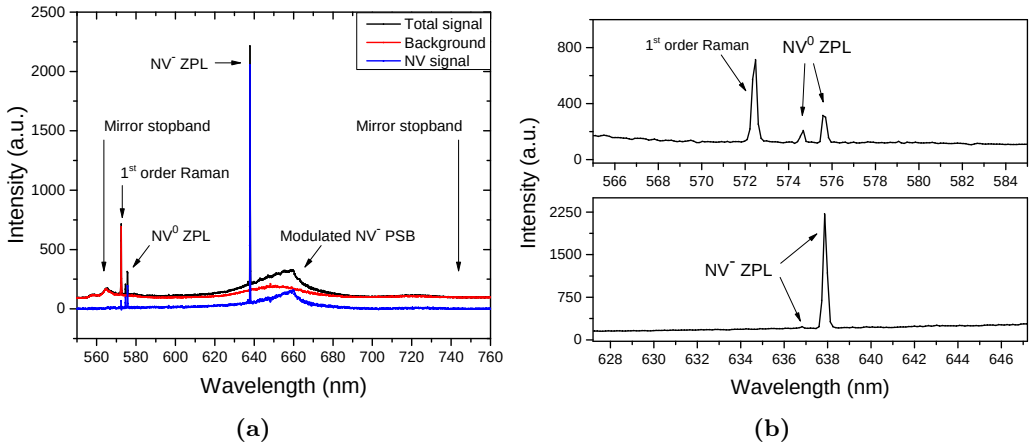

(a) **(b)**

Figure 6.5: The low-temperature NV spectrum **(a)** over the entire NV emission range and **(b)** around both the NV^0 and NV^- ZPL regions. Both the spectrum are in low-resolution setting of the spectrometer with a resolution of 0.13nm.

The high resolution spectrum in the NV^0 and NV^- ZPL regions are plotted in fig. (6.5)(b). The first-order Raman line of the 532nm excitation laser is visible at 572.5nm along with two NV^0 ZPLs around 575nm. Two NV^- ZPLs are present near the 637nm region while one is less visible in the current plot due to unfavourable excitation polarization setting. The splitting between the NV^0 ZPLs are roughly identical to the splitting between the NV^- ZPLs (spectrometer resolution= 0.13nm). We reckon all four ZPLs belong to the same defect because previous work [59] reported that lattice strain splits NV^0 and NV^- ZPLs to the same extent. The single-photon emission property of A4-NV4 is more formally confirmed with an HBT measurement in a later section.

The on-mirror ZPL branching ratio $\zeta_{\text{spec}}^{\text{mir}}$ of A4-NV4 is estimated using the 'NV signal' dataset in fig. (6.5)(a) which is obtained by subtracting the 'total signal' data with the 'spatial background' data. By dividing the area under ZPL by the area under the full NV spectrum (600nm to 850nm), $\zeta_{\text{spec}}^{\text{mir}}$ is found to be 10.35%. We note that for both integrations, the baseline is set at 0. This mimics the experimental filtering condition where a tiny portion of PSB photons in the ZPL region is included in ZPL photon collection. The obtained $\zeta_{\text{spec}}^{\text{mir}}$= 10.35% is a lot larger than the reported bulk values of 2-4% from some literature works, but is comparable to that in [94] where substrate-induced PSB

suppression is reported.

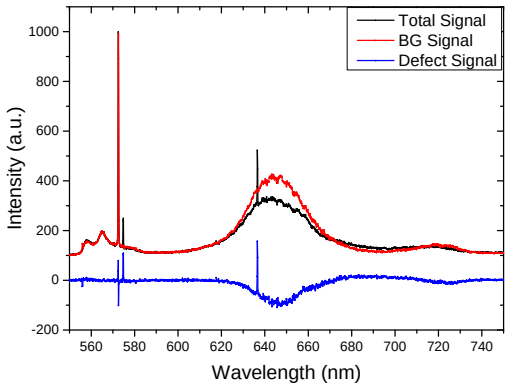

(a)

Figure 6.6: An example showing false background subtraction due to fluorescence modulation resulting in a negative area under the curve. Data were taken from A4-NV13 from the same area.

It has to be noted that $\zeta^{\text{mir}}_{\text{spec}}$ via spectrum analysis is less accurate for NVs in a membrane sample. Due to the membrane thickness wedge, both signal intensity and spectral composition are modulated differently at different locations. Such discrepancy can lead to some extent of false background subtraction, and an extreme example is shown in fig. (6.6). One might attempt to match the modulation in the 'total signal' and the 'spatial background' dataset by taking repeated readings, but the error is almost inevitable. As a result, $\zeta^{\text{mir}}_{\text{spec}}$ via spectrum analysis is likely to be an overestimation of the true value. An alternative method of obtaining ζ^{mir} via power saturation measurement is shown in the next section.

6.1.2 Power Saturation and ZPL Branching Ratio

As mentioned in last section, the membrane thickness wedge leads to a spectral modulation and an intensity modulation at different sample locations which is problematic in spectrum analysis. In order to account for these two effects and measure ζ^{mir} accurately, the fitting model introduced in section (3.5.3) is adopted. Recalling the power saturation fitting function for the 'total signal' dataset:

$$I = \frac{I_{\text{sat}} P}{P + P_{\text{sat}}} + A_{\text{pol}} \times H_{\text{bg}} + I_0 \qquad \text{(eq. (3.10) revisit)}$$

where H_{bg} is the polynomial approximation for the 'spatial background' dataset and A_{pol} is a scaling factor. To determine ζ^{mir} via power saturation measurement, two separate readings are taken with and without the 638/3nm filter to represent ZPL emission and full-spectrum emission.

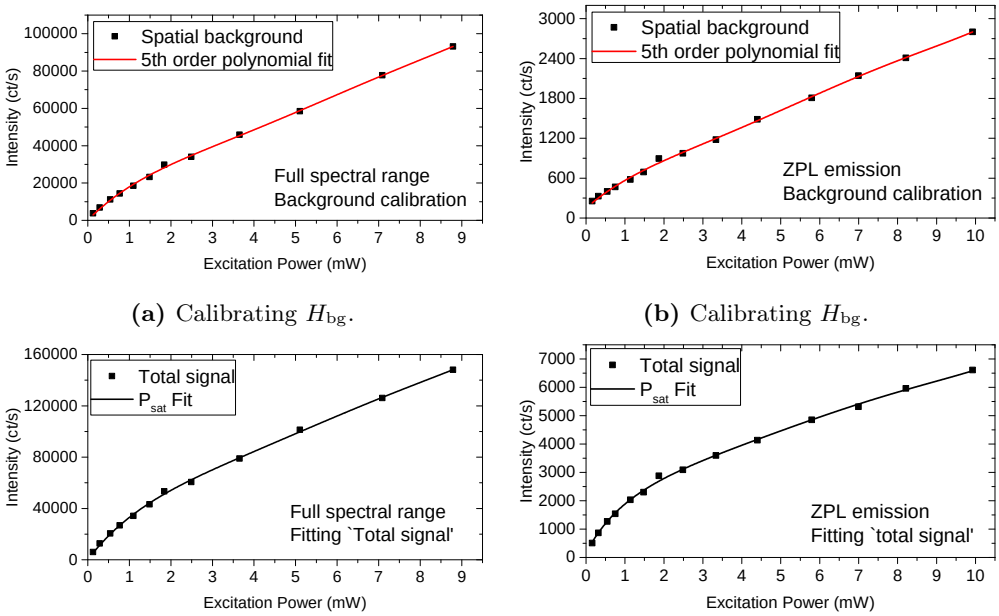

(a) Calibrating H_{bg}.

(b) Calibrating H_{bg}.

(c) Fitted $I^{\mathrm{mir}}_{\mathrm{sat,full}}$=36,253ct/s, $P^{\mathrm{mir}}_{\mathrm{sat}}$=2.67mW and A_{pol}=1.29.

(d) Fitted $I^{\mathrm{mir}}_{\mathrm{sat,zpl}}$=2,491ct/s, $P^{\mathrm{mir}}_{\mathrm{sat}}$=1.33mW and A_{pol}=1.60.

Figure 6.7: Power saturation measurement of A4-NV4: **(a)(c)** from the full spectral range; **(b)(d)** in the ZPL region only. Both background components in the 'total signal' dataset are calibrated with a polynomial fit H_{bg} of the 'spatial background' dataset with a scaling factor A_{pol}.

The 'spatial background' dataset in each scenario is firstly calibrated with a fifth order polynomial H_{bg}. Then H_{bg} is substituted back into eq. (3.10) to represent the background component in the 'total signal' dataset which is fitted by eq. (3.10) with A_{pol} left as a free fitting parameter. The fitted saturation intensities $I^{\mathrm{mir}}_{\mathrm{sat,full}}$ and $I^{\mathrm{mir}}_{\mathrm{sat,zpl}}$ are then used to calculated ζ^{mir}:

$$\zeta^{\mathrm{mir}}_{\mathrm{psat}} = \frac{I_{\mathrm{sat,zpl}}}{I_{\mathrm{sat,full}}} \tag{6.1}$$

The fitting results for A4-NV4 are plotted in fig. (6.7) for both spectral windows. The saturation intensities are found to be $I^{\mathrm{mir}}_{\mathrm{sat,full}}$=36,263ct/s and $I^{\mathrm{mir}}_{\mathrm{sat,zpl}}$=2,491ct/s. Dividing them yields $\zeta^{\mathrm{mir}}_{\mathrm{psat}}$=6.87%, which is lower than $\zeta^{\mathrm{mir}}_{\mathrm{spec}}$=10.35% obtained via spectrum analysis. For NVs in membrane $\zeta^{\mathrm{mir}}_{\mathrm{psat}}$ is more reliable because the membrane-induced spectral and intensity modulation of fluorescence signal is completely avoided via the polynomial

approximation of the 'spatial background' dataset.

6.1.3 Excited-State Lifetime and HBT

Due to time-constraints, the on-mirror excited-state lifetime measurement for A4-NV4 is taken at room-temperature after the low-temperature experiment. Although this is not ideal, we expect the two values to be relatively close.

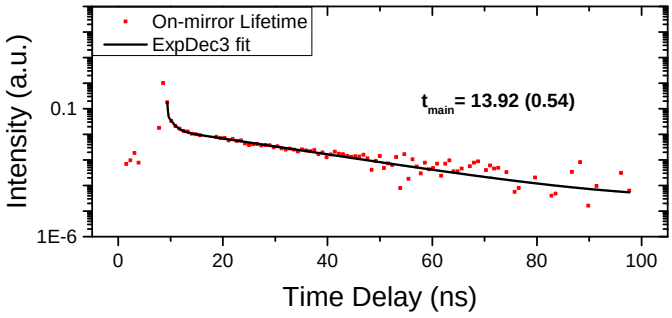

(a)

Fit model	Bin	Fitted Decay Components (ns)		
	(ns)	t_{main}	t_2	t_3
ExpDec3	0.78	13.92(0.54)	0.96(0.13)	0.07(7.98)

(b)

Figure 6.8: **(a)** The excited-state lifetime of A4-NV4 taken at room-temperature and **(b)** the fitting parameters used.

The measured lifetime data is shown in fig. (6.8)(a) which is fitted with a three-component exponential decay fit representing the defect signal, the background fluorescence and the instrument response. The on-mirror excited-state lifetime τ^{mir} is fitted to be 13.92ns which is slightly larger than the commonly reported value of 12ns. The NV emission rate is $\gamma_{\text{full}}=1/\tau^{\text{mir}}=71.84$MHz. Later in section (7.1.6), it is found that the increase in lifetime is related to the LDoS change in the diamond membrane.

The HBT measurement is also taken at room-temperature for A4-NV4 to verify its single photon emission property. The measured $g^{(2)}(t)$ correlation function after normalization is plotted in fig. (6.9) along with a fit using eq. (3.11). The fitted $g^{(2)}(0)$ is found to be 0.53 using eq. (3.14). The HBT baseline $g^{(2)}(0)_{\text{exp}}$ is calculated to be 0.43 using the *SNR*

on each SPAD measured before the acquisition using eq. (3.16):

$$g^{(2)}(0)_{\text{exp}} = 1 - \frac{SNR_{\text{A}}}{SNR_{\text{A}}+1} \times \frac{SNR_{\text{B}}}{SNR_{\text{B}}+1} \qquad \text{(eq. (3.16) revisit)}$$

Because the background baseline corresponds to the expected $g^{(2)}(0)$ value if there were

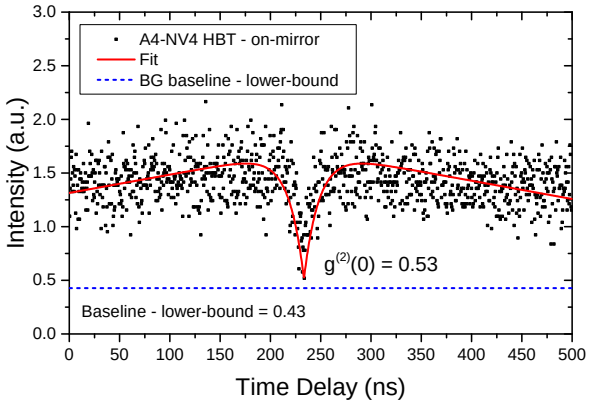

(a)

Parameter	Value
Acquisition	5,139sec
Bin	0.49ns
S_{A}	6,000c/s
BG_{A}	265c/s
S_{B}	2,000c/s
BG_{B}	800c/s
Normalisation	35
Baseline - Lower	0.43

(b)

Figure 6.9: **(a)** Room-temperature HBT measurement of A4-NV4 and **(b)** the corresponding fitting parameters used.

no background contribution, we reckon the fitted $g^{(2)}(0)$ of 0.53 is close enough to the baseline to justify A4-NV4 as a single emitter. This confirmed that the two spectral peaks around 637nm (section (6.1.1)) are the two strain-splitted NV^- ZPLs from A4-NV4. This allow us to use the two ZPLs to perform a simple polarization measurement to determine the NV orientation with respect to the system x-y plane in next section.

6.1.4 Polarization and Dipole Orientation

Assuming that the manufacturer-quoted single crystal orientation of {100} is relatively accurate, all four possible NV axis along [111] directions should be equivalent. Therefore, the dipole orientation of A4-NV4 is measured by monitoring the strain-splitted ZPL dipole intensity on spectrometer while varying the angle of a linear polarizer placed in the collection path. The excitation laser is left in an arbitrary polarization state and unvaried.

The two strain-splitted dipoles of A4-NV4 are identified to be at 637.14nm and 638.26nm respectively. The integrated areas under each dipole transition are plotted fig. (6.10)(a)

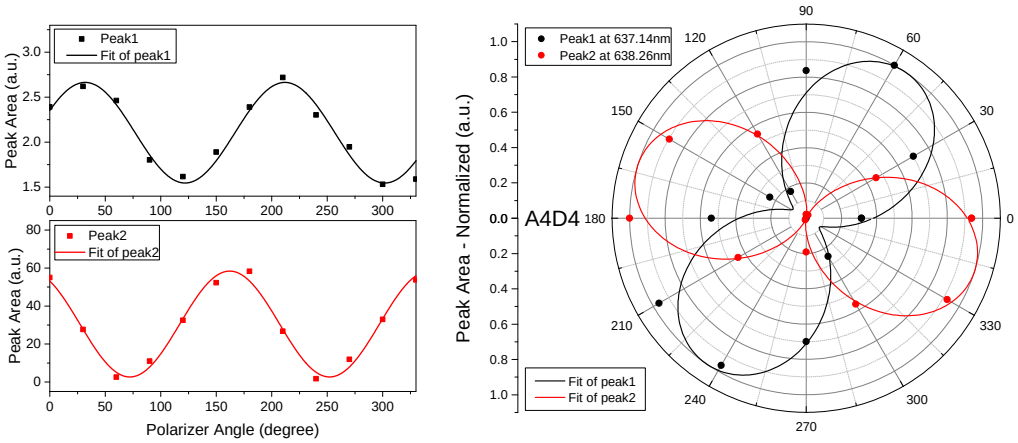

(a) **(b)**

Figure 6.10: Dipole orientation measurement of the strain-splitted ZPL transitions.

versus the polarizer angle and fitted with the Malus-law:

$$I(\phi) = I_0 + I_1 \cos^2(\phi_{\mathrm{x(y)}} + \phi) \qquad \text{(eq. (3.27) revisit)}$$

Clear modulations are observed in both plots and the fits yield ϕ_{peak1}= 2.585rad and ϕ_{peak2}= 0.312rad for the two ZPLs. The relative angle between the two dipoles is then $\Delta\phi$=2.273rad. Recalling the dipole orientation expression from section (3.5.5):

$$A = \frac{1}{2}\arcsin\left(\frac{2}{\sin B \tan B \tan \Delta\phi}\right) \qquad \text{(eq. (3.26) revisit)}$$

where A is the rotation angle in the dipole-dipole co-plane and B is the angle between the NV axis and the optical axis. According to the quoted crystal orientation of {100}, B is assumed to be 0.955rad which unfortunately leads to an unsolvable A using eq. (3.26). This indicates the NV axis is slightly tilted away from the [111] direction.

Nevertheless, it is still possible to obtain a valid range for both B and A angles by using $\Delta\phi$=2.273rad. To yield $\Delta\phi$=2.273rad, angle B has to be in the range of 1.100 to 1.571rad and the corresponding values of angle A are 0.660 to 0rad. Recalling the projection factors

$\cos(\theta_x)$ and $\cos(\theta_y)$ with respect to the system x-y plane for both dipoles from eq. (3.28):

$$\begin{aligned}\cos(\theta_x) &= \frac{X \cdot X_p}{|X||X_p|} = \sqrt{1 - \sin^2 B \sin^2 A} \\ \cos(\theta_y) &= \frac{Y \cdot Y_p}{|Y||Y_p|} = \sqrt{1 - \sin^2 B \cos^2 A}\end{aligned} \qquad \text{(eq. (3.28) revisit)}$$

Using estimated ranges of A and B, $\cos(\theta_x)$ is in the range of 0.838 to 1 and $\cos(\theta_y)$ is in the range of 0.701 to 0. Since the dipole transition at 638.26nm shows much stronger intensity than the 637.14nm dipole, it is reasonable to conclude that the projection factor $\cos(\theta_x)$ belongs to the 638.26nm dipole. The corresponding dipole orientation factor ξ^2 is hence calculated as $\xi^2 = \cos(\theta_x)^2 = 0.85 \pm 0.15$.

6.1.5 Summary of On-Mirror Characterization

Up till now, we have presented the on-mirror optical measurements of A4-NV4. The key measured quantities are summarised in table (6.1) and they will be compared to those of the in-cavity configuration to quantify the cavity-coupled emission enhancement of NV ZPL.

$I_{sat,full}$	$I_{sat,zpl}$	ζ^{mir}	τ^{mir}	$g^{(2)}(0)$ (baseline)	ξ^2
36,253ct/s	2,491ct/s	6.87%	13.92ns	0.53 (0.43)	0.85±0.15

Table 6.1: A summary of key data measured in the on-mirror configuration.

6.2 Benchmark Cavity Characterizations

Prior to the cavity-coupling experiment of A4-NV4, a series of benchmark cavity measurements are conducted to quantify the DBR coating quality and the stability of our cavity setup at low-temperature.

An optical microscope image of the FIB-milled cavity plinth used for the cavity-coupling experiment of A4-NV4 is shown in fig. (6.11). The cavity plinth has a lateral dimension of 300µm and is 250µm above the substrate. The cavities in each column has the same

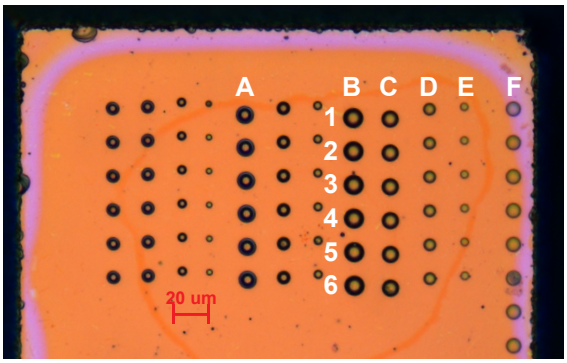

Figure 6.11: A map of cavity features on the high reflectivity cavity mirror that is used in this chapter.

geometry and the individual cavities are identified with a column letter and a row number. The cavity geometry parameters for each marked column in fig. (6.11) are listed in table (6.2).

	A	B	C	D	E	F
$\mathcal{R}$ (μm)	7	12	12	12	12	20
Cavity width (μm)	9.843	11.009	9.664	7.120	5.091	8.272
Cavity depth (μm)	2.022	1.360	1.009	0.540	0.273	0.432
Minimum achievable q	7	5	4	2	1	2

Table 6.2: The geometric parameters of fabricated cavity features: $\mathcal{R}$ is the radius of curvature of the concave cavity feature and q is the cavity mode index.

6.2.1 Finesse of Single-Medium Cavity

The resonant mode linewidth of the cavities in column B, D and E (data for column C was unfortunately corrupted) are measured to obtain cavity finesse benchmarks for the $\mathcal{R}$=12μm cavities. The linewidth measurement in this section is conducted with a transmission setup at room-temperature with no intra-cavity medium. The plinth used in this investigation has the same design as that in fig. (6.11).

Because the sample is mounted on an optical bench in the room-temperature setup, the cavity linewidth is susceptible to environmental disturbance including temperature fluctuation, air convection, mechanical and sound vibrations. The associated linewidth broadening is best minimized at the shortest cavity length where the two mirrors are in close proximity to contact. The cavity is illuminated is a high power supercontinuum broadband laser which helps to reduce integration time and eliminate longer timescale

mode broadening. A typical mode spectrum of 0.05sec integration time is plotted in fig. (6.12) where some mode asymmetry due to drift is still observable.

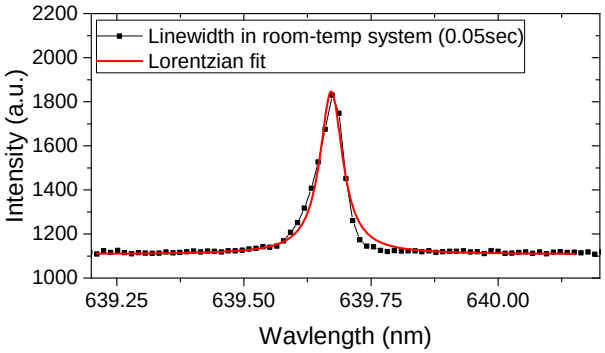

Figure 6.12: A typical cavity mode spectrum taken at integration time of 0.05sec using the supercontinuum laser excitation in transmission setup.

By optimally aligning the cavity mirror with respect to each other, the shortest cavity lengths achieved for column B, D and E are q=7, 5 and 4 respectively. The measured cavity metrics are summarised in table (6.3). Compared to the expected finesse $\mathcal{F}_{\text{fdtd}}$ calculated using FDTD simulations, the measured finesses are almost half of $\mathcal{F}_{\text{fdtd}}$ indicating a factor of two increase in cavity loss than numerical simulations. Translating into absolute round-trip loss, an extra 1,000 ppm loss is present in each cavity.

	q	w_{cav}	Q	$\mathcal{F}_{\text{meas}}$	$\mathcal{F}_{\text{ana}}$	$\mathcal{F}_{\text{tmm}}$	$\mathcal{F}_{\text{fdtd}}$
B	7	0.057nm	11,228	1,871	3,138	3,807	4,042
D	5	0.069nm	9,275	2,318	3,138	4,096	4,555
E	4	0.075nm	8,553	2,844	3,138	4,315	4,849

Table 6.3: The cavity figure of merits measured in a transmission setup at room-temperature. The measured cavity finesse is compared to the expected values calculated using analytical expression $\mathcal{F}_{\text{ana}}$, TMM treatment $\mathcal{F}_{\text{tmm}}$ and FDTD simulation $\mathcal{F}_{\text{fdtd}}$.

The source of these additional loss is less clear. The nominal absorption of DBR coating is about 10ppm which is negligible. One main contributor could be the mirror coating roughness which is measured to be around 0.8nm. Referring back to eq. (2.73), a 0.8nm RMS roughness on both mirrors is equivalent to 500ppm round-trip loss which is still short of the 1,000ppm of extra loss as measured. To fill the gap, it is probably down to arbitrary scattering loss and coating imperfections which are difficult to pinpoint precisely. So for now, we just refer to these as real-world hidden losses.

6.2.2 Low-Temperature System Linewidth Stability

On of the key differences between our low-temperature system and the room-temperature system in terms of stability is that the bath cryostat has no temperature fluctuation and air convection inside the vacuum tube. Extra measures are also taken to reduce mechanical and sound vibrations by placing the cryogenic vessel on a 150kg metal platform with a set of Thorlabs PWA074 passive isolation mount. These are capable of providing 90% of damping efficiency for >15Hz vibrations. The sidewalls are fitted with sound-proof foams.

To quantify the effectiveness of these measures, cavity linewidths are measured in the low-temperature system as a function of spectrometer integration time from 0.5sec to 60sec as shown in fig. (6.13). The minimum integration time is limited to 0.5sec because the illumination source used in this case is the mirror fluorescence which is much weaker than the supercontinuum laser excitation in the transmission setup.

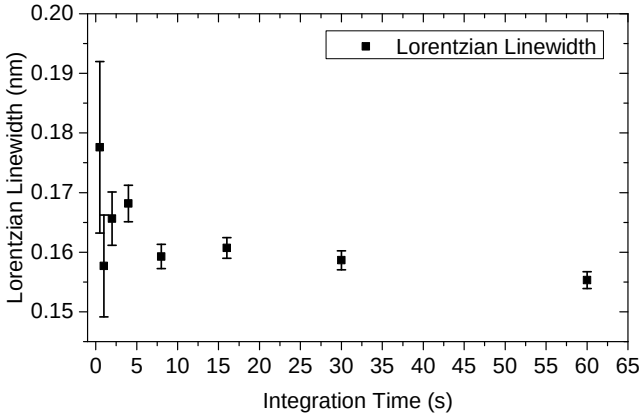

(a)

Figure 6.13: Fitted cavity linewidth versus spectrometer integration time in bath cryostat on the isolation enclosure platform.

Focusing on the trends of linewidth variation, the measured cavity linewidth clearly converges at larger integration time. The fitting error on the shorter timescale is expected because of the reduced data quality given the smaller integration time. The fact that the cavity linewidth is relatively consistent even at longer timescale indicates that there is limited contribution from vibration-related inhomogeneous broadening on these timescales. A comparison between a 60sec spectrum taken in the low-temperature apparatus and a 20sec spectrum taken with room-temperature setup is also shown in fig. (6.14). The

low-temperature cavity mode resembles the Lorentzian lineshape much better even the integration time is 3 times longer.

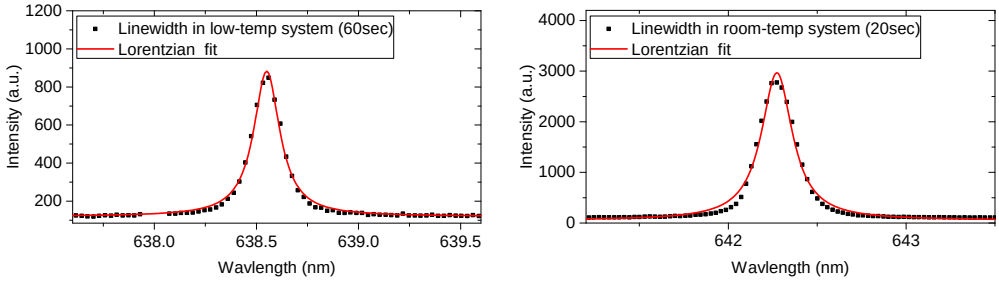

(a) 60sec integration in low-temperature system.

(b) 20sec integration in room-temperature system.

Figure 6.14: A comparison of cavity mode shape between **(a)** a low-temperature spectrum integrated for 60sec and **(b)** a room-temperature spectrum integrated for 20secs.

The system stability over a longer period of time in the low-temperature system is also assessed with a cavity-coupled ZPL emission from an NV centre. Figure (6.15)(a) shows 60 frames of 60sec-long spectrum taken over a span of 1hr around 3pm on a weekday. At the beginning of the measurement, the cavity-coupled ZPL signal is maximized by fine-tuning the cavity length. The integrated intensity over the spectral region for each time frame is plotted in Figure (6.15)(b).

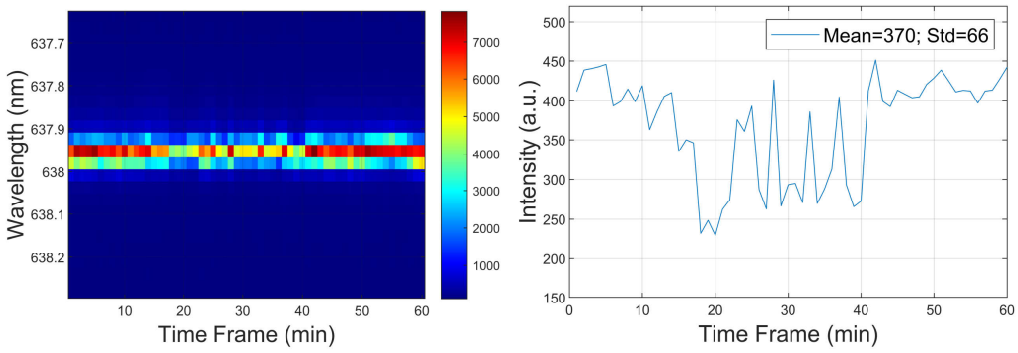

(a) **(b)**

Figure 6.15: **(a)** 60 frames of cavity-coupled NV ZPL spectrum over a span of 1hr. Each frame has an integration time of 60sec. **(b)** Integrated the photon count rate from each spectrum frame in **(a)**.

Although a number of fluctuation events on the timescale longer than 60sec are observed, the system does tend to recover to its original set point. This gives us the confidence in data quality in long acquisition measurements like lifetime and HBT. The maximum integrated intensity is around 440 at the start and the mean signal and standard deviation

is found to be 370 and 66. These statistics can serve as a guideline correction factor when considering fluctuations in long acquisition dataset.

6.3 Cavity-Coupling of A4-NV4

In this section, a complete set of characterization data of A4-NV4 coupled with a $\mathcal{R}$=12μm cavities is presented. Data from cavity D5 is also briefly mentioned because it shows the strongest observed ZPL output among all cavities that we attempted.Other cavities with different $\mathcal{R}$ have also been attempted, but the dataset is not as complete, and the data quality varies.

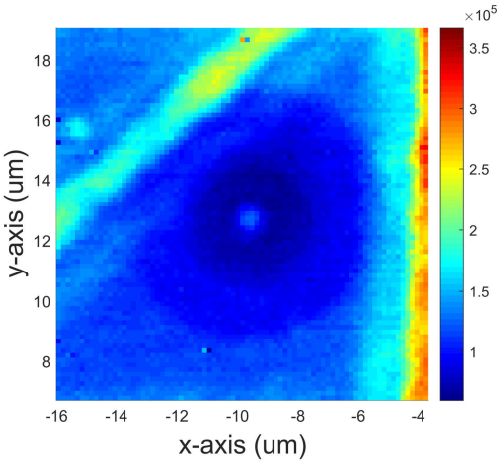

Figure 6.16: Confocal scanning image of a cavity formed at the location of A4-NV4 with the B5 cavity feature.

A typical PL image of cavity-coupled A4-NV4 is shown in fig. (6.16). Compared to the on-mirror configuration, imaging of NVs is generally much more difficult in the in-cavity configuration because the DBR mirror faces away from the collection optics. Defect relocation hence relies on the FIB-milled registration grids. The situation can be slightly improved by forming a cavity around the NV and roughly tune the cavity mode to the NV emission spectrum, as shown in fig. (6.16).

It has been mentioned previously that strong mirror background fluorescence is usually present at low-temperature. This problem gets even worse in the in-cavity configuration because the collection path goes through the whole DBR substrate. Therefore, the usage of narrow band collection filtering is very desirable to improve *SNR* for certain measurements. Figure (6.17) shows a comparison of PL images with and without the 638/3nm

narrow band-pass filter which helps the cavity-coupled NV ZPL to stand out.

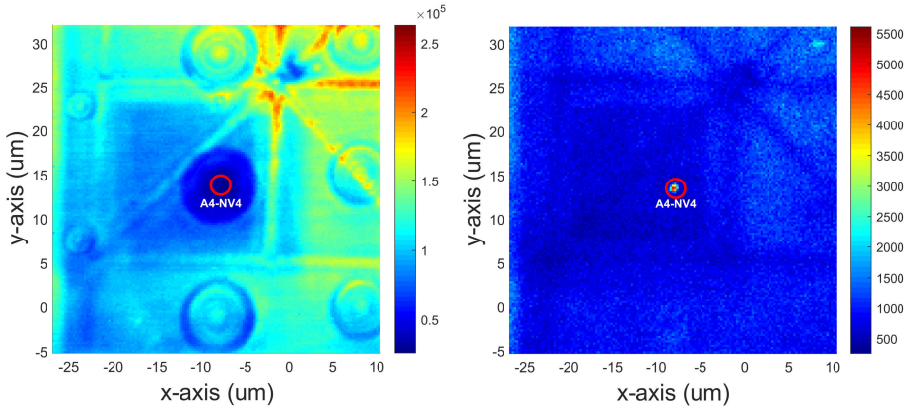

(a) **(b)**

Figure 6.17: Scanning confocal PL images at the A4-NV4 location **(a)** without and **(b)** with a 638/3nm narrow band-pass filter.

6.3.1 Excited-State Lifetime

On coupling A4-NV4 ZPL transition to the q=16 fundamental mode of cavity B5, a number of excited-state lifetime measurements are taken as a function of the cavity mode position. The tuning spectrum of this cavity mode sweeping through the NV ZPL is plotted in fig. (6.18).

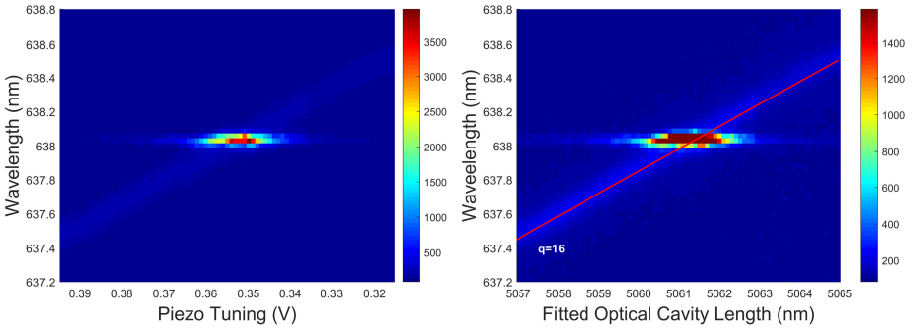

(a) **(b)**

Figure 6.18: High resolution cavity spectrum map showing the fundamental mode of the q=16 mode family sweeping through the ZPL of A4-NV4 **(a)** in tuning voltage scale and **(b)** with voltage scale calibrated to optical length scale. Using eq. (2.68), a fit to the mode tuning is drawn as a red line in **(b)**. The color scale of is adjusted to better show the sweeping direction.

Figure (6.19) shows a series of high resolution spectrum (right) along with the corresponding lifetime dataset (left) taken at four cavity positions. A factor of 10 increase in ZPL peak intensity is observed between the on-resonance and off-resonance spectrum.

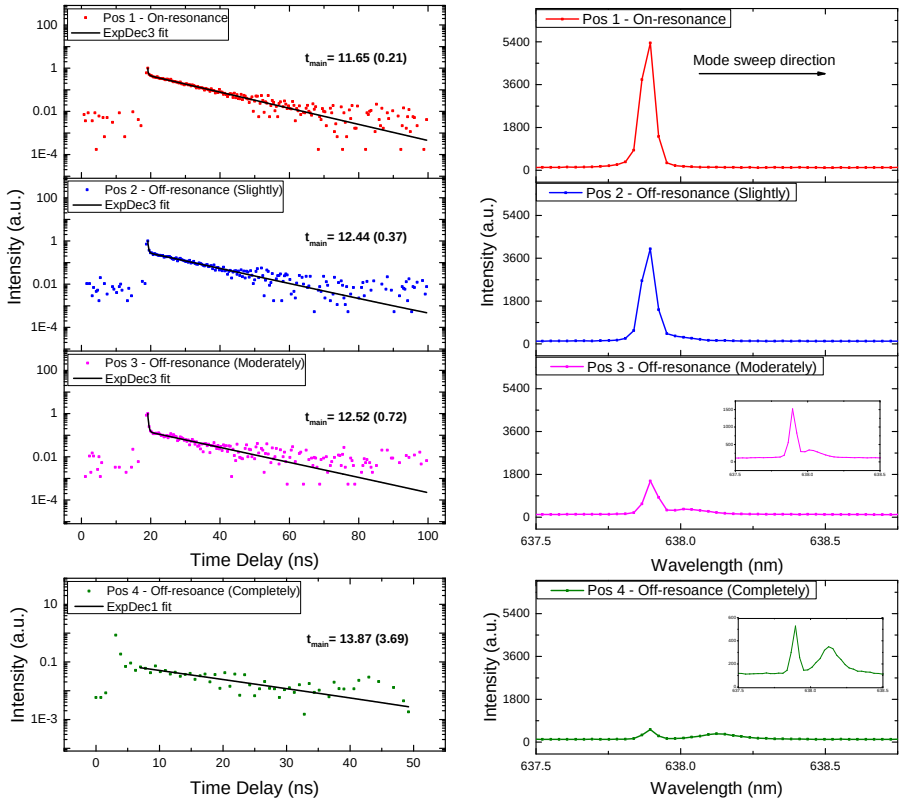

Figure 6.19: The **(a)** excited lifetime and **(b)** spectrum data taken at four different cavity mode positions. The lifetime data at position 4 is taken with a different bin width and fitted with a single exponential decay to accommodate the low count rate at that mode position.

At position 1-3 where high photon count rates is available, the lifetime measurement is taken with narrower bin width and the collected data are fitted with a tri-exponential decay starting from the highest data point. At position 4 where photon count rate is low, a slightly different acquisition setting is used. The lifetime data is fitted with a mono-exponential decay starting from at least 2ns away from the highest data point to exclude the background component which typically has a <1ns lifetime.

Cavity Positions	Fit	Bin (ns)	Fitted Decay Components (ns)		
			t_{main}	t_2	t_3
1 - On-res	ExpDec3	0.39	11.65 (0.21)	0.37 (0.48)	0.07 (0.80)
2 - Off-res	ExpDec3	0.39	12.44 (0.37)	0.24 (0.68)	0.11 (1.42)
3 - Off-res	ExpDec3	0.39	12.52 (0.72)	0.24 (0.50)	0.10 (1.51)
4 - Off-res	ExpDec1	0.78	13.87 (3.69)		

Table 6.4: Lifetime fitting parameters.

The fitting parameters for each dataset is summarised in table (6.4) where fitted t_{main}, t_2 and t_3 decay components belongs to the NV centre, the background fluorescence and the instrument response respectively. A noticeable reduction in excited-state lifetime is confirmed. Although the fitted lifetime of 13.87ns at position 4 has a larger error of 3.69ns, it is in good agreement with the on-mirror lifetime measured in fig. (6.8). The overall emission enhancement is therefore:

$$F_{\text{full}}^{\text{on/mir}} = \frac{\tau^{\text{mir}}}{\tau^{\text{on}}} = 1.195. \tag{6.2}$$

6.3.2 Power Saturation of Cavity-Couple ZPL

In addition to the overall emission enhancement obtained from lifetime measurement, power saturation measurement is taken to quantify the photon output of cavity-coupled ZPL which includes the effect of emission enhancement and collection enhancement. Similar to the treatment in section (6.1.2), the 'spatial background' dataset is calibrated with a polynomial H_{bg} and the 'total signal' is fitted with:

$$I_{\text{full}} = \frac{I_{\text{sat}} P}{P + P_{\text{sat}}} + A_{\text{pol}} \times H_{\text{bg}} + I_0 \qquad \text{(eq. (3.10) revisit)}$$

In the context of cavity-coupled power saturation measurement, the off-defect 'spatial background' dataset naturally contains a much stronger transverse mode contribution and a weaker fundamental mode contribution due to misaligned cavity resonance. Given the usage of the 638/3nm filter which only includes the fundamental mode in its spectral range, the scaling factor A_{pol} in eq. (3.10) is expected to be much larger than 1 because H_{bg} is calibrated using the off-defect 'spatial background' dataset.

Figure (6.20) shows the power saturation dataset when A4-NV4 ZPL is optimally coupled to the q=16 fundamental mode. The fitted saturation intensity of cavity-coupled ZPL is $I_{\text{sat}}^{\text{on}}$= 11,528ct/s. Comparing to the on-mirror ZPL saturation intensity of $I_{\text{sat}}^{\text{mir}}$=2,491ct/s (fig. (6.7)), the ZPL output enhancement is:

$$P_{\text{zpl}}^{\text{on/mir}} = \frac{I_{\text{zpl,sat}}^{\text{on}}}{I_{\text{zpl,sat}}^{\text{mir}}} = \frac{11528}{2491} = 4.628 \tag{6.3}$$

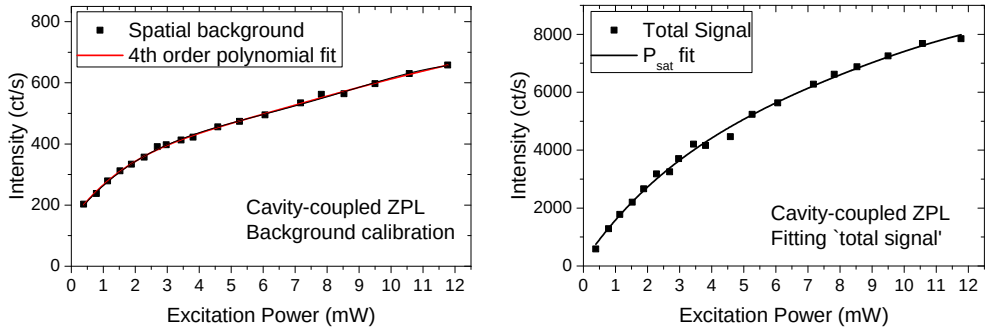

(a) Calibrating H_{bg}.

(b) Fitted $I_{\mathrm{sat}}^{\mathrm{on}}$=11,528ct/s, $P_{\mathrm{sat}}^{\mathrm{on}}$=9.18mW and A_{pol}=2.68.

Figure 6.20: Cavity-coupled ZPL power saturation data: **(a)** calibration of H_{bg} with the off-defect 'spatial background' dataset; **(b)** 'total signal' fitted with eq. (3.10) given H_{bg} and a free-fitting scaling factor A_{pol}.

In principle, $P_{\mathrm{zpl}}^{\mathrm{on/mir}}$ benefits from both emission and collection enhancements provided by the cavity. Hence it can be decomposed as:

$$P_{\mathrm{zpl}}^{\mathrm{on/mir}} = F_{\mathrm{zpl}}^{\mathrm{on/mir}} \times \eta_{\mathrm{zpl}}^{\mathrm{on/mir}} \tag{6.4}$$

where $F_{\mathrm{zpl}}^{\mathrm{on/mir}}$ is the emission enhancement and $\eta_{\mathrm{zpl}}^{\mathrm{on/mir}}$ is the collection enhancement. Unfortunately neither of these two quantities are measurable in experimental conditions. Instead, we estimate both $F_{\mathrm{zpl}}^{\mathrm{on/mir}}$ and $\eta_{\mathrm{zpl}}^{\mathrm{on/mir}}$ using FDTD simulations in chapter (7).

6.3.3 HBT Measurement

HBT measurement is one of the more challenging measurement to execute for cavity-coupled NV ZPL due to cavity instability. The 638/3nm narrow band filter is used here to reduce background contribution and the measured HBT dataset is plotted in fig. (6.21). The plotted intensity histogram is normalized using the detector $SNG_{\mathrm{A/B}}$ at t=0, i.e. when the cavity-ZPL spectral position is optimally aligned. This is not necessarily true given the signal fluctuations due to cavity instability (fig. (6.15)).

Nevertheless, the fitted $g^{(2)}(0)$ is 0.65 using eq. (3.14). The background baseline is calculated using:

$$g^{(2)}(0)_{\mathrm{exp}} = 1 - \frac{SNR_{\mathrm{A}}}{SNR_{\mathrm{A}}+1} \times \frac{SNR_{\mathrm{B}}}{SNR_{\mathrm{B}}+1} \qquad \text{(eq. (3.16) revisit)}$$

The lower-bound of $g^{(2)}(0)_{\text{exp}}$ is estimated to be 0.28 using SNR_{A}= 6.07 and SNR_{B}= 5.07 at t=0. As mentioned previously, $SNG_{\text{A/B}}$ are most likely functions of t because of cavity instability. Hence we also estimate the upper-bound of $g^{(2)}(0)_{\text{exp}}$= 0.93 using $SNR_{\text{A/B}}$= 0.59 obtained from the off-resonance spectra in fig. (6.19)(b). Strictly speaking, the normalization factor A_{hbt} is also a function of t to reflect signal fluctuation. For simplicity, A_{hbt} is also taken as its value at t= 0.

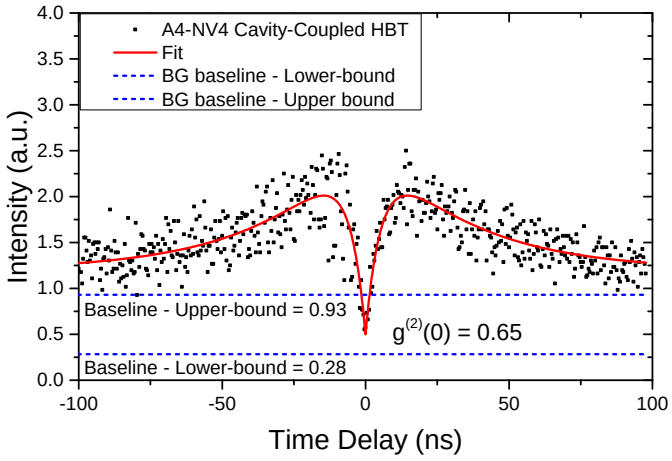

(a)

Parameter	Value
Acquisition	56454sec
Bin	0.39ns
S_{A}	2275c/s
BG_{A}	375c/s
S_{B}	760c/s
BG_{B}	150c/s
Normalisation	56
Baseline - Upper	0.86
Baseline - Lower	0.28

(b)

Figure 6.21: HBT of the cavity-coupled ZPL emission from A4-NV4. The ZPL emission is spectrally filtered with a 638/3nm narrow band-pass filter. The lower-bound and upper-bound background baselines are obtained from on-resonance and off-resonance signal-to-noise ratios, respectively. They indicate the expected range of $g^{(2)}(0)$ value if no background emission is present.

Under these treatments, the dip at zero time delay has an expected range of 0.28 to 0.98. The fitted $g^{(2)}(0)$= 0.65 certainly sits within this expected range. Compared to the on-mirror $g^{(2)}(0)$= 0.53, the measure in-cavity $g^{(2)}(0)$= 0.65 is slightly worse due to signal fluctuation and cavity instability.

There are two ways to improve the accuracy of HBT measurements for cavity-coupled transitions. Firstly, instead of passive stabilization, active cavity locking techniques can help to stabilize the cavity-coupled signal level such that $I_{\text{A/B}}$ becomes less dependent on t. Secondly, time-tagging apparatus can be implemented to record signal level as a function of t (more details in section (3.5.4.1)).

6.3.4 Membrane Thickness at Location of A4-NV4

In this section we determine the membrane thickness at A4-NV4 by fitting the cavity mode map with the analytical description as established in section (2.4).

Normally the cavity length of a single-medium cavity is easily found by measuring the longitudinal mode spacing δv from the cavity mode spectrum where $L{=}2q\delta v/c$. However, the cavity length of a hybrid-medium cavity is less trivial to determine from just a single cavity mode spectrum because the longitudinal mode spacing are modulated by not only L but also the membrane thickness t_{d}. An example of a single cavity mode spectrum from a $\mathcal{R}{=}12\mu$m cavity is shown in fig. (6.22). It is observed that δv varies between consecutive mode families, making a direct extraction of cavity length unreliable.

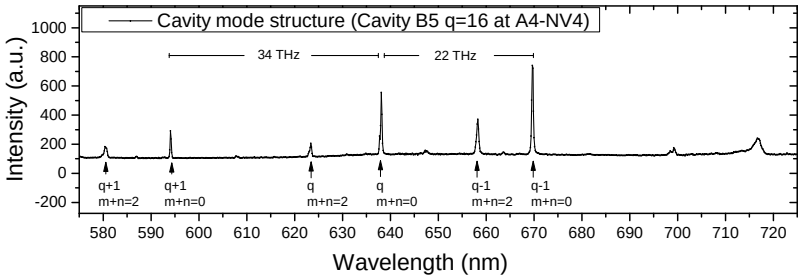

Figure 6.22: A single cavity mode spectrum of a hybrid-medium cavity showing the variation of longitudinal mode spacing which makes the identification of cavity mode index less trivial.

To determine L and t_{d} properly, we recall the analytical resonance condition for a hybrid-medium cavity from section (2.4):

$$v = \frac{c}{2\pi L}\left\{q\pi + (-1)^q \arcsin\left[\frac{n_{\mathrm{a}}-n_{\mathrm{d}}}{n_{\mathrm{a}}+n_{\mathrm{d}}}\sin\left(q\pi\frac{L-2n_{\mathrm{d}}t_{\mathrm{d}}}{L}\right)\right]\right\} \qquad \text{(eq. (2.68) revisit)}$$

A direct fit of (q, t_{d}, L) to the positions of three longitudinal modes in fig. (6.22) is firstly attempted. Unfortunately multiple parameter combinations yield local minimum in the fitting residue, indicating that fitting accuracy is low when only using a single cavity spectrum. Instead, a cavity mode map is extracted by sweeping the cavity over multiple mode families and it is plotted in fig. (6.23)(a) as a function of the piezo tuning voltage. Next, the longitudinal mode positions from all five visible mode families are sampled over the majority of piezo tuning range, yielding 121 data points in total. The whole dataset

is then fitted with eq. (2.68) assuming that the piezo responds linearly to the voltage tuning.

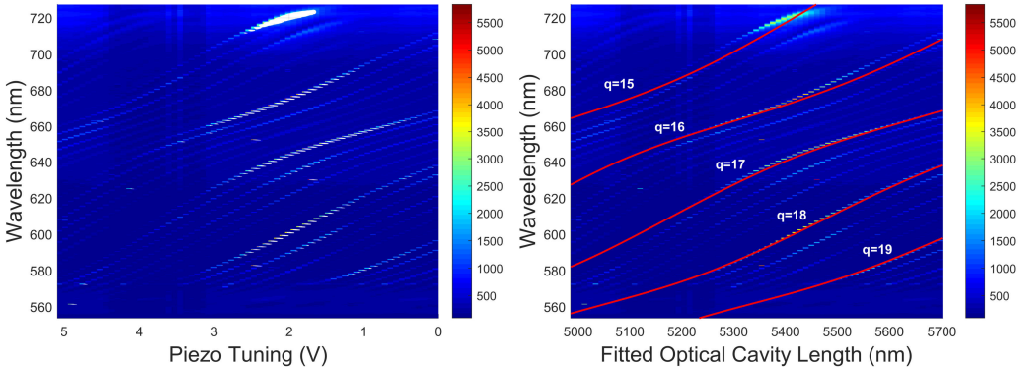

(a) **(b)**

Figure 6.23: Cavity mode maps from a $\mathcal{R}$=25µm cavity in **(a)** original piezo tuning voltage axis and **(b)** fitted and re-scaled optical cavity length axis. The calculated mode positions of all five longitudinal modes are plotted in **(b)** as red solid lines using the fitting parameters obtained from eq. (2.68).

The best-fit gives t_d= 757.5nm and a voltage to cavity length ratio of 140.2nm/V. The fitted mode map is plotted in fig. (6.23)(b) for all five mode families from q=15 to 19 and a good agreement has been observed. Excluding the q=15 mode, the average fitting residue per data point is 0.49THz (spectrum resolution≈0.2THz/0.26nm). Mode position discrepancies are observed for λ>680nm with both q=15 and 16 modes. We attribute this to the fact that all five mode families are fitted with the same length re-scaling factors between piezo voltage and optical cavity length. Alternatively, individual mode family fitting has been demonstrated in section (4.6.4) which could improve the mode position discrepancy here. But the resultant t_{d} should be comparable.

Although t_{d} is fitted to be 757.5nm under the 1D analytical description, in reality the cavity modes propagate according to the Gaussian beam expression (section (2.3.6)). To account for the additional phase shifts, the actual membrane thickness is corrected to t_{d}= 766nm.

6.3.5 Finesse of Hybrid-Medium Cavity

The cavity mode linewidth of the hybrid-medium cavity is also examined to determine the cavity finesse. The high resolution spectrum of q=16-18 fundamental modes of B5

cavity tuned to 638nm are plotted in fig. (6.24) and fitted with a Lorentzian lineshape. All the mode profiles resembles the Lorentzian lineshape nicely, confirming the decent vibration isolation of out low-temperature system.

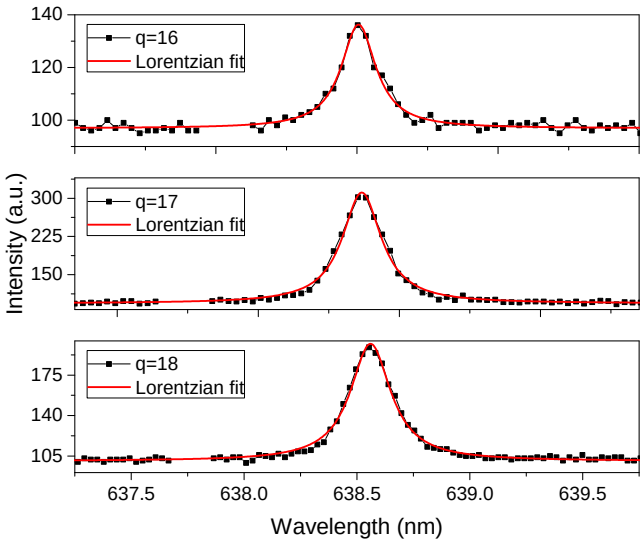

Figure 6.24: The cavity mode spectrum of the fundamental modes from the q=16-18 mode families in the hybrid-medium air-diamond cavity.

The fitted mode linewidth w_{cav} and other cavity metrics are listed in table (6.5). The measured cavity finesse is compared to the expected finesses calculated with different methods. Using $\mathcal{F}_{\mathrm{fdtd}}$ as a guideline, the q= 16 mode shows a factor of 10 drop in finesse, corresponding to an extra round-trip loss of $\Delta\mathcal{L}$= 20,864ppm.

	w_{cav}	Q	$\mathcal{F}_{\mathrm{meas}}$	$\mathcal{F}_{\mathrm{ana}}$	$\mathcal{F}_{\mathrm{tmm}}$	$\mathcal{F}_{\mathrm{fdtd}}$
q=16	0.150nm	4,274	267	2,243	1,822	2,355
q=17	0.173nm	3,697	217	2,243	1,827	-
q=18	0.208nm	3,068	170	2,243	1,845	-

Table 6.5: The hybrid-medium cavity figure of merits of fundamental modes from q=16-18 mode families measured around 640nm. Data is averaged from 5 repeated readings.

Following the same analysis approach for the single-medium cavity in section (6.2.1), the mirror scattering loss is estimated to be 500ppm for a 0.8nm roughness. The surface roughness of diamond membrane is measured to be 1nm. Since in one round-trip the photon passes the membrane surfaces 4 times, the associated scattering loss is 1,500ppm. Combining the two, the total scattering loss is around 2,000ppm which is still significant less than the $\Delta\mathcal{L}$= 20,864ppm as calculated from measured finesse. We reckon the

remaining unidentified loss is probably associated with lateral channeling effect of the membrane.

6.3.6 Cavity D5 - Only ZPL Power Saturation

In order to achieve a smaller cavity length in pursuit for a stronger ZPL emission enhancement, a shallower R=12μm cavity D5 is coupled to A4-NV4's ZPL. Cavity D5 has a depth of 540nm while cavity B5 is 1,360nm deep. Assuming a same angle between the two cavity mirrors, q= 16-2= 14 should be viable.

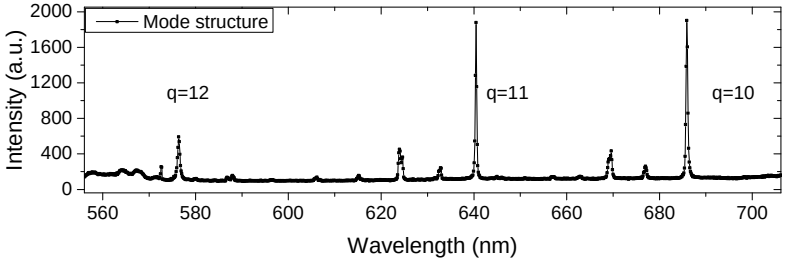

Figure 6.25: Mode structure of cavity D5 at q=11.

The mode spectrum of D5 with the smallest q is shown in fig. (6.25). Using t_{d}= 757.5nm obtained previously, the fundamental mode at 640nm is found to be q=11. The reduction of minimal mode index from q=15 for B5 to q=11 is made possible with some further tweaking of cavity mirror alignment.

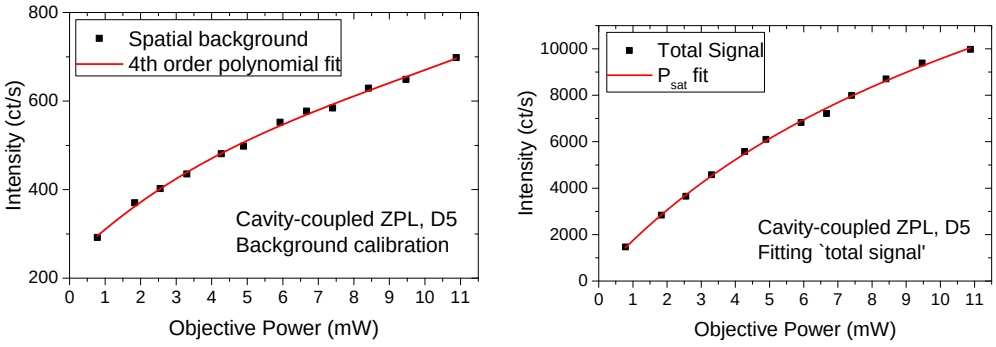

(a) Calibrating H_{bg}.

(b) Fitted $I_{\mathrm{sat}}^{\mathrm{on}}$=18,027ct/s, $P_{\mathrm{sat}}^{\mathrm{on}}$=13.90mW and A_{pol}=4.13.

Figure 6.26: Cavity-coupled ZPL power saturation data from cavity D5: **(a)** H_{bg} with off-defect 'spatial background' data; **(b)** 'total signal' fitted with eq. (3.10) given the calibrated H_{bg} from **(a)**.

The power saturation data of the cavity-coupled A4-NV44 ZPL is shown in Figure (6.26). The 'total signal' dataset is fitted with eq. (3.10) which yields an on-resonance ZPL

saturation intensity at $I_{\text{sat}}^{\text{on}}$=18,027ct/s. Compared to the on-mirror ZPL saturation at $I_{\text{sat}}^{\text{mir}}$=2,491ct/s, the output enhancement is about 7.24. This marks the largest ZPL emission enhancement factor observed.

Unfortunately due to time constraints, no lifetime measurement is taken with this cavity. As a result, FDTD simulation of this cavity is not possible hence no further analysis is followed.

6.3.7 Summary of In-Cavity Characterization

In summary, the cavity-coupled ZPL emission of A4-NV4 is presented in this section. A complete set of optical characterization is taken with cavity B5 in both on- and off-resonance cavity positions. The full spectrum emission enhancement of $F_{\text{full}}^{\text{on/mir}} = 1.195$ is obtained via excited-lifetime measurements. The cavity-coupled ZPL photon output is found to be $P_{\text{zpl}}^{\text{on/mir}} = 4.628$ via power saturation measurements.

6.4 Preliminary Emission Rate Analysis

Based on the on-mirror and in-cavity investigations, we have gathered all the available data concerning the emission properties of A4-NV4 in both configurations. Hence we proceed to establish a basic emission rate analysis based on the model described in section (2.2.4) where the NV emission is divided into a ZPL component and a PSB component. The two-part expression of the Purcell factor is given by eq. (2.26):

$$F_{\text{full}} = 1 + \eta_{\text{qe}}\left[\zeta^0 F_{\text{zpl}} + (1-\zeta^0)F_{\text{psb}} - 1\right] \qquad \text{(eq. (2.26) revisit)}$$

Assuming an unity internal quantum efficiency η_{qe}, eq. (2.26) simplifies to:

$$F_{\text{full}} = \zeta^0 F_{\text{zpl}} + (1-\zeta^0)F_{\text{psb}} \qquad \text{(eq. (2.27) revisit)}$$

Using eq. (2.27), an emission rate analysis table is constructed in table (6.6) where the relationships between the emission rates γ and the ZPL branching ratio ζ in various experimental configurations are listed. Another assumption we make is that since PSB

has a broadband peak shape, small deviation in cavity mode position does not change its emission rate significantly i.e. $\gamma_{\mathrm{psb}}^{\mathrm{off}} \approx \gamma_{\mathrm{psb}}^{\mathrm{on}}$. The parameters that can be obtained from our experiments and simulations are marked in bold font.

	Bulk	On-mir	On-res	Off-res
Full-spec (MHz)	$\gamma_{\mathrm{full}}^{0}$	$\gamma_{\mathrm{full}}^{\mathrm{mir}}=1/\boldsymbol{\tau^{\mathrm{mir}}}$	$\gamma_{\mathrm{full}}^{\mathrm{on}}=1/\boldsymbol{\tau^{\mathrm{on}}}$	$\gamma_{\mathrm{full}}^{\mathrm{off}}=1/\boldsymbol{\tau^{\mathrm{off}}}$
ZPL (MHz)	$\gamma_{\mathrm{zpl}}^{0}$	$\gamma_{\mathrm{zpl}}^{\mathrm{mir}}=\boldsymbol{\zeta^{\mathrm{mir}}}\gamma_{\mathrm{full}}^{\mathrm{mir}}$	$\gamma_{\mathrm{zpl}}^{\mathrm{on}}=\boldsymbol{F_{\mathrm{zpl}}^{\mathrm{on/mir}}}\ \gamma_{\mathrm{zpl}}^{\mathrm{mir}}$	$\gamma_{\mathrm{zpl}}^{\mathrm{off}}=\gamma_{\mathrm{full}}^{\mathrm{off}}-\gamma_{\mathrm{psb}}^{\mathrm{off}}$
PSB (MHz)	$\gamma_{\mathrm{psb}}^{0}$	$\gamma_{\mathrm{psb}}^{\mathrm{mir}}=\gamma_{\mathrm{full}}^{\mathrm{mir}}-\gamma_{\mathrm{zpl}}^{\mathrm{mir}}$	$\gamma_{\mathrm{psb}}^{\mathrm{on}}=\gamma_{\mathrm{full}}^{\mathrm{on}}-\gamma_{\mathrm{zpl}}^{\mathrm{on}}$	$\gamma_{\mathrm{psb}}^{\mathrm{off}} \approx \gamma_{\mathrm{psb}}^{\mathrm{on}}$
ζ	ζ^{0}	$\boldsymbol{\zeta^{\mathrm{mir}}}$	$\zeta^{\mathrm{on}}=\gamma_{\mathrm{zpl}}^{\mathrm{on}}/\gamma_{\mathrm{full}}^{\mathrm{on}}$	$\zeta^{\mathrm{off}}=\gamma_{\mathrm{zpl}}^{\mathrm{off}}/\gamma_{\mathrm{full}}^{\mathrm{off}}$

Table 6.6: An analysis template of NV emission rates γ and ZPL branching ratio ζ in all experimental configurations. The quantities in bold font are available from either experimental measurements or FDTD simulations. The emission enhancement of ZPL photon $F_{\mathrm{zpl}}^{\mathrm{on/mir}}$ needs to be derived from FDTD simulation.

To fill the table for A4-NV4 in cavity B5, we firstly note that all of the free-space bulk emission rates γ^0 are not directly measurable because A4-NV4 is identified when the sample is already in its membrane form. Using the excited-state lifetime data, the full-spectrum emission rate can all be filled given the on-mirror lifetime τ^{mir} of 13.92ns (71.84MHz), the on-resonance lifetime τ^{on} of 11.65ns (85.84MHz) and the off-resonance lifetime of τ^{off} of 13.87ns (72.10MHz). Next, given the on-mirror ZPL branching ratio ζ^{mir}= 6.87%. the on-mirror emission rate of ZPL and PSB photons are $\gamma_{\mathrm{zpl}}^{\mathrm{mir}}$= 4.94MHz and $\gamma_{\mathrm{psb}}^{\mathrm{mir}}$= 66.91MHz respectively. Now that the on-mirror column is completed.

	Bulk	On-mir	On-res	Off-res
Full-spec (MHz)	-	$\gamma_{\mathrm{full}}^{\mathrm{mir}}$= 71.84	$\gamma_{\mathrm{full}}^{\mathrm{on}}$= 85.84	$\gamma_{\mathrm{full}}^{\mathrm{off}}$= 72.10
ZPL (MHz)	-	$\gamma_{\mathrm{zpl}}^{\mathrm{mir}}$= 4.94	$\gamma_{\mathrm{zpl}}^{\mathrm{on}}$= 22.84/$\boldsymbol{\eta_{\mathrm{zpl}}^{\mathrm{on/mir}}}$	$\gamma_{\mathrm{zpl}}^{\mathrm{off}}$= $\gamma_{\mathrm{full}}^{\mathrm{off}}$-$\gamma_{\mathrm{psb}}^{\mathrm{off}}$
PSB (MHz)	-	$\gamma_{\mathrm{psb}}^{\mathrm{mir}}$= 66.91	$\gamma_{\mathrm{psb}}^{\mathrm{on}}=\gamma_{\mathrm{full}}^{\mathrm{on}}-\gamma_{\mathrm{zpl}}^{\mathrm{on}}$	$\gamma_{\mathrm{psb}}^{\mathrm{off}} \approx \gamma_{\mathrm{psb}}^{\mathrm{on}}$
ζ	-	ζ^{mir}= 6.87%	$\zeta^{\mathrm{on}}=\gamma_{\mathrm{zpl}}^{\mathrm{on}}/\gamma_{\mathrm{full}}^{\mathrm{on}}$	$\zeta^{\mathrm{off}}=\gamma_{\mathrm{zpl}}^{\mathrm{off}}/\gamma_{\mathrm{full}}^{\mathrm{off}}$

Table 6.7: The emission rate analysis for A4-NV4 when its ZPL is coupled to the q=16 fundamental mode of cavity B5. The table is filled with all the available information from previous in-cavity measurements.

The on-resonance ZPL emission rate is related to the on-mirror rate by the ZPL emission enhancement of $F_{\mathrm{zpl}}^{\mathrm{on/mir}}$, which is directly measurable. The measured ZPL output

enhancement of $P_{\text{zpl}}^{\text{on/mir}}$= 4.628 is related to $F_{\text{zpl}}^{\text{on/mir}}$ by $F_{\text{zpl}}^{\text{on/mir}}$= $P_{\text{zpl}}^{\text{on/mir}}/\eta_{\text{zpl}}^{\text{on/mir}}$. Unfortunately $\eta_{\text{zpl}}^{\text{on/mir}}$ is also not directly measurable. Given only experimental results, table (6.7) can not be completed beyond this point.

It is clear that a good estimation of either $\eta_{\text{zpl}}^{\text{on/mir}}$ or $F_{\text{zpl}}^{\text{on/mir}}$ is required to complete the emission rate analysis. It is necessary to resort to FDTD simulations to compare the ZPL photon collection capabilities between the on-mirror and in-cavity configurations. Table (6.8) lists the main parameters to be included in FDTD simulations in chapter (7).

Measured quantities					To be determined	
t_{d}	ζ^{mir}	$F_{\text{full}}^{\text{on/mir}}$	$P_{\text{zpl}}^{\text{on/mir}}$	ξ^2	$\eta_{\text{zpl}}^{\text{on/mir}}$	$F_{\text{zpl}}^{\text{on/mir}}$
766nm	6.87	1.195	4.628	0.85±0.15	-	-

Table 6.8: Summary of the measured variables up till now and the remaining variables to be determined from FDTD simulations.

6.5 Conclusions

To summarise, in this chapter we demonstrated both on-mirror and in-cavity characterizations of A4-NV4 in membrane Gen2-m3. Most of the key quantities measured in this chapter are summarised in table (6.9).

	τ (ns)	$g^{(2)}(0)$	$I_{\text{sat,full}}$ (ct/s)	$I_{\text{sat,zpl}}$ (ct/s)	ζ	ξ^2
On-mirror	13.92	0.53	36,253	2,491	6.87%	0.85±0.15
In-cavity	11.65	0.65	-	11,528	-	-
On/mir	$F_{\text{full}}^{\text{on/mir}}$=1.19	-	-	$P_{\text{zpl}}^{\text{on/mir}}$=4.628	-	-

Table 6.9: A summary of key measured quantities from this chapter.

Firstly, the excited-state lifetime measurement is carried out to quantify the full-spectrum emission enhancement $F_{\text{full}}^{\text{on/mir}}$= 1.19. Despite it being the most commonly quoted cavity metrics in literature work, we put more emphasis on the ZPL output enhancement $P_{\text{zpl}}^{\text{on/mir}}$= 4.628 as measured by power saturation measurement. For a cavity-coupled NV ZPL, the in-cavity photon output combines the effects of the emission enhancement $F_{\text{zpl}}^{\text{on/mir}}$ and the collection enhancement $\eta_{\text{zpl}}^{\text{on/mir}}$. Because neither of these two factors is

available experimentally, the cavity analysis is extended to FDTD simulation in the next chapter to decompose the measured $P_{\text{zpl}}^{\text{on/mir}}$.

The on-mirror ZPL branching ratio ζ^{mir} was initially estimated via PL spectrum analysis which is proved to be problematic due to modulations introduced by the diamond membrane. Instead, a better estimation of ζ^{mir} is obtained via power saturation measurement with different spectral filtering windows. The usage of polynomial background fitting is also proved to be very effective in dealing with modulated PL background in the membrane.

The dipole orientation factor ξ^2 was measured in the on-mirror configuration and is estimated to be 0.85±0.15. The on-mirror HBT measurement confirmed the single-photon emission property of the target NV centre, but the in-cavity HBT appears to be more difficult due to the cavity instability. To mitigate the problem with the fluctuating signal, we proposed possible improvements in HBT equipment and analysis methodology.

The cavity finesse of the single-medium and hybrid-medium cavities are quantified with spectrum analysis. Compared to expected finesse from mirror reflectivities, the measured single-medium cavities possesses an extra round-trip loss of 1,000ppm, while this figure is 20,000ppm for the hybrid-medium cavity. Excluding the quantifiable losses such as scattering loss at mirror and membrane surfaces, the hybrid-medium cavity still contains a large amount of unidentifiable loss. A possible explanation of the extra loss could be the wedge of the membrane thickness, which acts as a partial reflector. As a result, during each cavity photon round-trip, about 2% (20,000ppm) of photon is scattered sideways due to the wedged air-diamond interface. This figure is not too unrealistic considering the metrics of other real-world beam samplers. To verify this hypothesis, FDTD simulation of a wedged membrane in the cavity can be run to compare with real device performance.

Chapter 7

FDTD Analysis of Cavity-Coupling Results

Following the on-mirror and in-cavity characterization of A4-NV4 in chapter (6), we attempt to match experimental data with realistic FDTD simulations which is absolutely critical in completing the emission analysis of cavity-coupling data, as discussed in section (6.4).

The single-frequency analysis model established in section (4.3) is extended to a multi-frequency integration approach to match NV emission spectrum. By taking both the emission enhancement F_{zpl} and the collection enhancement η_{zpl} into account, good agreement is obtained between experimental and simulated results.

Naming convention in this chapter follows that in chapter (4).

7.1 Analysis Methodology Adaptation

The modified analysis protocol with a multi-frequency approach for cavity-coupled NV data will have to be introduced. This adaptation is made possible because the Purcell monitors have a customizable frequency resolution. The collection analysis remains as a single-frequency approach due to the limited frequency resolution of the f-domain monitors. Next, necessary analytical parameters are constructed, and a series of calibration simulations are carried out.

The DBR mirrors are made of Ta-Si coating with 10/17 DBR pairs on the planar/featured

mirrors. A broadband dipole source with a 90fs pulse length is used as the illumination source. The two sub-simulation setups are used to distinguish between the cavity and non-cavity photon with a t-domain cut-off at t=100fs. Far-field emission pattern is analyzed with a NA=0.8 air objective lens, corresponding to a full collection angle of 0.927rad.

7.1.1 Modifications to Emission Analysis

Under the multi-frequency treatment, the emission enhancement factor F^{dev} of an NV in a given dielectric structure is calculated using a wavelength integral:

$$F^{\mathrm{dev}} = \int F^{\mathrm{dev}}(\lambda) S^0(\lambda) d\lambda \tag{7.1}$$

where $F^{\mathrm{dev}}(\lambda)$ is the enhancement spectrum (or the local density of states distribution) of the simulated structure and $S^0(\lambda)$ is the generic free-space NV emission spectrum in a bulk lattice. The emission enhancement between the in-cavity and the free-space configuration, $F^{\mathrm{dev}/0}(\lambda)$, is thus written as:

$$F^{\mathrm{dev}/0} = \frac{\int F^{\mathrm{dev}}(\lambda) S^0(\lambda) d\lambda}{\int F^0(\lambda) S^0(\lambda) d\lambda} = \frac{\int F^{\mathrm{dev}}(\lambda) S^0(\lambda) d\lambda}{\int S^0(\lambda) d\lambda} \tag{7.2}$$

where the free-space enhancement spectrum $F^0(\lambda)$ is unity for all λ.

By setting the integral range properly, the full-spectrum emission enhancement F_{full} and the ZPL emission enhancement F_{zpl} are written as:

$$F_{\mathrm{full}}^{\mathrm{dev}/0} = \frac{\int_{\mathrm{full}} F^{\mathrm{dev}}(\lambda) S^0(\lambda) d\lambda}{\int_{\mathrm{full}} S^0(\lambda) d\lambda} \tag{7.3a}$$

$$F_{\mathrm{zpl}}^{\mathrm{dev}/0} = \frac{\int_{\mathrm{zpl}} F^{\mathrm{dev}}(\lambda) S^0(\lambda) d\lambda}{\int_{\mathrm{zpl}} S^0(\lambda) d\lambda} \tag{7.3b}$$

The modified ZPL branching ratios ζ^{dev} for a given simulation structure is written as:

$$\zeta^{\mathrm{dev}} = \frac{\int_{\mathrm{zpl}} F^{\mathrm{dev}}(\lambda) S^0(\lambda) d\lambda}{\int_{\mathrm{full}} F^{\mathrm{dev}}(\lambda) S^0(\lambda) d\lambda} \tag{7.4}$$

We note that the ζ^{dev} integrals always contain some contribution from the underlying PSB photons. This agrees the experimental filtering condition where photons within a spectral window are all collected regardless of the origin of the photon. In next section

we will introduce an analytical ZPL branching ratio ζ^* which is only used to construct the generic NV spectrum $S^0(\lambda)$ analytically.

For simplicity the area under $S^0(\lambda)$ is normalized to unity:

$$\int_{\text{full}} S^0(\lambda)d\lambda = 1 \tag{7.5}$$

Using eqs. (7.4) and (7.5), the free-space ZPL branching ratio ζ^0 is given by:

$$\zeta^0 = \frac{\int_{\text{zpl}} F^0(\lambda)S^0(\lambda)d\lambda}{\int_{\text{full}} F^0(\lambda)S^0(\lambda)d\lambda} = \frac{\int_{\text{zpl}} S^0(\lambda)d\lambda}{\int_{\text{full}} S^0(\lambda)d\lambda} = \int_{\text{zpl}} S^0(\lambda)d\lambda \tag{7.6}$$

Substituting eq. (7.4) and eq. (7.6) back into eq. (7.3), the expression for $F_{\text{full}}^{\text{dev}/0}$ and $F_{\text{zpl}}^{\text{dev}/0}$ simplifies to a more convenient form:

$$\begin{aligned} F_{\text{full}}^{\text{dev}/0} &= \int_{\text{full}} F^{\text{dev}}(\lambda)S^0(\lambda)d\lambda \\ F_{\text{zpl}}^{\text{dev}/0} &= \frac{\int_{\text{zpl}} F^{\text{dev}}(\lambda)S^0(\lambda)d\lambda}{\zeta^0} \end{aligned} \tag{7.7}$$

The expression for the emission enhancement in PSB $F_{\text{psb}}^{\text{dev}/0}$ is derived from eq. (2.27) as:

$$F_{\text{psb}}^{\text{dev}/0} = \frac{F_{\text{full}}^{\text{dev}/0} - \zeta^0 F_{\text{zpl}}^{\text{dev}/0}}{1-\zeta^0} \tag{7.8}$$

In practice, $F^{\text{dev}}(\lambda)$ is extracted from the Purcell monitors. Particular attention is paid to the f-domain resolution because the wavelength axis is shared between $F^{\text{dev}}(\lambda)$ and $S^0(\lambda)$. In order to resolve the MHz NV ZPL in $S^0(\lambda)$, comparable resolution is required at 637nm.

For general spectrum integration for λ= 550-850nm, we use a frequency axis resolution of 9×10^{-4} nm (380MHz) which is capable of resolving any cavity mode with Q<685,000. For λ= 635-640nm, the resolution is refined to 1×10^{-5} nm (7MHz) which is capable of resolving emission peaks with a linewidth w_{zpl}>30MHz. This is a good trade-off between computation burden and marginal benefit of further resolution refinement.

7.1.2 Constructing Free-Space NV Spectrum

Normally the generic NV spectrum $S^0(\lambda)$ in free-space is extracted from a low- temperature emission spectrum of the same NV centre in its bulk lattice. However, such data can not be obtained in our case. In fact, due to the need to precisely tailor the ZPL position to meet the simulated cavity modes, it is more preferable to construct $S^0(\lambda)$ analytically with two contributing components: a Lorentzian function $S^0_{\text{zpl}}(\lambda)$ to represent the ZPL transition and a Gaussian function $S^0_{\text{psb}}(\lambda)$ to represent the PSB contribution:

$$S^0_{\text{zpl}}(\lambda) = A_{\text{zpl}} \frac{2w_{\text{zpl}}}{\pi(4(\lambda - \lambda_{\text{zpl}})^2 + w^2_{\text{zpl}})} \tag{7.9a}$$

$$S^0_{\text{psb}}(\lambda) = A_{\text{psb}} \frac{1}{w_{\text{psb}}\sqrt{\pi/2}} e^{-2(\lambda-\lambda_{\text{psb}})^2/w^2_{\text{psb}}} \tag{7.9b}$$

Note that w_{psb} is not the FWHM, but twice the standard deviation σ of the Gaussian distribution. The analytical ZPL branching ratio ζ^* is obtained using the area pre-factors:

$$\zeta^* = \frac{A_{\text{zpl}}}{A_{\text{zpl}} + A_{\text{psb}}}$$

Just like how $S^0(\lambda)$ is treated in eq. (7.5), the total area $(A_{\text{zpl}} + A_{\text{psb}})$ is set to 1 which leads to:

$$\zeta^* = A_{\text{zpl}} \tag{7.10}$$

We note again that ζ^* is different from the free-space ζ^0 from eq. (7.6). Although the two terms have similar values, ζ^0 contains some PSB contribution while ζ^* is only an analytical parameter used for $S^0(\lambda)$ construction.

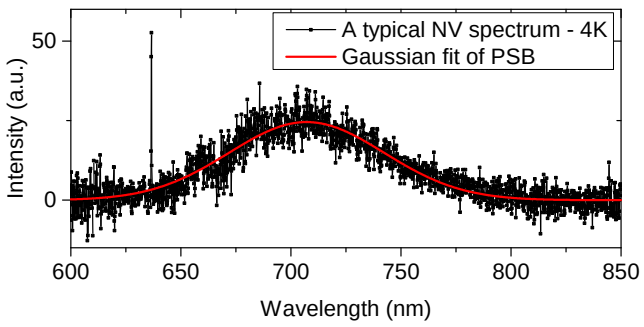

Figure 7.1: Extracting parameters for the PSB profile S^0_{psb} from a reference PL spectrum from a reference NV in a bulk lattice.

The parameters for the PSB function $S^0_{\text{psb}}(\lambda)$ is coarsely approximated by fitting a reference low-temperature spectrum from a single NV in a bulk lattice as shown in fig. (7.1). The $S^0_{\text{psb}}(\lambda)$ profile (red solide line) is constructed using fitted λ_{psb}= 707.1nm and w_{psb}= 70.5nm.

On the other hand, the ZPL peak function $S^0_{\text{zpl}}(\lambda)$ is mainly determined by the ZPL position λ_{zpl} and the ZPL linewidth w_{zpl}. Value λ_{zpl} is determined by the simulated mode position to ensure perfect cavity-NV coupling at ZPL. The treatment for w_{zpl} is slightly more complicated because it can take any value from MHz to GHz corresponding to realistic inhomogeneous ZPL linewidths. Because of the linear multiplication between $F^{\text{dev}}(\lambda)$ and $S^0(\lambda)$, the final results depend on the relative magnitude between w_{zpl} and the cavity linewidth w_{cav}. A convergence test of w_{zpl} is presented in next section to comment on this dependence.

7.1.3 Calibrating Analytical ZPL Branching Ratio

In chapter (6) we measured an on-mirror ZPL branching ratio ζ^{mir}= 6.87%. In order to construct $S^0(\lambda)$, the analytical ZPL branching ratio ζ^* (A_{zpl}) has to be determined. An on-mirror simulation with realistic parameters (table (7.1)) is ran to calibrate ζ^* using ζ^{mir}.

Variables	Fixed		Dependent	Target
	t_{d}	N_{plan}	ζ^{mir}	ζ^*
Values	766nm	10pairs	6.87%	-

Table 7.1: Realistic parameters used in the on-mirror simulation to find the analytical ZPL branching ratio ζ^*.

The simulation structure and the dipole emission profile are shown in fig. (7.2) where the dipole source is placed in the membrane layer 66nm away from the DBR mirror interface. The multi-frequency analysis introduced in the previous two sections is applied to find the ζ^* with a trial and error approach. The value of ζ^* is swept until the resulting emitter-cavity enhancement spectrum gives an on-mirror ZPL branching ratio of ζ^{mir}= 6.87% using eq. (7.4).

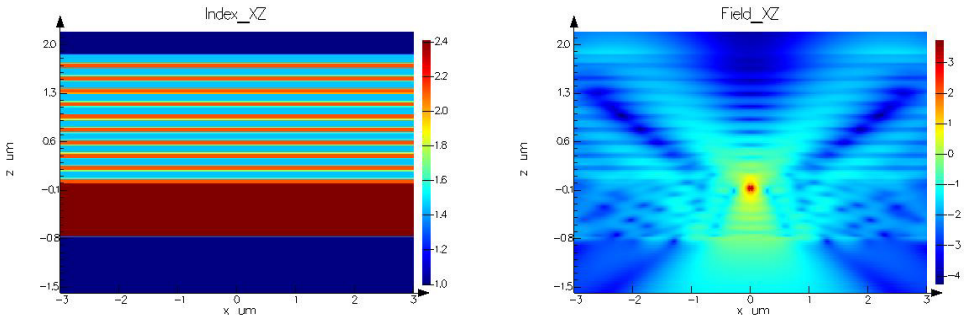

(a) **(b)**

Figure 7.2: **(a)** Index profile in x-z cross-section to show the simulation structure. **(b)** The dipole emission profile in x-z cross-section. The dipole is placed 66nm away from the DBR-diamond interface.

Because the shape of $S^0_{\text{zpl}}(\lambda)$ depends on both the area coefficient A_{zpl} (ζ^*) and the ZPL linewidth w_{zpl}, one variable has to be fixed while varying the other. Provided that the measured ZPL overall linewidth in this work and in the literature are often in the GHz range, we assign w_{zpl}=2GHz as the initial estimation which will be reviewed later in section (7.1.5). Proceeding with w_{zpl}=2GHz, $S^0(\lambda)$ is calculated and plotted in fig. (7.3) along with $F^{\text{mir}}(\lambda)$ extracted from the simulation and their product $F^{\text{mir}}(\lambda)S^0(\lambda)$.

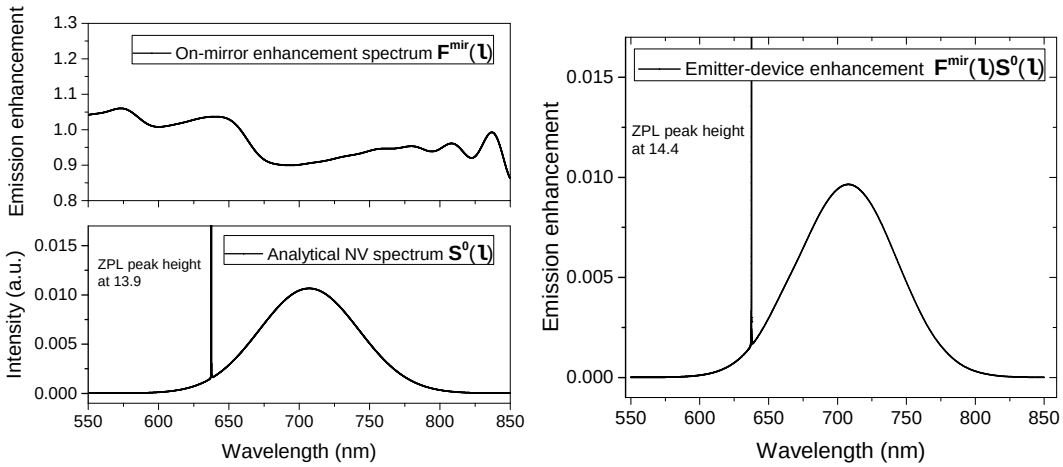

(a) **(b)**

Figure 7.3: Plots of **(a)** he simulated device enhancement spectrum $F^{\text{mir}}(\lambda)$ and the calculated emitter spectrum $S^0(\lambda)$ using w_{zpl}=2GHz and ζ^*=5.9%; **(b)** the combined emitter-cavity enhancement spectrum $F^{\text{mir}}(\lambda)S^0(\lambda)$.

Using the computed dataset of $F^{\text{mir}}(\lambda)S^0(\lambda)$, after some trials the value of ζ^* is settles at 5.90%. The corresponding area integrals for the full-spectrum and ZPL regions are:

$$\int_{\text{full}} F^{\text{mir}}(\lambda)S^0(\lambda)d\lambda = 0.935$$
$$\int_{\text{zpl}} F^{\text{mir}}(\lambda)S^0(\lambda)d\lambda = 0.0642$$
$$\zeta^{\text{mir}} = \frac{\int_{\text{zpl}} F^{\text{mir}}(\lambda)S^0(\lambda)d\lambda}{\int_{\text{full}} F^{\text{mir}}(\lambda)S^0(\lambda)d\lambda} = \frac{0.0642}{0.935} = 6.87\%$$

The calculated value of ζ^{mir} using ζ^*= 5.90% matches with the measured value of 6.87%.

7.1.4 Emission and Collection Analysis - Membrane-On-Mirror

Given ζ^*=5.9%, the generic NV spectrum $S^0(\lambda)$ can be constructed. Next, by using eq. (7.6) the ZPL branching ratio in the free-space bulk configuration ζ^0 is found to be 6.2%. The relative emission enhancement between on-mirror and free-space configurations are thus obtained using eq. (7.7) and eq. (7.8):

$$F_{\text{full}}^{\text{mir}/0} = \int_{\text{full}} F^{\text{mir}}(\lambda)S^0(\lambda)d\lambda = 0.935$$
$$F_{\text{zpl}}^{\text{mir}/0} = \frac{\int_{\text{zpl}} F^{\text{mir}}(\lambda)S^0(\lambda)d\lambda}{\zeta^0} = \frac{0.0642}{0.0620} = 1.035$$
$$F_{\text{psb}}^{\text{mir}/0} = \frac{F_{\text{full}}^{\text{mir}/0} - \zeta^0 F_{\text{zpl}}^{\text{mir}/0}}{1-\zeta^0} = \frac{0.935 - 0.062 \times 1.035}{1 - 0.062} = 0.928$$

The obtained $F_{\text{full}}^{\text{mir}/0}$ and $F_{\text{psb}}^{\text{mir}/0}$ are both less than 1. This indicates that the NV emission is suppressed in this membrane-on-mirror configuration, mainly due to the modification of LDoS in the PSB spectral region. This explains the measured on-mirror lifetime of τ^{mir}= 13.92ns (from chapter (6)) which is slightly longer than the more commonly reported NV lifetime around 12ns.

All η	η_{guid}	η_{bot}	η_{top}	$\eta_{\text{bot,NA}}$	$\eta_{\text{zpl}}^{\text{mir}}$=$\eta_{\text{bot}}$ $\eta_{\text{bot,NA}}$	$F_{\text{zpl}}^{\text{mir}/0}$	$P_{\text{out}}^{\text{mir}}$
($\%P^{\text{mir}}$)				($\%\eta_{\text{bot}}$)	($\%P^{\text{mir}}$)	(P^{mir}/P^0)	($\%P^0$)
100	79.85	18.76	1.39	96.82	18.16	1.035	18.80

Table 7.2: Collection and ZPL output analysis of the on-mirror simulation. The overall photon output $P_{\text{out}}^{\text{mir}/0}$ in the on-mirror configuration at the ZPL frequency is calculated using eq. (4.9b).

Moving on to the collection analysis, the channel-specific photon collection η_{ch} are summarised in table (7.2) along with ZPL photon output efficiency $\eta_{\text{zpl}}^{\text{mir}}$. The photons are collected from the bottom of the simulation region (see in fig. (7.2)).

Recalling eq. (4.9b) from chapter (4):

$$\begin{aligned} P_{\text{out}}^{\text{mir}} &= P^0 \times F_{\text{tot}}^{\text{mir}} \times \eta_{\text{zpl}}^{\text{mir}} \\ &= P^0 \times F_{\text{tot}}^{\text{mir}} \times \eta_{\text{bot}} \times \eta_{\text{bot}}^{\text{NA}} \end{aligned} \qquad \text{(eq. (4.9b) revisit)}$$

where $F_{\text{zpl}}^{\text{mir}/0} = 1.035$ and $\eta_{\text{zpl}}^{\text{mir}} = 18.16\% P^{\text{mir}}$. Hence the on-mirror ZPL output $P_{\text{out}}^{\text{mir}}$ is found to be $18.80\% P^0$ where P^0 is the dipole sourcepower.

At this point we have thoroughly analyzed the on-mirror simulation and all the obtained parameters are summarised in table (7.3). During this whole process we only used one measured figure that is $\zeta^{\text{mir}} = 6.87\%$. This shows how powerful the FDTD approach can be with an appropriate analysis protocol.

	$F_{\text{full}}^{\text{mir}/0}$	$F_{\text{psb}}^{\text{mir}/0}$	$F_{\text{zpl}}^{\text{mir}/0}$	ζ^{mir}	ζ^0	$P_{\text{out}}^{\text{mir}}$	ζ^*
Measured	-	-	-	6.87%	-	-	-
Simulated	0.935	0.928	1.035	6.87%	6.20%	$18.80\% P^0$	5.9%

Table 7.3: A summary of the simulation data obtained from on-mirror simulation.

7.1.5 Validating Analytical ZPL Linewidth with Convergence Test

Now we go back to review the initial estimation we made by setting $w_{\text{zpl}} = 2\text{GHz}$. This time ζ^* is fixed at 5.90%, while w_{zpl} is being varied. The convergence behaviours of emission enhancement factors ($F_{\text{full}}^{\text{mir}/0}$ and $F_{\text{zpl}}^{\text{mir}/0}$) and the ZPL branching ratio (ζ^{mir}) are monitored.

The results are plotted in fig. (7.4) as a function of w_{zpl} which ranges from 36MHz to 7.4GHz. It can be observed that the ZPL linewidth dependence is very weak for all three variables, suggesting the corresponding value of $\zeta^* = 5.90\%$ should be valid for all ranges w_{zpl}. Judging by these trends, the initial estimation of w_{zpl}=2GHz is regarded as a reliable assumption.

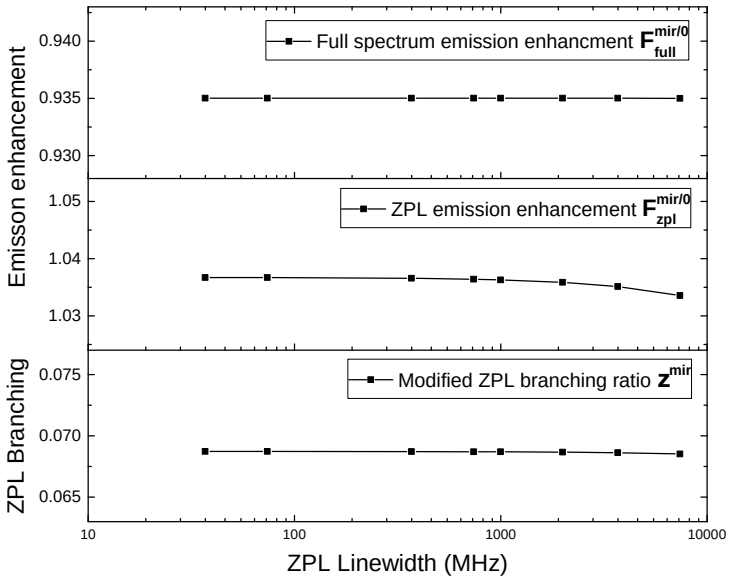

Figure 7.4: Convergence test of the ZPL linewidth w_{zpl} term in $S^0(\lambda)$ and its influence on key variable including the emission enhancement factors and ZPL branching ratio.

The explanation behind this observation is rather simple if considering the relative linewidth between the constructed ZPL and the 'cavity' mode. Yes there is no cavity mode forming in on-mirror simulation, but one can assign the simulated $F^{\text{dev}}(\lambda)$ with an effective photonic mode with a linewidth w_{mir} that is on the order of THz.

When multiplying $F^{\text{dev}}(\lambda)$ and $S^0(\lambda)$, because $w_{\text{zpl}} \sim$ GHz while $w_{\text{mir}} \sim$ THz, in the ZPL spectral region $F^{\text{dev}}(\lambda)$ is effectively flat. As a result, all enhancement parameters becomes insensitive to ZPL linewidth w_{zpl} but only depend on the area pre-factor A_{zpl} (or ζ^*).

Same analysis and linewidth comparison can also be applied to the in-cavity configuration which has a more well-defined photonic mode linewidth w_{cav}. If the value of w_{cav} and w_{zpl} differs by several orders of magnitude, the choice of w_{zpl} when constructing $S^0(\lambda)$ becomes less impactful on the accuracy of the F and ζ calculations.

7.1.6 Lateral Photon Channeling in Membrane

In addition to the on-mirror simulation, the emission and collection efficiency of a dipole located in a free-standing membrane is also examined. Because we do not have experimental data associated with this configuration, this simple simulation is carried out mainly

to investigate the effect of lateral channeling loss.

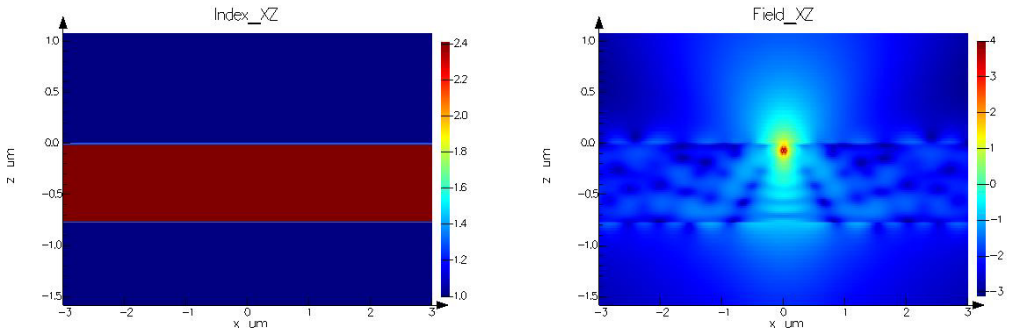

(a) **(b)**

Figure 7.5: **(a)** Index profile in x-z cross-section to show the simulation structure. **(b)** The dipole emission profile in x-z cross-section. The dipole is placed 66nm away from the top surface.

The simulation uses a membrane thickness of t_{d}=766nm and the dipole source is placed 66nm below the top surface. The simulation structure and dipole emission profile are plotted in fig. (7.5). The emission is clearly stronger towards the top of the simulation region. The simulated $F^{\mathrm{mem}}(\lambda)$ is plotted in fig. (7.6).

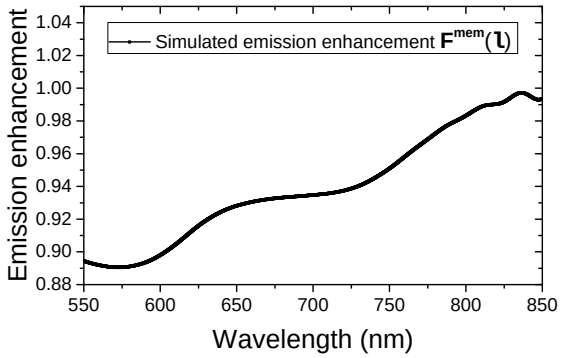

Figure 7.6: The simulated emission spectrum $F^{\mathrm{mem}}(\lambda)$ of the membrane-only simulation.

Using eq. (7.7) and eq. (7.8), the emission modifications are calculated as following:

$$
\begin{aligned}
F_{\mathrm{full}}^{\mathrm{mem}/0} &= \int_{\mathrm{full}} F^{\mathrm{mem}}(\lambda) S^0(\lambda) d\lambda = 0.938 \\
F_{\mathrm{zpl}}^{\mathrm{mem}/0} &= \frac{\int_{\mathrm{zpl}} F^{\mathrm{mem}}(\lambda) S^0(\lambda) d\lambda}{\zeta^0} = \frac{0.0573}{0.0620} = 0.924 \\
F_{\mathrm{psb}}^{\mathrm{mem}/0} &= \frac{F_{\mathrm{full}}^{\mathrm{mem}/0} - \zeta^0 F_{\mathrm{zpl}}^{\mathrm{mem}/0}}{1-\zeta^0} = \frac{0.938 - 0.062 \times 0.924}{1 - 0.062} = 0.935
\end{aligned}
$$

Interestingly, the dipole emission is suppressed over the whole spectral range. Due to the absence of DBR stacks, the ZPL spectral region no longer has a favourable LDoS.

This leads to a drop of ZPL emission enhancement F_{zpl} from 1.035 (on-mirror) to 0.924 (membrane-only). Therefore, the measured lifetime of 13.92ns is likely to be associated with the membrane itself, not the DBR mirror.

The collection analysis is summarised in table (7.4). The ZPL output power P^{mem} towards the top and bottom of the simulation region are found to be $5.03\%P^0$ and $1.52\%P^0$ respectively. If only considering the bottom collection which is in the same geometry as in the on-mirror simulation, the presence of DBR boosted the photon output from $1.52\%P^0$ to $18.80\%P^0$, which is about an order of magnitude change.

All η	η_{guid}	η_{bot}	η_{top}	$\eta_{\text{bot,NA}}$	$\eta_{\text{top,NA}}$	$F_{\text{zpl}}^{\text{mem}/0}$	$P_{\text{out,bot}}^{\text{mem}}$	$P_{\text{out,top}}^{\text{mem}}$
($\%P^{\text{mem}}$)				($\%\eta_{\text{bot}}$)	($\%\eta_{\text{top}}$)	(P^{mem}/P^0)	($\%P^0$)	
100	91.46	2.18	6.36	75.58	85.62	0.924	1.52	5.03

Table 7.4: Collection and ZPL output analysis of the membrane-only simulation. The overall ZPL photon output P towards the top and bottom of the simulation region are both listed.

7.2 Ideal High-Q Cavity Simulation

Having established the analysis model in previous sections, now we proceed to simulate the hybrid-medium cavity with realistic parameters. The focus of this investigation is to complete the emission rate analysis introduced in section (6.4) by quantifying either $\eta_{\text{zpl}}^{\text{on/mir}}$ or $F_{\text{zpl}}^{\text{on/mir}}$ using FDTD analysis. The key measured quantities from chapter (6) includes the full-spectrum emission enhancement $F_{\text{full}}^{\text{on/mir}}= 1.195$, the ZPL output enhancement $P_{\text{zpl}}^{\text{on/mir}}= 4.628$ and the on-mirror ZPL branching ratio $\zeta^{\text{mir}}= 6.87\%$.

Taking the dipole orientation factor $\xi^2= 0.85$ into account, $F_{\text{full}}^{\text{on/mir}}$ is formally written as:

$$F_{\text{full}}^{\text{on/mir}} = \xi^2 \frac{F_{\text{full}}^{\text{on/0}}}{F_{\text{full}}^{\text{mir/0}}} \tag{7.12}$$

The on-mirror emission enhancement is $F_{\text{full}}^{\text{mir/0}}$=0.935 as calculated in section (7.1.4). The value of on-resonance $F_{\text{full}}^{\text{on/0}}$ is to be obtained from FDTD simulations.

To match the ZPL output enhancement $P_{\text{zpl}}^{\text{on/mir}}$ between measurement and simulation, eq. (6.4) is adapted to include ξ^2 as well:

$$P_{\text{zpl}}^{\text{on/mir}} = \xi^2 F_{\text{zpl}}^{\text{on/mir}} \eta_{\text{zpl}}^{\text{on/mir}} = \xi^2 \frac{F_{\text{zpl}}^{\text{on/0}}}{F_{\text{zpl}}^{\text{mir/0}}} \frac{\eta_{\text{zpl}}^{\text{on/0}}}{\eta_{\text{zpl}}^{\text{mir/0}}} = \xi^2 \frac{P_{\text{out}}^{\text{on}}}{P_{\text{out}}^{\text{mir}}} \tag{7.13}$$

The on-mirror ZPL output has been simulated in section (7.1.4) and $P_{\text{out}}^{\text{mir}}$= 18.80%$P^0$. The inclusion of the same dipole orientation factor ξ^2 here is rather a simplified treatment. Rigorously speaking, ξ^2 only applies to cavity photons and the collection efficiency η of non-cavity photon probably has a different dipole orientation dependence. However, given the extremely long run-time of high-Q simulations, we reckon it is a close enough approximation to include ξ^2 as it is.

7.2.1 Simulation Setup and Cavity Mode Structure

A high-Q simulation is ran to investigate the most ideal performance of cavity B5. The cavity structure consist of a $\mathcal{R}$= 12µm cavity with a t_{d}=766nm membrane at q=16. The cavity depth L_{depth} was initially set to 1,360nm which is later reduced to 360nm for easier mode identification.

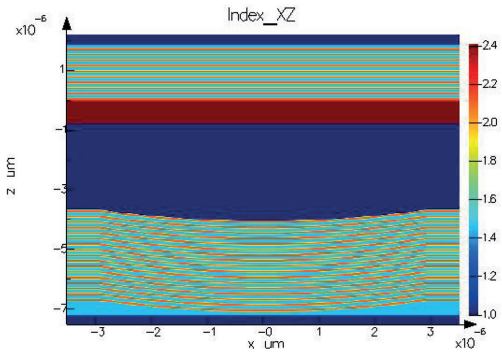

Figure 7.7: 2D cross-section plots of refractive index to show the cavity simulation structure.

The planar mirror is coated with 10 pairs of Ta-Si DBRs and 22nm of silica substrate while the featured mirror is coated with 17 pairs of Ta-Si DBRs and 27nm of silica substrate. This matches the real world mirror specification of R_{plan}=99.8% and R_{feat}=99.999% which has an expected finesse of $\mathcal{F}_{\text{tmm}}$= 3,461 at q=16 from TMM calculation. With the

introduction of a t_{d}=766nm membrane the reflectivity of the planar mirror drops down to R_{plan}=99.63% which reduces $\mathcal{F}_{\mathrm{tmm}}$ to 1,822.

Again, two sub-simulations are ran to distinguish between cavity photon (t= 100-835,000fs) and non-cavity photon (t= 0-100fs). The simulation mesh accuracy is set to 3. The 2D cross-section plot of the cavity structure is shown in fig. (7.7).

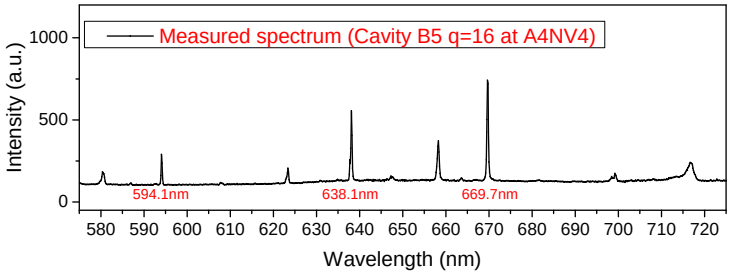

(a) Measured cavity mode spectrum.

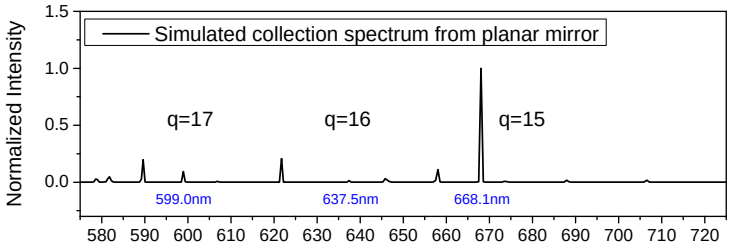

(b) Simulated collection spectrum from the planar mirror f-domain monitor.

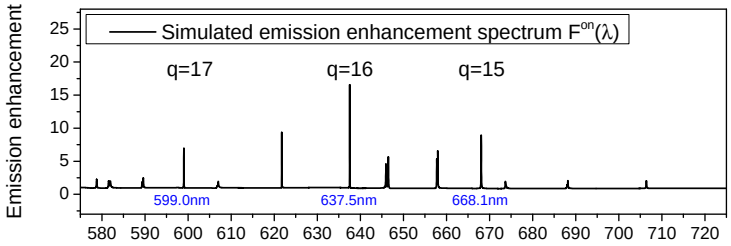

(c) Simulated emission enhancement spectrum $F(\lambda)$.

Figure 7.8: A comparison cavity mode spectrum: **(a)** the measured spectrum from chapter (6); **(b)** the simulated collection spectrum through the planar mirror; **(c)** the simulated emission enhancement spectrum from the Purcell monitors.

The simulated cavity spectrum are plotted in fig. (7.8)(b)(c) and three mode families at q=15-17 are identified. Compared to the measured spectrum in fig. (7.8)(a), a good agreement in mode structure is observed including the positions of higher order modes. There are some discrepancies in the mode position of the q=17 mode families which we attribute to the error in fitted membrane thickness t_{d}. But this should not affect the analysis of the target q=16 fundamental mode.

The simulated collection spectrum through the planar mirror in fig. (7.8)(b) suggests

that the q=15 mode at 668.1nm has the largest mode intensity among the three observed modes. The measured spectrum in fig. (7.8)(a) exhibits the same behaviour. The explanation for it is two-fold. Firstly, the DBR mirror reflectivity is naturally lower away from the centre of stopband (640nm). Secondly, given t_{d}= 766nm, the intra-diamond mode index for λ= 668.1nm is q_{d}= 5.46 which is very close to being a pure diamond-like mode. This leads to a further increase in planar mirror transmission.

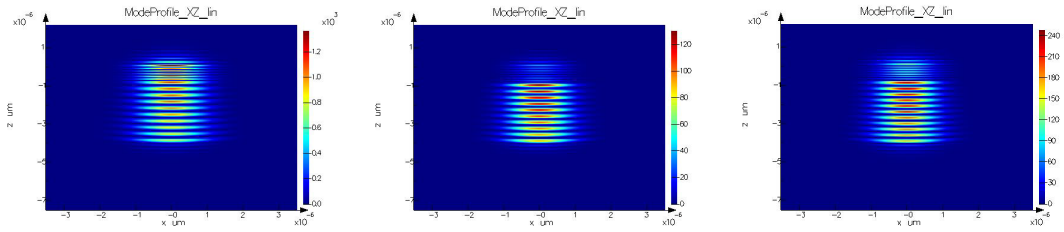

(a) Profile of q=15 mode at 668.1nm.

(b) Profile of q=16 mode at 637.5nm.

(c) Profile of q=17 mode at 599.0nm.

Figure 7.9: Mode profile of the fundamental modes from the q=15-17 mode families. Note for the q=15 and 17 modes the field intensity is relatively even across the air-diamond interface but for q=16 mode the field intensity is much stronger in the air portion of the cavity.

By examining the 2D cross-sectional mode profiles fig. (7.9)(a), it is confirmed that the q=15 mode has a relatively even $|\mathcal{E}|^2$ distribution across the diamond-air interface. This is a feature of a diamond-like mode. As a result, the q=15 mode experience a lower emission enhancement (fig. (7.8)(c)) but at the same time higher transmission through the planar mirror (fig. (7.8)(a)(b)).

The cavity metrics of the q=16 mode are summarised in table (7.5) where Q= 37,672, $\mathcal{F}_{\mathrm{fdtd}}$=2,355, and V_{int}=3.07μm^3. The simulated cavity volume is V=164$(\lambda/n)^3$. The simulated finesse is slightly higher than $\mathcal{F}_{\mathrm{ana}}$ because q= 16 is in the short-cavity limit for a $\mathcal{R}$= 12μm cavity (q_{max}=42). We note that these are single frequency readings. The multi-frequency integration results are presented in later sections.

	λ_0 (nm)	Q	V_{int} (μm^3)	F	$\mathcal{F}_{\mathrm{fdtd}}$	$\mathcal{F}_{\mathrm{ana}}$	$\mathcal{F}_{\mathrm{tmm}}$
q=16	637.54	37,672	3.07	17.91	2,355	2,243	1,822

Table 7.5: Cavity figure of merits of the q=16 mode. The expected finesse $\mathcal{F}_{\mathrm{ana}}$ and $\mathcal{F}_{\mathrm{tmm}}$ are also included. Note that these are single frequency readings. The multi-frequency integration results are presented in later sections.

A closer look of the field intensity and field energy distribution along the cavity axis for the q=16 fundamental mode is shown in fig. (7.10). The field intensity $|\mathcal{E}|^2$ is much higher in the air sub-cavity (air-like mode) but the field energy density $n^2|\mathcal{E}|^2$ is slightly higher in the diamond sub-cavity (diamond-like mode). Given the membrane thickness of t_{d}=766nm, the intra-diamond mode index at λ= 637.5nm is q_{d}=5.73. All these observations indicate that the supported q=16 fundamental mode is somewhere between a diamond-like mode and an air-like mode.

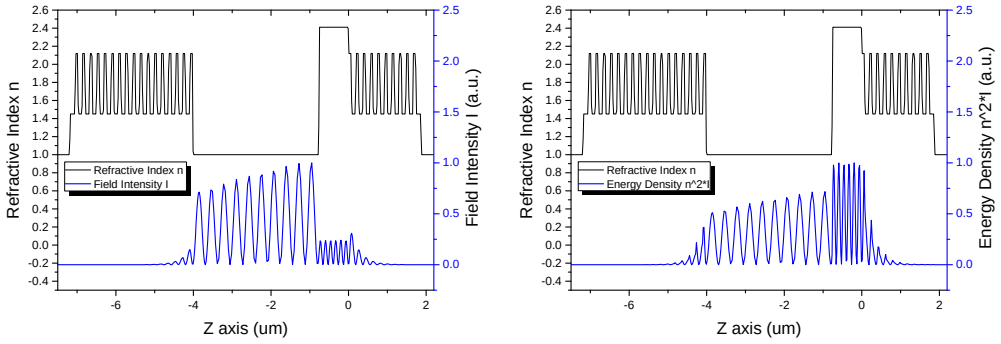

(a) Profile of $|\mathcal{E}|^2$. **(b)** Profile of $n^2|\mathcal{E}|^2$.

Figure 7.10: The axial distribution profiles of the q= 16 mode: **(a)** mode field intensity $|\mathcal{E}|^2$ and **(b)** cavity mode energy density product $n^2|\mathcal{E}|^2$.

The higher order transverse modes of the q=16 modes are plotted in fig. (7.11) which are assigned as $\mathrm{TEM}_{\mathrm{q=16,m+n=2}}$ and $\mathrm{TEM}_{\mathrm{q=16,m+n=4}}$. Since the cavity depth is set to 360nm which is rather shallow, it is reasonable that only the TEM modes with an axial component is well-supported in the cavity.

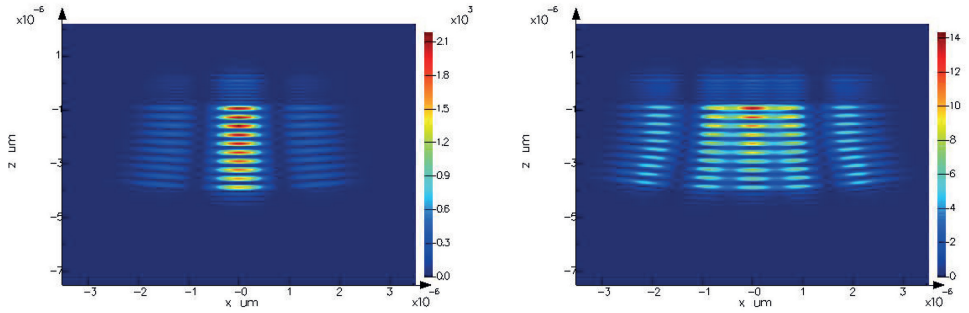

(a) Profile of q=16,m+n=2 mode at 621.8nm. **(b)** Profile of q=16,m+n=4 mode at 607.0nm.

Figure 7.11: Mode profiles of the higher order TEM modes in the q=16 mode family.

7.2.2 Emission Analysis

Using the the analytical branching ratio ζ^*=5.90% obtained in section (7.1.3), the analytical NV emission spectrum $S^0(\lambda)$ is constructed by again assuming a ZPL linewidth w_{zpl}=2GHz to start with. By extracting the cavity emission enhancement spectrum $F^{\text{on}}_{\text{cav}}(\lambda)$ from the simulation, the emitter-cavity enhancement spectrum $F^{\text{on}}_{\text{cav}}(\lambda)S^0(\lambda)$ is calculated and plotted in fig. (7.12). It is obvious that the majority of the NV emission are suppressed except the cavity-coupled ZPL emission.

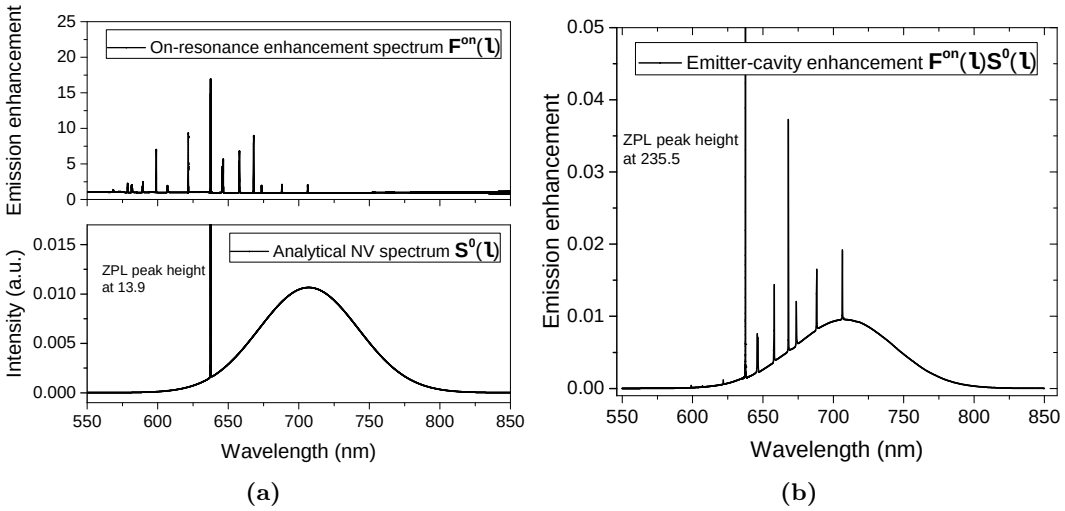

Figure 7.12: High-Q cavity plots of **(a)** the simulated device enhancement spectrum $F^{\text{on}}(\lambda)$ and the calculated emitter spectrum $S^0(\lambda)$ using w_{zpl}=2GHz and ζ^*=5.9%; **(b)** the combined emitter-cavity enhancement spectrum $F^{\text{on}}(\lambda)S^0(\lambda)$.

Integrating $F^{\text{on}}_{\text{cav}}(\lambda)S^0(\lambda)$ over the full spectrum range and in the ZPL region respectively, the :

$$\int_{\text{full}} F^{\text{on}}(\lambda)S^0(\lambda)d\lambda = 1.755$$

$$\int_{\text{zpl}} F^{\text{on}}(\lambda)S^0(\lambda)d\lambda = 0.886$$

$$\zeta^{\text{on}} = \frac{\int_{\text{zpl}} F^{\text{on}}(\lambda)S^0(\lambda)d\lambda}{\int_{\text{full}} F^{\text{on}}(\lambda)S^0(\lambda)d\lambda} = \frac{0.886}{1.755} = 0.5048$$

Substituting these integrals into eq. (7.7) and eq. (7.8), the emission enhancement factors are obtained as:

$$
\begin{aligned}
F_{\text{full}}^{\text{on/0}} &= \int_{\text{full}} F^{\text{on}}(\lambda) S^{0}(\lambda) d\lambda = 1.755 \\
F_{\text{zpl}}^{\text{on/0}} &= \frac{\int_{\text{zpl}} F^{\text{on}}(\lambda) S^{0}(\lambda) d\lambda}{\zeta^{0}} = \frac{0.886}{0.062} = 14.290 \\
F_{\text{psb}}^{\text{on/0}} &= \frac{F_{\text{full}}^{\text{on/0}} - \zeta^{0} F_{\text{zpl}}^{\text{on/0}}}{1 - \zeta^{0}} = \frac{1.755 - 0.062 \times 14.290}{1 - 0.062} = 0.926
\end{aligned}
$$

where a strong emission enhancement at ZPL of $F_{\text{zpl}}^{\text{on/0}}$=14.29 is observed. It should be noted that the in-cavity emission factor of PSB photons is $F_{\text{psb}}^{\text{on/0}}$=0.926 which is close to that from on-mirror simulation ($F_{\text{psb}}^{\text{mir/0}}$=0.928) and the free-standing membrane simulation ($F_{\text{psb}}^{\text{mem/0}}$=0.924). This confirms that the PSB emission suppression is caused by the geometry of the host material rather than the cavity mode interactions.

7.2.3 Validating Analytical ZPL Linewidth

At the beginning of the analysis, we assumed a ZPL linewidth of w_{zpl}= 2GHz as an initial estimation. Because the obtained Q=37,672 corresponds to a cavity linewidth of w_{cav}= 25GHz which is very close to the w_{zpl}, a convergence test of w_{zpl} is ran to validate the choice of w_{zpl}= 2GHz. The key simulation metrics are monitored while varying w_{zpl} from 36MHz to 7.4GHz and the results are plotted in fig. (7.13).

Compared to the first convergence test in fig. (7.4) for the on-mirror simulation were an effective emission linewidth w_{mir} in THz range is assumed, a stronger ZPL linewidth dependence is observed in all three plotted variables. This is expected because w_{cav} and w_{zpl} are closer in magnitude.

The trends in all three plots show a diminishing return for w_{zpl}< 1GHz. Taking the ZPL enhancement $F_{\text{zpl}}^{\text{on/0}}$ as an example, as w_{zpl} decreases from 7.4GHz to 740MHz, $F_{\text{zpl}}^{\text{on/0}}$ increases from 10.852 to 15.421 which is a 42% improvement. However, as w_{zpl} decreased further from 740MHz to 74MHz, $F_{\text{zpl}}^{\text{on/mir}}$ only showed a 4% improvement from 15.421 to 16.091. At this point w_{zpl}= 74MHz is more than two orders of magnitude smaller than w_{cav}=3 4GHz.

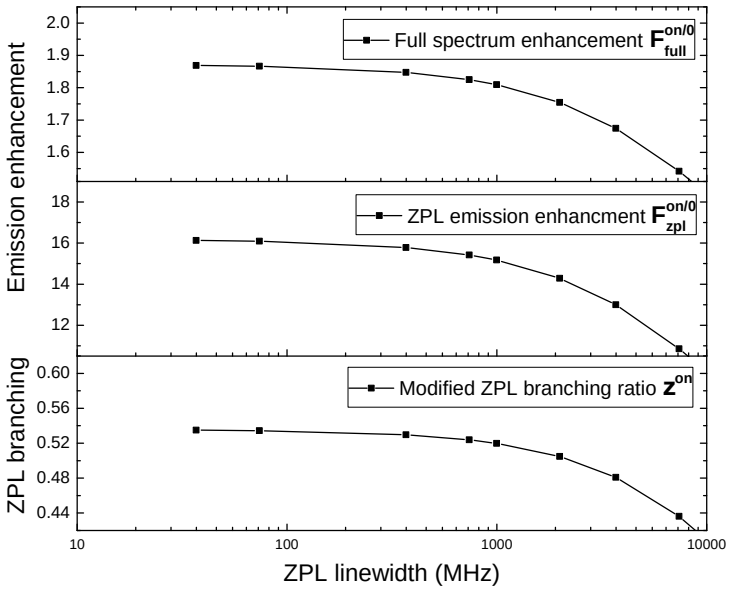

Figure 7.13: Convergence test of the ZPL linewidth w_{zpl} term in $S^0(\lambda)$ and its influence on key variable including the emission enhancement factors and ZPL branching ratio.

In reality, the measured quality factor Q is only 4,274, which is equivalent to w_{cav}= 300GHz. From a device engineering point of view, reduction of w_{zpl} below 1GHz does not yield much of $F^{\text{on/0}}_{\text{zpl}}$ improvement. Of course, this neglects the optical coherence considerations, which is also crucial for quantum network applications.

7.2.4 Collection and ZPL Output Analysis

Now we proceed to quantify the on-resonance collection behaviour and the ZPL output $P^{\text{on}}_{\text{out}}$. The t-domain field decay plot including all wavelengths is plotted in fig. (7.14)(a) and the 2D field profiles of the non-cavity and cavity photons are plotted in fig. (7.14)(b)(c). Different emission pattern is clearly observed.

The ZPL photon collection efficiencies into different spatial channels are listed in table (7.6). The collection through the planar mirror is corrected with the far-field collection efficiency $\eta^{\text{NA}}_{\text{plan}}$. The overall ZPL photon collection efficiency is $\eta^{\text{on}}_{\text{zpl}}$= 8.57%$P^{\text{on}}$ and the ZPL output $P^{\text{on}}_{\text{out}}$ is given by:

$$P^{\text{on}}_{\text{out}} = F^{\text{on/0}}_{\text{zpl}} \eta^{\text{on}}_{\text{zpl}} = 8.57 \times 14.29 = 122.46\% P^0$$

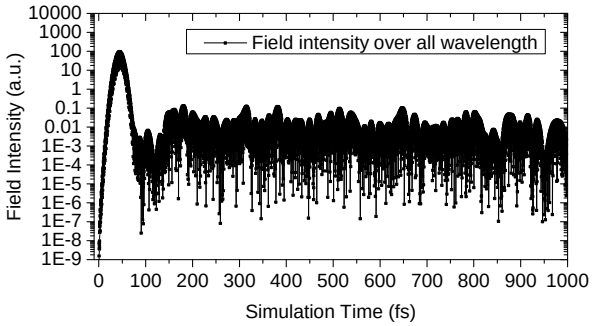

(a) Field decay data from t-domain monitor.

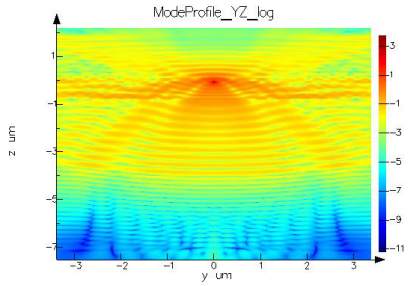

(b) Field profile of non-cavity photon.

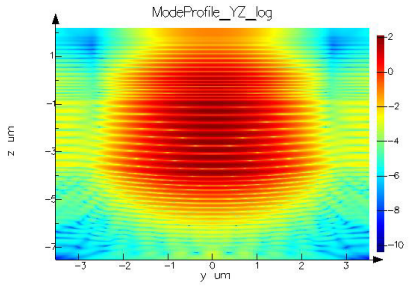

(c) Field profile of cavity photon.

Figure 7.14: **(a)** The t-domain field decay data over all wavelength. **(b)-(c)** The 2D cross-sectional field profile of the non-cavity and cavity photons respectively.

From the collection analysis in table (7.6), we note that the majority of the dipole emission (P^{on}) in the cavity structure is lost as non-cavity photon (>90%) which does not experience any cavity-related emission enhancement. Among the three spatial loss channels, the loss through 2D guided mode is the most dominant loss component. This is expected for a q=16 cavity made of high reflectivity mirrors. The large mirror separation naturally supports strong lateral guided modes (refer to section (4.5.1)), while the high mirror reflectivies renders the guided modes even more favourable than the mirror transmissions (refer to section (4.5.4)).

	All η	η_{guid}	η_{feat}	η_{plan}	$\eta_{\text{plan}}^{\text{NA}}$	$\eta_{\text{zpl}}^{\text{on}}=\eta_{\text{p}}\eta_{\text{p}}^{\text{NA}}$	$F_{\text{zpl}}^{\text{on/0}}$	$P_{\text{out}}^{\text{on}}$
	($\%P^{\text{on}}$)				($\%\eta_{\text{plan}}$)	($\%P^{\text{on}}$)	(P^{on}/P^{0})	($\%P^{0}$)
Non-cav	90.27	88.85	0.000	1.42	42.30	0.60	-	-
Cav	9.73	1.72	0.04	7.97	100	7.97	-	-
Sum	100	90.57	0.04	9.39	-	8.57	14.29	122.46

Table 7.6: Collection and ZPL output analysis of the high-Q cavity simulation where P^{on} is the dipolepower in simulated structure and P^{0} is the sourcepower in a homogeneous medium.

7.2.5 High-Q Simulation vs Experimental Data

After some lengthy but rigorous analysis of both the on-mirror and in-cavity simulations, all the relevant variables that are required to compare with experimental data have been obtained. Just to recall, the experimentally measured quantities are ξ^2= 0.85, ζ^{mir}= 6.87%, $F_{\text{full}}^{\text{on/mir}}$= 1.19 and $P_{\text{zpl}}^{\text{on/mir}}$= 4.628 respectively.

The simulated quantities are calculated as following. Firstly, the full-spectrum emission enhancement $F_{\text{full}}^{\text{on/mir}}$ between the in-cavity and on-mirror configurations is calculated using eq. (7.12):

$$F_{\text{full}}^{\text{on/mir}} = \xi^2 \frac{F_{\text{full}}^{\text{on/0}}}{F_{\text{full}}^{\text{mir/0}}} = 0.85 \times \frac{1.755}{0.935} = 1.59$$

Compared to the measured value of 1.19, the simulated result is clearly an overestimation. This is not surprising because the quality factor of simulated cavity is Q=37,672 while the measured cavity only has Q=4,274. In order to match $F_{\text{full}}^{\text{on/mir}}$ results, a low-Q version of the simulation is carried out in section (7.3).

Next, the ZPL output enhancement $P_{\text{zpl}}^{\text{on/mir}}$ is calculated using eq. (7.13):

$$P_{\text{zpl}}^{\text{on/mir}} = \xi^2 \frac{P_{\text{out}}^{\text{on}}}{P_{\text{out}}^{\text{mir}}} = 0.85 \times \frac{122.46\% P^0}{18.80\% P^0} = 5.537$$

The obtained value of $P_{\text{zpl}}^{\text{on/mir}}$ is also an overestimation compared to the measured value of 4.628.

Although both simulated cavity metrics are larger than the measured values, they are still good estimation of cavity performance, assuming no real-world hidden loss is present. To further address the discrepancy in both $F_{\text{full}}^{\text{on/mir}}$ and $P_{\text{zpl}}^{\text{on/mir}}$, a low-$Q$ cavity simulation is with more realistic constraints is ran in the following section.

7.3 Realistic Low-Q Cavity Simulations

In addition to Q discrepancy which is to be addressed with low-Q simulations, the simulated high-Q cavity also used a reduced cavity depth of L_{depth}= 360nm which is different from the real cavity geometry. As presented in the L_{depth} investigation in section (4.5.1),

both emission and collection properties of the cavity might have a L_{depth} dependence. Although the high-Q simulation with L_{depth}= 1,360nm is not re-ran due to long simulation time, the effect of L_{depth} will be inferred from two low-Q simulations with L_{depth}= 360nm and L_{depth}= 1,360nm.

More importantly, we note that implementing Q downgrade in FDTD simulation involves some caveats. In principle, the extra loss associated with the measured low cavity Q should be addressed in a way that reflects the actual loss distribution in the real cavity. However, it is almost impossible to pinpoint the loss distribution for a real cavity with hidden losses. The only quantifiable source of real-world loss is the interface scattering loss, but nm-scale scattering features are too computationally demanding to simulation. Material absorption is usually too small compared to the required Q downgrade.

In this work, the low-Q cavity is constructed by symmetrically reducing the number of DBR pairs on both cavity mirrors. According to 1D TMM calculations, 7-14 (planar-featured) DBR pairs yields a factor of 10 reductions in Q compared to the 10-17 DBR pairs used in the high-Q simulation.

Note that this method yields a slightly different emission pattern compared to the real experiment. To maintain the collection setup of the cavity device, it can be desirable maintain the DBR setup on the planar mirror and assign the additional losses to other loss channels, e.g. by adding materials absorption or reducing the DBR pairs on the featured mirror transmission. Nevertheless, the symmetrical reduction of DBR pairs used in following sections still gives a good indication of the performance of real cavities.

7.3.1 Shallow Low-Q Cavity

The shallow low-Q simulation has a q=16 fundamental mode at 637.424nm with a quality factor of Q=3,938. This is reasonably close to the measured Q= 4,274. The simulated cavity volume is V=162$(\lambda/n)^3$. By constructing $S^0(\lambda)$ analytically and extracting $F^{\text{on}}_{\text{cav}}(\lambda)$ from the simulation, $F^{\text{on}}_{\text{cav}}(\lambda)S^0(\lambda)$ is plotted in fig. (7.15).

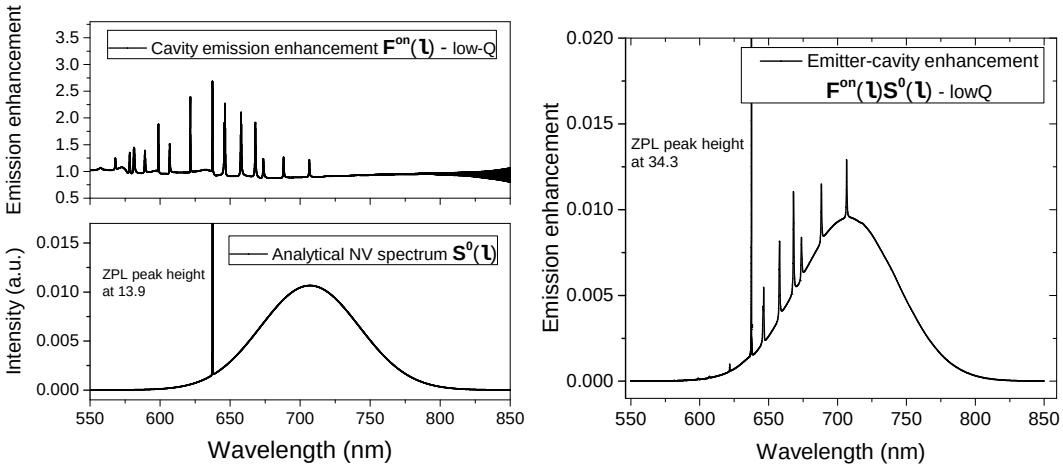

Figure 7.15: Low-Q cavity plots of **(a)** the simulated device enhancement spectrum $F^{\text{on}}(\lambda)$ and the calculated emitter spectrum $S^0(\lambda)$ using w_{zpl}=2GHz and ζ^*=5.9%; **(b)** the combined emitter-cavity enhancement spectrum $F^{\text{on}}(\lambda)S^0(\lambda)$.

The full-spectrum and ZPL integrals are calculated from $F^{\text{on}}_{\text{cav}}(\lambda)S^0(\lambda)$ as:

$$\int_{\text{full}} F^{\text{mir}}(\lambda)S^0(\lambda)d\lambda = 1.029$$
$$\int_{\text{zpl}} F^{\text{mir}}(\lambda)S^0(\lambda)d\lambda = 0.160$$
$$\zeta^{\text{mir}} = \frac{\int_{\text{zpl}} F^{\text{mir}}(\lambda)S^0(\lambda)d\lambda}{\int_{\text{full}} F^{\text{mir}}(\lambda)S^0(\lambda)d\lambda} = \frac{0.160}{1.029} = 0.155$$

Substituting the integrals into eq. (7.7) and eq. (7.8) the emission enhancement factors of the low-Q cavity simulations are:

$$F^{\text{on/0}}_{\text{full}} = \int_{\text{full}} F^{\text{on}}(\lambda)S^0(\lambda)d\lambda = 1.029$$
$$F^{\text{on/0}}_{\text{zpl}} = \frac{\int_{\text{zpl}} F^{\text{on}}(\lambda)S^0(\lambda)d\lambda}{\zeta^0} = \frac{0.160}{0.062} = 2.581$$
$$F^{\text{on/0}}_{\text{psb}} = \frac{F^{\text{on/0}}_{\text{full}} - \zeta^0 F^{\text{on/0}}_{\text{zpl}}}{1-\zeta^0} = \frac{1.029 - 0.062 \times 2.581}{1 - 0.062} = 0.926$$

where both $F^{\text{on/0}}_{\text{full}}$ and $F^{\text{on/0}}_{\text{zpl}}$ are much lower than that of the high-Q simulation. The PSB emission suppression remained similar to those of the on-mirror and membrane-only simulations. The w_{zpl} dependency test is skipped in this case.

The collection analysis and ZPL output results are given in table (7.7) and the ZPL output is $P^{\text{on}}_{\text{out}}$= 114.21%$P^0$. Compared to the high-$Q$ simulation, the low-Q simulation

	All η	η_{guid}	η_{feat}	η_{plan}	$\eta_{\text{plan}}^{\text{NA}}$	$\eta_{\text{zpl}}^{\text{on}}=\eta_{\text{p}}\eta_{\text{p}}^{\text{NA}}$	$F_{\text{zpl}}^{\text{on/0}}$	$P_{\text{out}}^{\text{on}}$
	($\%P^{\text{on}}$)				($\%\eta_{\text{plan}}$)	($\%P^{\text{on}}$)	(P^{on}/P^{0})	($\%P^{0}$)
Non-cav	55.85	54.53	0.00	1.32	77.27	1.02	-	-
Cav	44.15	7.87	0.14	43.23	100	43.23	-	-
Sum	100	62.4	0.14	44.55	-	44.25	2.581	114.21

Table 7.7: Collection and ZPL output analysis of the shallow low-Q cavity simulation where P^{on} is the dipolepower in simulated structure and P^{0} is the sourcepower in a homogeneous medium.

has 44.15% of dipolepower P^{on} emitted into the cavity mode. This is mainly attributed to the reduced mirror reflectivity such that the mirror transmission losses becomes more competitive against the 2D guided mode losses.

7.3.2 Deep Low-Q Cavity

The deep low-Q cavity features a cavity depth of L_{depth}= 1360nm and a larger cavity width to accommodate L_{depth} change. A comparison of simulated cavity mode spectrum and mode profiles between the shallow and deep cavities is shown in fig. (7.16). It is observed in both plots that due to the deeper and wider cavity feature, the deep cavity supports a lot more higher-order TEM modes.

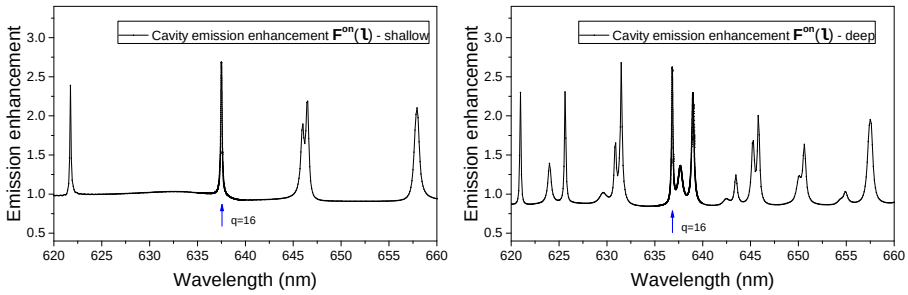

(a) Shallow cavity. **(b)** Deep cavity.

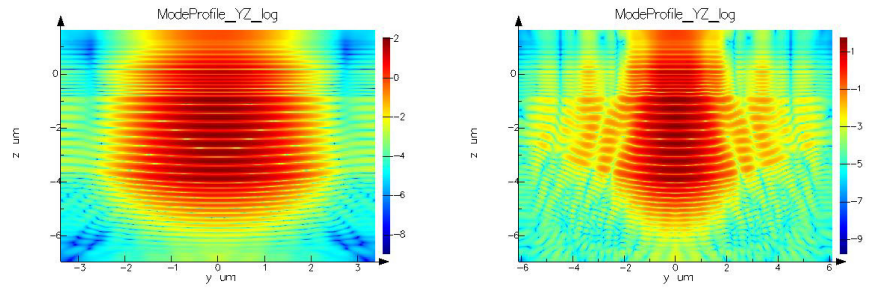

(c) Shallow cavity. **(d)** Deep cavity.

Figure 7.16: The cavity mode structure and the q=16 fundamental mode profile of **(a)(c)** the shallow and **(b)(d)** the deep cavity simulation.

The cavity quality factor of the deep cavity increased to Q=4,021 compared to Q=3,938 of the shallow cavity. The simulated cavity volume is V=201$(\lambda/n)^3$. This is probably due to the contribution of overlapping TEM modes. However, most of the higher-order TEM modes have a larger spatial span and stronger lateral propagating components. As a result, the emission enhancements is found to drop slightly:

$$
\begin{aligned}
F^{\mathrm{on/0}}_{\mathrm{full}} &= \int_{\mathrm{full}} F^{\mathrm{on}}(\lambda) S^0(\lambda) d\lambda = 1.025 \\
F^{\mathrm{on/0}}_{\mathrm{zpl}} &= \frac{\int_{\mathrm{zpl}} F^{\mathrm{on}}(\lambda) S^0(\lambda) d\lambda}{\zeta^0} = \frac{0.1565}{0.062} = 2.524 \\
F^{\mathrm{on/0}}_{\mathrm{psb}} &= \frac{F^{\mathrm{on/0}}_{\mathrm{full}} - \zeta^0 F^{\mathrm{on/0}}_{\mathrm{zpl}}}{1-\zeta^0} = \frac{1.025 - 0.062 \times 2.581}{1 - 0.062} = 0.926
\end{aligned}
$$

The collection analysis is summarised in table (7.8) and the ZPL output of the deep low-Q

	All η	η_{guid}	η_{feat}	η_{plan}	$\eta^{\mathrm{NA}}_{\mathrm{plan}}$	$\eta^{\mathrm{on}}_{\mathrm{zpl}}$=$\eta_{\mathrm{p}}\eta^{\mathrm{NA}}_{\mathrm{p}}$	$F^{\mathrm{on/0}}_{\mathrm{zpl}}$	$P^{\mathrm{on}}_{\mathrm{out}}$
	($\%P^{\mathrm{on}}$)				($\%\eta_{\mathrm{plan}}$)	($\%P^{\mathrm{on}}$)	(P^{on}/P^0)	($\%P^0$)
Non-cav	14.02	12.18	0.00	1.84	76.11	1.40	-	-
Cav	85.98	52.56	0.30	33.12	100	33.12	-	-
Sum	100	64.74	0.30	34.96	-	34.52	2.524	87.12

Table 7.8: Collection and ZPL output analysis of the deep low-Q cavity simulation where P^{on} is the dipolepower in simulated structure and P^0 is the sourcepower in a homogeneous medium.

cavity is $P^{\mathrm{on}}_{\mathrm{out}}$= 87.12%$P^0$. According to the collection distribution in table (7.8), even more dipole emission is channelled into the cavity modes at 85.98%P^{on}. Although due to more contributions from higher-order TEM modes, the loss through 2D guided modes becomes slightly more dominant too.

A direct comparison of collection distribution between shallow high-Q, shallow low-Q and deep low-Q simulations are summarised in fig. (7.17). The channel-specific collection efficiency η_{ch} is plotted in fig. (7.17)(a) and a better visualization is provide by the collection distribution in term of absolute power P_{ch} in fig. (7.17)(b).

It is observed that although the high-Q cavity provides the strongest emission enhancement ($F^{\mathrm{on/0}}_{\mathrm{zpl}}$= 14.29), most of those additional photons are lost in the first 100fs of simulation through lateral 2D guided modes. In comparison, the low-Q cavities only enhanced the dipole emission by $F^{\mathrm{on/0}}_{\mathrm{zpl}}$= 2.58/2.524 but a larger portion of the enhancement

emission is collected through the planar transmission loss. This is consistent with the results in section (4.5.4) where cavity performance is investigated as a function of mirror reflectivities. The high R mirrors does not yield the best ZPL output for reasons stated above.

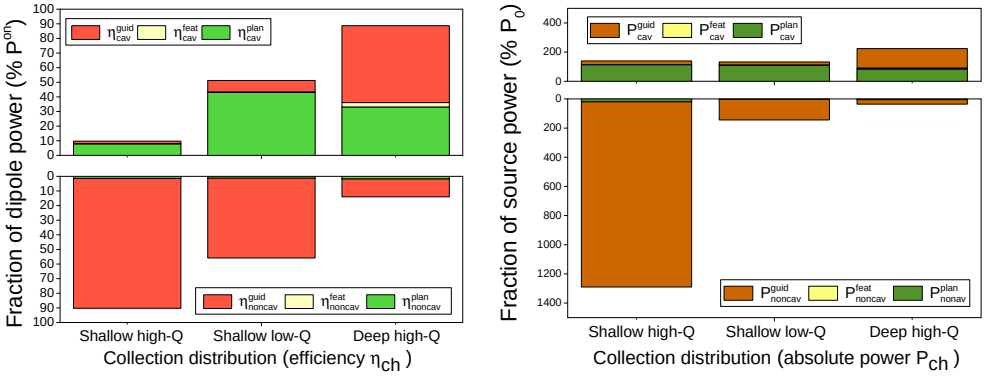

(a) Collection efficiency η_{ch}. **(b)** Collection power P_{ch}.

Figure 7.17: A comparison of collection distribution between shallow high-Q, shallow low-Q and deep low-Q simulations: **(a)** the collection efficiency distribution η_{ch} and **(b)** the absolute power distribution P_{ch}.

Moreover, the deep cavity is better at channeling the photon into the cavity mode thanks to the reduced mirror separation $L_{2\text{D}}$ and increased solid angle coverage over the dipole emitter. Although this benefit is put off by the participation of higher-order TEM modes which channels more photons sideways. As a result, the ZPL output through the planar mirror of the deep cavity is slight worse than that of the shallow cavity.

7.3.3 Low-Q vs Experimental Data

Again we recall the experimental data:ξ^2= 0.85, ζ^{mir}= 6.87%, $F_{\text{full}}^{\text{on/mir}}$ = 1.19 and $P_{\text{zpl}}^{\text{on/mir}}$ = 4.628. For comparison,the shallow and deep low-Q simulation results are averaged. Substituting the averaged $F_{\text{full}}^{\text{on/mir}}$= (1.025+1.10)/2= 1.063 into eq. (7.12), the relative emission enhancement $F_{\text{full}}^{\text{on/mir}}$ is given by:

$$F_{\text{full}}^{\text{on/mir}} = \xi^2 \frac{F_{\text{full}}^{\text{on/0}}}{F_{\text{full}}^{\text{mir/0}}} = 0.85 \times \frac{1.063}{0.935} = 0.966$$

which is a clear underestimation of the measured 1.19 but much closer than the high-Q cavity estimation of 1.59. The relative ZPL output enhancement $P_{\text{zpl}}^{\text{on/mir}}$ is found by

substituting the averaged $P_{\text{out}}^{\text{on}}$= (114.21+87.12)= 100.67%P^0 into eq. (7.13):

$$P_{\text{zpl}}^{\text{on/mir}} = \xi^2 \frac{P_{\text{out}}^{\text{on}}}{P_{\text{out}}^{\text{mir}}} = 0.85 \times \frac{100.67\%P^0}{18.80\%P^0} = 4.552$$

which yields a better good agreement with the measured value of 4.628 than the high-Q simulation result (5.537).

It is not surprising that there are still some discrepancies between the low-Q simulations and the experimental data. As mentioned previously, the way Q is downgraded to match measured Q is not ideal. So in a sense, the low-Q and high-Q simulations set the lower- and upper-bounds of the experimental data.

7.4 Completing the Emission Rate Analysis Table

Now that the the ZPL emission enhancement has been quantified via a series of simulation, we can proceed to complete the emission rate analysis from section (6.4). The lower-bound estimations provided by the low-Q simulations are used here.

Starting off with the on-resonance emission rates and branching ratio:

$$\gamma_{\text{zpl}}^{\text{on}} = \gamma_{\text{zpl}}^{\text{mir}} \times F_{\text{zpl}}^{\text{on/mir}} = 4.94 \times 2.552 = 12.61$$
$$\gamma_{\text{zpl}}^{\text{off}} = \gamma_{\text{full}}^{\text{off}} - \gamma_{\text{psb}}^{\text{off}} = 85.84 - 12.61 = 73.23$$
$$\zeta^{\text{on}} = \frac{\gamma_{\text{zpl}}^{\text{on}}}{\gamma_{\text{full}}^{\text{on}}} = \frac{12.61}{85.84} = 14.69\%$$

The off-resonance column is calculated accordingly and all the results are summarised in table (7.9). One obvious problem is noticed here: the off-resonance column has a negative ZPL emission rate which is not realistic. This is attributed to the error in the ZPL output enhancement $F_{\text{zpl}}^{\text{on/mir}}$= 2.552 used in the on-resonance column. As mentioned in previous sections, the low-Q simulation underestimates the cavity performance given how the Q is downgraded to match the experimental data. As a result, all related rate terms are affected. If $F_{\text{zpl}}^{\text{on/mir}}$ is taken at a higher value, the table can be filled with no issue.

	Bulk	On-mir	On-res	Off-res
Full-spec (MHz)	-	$\gamma_{\text{full}}^{\text{mir}}$= 71.84	$\gamma_{\text{full}}^{\text{on}}$= 85.84	$\gamma_{\text{full}}^{\text{off}}$= 72.10
ZPL (MHz)	-	$\gamma_{\text{zpl}}^{\text{mir}}$= 4.94	$\gamma_{\text{zpl}}^{\text{on}}$= 12.61*	$\gamma_{\text{zpl}}^{\text{off}}$= -1.13*
PSB (MHz)	-	$\gamma_{\text{psb}}^{\text{mir}}$= 66.91	$\gamma_{\text{psb}}^{\text{on}}$= 73.23*	$\gamma_{\text{psb}}^{\text{off}}$≈73.23*
ζ	-	ζ^{mir}= 6.87%	ζ^{on}=14.69%*	ζ^{off}= N/A*

Table 7.9: A failed attempt to complete emission rate analysis for A4-NV4 in cavity B5 with the help of FDTD simulations. The numbers with a '*' sign are calculated using low-Q simulation results which are mostly lower-bound estimations.

7.4.1 Emission Analysis with an Alternative Approach

The emission analysis demonstrated above is based on the assumption that the PSB photon is a free-parameter. In fact, according to the simulated F_{psb} in membrane-only (0.928), on-mirror (0.935) and in-cavity (0.926), it is actually a pretty consistent parameter across all three configurations. Therefore, the emission analysis can be completed solely using this finding.

	Bulk	On-mir	On-res	Off-res
Full-spec (MHz)	-	$\gamma_{\text{full}}^{\text{mir}}$= 71.84	$\gamma_{\text{full}}^{\text{on}}$= 85.84	$\gamma_{\text{full}}^{\text{off}}$= 72.10
ZPL (MHz)	-	$\gamma_{\text{zpl}}^{\text{mir}}$= 4.94	$\gamma_{\text{zpl}}^{\text{on}}$= 18.93	$\gamma_{\text{zpl}}^{\text{off}}$= 5.19
PSB (MHz)	-	$\gamma_{\text{psb}}^{\text{mir}}$= 66.91	$\gamma_{\text{psb}}^{\text{on}}$≈ 66.91	$\gamma_{\text{psb}}^{\text{off}}$≈66.91
ζ	-	ζ^{mir}= 6.87%	ζ^{on}=22.09%	ζ^{off}= 7.20%

Table 7.10: An alternative approach to complete the emission analysis based on the fact that F_{psb} is almost constant in all three conditions.

Using the same $\gamma_{\text{psb}}^{\text{mir}}$=66.91MHz, the table in table (7.10) is completed with no outstanding issues. The updated experimental cavity parameters are therefore F_{zpl}=3.832, ζ^{on}=22.09%. The experimental collection enhancement $P_{\text{out}}^{\text{on/mir}}$ is then obtained as 4.628/3.832=1.208. Given the simulated $P_{\text{out}}^{\text{mir}}$= 18.80%$P^0$ and $P_{\text{out}}^{\text{on}}$ ≈ (87.12+114.21)/2= 100.67%P^0. Consequently the collection efficiency η of the experimental data is estimated as:

$$\eta = \frac{P_{\text{out}}^{\text{mir}} \times 1.208}{P_{\text{out}}^{\text{on}}} = \frac{18.80P^0 \times 1.208}{100.67\%P^0} = 22.56 \tag{7.17}$$

The obtained cavity matrices from revised emission analysis are within the range set by the low-Q and high-Q simulations which is a good sign. The cavity metrics from experimental data, simulations and emission analysis is summarised in table (7.11).

	$F_{\text{full}}^{\text{on/mir}}$	$P_{\text{zpl}}^{\text{on/mir}}$	$F_{\text{zpl}}^{\text{on/mir}}$	ζ	η
Experimental data	1.19	4.628	-	6.87%	-
High-Q simulation	1.59	5.537	14.29	50.48%	8.57%
Low-Q simulation	0.97	4.552	2.552	15.38%	39.39%
Updated γ analysis	1.19*	4.628*	3.83	22.09%	22.56%

The simulated on-mirror η=18.16%.

Table 7.11: A comparison of cavity metrics between the high-Q, the low-Q and the experimental results. The low-Q data are averaged between the shallow and deep cavity simulations. The cavity metrics are full-spectrum emission enhancement $F_{\text{full}}^{\text{on/mir}}$, ZPL photon output $P_{\text{zpl}}^{\text{on/mir}}$, ZPL emission enhancement $F_{\text{zpl}}^{\text{on/mir}}$, ZPL branching ratio ζ and device photon collection efficiency η.

7.5 Conclusions

In summary, FDTD simulation analysis established in chapter (4) and its adaption to the multi-frequency approach have been proved to be an effective and innovative way of understanding the experimental cavity-coupling data. The simulations presented in this chapter successfully set the lower- and upper-bound estimations of the experimental data.

The measured ZPL output enhancement $P_{\text{zpl}}^{\text{on/mir}}$= 4.628 is decomposed into an emission enhancement component $F_{\text{zpl}}^{\text{on/mir}}$ and a collection enhancement component $\eta^{\text{on/mir}}$. By quantifying $F_{\text{zpl}}^{\text{on/mir}}$= 3.832 using low-$Q$ cavity simulations, the collection enhancement is $\eta^{\text{on/mir}}$= 1.208. The change in ZPL branching ratio is given by $\zeta^{\text{on/mir}}$= 22.09%/6.87%= 3.215. In the context of entanglement generation in a double-heralding scheme (section (1.1.5)), $\zeta^{\text{on/mir}}$ and $\eta^{\text{on/mir}}$ contribute to the indistinguishable photon emission efficiency η_{em} and the photon collection efficiency η_{co} respectively. The entanglement success rate has a quadratic dependence on both η_{em} and η_{co}.

By simulating the cavity structure with high reflectivity mirrors, the upper-bound of cavity performance is also determined. In this regime, the dipole emission enhancement is as high as $F_{\text{zpl}}^{\text{on/mir}}$= 14.29. However, the dipole emission pattern does not favour collection through the planar mirror. The majority of additional photons are not channelled into the cavity modes (η=8.57%), which has better external optics coupling. In contrast, the low-Q cavities show much lower emission enhancement, but the collection is a lot more efficient (η=39.39%). The emission analysis approach yields a more realistic estimate of the cavity metrics.

Throughout the analysis of all the FDTD simulation in this work, the lateral 2D guided modes is proved to be a dominant source of photon loss for the Fabry-Perot type cavity used in this work. Huge improvement of cavity performance can be expected if the separation between the planar part of the mirrors (L_{2D}) could be eliminated to limit intra-cavity guided losses.

Chapter 8

Conclusions and Outlook

Here we summarise the key theoretical and experimental results in this work, followed by a review on how the membrane-in-cavity setup can be improved in the future.

8.1 Conclusions

Firstly, the extensive FDTD simulation study of the Fabry-Perot cavity is demonstrated. A comprehensive analysis methodology is proposed where the cavity ZPL output P_{out} is decomposed into emission enhancement F and collection enhancement P_{plan}. The cavity loss through 2D guided mode P_{guid}, which is normally disregarded in 1D approaches, was proved to be the most influential loss mechanism in Fabry-Perot cavities. In principle, both F and P_{plan} are determined by the balance between various loss mechanisms. The deviation of P_{out} from the 1D models in the long-cavity limit ($q{>}q_{\mathrm{max}}/2$) is explained by the increasing contribution of P_{guid}, in contrary to the commonly believed mode clipping loss at the cavity features.

The results from membrane-in-cavity simulations suggest that the hybrid-medium cavity is not too different from a single-medium cavity with additional P_{guid} mediated by the high-index diamond membrane. The emission enhancement F and the collection of the non-cavity photon are both degraded, but the collection of cavity photon is not affected. No significant performance discrepancy is observed between the diamond-like and air-like modes, which agrees with the TMM calculations.

The successful fabrication of μm-thick diamond membranes containing ion-implanted NVs

is demonstrated following a multi-stage sample preparation procedure. The cause of NV fluorescence quenching in earlier diamond membranes is correlated to chlorine-related etching damages. In response, an oxygen-based etch has to be added into the fabrication flow, which limits the membrane surface roughness to 1nm. Compared to the starting materials, the density of NV centres is much lower in the membranes potentially due to residual etching damages. The preliminary characterisation data from a diamond membrane with laser-written NVs is also demonstrated. The scalable free-running laser-writing method is capable of covering the whole 4x4mm sample area.

The optical coherence of both ion-implanted and laser-written NVs are compared against each other. The average homogeneous and total ZPL linewidth of ion-implanted NVs are $\delta\upsilon_{\mathrm{hom}}$=400MHz and $\delta\upsilon_{\mathrm{tot}}$=5GHz respectively. In contrast, much better linewidth at $\delta\upsilon_{\mathrm{hom}}$=50MHz and $\delta\upsilon_{\mathrm{tot}}$=100MHz is observed with laser-written NVs. We further quantified the charge-state stability using the measurement statistics. The laser-writing NVs show an average PLE validation rate $p_{\mathrm{val}}\approx$0.5 with the best p_{val}=0.97 while most of the ion-implanted NVs has $p_{\mathrm{val}}<$0.3. By comparing p_{val} with the recharge probability p_{rec}, we also identified that laser-writing NVs exhibits long-lived bright PLE states without the need of repumping. The good charge-state stability under resonant excitation is particularly encouraging in improving the attempt rate of quantum entanglement operations.

The cavity-enhanced NV emission in the membrane is demonstrated with an ion-implanted NV coupled to the q=16 fundamental mode of a $\mathcal{R}$=12μm cavity at 4K. The NV ZPL emission properties are compared between the in-cavity and on-mirror configurations. While coupled to the cavity mode, a total emission enhancement of F_{full}=1.195 is quantified using lifetime measurement and observed ZPL emission increases by a factor of $P_{\mathrm{zpl}}^{\mathrm{on/mir}}$=4.628. The on-mirror ZPL ranching ratio is measured to be ζ^{mir}=6.87%, and the membrane thickness of t_{d}=766nm is determined by fitting the cavity mode map using the analytical resonance expression. An emission analysis is attempted with measured data, but a breakdown of $P_{\mathrm{zpl}}^{\mathrm{on/mir}}$ into the collection and emission enhancement components are required from FDTD simulations.

According to the finesse measurement, the real-world performance of the hybrid-medium cavity is almost ten times lossier than the simulated values. This degradation exceeds the

magnitude of quantifiable scattering losses assuming a surface roughness of 1nm and the source of the extra loss is not identified. In contrary, the measured performance of single-medium cavity only drops by a factor of 2 from the expected values. Cavity instability on the order of minute is observed by monitoring the long-term signal fluctuation. As a result, long acquisition time measurement, such as HBT is associated with large uncertainty.

In order to process the experimental data, the analyse methodology established in the FDTD chapter is adapted to a multi-frequency integration approach. A cavity enhancement spectrum $F^{\mathrm{dev}}(\lambda)$ is extracted from FDTD simulations with realistic cavity parameters and an analytical NV spectrum $S^0(\lambda)$ is constructed using two peak functions to represent ZPL and PSB contributions. By combining the two spectrum and setting proper integration limits, the full-spectrum emission enhancement F_{full} and the ZPL emission enhancement F_{zpl} can be obtained. The parameters for $S^0(\lambda)$ is calibrated by using the measured on-mirror ZPL branching ratio of ζ^{mir}=6.87%.

The realistic cavity is firstly simulated with a high-Q setup yielding ZPL emission enhancement F_{zpl}=14.29, ZPL branching ratio ζ^{on}=50.48% and ZPL collection efficiency η^{on}=8.57%. This simulation is an overestimation because the simulated high-Q cavity has a Q=37,672 while the measured Q is only 4,274. Hence a low-Q simulation is required where Q is matched by dropping DBR pairs. The revised simulation gives F_{zpl}=2.552, ζ^{on}=15.38% and η^{on}=39.39%. Despite the drop in ZPL branching ratio ζ^{on}, the low-Q simulation does exhibit better collection efficiency η^{on}. This is somewhat alarming, suggesting that the presence of 2D guided mode is harming the cavity performance by deteriorating the cavity collection efficiency.

With the FDTD simulations in the membrane-only, on-mirror and in-cavity simulations, it is found that the PSB emission rate is almost constant across all three configurations. Based on this finding, an updated emission analysis of the experimental results yield F_{zpl}=3.83, ζ^{on}=22.09% and η^{on}=22.56% with the help from simulation photon output figures. We reckon that this is the most accurate interpretation of the experimental data.

8.2 Future Prospects

To build upon the cavity-coupled NV results achieved in this work, some outstanding issues remain to be addressed in order to realise an efficient spin-photon interface. The main considerations are summarised as follows:

Diamond membrane fabrication The fabrication of diamond nano-photonic devices containing NV centres has always been difficult due to the balance between aggressive fabrication technique and the susceptibility of NV centres to structure interfaces. The membrane-in-cavity device in this work is no exception. The optical coherence of ion-implanted NVs in membrane degraded from the bulk values and the real-world performance of the hybrid-medium cavity is also inferior to the expected values.

Despite the quoted roughness of 1nm, the diamond surfaces do exhibit etching-pits due to material re-deposition during the O^2 etch. A solution has been reported by Ruf et al. [28] where a quartz etching mask is used to prevent re-deposition effect. The potential gain in cavity performance could be expected with this approach.

At the end of chapter (6), we proposed a hypothesis that explains the extra unaccounted cavity loss as a result of membrane wedge acting like a partial reflector. Hence, in this regard, membrane flatness could also be an important factor in future membrane fabrications.

NV centre generation The cavity-NV coupling demonstrated in this work uses ion-implanted NVs, which does not possess the required optical coherence for two-photon interference type measurements. Although the laser-written NVs have shown promises with excellent optical properties, the fabrication of near-surface ($<1\mu m$) coherent laser-written NVs is yet to be demonstrated.

For an ideal membrane-in-cavity setup, it is demanding in fabrication precision to overlap the NVs with the electric field of the cavity mode. This condition demands the axial positioning accuracy to be on the order of tens of nm. Currently, the laser-writing technique allows a sub-μm axial positioning accuracy [95], which is fundamentally limited by the spread of laser spot in vertical directions. A possible solution is to combine laser-writing with delta-doping technique [96].

Fabry-Perot cavity What accompanies the tunability of the Fabry-Perot type cavity is the system instability. Despite the extensive passive isolation measures adopted in this work, jittering of cavity mode position due to mechanical vibrations is an outstanding issue, as demonstrated in chapter (6). Cavity mode instability can deteriorate the effectiveness of emission enhancement provided by cavity-NV interaction, and it is especially harmful to long acquisition measurements. It is partially due to this reason, one of our cavity mirrors is chosen to be at lower reflectivity (R=0.998) such that the stability requires is loosened.

The observed instability in our work is mainly the mode drift on the timescale of minutes rather than high-frequency vibrations. Hence cavity locking mechanism with a moderate locking frequency should be sufficient to correct for mode drifts and improve the overall device efficiency. A relatively simple option is to use a PID control loop based on webcam image processing of the interference fringe pattern between the cavity mirrors. If high-frequency locking is demanded, control loop based on the coupling of another laser wavelength with a different cavity feature is also a viable option. Although this requires additional optics to be installed and their compatibility with resonant fluorescence experiments requires further considerations.

The presence of 2D guided mode loss also requires addressing. As shown in section (7.3.3), although the high-Q cavity gives better emission enhancement, the ZPL collection efficiency is very low compared to that of the low-Q cavity. Referring to the η factor in the entanglement success rate P_{succ} expression in eq. (1.21), both the indistinguishable photon emission efficiency η_{em} and the η_{co} should be optimized at the same time for an overall improvement of P_{succ}.

Monolithic cavity construction In pursuit of device robustness and fabrication scalability, a monolithic cavity design is certainly an appealing option. Although this approach abandons the tuning flexibility of the two-mirror Fabry-Perot setup, some degrees of resonance tuning should be viable by adjusting the DBR coating thickness. Starting with a relatively thin and flat diamond membrane, NV centres are laser-written in a grid structure close to one of the surfaces. SIL-like structures are then fabricated on top of each NV from the reverse side and coated with high-R

DBR coatings. At this point, the structure is similar to that of a parabolic reflector [97] and the milled SIL acts as the concave mirror. The NV emission properties are then characterised in this configuration before the flat surface is also coated with DBRs. After the formation of the cavity, some post-selection is inevitably required to pick out the best performing devices. Combined with the scalable laser-writing and SIL fabrication techniques, this approach might be supported by a large number of device sampling.

Bibliography

1. *Quantum Computing: Progress and Prospects* https://www.nap.edu/catalog/25196/quantum-computing-progress-and-prospects (The National Academies Press, Washington, DC, 2019).
2. Arute, F. *et al.* Quantum Supremacy using a Programmable Superconducting Processor. *Nature* **574,** 505 (2019).
3. Feynman, R. P. Simulating Physics With Computers. *International Journal of Theoretical Physics* **21,** 467–488 (1982).
4. S., P. W. *Algorithms for Quantum Computation: Discrete Logarithms and Factoring* in *Proceedings 35th Annual Symposium on Foundations of Computer Science* (1994), 124–134.
5. DiVincenzo, D. P. The Physical Implementation of Quantum Computation. *Fortschritte der Physik* **48,** 771–783 (2000).
6. Cabrillo, C., Cirac, J. I., García-Fernández, P. & Zoller, P. Creation of Entangled States of Distant Atoms by Interference. *Physical Review A* **59,** 1025–1033. https://link.aps.org/doi/10.1103/PhysRevA.59.1025 (1999).
7. Raussendorf, R. & Briegel, H. J. A One-Way Quantum Computer. *Physical Review Letters* **86,** 5188–5191. https://link.aps.org/doi/10.1103/PhysRevLett.86.5188 (2001).
8. Chou, C. W. *et al.* Measurement-Induced Entanglement for Excitation Stored in Remote Atomic Ensembles. *Nature* **438,** 828–832 (2005).
9. Moehring, D. L. *et al.* Entanglement of Single-Atom Quantum Bits at a Distance. *Nature* **449,** 68–U48 (2007).
10. Barrett, S. D. & Kok, P. Efficient High-Fidelity Quantum Computation using Matter Qubits and Linear Optics. *Physical Review A* **71,** 060310 (2005).

11. Benjamin, S., Lovett, B. & Smith, J. Prospects for Measurement-Based Quantum Computing with Solid State Spins. *Laser & Photonics Reviews* **3,** 556–574. https://onlinelibrary.wiley.com/doi/abs/10.1002/lpor.200810051 (2009).

12. Johnson, S., Dolan, P. R. & Smith, J. M. Diamond Photonics for Distributed Quantum Networks. *Progress in Quantum Electronics* **55,** 129 –165. http://www.sciencedirect.com/science/article/pii/S0079672717300162 (2017).

13. Fox, M. *Quantum Optics: an Introduction* eng (Oxford University Press, Oxford ; New York, 2006).

14. Jarmola, A., Acosta, V. M., Jensen, K., Chemerisov, S. & Budker, D. Temperature- and Magnetic-Field-Dependent Longitudinal Spin Relaxation in Nitrogen-Vacancy Ensembles in Diamond. *Physical Review Letters* **108,** 197601. https://link.aps.org/doi/10.1103/PhysRevLett.108.197601 (2012).

15. Bylander, J., Robert-Philip, I. & Abram, I. Interference and Correlation of Two Independent Photons. *European Physical Journal D* **22,** 295–301 (2003).

16. Grange, T. *et al.* Cavity-Funneled Generation of Indistinguishable Single Photons from Strongly Dissipative Quantum Emitters. *Physical Review Letters* **114,** 193601. https://link.aps.org/doi/10.1103/PhysRevLett.114.193601 (2015).

17. Kunze, H.-J. *Introduction to Plasma Spectroscopy* Chapter 9 Line Broadening (Springer, 2009).

18. Tamarat, P. *et al.* Stark Shift Control of Single Optical Centers in Diamond. *Physical Review Letters* **97,** 083002. https://link.aps.org/doi/10.1103/PhysRevLett.97.083002 (2006).

19. Chen, Y.-C. *et al.* Laser Writing of Coherent Colour Centres in Diamond. *Nature Photonics* **11,** 77–80 (2017).

20. Robledo, L., Bernien, H., van Weperen, I. & Hanson, R. Control and Coherence of the Optical Transition of Single Nitrogen Vacancy Centers in Diamond. *Physical Review Letters* **105,** 177403. https://link.aps.org/doi/10.1103/PhysRevLett.105.177403 (2010).

21. Allen, L & Eberly, J. H. *Optical Resonance and Two-Level Atoms* Repr. eng (Dover, New York, 1987).

22. Bernien, H. *et al.* Heralded Entanglement between Solid-State Qubits Separated by Three Metres. *Nature* **497,** 86–90 (2013).

23. Legero, T., Wilk, T., Kuhn, A. & Rempe, G. Time-Resolved Two-Photon Quantum Interference. *Applied Physics B - Lasers and Optics* **77.** Meeting of the German-Physical-Society, UNIV HANOVER, HANNOVER, GERMANY, MAR 24-28, 2003, 797–802 (2003).

24. Legero, T., Wilk, T., Hennrich, M., Rempe, G. & Kuhn, A. Quantum Beat of Two Single Photons. *Physical Review Letters* **93,** 070503. https://link.aps.org/doi/10.1103/PhysRevLett.93.070503 (2004).

25. Hong, C. K., Ou, Z. Y. & Mandel, L. Measurement of Subpicosecond Time Intervals between Two Photons by Interference. *Physical Review Letters* **59,** 2044–2046. https://link.aps.org/doi/10.1103/PhysRevLett.59.2044 (1987).

26. Metz, J. & Barrett, S. D. Effect of Frequency-Mismatched Photons in Quantum-Information Processing. *Physical Review A* **77,** 042323. https://link.aps.org/doi/10.1103/PhysRevA.77.042323 (2008).

27. Zhao, T.-M. *et al.* Entangling Different-Color Photons via Time-Resolved Measurement and Active Feed Forward. *Physical Review Letters* **112,** 103602. https://link.aps.org/doi/10.1103/PhysRevLett.112.103602 (2014).

28. Ruf, M. *et al.* Optically Coherent Nitrogen-Vacancy Centers in Micrometer-Thin Etched Diamond Membranes. *Nano Letters* **19.** PMID: 31136192, 3987–3992. https://doi.org/10.1021/acs.nanolett.9b01316 (2019).

29. Nickerson, N. H., Fitzsimons, J. F. & Benjamin, S. C. Freely Scalable Quantum Technologies Using Cells of 5-to-50 Qubits with Very Lossy and Noisy Photonic Links. *Physical Review X* **4,** 041041. https://link.aps.org/doi/10.1103/PhysRevX.4.041041 (2014).

30. Doherty, M. W. *et al.* The Nitrogen-Vacancy Colour Centre in Diamond. *Physics Reports* **528,** 1 –45. http://www.sciencedirect.com/science/article/pii/S0370157313000562 (2013).

31. Jelezko, F., Gaebel, T., Popa, I., Gruber, A. & Wrachtrup, J. Observation of Coherent Oscillations in a Single Electron Spin. *Physical Review Letters* **92,** 076401. https://link.aps.org/doi/10.1103/PhysRevLett.92.076401 (2004).

32. Abobeih, M. H. *et al.* One-Second Coherence for a Single Electron Spin Coupled to a Multi-Qubit Nuclear-Spin Environment. *Nature Communications* **9,** 2552 (2018).

33. Bernien, H. *et al.* Two-Photon Quantum Interference from Separate Nitrogen Vacancy Centers in Diamond. *Physical Review Letters* **108,** 043604. https://link.aps.org/doi/10.1103/PhysRevLett.108.043604 (2012).

34. Sipahigil, A. *et al.* Quantum Interference of Single Photons from Remote Nitrogen-Vacancy Centers in Diamond. *Physical Review Letters* **108,** 143601. https://link.aps.org/doi/10.1103/PhysRevLett.108.143601 (2012).

35. Pfaff, W. *et al.* Unconditional Quantum Teleportation between Distant Solid-state Quantum Bits. *Science* **345,** 532–535 (2014).

36. Hensen, B. *et al.* Loophole-free Bell Inequality Violation using Electron Spins Separated by 1.3 Kilometres. *Nature* **526,** 682–686 (2015).

37. Fu, K.-M. C. *et al.* Observation of the Dynamic Jahn-Teller Effect in the Excited States of Nitrogen-Vacancy Centers in Diamond. *Physical Review Letters* **103,** 256404. https://link.aps.org/doi/10.1103/PhysRevLett.103.256404 (2009).

38. Fu, K.-M. C., Santori, C., Barclay, P. E. & Beausoleil, R. G. Conversion of Neutral Nitrogen-Vacancy Centers to Negatively Charged Nitrogen-Vacancy Centers through Selective Oxidation. *Applied Physics Letters* **96,** 121907. https://doi.org/10.1063/1.3364135 (2010).

39. Acosta, V. M. *et al.* Dynamic Stabilization of the Optical Resonances of Single Nitrogen-Vacancy Centers in Diamond. *Physical Review Letters* **108,** 206401. https://link.aps.org/doi/10.1103/PhysRevLett.108.206401 (2012).

40. Stacey, A. *et al.* Depletion of Nitrogen-Vacancy Color Centers in Diamond via Hydrogen Passivation. *Applied Physics Letters* **100,** 071902. https://doi.org/10.1063/1.3684612 (2012).

41. Siyushev, P. *et al.* Optically Controlled Switching of the Charge State of a Single Nitrogen-Vacancy Center in Diamond at Cryogenic Temperatures. *Physical Review Letters* **110,** 167402. https://link.aps.org/doi/10.1103/PhysRevLett.110.167402 (2013).

42. Chu, Y. *et al.* Coherent Optical Transitions in Implanted Nitrogen Vacancy Centers. *Nano Letters* **14.** PMID: 24588353, 1982–1986. https://doi.org/10.1021/nl404836p (2014).

43. Van Dam, S. B. *et al.* Optical Coherence of Diamond Nitrogen-Vacancy Centers Formed by Ion Implantation and Annealing. *Physical Review B* **99,** 161203. https://link.aps.org/doi/10.1103/PhysRevB.99.161203 (2019).

44. Riedel, D. *et al.* Deterministic Enhancement of Coherent Photon Generation from a Nitrogen-Vacancy Center in Ultrapure Diamond. *Physical Review X* **7,** 031040. https://link.aps.org/doi/10.1103/PhysRevX.7.031040 (2017).

45. Faraon, A., Santori, C., Huang, Z., Acosta, V. M. & Beausoleil, R. G. Coupling of Nitrogen-Vacancy Centers to Photonic Crystal Cavities in Monocrystalline Diamond. *Physical Review Letters* **109,** 033604. https://link.aps.org/doi/10.1103/PhysRevLett.109.033604 (2012).

46. Mouradian, S. L. *et al.* Scalable Integration of Long-Lived Quantum Memories into a Photonic Circuit. *Physical Review X* **5,** 031009. https://link.aps.org/doi/10.1103/PhysRevX.5.031009 (2015).

47. Smith, J. M., Meynell, S. A., Jayich, A. C. B. & Meijer, J. Colour Centre Generation in Diamond for Quantum Technologies. *Nanophotonics* **8,** 1889 –1906. https://www.degruyter.com/view/journals/nanoph/8/11/article-p1889.xml (2019).

48. Purcell, E. M., Torrey, H. C. & Pound, R. V. Resonance Absorption by Nuclear Magnetic Moments in a Solid. *Physical Review* **69,** 37–38. https://link.aps.org/doi/10.1103/PhysRev.69.37 (1946).

49. Faraon, A., Barclay, P. E., Santori, C., Fu, K.-M. C. & Beausoleil, R. G. Resonant enhancement of the Zero-Phonon Emission from a Colour Centre in a Diamond Cavity. *Nature Photonics* **5,** 301–305 (2011).

50. Gould, M., Schmidgall, E. R., Dadgostar, S., Hatami, F. & Fu, K.-M. C. Efficient Extraction of Zero-Phonon-Line Photons from Single Nitrogen-Vacancy Centers in an Integrated GaP-on-Diamond Platform. *Physical Review Applied* **6,** 011001. https://link.aps.org/doi/10.1103/PhysRevApplied.6.011001 (2016).

51. Li, L. *et al.* Coherent Spin Control of a Nanocavity-Enhanced Qubit in Diamond. *Nature Communications* **6,** 6173 (2015).

52. Johnson, S. *et al.* Tunable Cavity Coupling of the Zero Phonon Line of a Nitrogen-Vacancy defect in diamond. *New Journal of Physics* **17,** 122003 (2015).

53. Wang, C. F. *et al.* Observation of Whispering Gallery Modes in Nanocrystalline Diamond Microdisks. *Applied Physics Letters* **90,** 081110. https://doi.org/10.1063/1.2709626 (2007).

54. Barclay, P. E., Fu, K.-M. C., Santori, C. & Beausoleil, R. G. Chip-based Microcavities Coupled to Nitrogen-Vacancy Centers in Single Crystal Diamond. *Applied Physics Letters* **95,** 191115. https://doi.org/10.1063/1.3262948 (2009).

55. Fu, K.-M. C., Barclay, P. E., Santori, C., Faraon, A. & Beausoleil, R. G. Low-Temperature Tapered-Fiber Probing of Diamond Nitrogen-Vacancy Ensembles Coupled to GaP Microcavities. *New Journal of Physics* **13,** 055023. https://doi.org/10.1088/1367-2630/13/5/055023 (2011).

56. Englund, D. *et al.* Deterministic Coupling of a Single Nitrogen Vacancy Center to a Photonic Crystal Cavity. *Nano Letters* **10.** PMID: 20825160, 3922–3926. https://doi.org/10.1021/nl101662v (2010).

57. Hunger, D. *et al.* A Fiber Fabry–Perot Cavity with High Finesse. *New Journal of Physics* **12,** 065038. https://doi.org/10.1088/1367-2630/12/6/065038 (2010).

58. Gaebel, T. *et al.* Photochromism in Single Nitrogen-Vacancy Defect in Diamond. *Applied Physics B - Laser and Optics* **82,** 243–246 (2006).

59. Manson, N. B. *et al.* Assignment of the NV0 575-nm Zero-Phonon Line in Diamond to a 2E-2A2 Transition. *Physical Review B* **87,** 155209. https://link.aps.org/doi/10.1103/PhysRevB.87.155209 (2013).

60. Maze, J. R. *et al.* Properties of Nitrogen-Vacancy Centers in Diamond: the Group Theoretic Approach. *New Journal of Physics* **13,** 025025. https://doi.org/10.1088/1367-2630/13/2/025025 (2011).

61. Batalov, A. *et al.* Low Temperature Studies of the Excited-State Structure of Negatively Charged Nitrogen-Vacancy Color Centers in Diamond. *Physical Review Letters* **102,** 195506. https://link.aps.org/doi/10.1103/PhysRevLett.102.195506 (2009).

62. Rogers, L. J., McMurtrie, R. L., Sellars, M. J. & Manson, N. B. Time-Averaging within the Excited State of the Nitrogen-Vacancy Centre in Diamond. *New Journal of Physics* **11,** 063007. https://doi.org/10.1088/1367-2630/11/6/063007 (2009).

63. Tamarat, P. *et al.* Spin-Flip and Spin-Conserving Optical Transitions of the Nitrogen-Vacancy Centre in Diamond. *New Journal of Physics* **10,** 045004 (2008).

64. Bluvstein, D., Zhang, Z. & Jayich, A. C. B. Identifying and Mitigating Charge Instabilities in Shallow Diamond Nitrogen-Vacancy Centers. *Physical Review Letters* **122,** 076101. https://link.aps.org/doi/10.1103/PhysRevLett.122.076101 (2019).

65. Beha, K., Batalov, A., Manson, N. B., Bratschitsch, R. & Leitenstorfer, A. Optimum Photoluminescence Excitation and Recharging Cycle of Single Nitrogen-Vacancy Centers in Ultrapure Diamond. *Physical Review Letters* **109,** 097404. https://link.aps.org/doi/10.1103/PhysRevLett.109.097404 (2012).

66. Waldherr, G. *et al.* Dark States of Single Nitrogen-Vacancy Centers in Diamond Unraveled by Single Shot NMR. *Physical Review Letters* **106,** 157601. https://link.aps.org/doi/10.1103/PhysRevLett.106.157601 (2011).

67. Aslam, N., Waldherr, G., Neumann, P., Jelezko, F. & Wrachtrup, J. Photo-Induced Ionization Dynamics of the Nitrogen Vacancy Defect in Diamond Investigated by Single-Shot Charge State Detection. *New Journal of Physics* **15,** 013064. https://doi.org/10.1088/1367-2630/15/1/013064 (2013).

68. Hecht, E. *Optics* Fifth edition. Global edition. eng (Harlow, England : Pearson Education Limited, Harlow, England, 2017).

69. Van Dam, S. B., Ruf, M. & Hanson, R. Optimal Design of Diamond-Air Microcavities for Quantum Networks Using an Analytical Approach. *New Journal of Physics* **20,** 115004. https://doi.org/10.1088/1367-2630/aaec29 (2018).

70. Brooker, G. *Modern Classical Optics* eng (Oxford University Press, Oxford, 2003).

71. Orfanidis, S. *Electromagnetic Waves and Antennas* www.ece.rutgers.edu/~orfanidi/ewa (Orfanidis, S. J., 2016).

72. Milonni, P. W. & Eberly, J. H. *Laser Physics* eng (John Wiley & Sons, Hoboken, NJ, 2010).

73. Benedikter, J. *et al.* Transverse-Mode Coupling and Diffraction Loss in Tunable Fabry–Pérot Microcavities. *New Journal of Physics* **17,** 053051. https://doi.org/10.1088/1367-2630/17/5/053051 (2015).

74. Klaassen, T., van Exter, M. P. & Woerdman, J. P. Characterization of Scattering in an Optical Fabry-Perot Resonator. *Applied Optics* **46,** 5210–5215. http://ao.osa.org/abstract.cfm?URI=ao-46-22-5210 (2007).

75. Katsidis, C. C. & Siapkas, D. I. General Transfer-Matrix Method for Optical Multilayer Systems with Coherent, Partially Coherent, and Incoherent Interference. *Applied Optics* **41,** 3978–3987. http://ao.osa.org/abstract.cfm?URI=ao-41-19-3978 (2002).

76. Orwa, J. O. *et al.* Engineering of Nitrogen-Vacancy Color Centers in High Purity Diamond by Ion Implantation and Annealing. *Journal of Applied Physics* **109,** 083530. https://doi.org/10.1063/1.3573768 (2011).

77. Chen, Y.-C. *Laser Writing of Coherent Colour Centres in Diamond.* PhD thesis (University of Oxford, 2017).

78. Cui, S. *Near-surface Nitrogen Vacancy Centers in Diamond.* PhD thesis (Harvard University, 2014). http://nrs.harvard.edu/urn-3:HUL.InstRepos:13064815.

79. Osswald, S., Yushin, G., Mochalin, V., Kucheyev, S. O. & Gogotsi, Y. Control of sp2/sp3 Carbon Ratio and Surface Chemistry of Nanodiamond Powders by Selective Oxidation in Air. *Journal of the American Chemical Society* **128.** PMID: 16939289, 11635–11642. https://doi.org/10.1021/ja063303n (2006).

80. Favaro de Oliveira, F. *et al.* Effect of Low-Damage Inductively Coupled Plasma on Shallow Nitrogen-Vacancy Centers in Diamond. *Applied Physics Letters* **107,** 073107. https://doi.org/10.1063/1.4929356 (2015).

81. Moulder, J. F., Stickle, W. F., Sobol, P. E. & Bomben, K. D. *Handbook of X-Ray Photoelectron Spectroscopy: a Reference Book of Standard Spectra for Identification and Interpretation of XPS Data* (Physical Electronics, Inc., 1995).

82. Dolan, P. R., Hughes, G. M., Grazioso, F., Patton, B. R. & Smith, J. M. Femtoliter Tunable Optical Cavity Arrays. *Optics Letters* **35,** 3556–3558. http://ol.osa.org/abstract.cfm?URI=ol-35-21-3556 (2010).

83. Trichet, A. A. P., Dolan, P. R., Coles, D. M., Hughes, G. M. & Smith, J. M. Topographic Control of Open-Access Microcavities at the Nanometer Scale. *Optical Express* **23,** 17205–17216. http://www.opticsexpress.org/abstract.cfm?URI=oe-23-13-17205 (2015).

84. Olivero, J. J. & Longbothum, R. L. Empirical Fits to the Voigt Line Width: a Brief Review. *Journal of Quantitative Spectroscopy and Radiative Transfer* **17,** 233 –236. http://www.sciencedirect.com/science/article/pii/0022407377901613 (1977).

85. Kurtsiefer, C., Mayer, S., Zarda, P. & Weinfurter, H. Stable Solid-State Source of Single Photons. *Physical Review Letters* **85,** 290–293. https://link.aps.org/doi/10.1103/PhysRevLett.85.290 (2000).

86. Yee, K. Numerical Solution of Initial Boundary Value Problems Involving Maxwell's Equations in Isotropic Media. *IEEE Transactions on Antennas and Propagation* **14,** 302–307 (1966).

87. Inc., L. *Quality Factor Calculations for a Resonant Cavity* https://support.lumerical.com/hc/en-us/articles/360041611774.

88. Janitz, E. *et al.* Fabry-Perot Microcavity for Diamond-Based Photonics. *Physical Review A* **92,** 043844. https://link.aps.org/doi/10.1103/PhysRevA.92.043844 (2015).

89. Lehtinen, O. *et al.* Molecular Dynamics Simulations of Shallow Nitrogen and Silicon Implantation into Diamond. *Physical Review B* **93,** 035202. https://link.aps.org/doi/10.1103/PhysRevB.93.035202 (2016).

90. D'Haenens-Johansson, U., Katrusha, A., Soe moe, K., Johnson, P. & Wang, W. Large Colorless HPHT-Grown Synthetic Gem Diamonds from New Diamond Technology, Russia. *Gem & Gemology* **51,** 260–279 (2015).

91. Tallaire, A. *et al.* Thick CVD Diamond Films Grown on High-Quality Type IIa HPHT Diamond Substrates from New Diamond Technology. *Diamond and Related Materials* **77,** 146 –152. http://www.sciencedirect.com/science/article/pii/S092596351730287X (2017).

92. Nedy, J. G. *et al.* Low Damage Dry Etch for III-Nitride Light Emitters. *Semiconductor Science and Technology* **30,** 085019. https://doi.org/10.1088/0268-1242/30/8/085019 (2015).

93. Stephen, C. J. *et al.* Deep Three-Dimensional Solid-State Qubit Arrays with Long-Lived Spin Coherence. *Physical Review Applied* **12,** 064005. https://link.aps.org/doi/10.1103/PhysRevApplied.12.064005 (2019).

94. Zhao, H.-Q., Fujiwara, M. & Takeuchi, S. Suppression of Fluorescence Phonon Sideband from Nitrogen Vacancy Centers in Diamond Nanocrystals by Substrate Effect. *Optics Express* **20,** 15628–15635. http://www.opticsexpress.org/abstract.cfm?URI=oe-20-14-15628 (2012).

95. Chen, Y.-C. *et al.* Laser Writing of Individual Nitrogen-Vacancy Defects in Diamond with Near-Unity Yield. *Optica* **6,** 662–667. http://www.osapublishing.org/optica/abstract.cfm?URI=optica-6-5-662 (2019).

96. Ohno, K. *et al.* Engineering Shallow Spins in Diamond with Nitrogen Delta-Doping. *Applied Physics Letters* **101,** 082413 (2012).

97. Wan, N. H. *et al.* Efficient Extraction of Light from a Nitrogen-Vacancy Center in a Diamond Parabolic Reflector. *Nano Letters* **18.** PMID: 29601205, 2787–2793. https://doi.org/10.1021/acs.nanolett.7b04684 (2018).

98. Wang, X.-J. *et al.* Experimental Time-Resolved Interference with Multiple Photons of Different Colors. *Physical Review Letters* **121,** 080501. https://link.aps.org/doi/10.1103/PhysRevLett.121.080501 (2018).

99. Duan, Z.-C. *et al.* Quantum Beat between Sunlight and Single Photons. *Nano Letters* **20.** PMID: 31841348, 152–157 (2020).

100. Kaye, P., Laflamme, R. & Mosca, M. *An Introduction to Quantum Computing* (Oxford University Press, Oxford, 2007).

101. Bennett, C. H. & DiVincenzo, D. P. Quantum Information and Computation. *Nature* **404,** 247–255 (2000).

102. H., K. *Google and IBM Clash Over Milestone Quantum Computing Experiment* 2019. https://www.quantamagazine.org/google-and-ibm-clash-over-quantum-supremacy-claim-20191023.

103. Rogers, L. J., Armstrong, S., Sellars, M. J. & Manson, N. B. Infrared emission of the NV centre in diamond: Zeeman and uniaxial stress studies. *New Journal of Physics* **10,** 103024. https://doi.org/10.1088/1367-2630/10/10/103024 (2008).

104. Manson, N. & Harrison, J. Photo-Ionization of the Nitrogen-Vacancy Center in Diamond. *Diamond and Related Materials* **14,** 1705 –1710. http://www.sciencedirect.com/science/article/pii/S0925963505002402 (2005).

105. Liu, H. *Diamond Processing for Advanced Photonic Devices.* PhD thesis (Universtiy of Strathclyde, 2016).

106. Trichet, A. A. P., Dolan, P. R. & Smith, J. M. Strong Coupling between 0D and 2D Modes in Optical Open Microcavities. *Journal of Optics* **20,** 035402 (2018).

107. Huang, T.-Y. *et al.* A Monolithic Immersion Metalens for Imaging Solid-State Quantum Emitters. *Nature Communications* **10,** 2392 (2019).

108. Marseglia, L. *et al.* Nanofabricated Solid Immersion Lenses Registered to Single Emitters in Diamond. *Applied Physics Letters* **98,** 133107. https://doi.org/10.1063/1.3573870 (2011).

109. Siyushev, P. *et al.* Monolithic Diamond Optics for Single Photon Detection. *Applied Physics Letters* **97,** 241902. https://doi.org/10.1063/1.3519849 (2010).

110. Hadden, J. P. *et al.* Strongly Enhanced Photon Collection from Diamond Defect Centers under Microfabricated Integrated Solid Immersion Lenses. *Applied Physics Letters* **97,** 241901. https://doi.org/10.1063/1.3519847 (2010).

111. Santori, C., Barclay, P. E., Fu, K.-M. C. & Beausoleil, R. G. Vertical Distribution of Nitrogen-Vacancy Centers in Diamond Formed by Ion Implantation and Annealing. *Physical Review B* **79,** 125313. https://link.aps.org/doi/10.1103/PhysRevB.79.125313 (2009).

112. Lerondel, G. & Romestain, R. Fresnel Coefficients of a Rough Interface. *Applied Physics Letters* **74,** 2740–2742. https://doi.org/10.1063/1.123999 (1999).

113. Shih, Y. *Introduction to Quantum Optics: Photon and Biphoton Physics* (CRC Press, 2011).

114. Bernien, H. *et al.* Heralded Entanglement between Solid-State Qubits Separated by Three Metres. *Nature* **497,** 86–90 (2013).